

Elastic Wave Propagation Along a Borehole in an Anisotropic Medium

by

Karl John Ellefsen

M.S., University of Connecticut (1984)

B.S., University of Connecticut (1982)

B.S., Lehigh University (1977)

Submitted to the Department of Earth, Atmospheric, and Planetary Sciences

in partial fulfillment of the requirements for the degree of

Doctor of Science

at the

MASSACHUSETTS INSTITUTE OF TECHNOLOGY

June 1990

© Massachusetts Institute of Technology 1990

All rights reserved

Signature of Author
Department of Earth, Atmospheric, and Planetary Sciences
May 1, 1990

Certified by
M. Nafi Toksöz
Professor of Geophysics
Thesis Advisor

Certified by
Chuen H. Cheng
Principal Research Scientist
Thesis Co-Advisor

Accepted by
Thomas H. Jordan
Chairman

Department of Earth, Atmospheric, and Planetary Sciences

MASSACHUSETTS INSTITUTE
OF TECHNOLOGY
WITHDRAWN
FROM

Elastic Wave Propagation Along a Borehole in an Anisotropic Medium

by

Karl John Ellefsen

Submitted to the Department of Earth, Atmospheric, and Planetary Sciences
on May 1, 1990, in partial fulfillment of the
requirements for the degree of
Doctor of Science

Abstract

In the first part of this thesis, several applications of perturbation theory are developed to study normal mode propagation along a borehole. This theory is used to relate first order perturbations in frequency, wavenumber, elastic moduli, densities, and locations of interfaces. Although the perturbation equation is derived for a general model with many fluid and solid layers which have any cross-sectional shape, the equation is applied to a two-layer model consisting of a fluid-filled borehole through a transversely isotropic solid (with its symmetry axis parallel to the borehole). Because analytical expressions for the displacements exist for this particular model, the terms in the perturbation equation simplify greatly. Formulas are derived to calculate (1) phase velocities for a model with slight, general anisotropy, (2) partial derivatives of either the wavenumber or frequency with respect to either an elastic modulus or density, (3) group velocity, and (4) phase velocities for a model with a slightly irregular borehole. These formulas are applicable also to models with an isotropic solid because it is a special case of a transversely isotropic solid.

In the second part, the effects of anisotropy upon elastic wave propagation are determined. The wave equation is solved in the frequency-wavenumber domain with a variational method, and the solution yields the phase velocities, group velocities, pressures, and displacements for the normal modes. (The phase and group velocities obtained with this variational method match those obtained with the perturbation method indicating that both are correctly formulated and implemented.) These properties are studied for two cases: a transversely isotropic model for which the borehole has several different orientations with respect to the symmetry axis and an orthorhombic model for which the borehole is parallel to the intersection of two symmetry planes. The normal modes for these two cases show several effects which do not exist when the solid is isotropic or transversely isotropic with its symmetry axis parallel to the borehole:

1. The phase velocities for the quasi-pseudo-Rayleigh, both quasi-flexural, and both quasi-screw waves do not exceed the phase velocity of the slowest qS -wave. (The phase velocities of the leaky modes, which were not investigated, will exceed this threshold.)
2. The two quasi-flexural waves have different phase and group velocities; the differences are greatest at low frequencies and diminish as the frequency increases. In general, the two quasi-screw waves behave similarly.
3. The greater the difference between the phase velocities of the qS -waves, the greater the difference between the phase velocities of the quasi-flexural waves at all frequencies. The two quasi-screw waves behave similarly.
4. Near the limiting qS -wave velocity, the difference between the phase velocities of the two quasi-flexural waves is greater than that for the two quasi-screw waves.
5. For the slow quasi-flexural wave, the particle displacements in the plane perpendicular to the borehole, when viewed together, are aligned with the polarization of the slow qS -wave.
6. For the fast quasi-flexural wave, the particle displacements in the plane perpendicular to the borehole, when viewed together, are aligned with the polarization of the fast qS -wave.
7. For the slow quasi-screw wave, the particle displacements in the plane perpendicular to the borehole, when viewed together, are aligned along two mutually perpendicular directions which are rotated 45° with respect to the polarizations of both qS -waves.
8. For the fast quasi-screw wave, the particle displacements in the plane perpendicular to the borehole, when viewed together, are aligned along two mutually perpendicular directions which are parallel with the polarizations of both qS -waves.

(In this list, the qS -waves are those plane waves whose wavenumber vectors are parallel to the borehole.) Despite these significant effects, the general characteristics of the phase and group velocities, pressures, and displacements are similar (but not identical) to those that would exist if the solid were isotropic or transversely isotropic with its symmetry axis parallel to the borehole. This result is expected because the models are only slightly anisotropic.

In the last part, a method to estimate c_{66} , which is a shear modulus of a transversely isotropic formation (with its symmetry axis parallel to the borehole), is developed and tested. The inversion for c_{66} is based upon a cost function which has three terms: a measure of the misfit between the observed and predicted wavenumbers, a measure of the misfit between the current estimate for c_{66} and the initial guess of its

value, and penalty functions which constrain the estimate for c_{66} to physically acceptable values. The inversion is applied to synthetic data for fast and slow formations, and the estimates for c_{66} are within 5% of their correct values and are moderately well resolved. When the inversion was applied to field data, the estimates for c_{66} were significantly higher than the values for c_{44} in a zone with low permeability and high clay content. The percentage of S -wave anisotropy ranged from 5 to 20%.

Thesis Advisor: M. Nafi Toksöz

Title: Professor of Geophysics

Thesis Co-Advisor: Chuen H. Cheng

Title: Principal Research Scientist

Acknowledgments

I wish to thank the staff and students of Earth Resources Laboratory. Nafi Toksöz, Arthur Cheng, Roger Turpening, and others have created a stimulating research environment at ERL which has helped all students. I especially appreciate their efforts to teach the students to think independently and critically. Sara Brydges, Naida Buckingham, Dan Burns, Ted Charrette, Carol Caravana, Vern Cormier, Anton Dainty, Rick Gibson, Steve Gildea, Liz Henderson, Jane Maloof, Batakrishna Mandal, Joe Matarese, Jim Mendelson, Jeff Meredith, Mike Prange, Arcangelo Sena, Denny Schmidt, Xiao-ming Tang, Al Taylor, and Sue Turbak have been helpful with technical and administrative matters. My wife, Lisa Block, who is also an ERL student deserves special recognition for her friendship and support.

I also wish to acknowledge several people outside ERL. Greg Duckworth and Gene Simmons were my advisors during my first two years at MIT. Eduardo Kausel gave me valuable advise about using finite elements to simulate wave propagation.

During two summers, I learned some of the basics of acoustic logging from Michael Williams and Joesph Zemanek at Mobil Research and Development Corporation and from Kenneth Tubman at ARCO Oil and Gas Company. I am also grateful to ARCO Oil and Gas Company for providing the televiwer data and logging data which are used in Chapters 2 and 4, respectively.

Part of my financial support has come from the fellowship provided by the Phillips Petroleum Company.

Contents

1	Introduction	9
1.1	Background	9
1.2	Scope	10
1.3	Review Topics	12
1.3.1	Historical Background	12
1.3.2	Abbreviated Subscript Notation	16
1.3.3	Elastic Symmetry	23
1.3.4	Plane Wave Propagation	26
1.3.5	Normal Modes Propagating along a Borehole	29
2	Applications of Perturbation Theory to the Normal Modes	52
2.1	Introduction	52
2.2	Derivation of the Perturbation Equation	53
2.3	Applications	58
2.3.1	Phase Velocities for a Slightly Anisotropic Solid	61
2.3.2	Partial Derivatives	62
2.3.3	Group Velocities	64
2.3.4	Phase Velocities for a Slightly Irregular Borehole	65
2.4	Summary	66
3	Effects of Anisotropy upon the Normal Modes	83

3.1	Introduction	83
3.2	Method	85
3.2.1	Formulation	85
3.2.2	Solution	91
3.2.3	Discussion of the Method	101
3.3	Results	104
3.3.1	Transversely Isotropic Models	105
3.3.2	Orthorhombic Model	107
3.3.3	Discussion of the Results	108
3.4	Summary and Conclusions	110
4	Estimating a Shear Modulus of a Transversely Isotropic Formation	159
4.1	Introduction	159
4.2	Method	160
4.3	Results and Discussion	163
4.3.1	Sensitivity of the Data to the Elastic Moduli	163
4.3.2	Testing the Inversion with Synthetic Data	165
4.3.3	Field Data	166
4.4	Conclusions	169
5	Summary and Conclusions	202
	Appendices	
A	Propagation along a Borehole in a Transversely Isotropic Medium	206
A.1	Propagation in the Fluid	207
A.2	Propagation in the Solid	208
A.3	Dispersion Equation	215
B	Evaluation of an Integrand in the Perturbation Equation	219
C	Evaluation of the Integrals in the Perturbation Equation	221

D Separability of the Wave Equation	228
E Sensitivities of the Wavenumbers for the Normal Modes	232
References	262

Chapter 1

Introduction

1.1 Background

For the first part of this century, seismologists obtained a good match between seismic data and predictions based upon an isotropic model of the Earth. As the quality of seismic data improved, particularly within the last thirty years, seismologists sometimes noted significant discrepancies between the data and the model predictions. A hypothesis, which accounts for some of these discrepancies and which is now generally accepted, is that some parts of the Earth are anisotropic. This hypothesis is further substantiated by laboratory measurements and mathematical models of rocks (White and Angona, 1955; Backus, 1962; Thill et al., 1973; Thomsen, 1986).

The anisotropy is related to geological processes and rock properties which have scientific importance. One example is the anisotropy caused by fractured rock. When rocks containing fractures are subjected to a nonhydrostatic stress in a laboratory, the rock becomes anisotropic because the open fractures tend to be aligned (Nur and Simmons, 1969). Hence anisotropy in the crust caused by aligned fractures might be used to determine some components of the deviatoric stress tensor. In addition, because the open fractures affect the flow of fluids, the anisotropy might be used to predict the likely directions of flow. Another example is transverse isotropy with a

vertical symmetry axis which is prevalent in sedimentary basins (Winterstein, 1986). Better images of the subsurface geology could be obtained if the processing of the seismic data accounted for the effects of this transverse isotropy.

One technique which might measure the anisotropy of the crust is acoustic logging. Logging refers to a large variety of measurements which are made inside boreholes and whose purpose is usually to determine a property of the rocks around the borehole. That measurement which involves elastic wave propagation is called acoustic logging. Waves are generated by a source in the borehole and propagate either along the borehole (where they can be detected by a receiver) or into the formation. Because surface waves, which are similar to borehole waves, are affected by anisotropy (see e.g., Farnell, 1970), the borehole waves should be able to detect the anisotropy.

1.2 Scope

The goal of this thesis is to determine how anisotropy can be detected with acoustic logging. To this end, the thesis addresses two issues: the effects of general anisotropy upon elastic wave propagation in a borehole and the estimation of a shear modulus of a transversely isotropic formation. In regard to the later issue, an ideal inversion could estimate all of the elastic moduli of a formation with general anisotropy. However, this ideal inversion is not practical because the elastic waves which are recorded during acoustic logging are not sensitive to all of the elastic moduli. Consequently, the inversion is developed specifically to estimate a shear modulus of a transversely isotropic formation because the data are sensitive to this modulus and transversely isotropy is believed to be the largest component of anisotropy in many sedimentary rocks (S. Crampin, 1988, oral communication; D. Corrigan, 1989, oral communication; D. F. Winterstein, 1989, oral communication).

The thesis is divided into five chapters. In the next section of this chapter is a review of several topics: historical background on wave propagation for a cylindrical

geometry, abbreviated subscript notation, elastic symmetry, plane wave propagation in anisotropic media, and normal mode propagation along a borehole in an isotropic formation.

In Chapter 2, perturbation theory is applied to four different problems related to normal mode propagation. First a method to calculate the phase velocities of the modes when the solid has general anisotropy is developed; these calculated velocities are an independent check of the results presented in Chapter 3. Second, a method to calculate partial derivatives is developed. These derivatives are an important part of the inversion which is presented in Chapter 4. Third, a method of calculating group velocities is developed. Fourth, a method to calculate the phase velocities of the modes when the borehole wall is irregular is derived. Examples of each application are presented also.

In Chapter 3, elastic wave propagation along a borehole in a general anisotropic medium is studied. To this end the wave equation is solved with a variational method, and the behavior of the normal modes is determined by studying their phase velocities, group velocities, and particle displacements. Special attention is given to the modes commonly encountered during acoustic logging: the tube, pseudo-Rayleigh, flexural, and screw waves.

In Chapter 4, the tube wave is used to estimate a shear modulus of a transversely isotropic formation with its symmetry axis parallel to the borehole, which is a good model for many sedimentary rocks like shales. The estimation is performed in the frequency-wavenumber domain. The method is tested with synthetic data from fast, slow, and very slow formations and also is applied to field data.

Chapter 5 is a summary of the most important results obtained in this thesis.

Although the problems addressed in this thesis are important to people who study acoustic logging, the problems should be pertinent to a much larger audience. People who study vertical seismic profiling will be interested in how the anisotropy affects the tube wave. The variational method developed in Chapter 3 could be modified to

study wave propagation in many structures like the Earth, composite materials, and semiconductors. Civil engineers, who must know the shear properties of soils and other construction materials, will find that the inversion in Chapter 4 is relevant to their work.

1.3 Review Topics

1.3.1 Historical Background

The early investigations related to wave propagation for a circular cylindrical geometry applied to rods which were isotropic and had a finite length. The rod was assumed to be very long compared to its diameter, and so a reasonable approximation, which was used to simplify the mathematics, was that the mass of the rod was concentrated along its axis (see Rayleigh 1878, Chapters 7 and 8). Pochhammer (1876) derived the solution for propagation along an infinite cylinder without making any assumption about the concentration of the mass. His solutions were for the so called longitudinal modes whose displacements are in the radial and axial directions and are independent of azimuth. Apparently independently, Chree (1886) developed a solution for the longitudinal modes in a cylinder with finite length. Later Chree (1889) developed the dispersion equation for longitudinal modes in cylinders and cylindrical shells with infinite length and the equations describing the vibrations of these structures due to surface and body forces. The expressions for the torsional and flexural modes in a cylinder with infinite length were derived by Love (1892, Sections 200 and 202). (A torsional mode has displacements in the tangential direction which are independent of azimuth (θ), and a flexural mode has radial and axial displacements that depend upon the $\cos \theta$ and tangential displacements that depend upon $\sin \theta$. A flexural mode is also called a transverse mode.) Using the Rayleigh-Ritz method to study wave propagation along a isotropic cylinder, Kynch (1955) found a mode, for which radial and axial displacements vary according to $\cos 2\theta$ and the tangential displacements

according to $\sin 2\theta$, and he called it a screw wave. The recent research in this field is summarized by Redwood (1960), Miklowitz (1978), and Thurston (1978), and an extensive compilation of the frequencies and displacements for the modes in different cylinders and cylindrical shells is given by Armenàkas et al. (1969).

Several theoretical investigations have focused on elastic wave propagation in a solid circular cylinder which is transversely isotropic with the symmetry axis parallel to the axis of the cylinder. Chree (1890) developed a solution for the longitudinal modes in a cylinder with finite length. Because he expresses the displacements with the first few terms of a power series in radial distance, his solution is valid only when the diameter of the cylinder is small compared to its total length. Morse (1954) developed a solution for the longitudinal modes in an infinite cylinder. Since the displacements in his solution are expressed with Bessel functions, no restrictions on the diameter of the cylinder are necessary. Einspruch and Truell (1959) extended Morse's formulation to the torsional modes and showed that they are not coupled to the longitudinal modes. Mirsky (1965) and Eliot and Mott (1967) found a complete solution to the wave equation and derived dispersion equations for all of the modes (i.e., longitudinal, torsional, flexural, screw, and all higher order modes) in infinite cylinders and cylindrical shells. The solution to the wave equation for longitudinal modes propagating along a cylindrical shell with three transversely isotropic layers was found by Keck and Armenàkas (1971).

Wave propagation along infinite cylinders and cylindrical shells, whose anisotropy is defined in the cylindrical coordinate system (see Love, 1892, section 110) and is more general than transverse isotropy, has also been investigated. Using a power series expansion, Mirsky (1964) and Nowinski (1967) derived the solution for the longitudinal mode in a cylinder with orthorhombic anisotropy. Using a power series expansion also, Chou and Achenbach (1972) and Armenàkas and Reitz (1973) developed the solution for all modes in a cylinder with orthorhombic anisotropy. What was clear from the research done by these four groups was that deriving a solution for a simple

cylinder required an enormous amount of algebra and that deriving a solution for a cylinder with multiple, concentric layers would be a daunting task. For this reason, Nelson et al. (1971) used a variational method to develop a complete solution to the wave equation for cylinders and cylindrical shells with orthorhombic anisotropy. They used analytical expressions for propagation in the axial and tangential directions and finite elements for propagation in the radial direction. The great advantage of their approach is that same computer program could easily calculate solutions for cylinders or cylindrical shells with any number of layers and with any type of anisotropy having higher symmetry than orthorhombic anisotropy. This variational method was developed further by Huang and Dong (1984) to study propagation in cylinders and cylindrical shells with general anisotropy. (Note that problems studied in Chapters 2 and 3 differ significantly from those mentioned here. That is, Chapters 2 and 3 apply to wave propagation in a cylindrical geometry with the anisotropy defined in the Cartesian coordinate system, whereas the anisotropy in the problems reviewed here is defined in the circular cylindrical coordinate system.)

The basic theory related to wave propagation in a fluid-filled borehole, which is the model used in acoustic logging, has followed three complimentary lines of development. First, the dispersion equation related to guided wave propagation was derived, and this equation was used to calculate phase and group velocities to gain some insight into the behavior of the waves (Biot, 1952; Peterson, 1974). Second, numerical methods were developed to calculate synthetic seismograms which were studied to determine how the amplitude and attenuation of the waves is affected by the formation, fluid, and tool (White and Zechman, 1968; Roever et al., 1974; Tsang and Kong, 1979; Tsang and Rader, 1979; Cheng and Toksöz, 1981; Kurkjian, 1985; Kurkjian and Chang, 1986). Third, perturbation theory has been used to calculate partial derivatives in the frequency-wavenumber domain, which reseachers use to determine how different formation and fluid properties affect the phase velocities of the modes (Cheng et al., 1982; Burns, 1986).

Many researchers have studied wave propagation in complicated borehole models to gain a better understanding of how the actual conditions in the Earth affect the waves. The complications include permeable rock (Rosenbaum, 1974; Schmitt, 1988a; Schmitt et al., 1988; Norris, 1989; Schmitt 1989), a damaged or invaded zone around the borehole or a cased borehole (Chan and Tsang, 1983; Tubman et al., 1984; Stephen et al., 1985; Tubman et al., 1986; Burns, 1986; Schmitt, 1988a; Schmitt, 1988b; Schmitt, 1989), a viscous fluid (Burns, 1988), a borehole with an irregular cross section (Willen, 1983; Nicoletis et al., 1990), a borehole in which the diameter changes along the axis (Bouchon and Schmitt, 1989), fractures intersecting the borehole (Bhasavanija, 1983; Mathieu, 1984; Stephen et al., 1985), and anisotropy. Tongtaow (1980), White and Tongtaow (1981), Tongtaow (1982), Chan and Tsang (1983), and Schmitt (1989) focused on the special case of transversely isotropy with the symmetry axis aligned with the borehole. White and Tongtaow studied the waves generated by monopole and dipole sources and determined what affects the velocities and amplitudes of the refracted and guided waves. Chan and Tsang examined the amplitudes and velocities of the refracted waves in concentrically-layered, transversely isotropic formations. Schmitt studied the velocity dispersion curves, the attenuation curves, and the frequency-dependent sensitivities for the normal modes when the formation is transversely isotropic and permeable. Recently, some researchers have focused on transverse isotropy when the symmetry axis is perpendicular to the borehole. Leveille and Seriff (1989) determined the particle motion of the tube wave at the zero frequency limit, and they studied the horizontal displacement on the inner wall of a finite length, cylindrical shell which has been excited by a horizontal point force. Nicoletis et al. (1990) determined the phase velocity and particle displacements of a tube wave at the zero frequency limit.

Some researchers are using the waves to estimate the properties of the rocks surrounding the borehole. The estimated properties include the *S*-wave velocity of the formation (Cheng and Toksöz, 1983; Stevens and Day, 1986), permeability (Cheng et

al., 1987), attenuation (Burns, 1987), effective aperture of a fracture (Hornby et al., 1989a), and the structure around borehole (Pasternoster, 1985; Hornby, 1989b).

1.3.2 Abbreviated Subscript Notation

Throughout this thesis abbreviated subscript notation is used to perform tensor algebra. This notation has two outstanding advantages: it performs the algebra in a systematic manner reducing the likelihood of an error, and it expresses the tensors in terms of vectors and matrices which can be readily incorporated into a computer program. In this section, this notation will be presented following the conventions established by Bond (1943), Nye (1957, p. 134-137), Hearmon (1961, p. 8-9), Fedorov (1968, p. 13-18), Musgrave (1970, p. 32-34), and Auld (1973, p. 27-29, 49-52, 64-67, 73-82, 351-352, 354-356).

Cartesian Coordinates

In Cartesian coordinates, the strain tensor

$$\mathcal{E} = \begin{pmatrix} e_{xx} & e_{xy} & e_{xz} \\ e_{xy} & e_{yy} & e_{yz} \\ e_{xz} & e_{yz} & e_{zz} \end{pmatrix} , \quad (1.1)$$

is replaced by the strain vector,

$$\mathbf{E} = \begin{pmatrix} e_{xx} \\ e_{yy} \\ e_{zz} \\ 2e_{yz} \\ 2e_{xz} \\ 2e_{xy} \end{pmatrix} . \quad (1.2)$$

The factor of 2 is introduced to simplify Hooke's Law and the wave equation. Its elements are

$$\mathbf{E} = \begin{pmatrix} \partial_x u_x \\ \partial_y u_y \\ \partial_z u_z \\ \partial_y u_z + \partial_z u_y \\ \partial_x u_z + \partial_z u_x \\ \partial_y u_x + \partial_x u_y \end{pmatrix} \quad (1.3)$$

(Malvern, 1969, p. 131) where $\partial_x u_x$ means $\frac{\partial u}{\partial x}$, etc.

The stress tensor,

$$\mathcal{T} = \begin{pmatrix} \tau_{xx} & \tau_{xy} & \tau_{xz} \\ \tau_{xy} & \tau_{yy} & \tau_{yz} \\ \tau_{xz} & \tau_{yz} & \tau_{zz} \end{pmatrix} , \quad (1.4)$$

is replaced by the stress vector,

$$\mathbf{T} = \begin{pmatrix} \tau_{xx} \\ \tau_{yy} \\ \tau_{zz} \\ \tau_{yz} \\ \tau_{xz} \\ \tau_{xy} \end{pmatrix} . \quad (1.5)$$

The fourth order stiffness tensor is replaced by a 6×6 symmetric matrix according to the rules in Table 1.1 which are based upon the symmetry properties of the tensor.

The stiffness matrix is

$$\mathbf{C} = \begin{pmatrix} c_{11} & c_{12} & c_{13} & c_{14} & c_{15} & c_{16} \\ & c_{22} & c_{23} & c_{24} & c_{25} & c_{26} \\ & & c_{33} & c_{34} & c_{35} & c_{36} \\ & & & c_{44} & c_{45} & c_{46} \\ & & & & c_{55} & c_{56} \\ \text{symmetric} & & & & & c_{66} \end{pmatrix} . \quad (1.6)$$

The divergence of the stress vector, which is needed in the wave equation, is calculated with an operator:

$$\mathbf{D} = \begin{pmatrix} \partial_x & 0 & 0 & 0 & \partial_z & \partial_y \\ 0 & \partial_y & 0 & \partial_z & 0 & \partial_x \\ 0 & 0 & \partial_z & \partial_y & \partial_x & 0 \end{pmatrix} \quad (1.7)$$

(Auld, 1973, p. 51).

Using this notation, the wave equation is

$$\mathbf{D}\mathbf{T} = \rho\partial_{tt}\mathbf{u} \quad (1.8)$$

where \mathbf{u} is the displacement vector and t is time. The constitutive equation (i.e., Hooke's Law) is

$$\mathbf{T} = \mathbf{C}\mathbf{E} \quad . \quad (1.9)$$

Cylindrical Coordinates

In cylindrical coordinates, the strain tensor,

$$\mathcal{E}_c = \begin{pmatrix} e_{rr} & e_{r\theta} & e_{rz} \\ e_{r\theta} & e_{\theta\theta} & e_{\theta z} \\ e_{rz} & e_{\theta z} & e_{zz} \end{pmatrix} \quad , \quad (1.10)$$

is replaced by the strain vector,

$$\mathbf{E}_c = \begin{pmatrix} e_{rr} \\ e_{\theta\theta} \\ e_{zz} \\ 2e_{\theta z} \\ 2e_{rz} \\ 2e_{r\theta} \end{pmatrix} \quad . \quad (1.11)$$

Its elements are

$$\mathbf{E}_c = \begin{pmatrix} \partial_r u_r \\ (\partial_\theta u_\theta + u_r)/r \\ \partial_z u_z \\ \partial_z u_\theta + \partial_\theta u_z/r \\ \partial_z u_r + \partial_r u_z \\ \partial_r u_\theta + (\partial_\theta u_r - u_\theta)/r \end{pmatrix} \quad (1.12)$$

(Malvern, 1969, p. 668).

The stress tensor,

$$\mathcal{T}_c = \begin{pmatrix} \tau_{rr} & \tau_{r\theta} & \tau_{rz} \\ \tau_{r\theta} & \tau_{\theta\theta} & \tau_{\theta z} \\ \tau_{rz} & \tau_{\theta z} & \tau_{zz} \end{pmatrix}, \quad (1.13)$$

is replaced by the stress vector,

$$\mathbf{T}_c = \begin{pmatrix} \tau_{rr} \\ \tau_{\theta\theta} \\ \tau_{zz} \\ \tau_{\theta z} \\ \tau_{rz} \\ \tau_{r\theta} \end{pmatrix}. \quad (1.14)$$

The stiffness matrix in cylindrical coordinates, \mathbf{C}_c , is symmetric and has size 6×6 . The matrix is written in the same manner as the stiffness matrix in Cartesian coordinates is.

The divergence operator, which is used in the wave equation, is

$$\mathbf{D}_c = \begin{pmatrix} \partial_r + 1/r & -1/r & 0 & 0 & \partial_z & \partial_\theta/r \\ 0 & \partial_\theta/r & 0 & \partial_z & 0 & \partial_r + 2/r \\ 0 & 0 & \partial_z & \partial_\theta/r & \partial_r + 1/r & 0 \end{pmatrix} \quad (1.15)$$

(Auld, 1973, p. 354).

The wave equation in cylindrical coordinates is

$$\mathbf{D}_c \mathbf{T}_c = \rho \partial_{tt} \mathbf{u}_c \quad (1.16)$$

where \mathbf{u}_c is the displacement vector, and the constitutive equation is

$$\mathbf{T}_c = \mathbf{C}_c \mathbf{E}_c \quad . \quad (1.17)$$

Coordinate Transformations

The transformation laws for the stress vector, strain vector, and stiffness matrix are developed from the transformation laws of the equivalent tensors. The transformation of the stress tensor from one Cartesian coordinate system to another (which is denoted with a prime) is

$$\tau_{i'j'} = a_{i'k} a_{j'l} \tau_{kl} \quad (1.18)$$

where

$$k, l = x, y, z \quad (1.19)$$

$$i', j' = x', y', z' \quad (1.20)$$

(Jeffreys, 1931, p. 4). The factor, $a_{i'k}$, is a direction cosine: the cosine of angle between the axis labeled i' and that labeled k . One component of the stress tensor is

$$\tau_{x'x'} = a_{x'x}^2 \tau_{xx} + a_{x'y}^2 \tau_{yy} + a_{x'z}^2 \tau_{zz} + 2a_{x'y} a_{x'z} \tau_{yz} + 2a_{x'x} a_{x'z} \tau_{xz} + 2a_{x'x} a_{x'y} \tau_{xy} \quad . \quad (1.21)$$

The transformation law in abbreviated subscript notation is derived by writing all six equations (for the six components of stress) as one system:

$$\mathbf{T}' = \mathbf{M} \mathbf{T} \quad (1.22)$$

where the elements of \mathbf{M} are

$$m_{11} = n_{11} = a_{x'x}^2$$

$$m_{12} = n_{12} = a_{x'y}^2$$

$$\begin{aligned}
m_{13} &= n_{13} = a_{x'z}^2 \\
m_{14} &= 2n_{14} = 2a_{x'y}a_{x'z} \\
m_{15} &= 2n_{15} = 2a_{x'z}a_{x'x} \\
m_{16} &= 2n_{16} = 2a_{x'x}a_{x'y} \\
m_{21} &= n_{21} = a_{y'x}^2 \\
m_{22} &= n_{22} = a_{y'y}^2 \\
m_{23} &= n_{23} = a_{y'z}^2 \\
m_{24} &= 2n_{24} = 2a_{y'y}a_{y'z} \\
m_{25} &= 2n_{25} = 2a_{y'z}a_{y'x} \\
m_{26} &= 2n_{26} = 2a_{y'x}a_{y'y} \\
m_{31} &= n_{31} = a_{z'x}^2 \\
m_{32} &= n_{32} = a_{z'y}^2 \\
m_{33} &= n_{33} = a_{z'z}^2 \\
m_{34} &= 2n_{34} = 2a_{z'y}a_{z'z} \\
m_{35} &= 2n_{35} = 2a_{z'z}a_{z'x} \\
m_{36} &= 2n_{36} = 2a_{z'x}a_{z'y} \\
m_{41} &= \frac{n_{41}}{2} = a_{y'x}a_{z'x} \\
m_{42} &= \frac{n_{42}}{2} = a_{y'y}a_{z'y} \\
m_{43} &= \frac{n_{43}}{2} = a_{y'z}a_{z'z} \\
m_{44} &= n_{44} = a_{y'y}a_{z'z} + a_{y'z}a_{z'y} \\
m_{45} &= n_{45} = a_{y'x}a_{z'z} + a_{y'z}a_{z'x} \\
m_{46} &= n_{46} = a_{y'y}a_{z'x} + a_{y'x}a_{z'y} \\
m_{51} &= \frac{n_{51}}{2} = a_{z'x}a_{x'x} \\
m_{52} &= \frac{n_{52}}{2} = a_{z'y}a_{x'y} \\
m_{53} &= \frac{n_{53}}{2} = a_{z'z}a_{x'z}
\end{aligned} \tag{1.23}$$

$$\begin{aligned}
m_{54} &= n_{54} = a_{x'y}a_{z'z} + a_{x'z}a_{z'y} \\
m_{55} &= n_{55} = a_{x'x}a_{z'z} + a_{x'z}a_{z'x} \\
m_{56} &= n_{56} = a_{x'y}a_{z'x} + a_{x'x}a_{z'y} \\
m_{61} &= \frac{n_{61}}{2} = a_{x'x}a_{y'x} \\
m_{62} &= \frac{n_{62}}{2} = a_{x'y}a_{y'y} \\
m_{63} &= \frac{n_{63}}{2} = a_{x'z}a_{y'z} \\
m_{64} &= n_{64} = a_{x'y}a_{y'z} + a_{x'z}a_{y'y} \\
m_{65} &= n_{65} = a_{x'x}a_{y'z} + a_{x'z}a_{y'x} \\
m_{66} &= n_{66} = a_{x'y}a_{y'x} + a_{x'x}a_{y'y}
\end{aligned}$$

The derivation of the transformation law for the stress vector is very similar, and the law is

$$\mathbf{E}' = \mathbf{N}\mathbf{E} \quad (1.24)$$

where the elements of \mathbf{N} are listed in equation 1.23.

To derive the transformation law for the stiffness matrix, the constitutive equation (1.9) is multiplied on the left by \mathbf{M} to get the stress in the rotated coordinate system:

$$\mathbf{T}' = \mathbf{M}\mathbf{C}\mathbf{E} \quad (1.25)$$

Using equation 1.24, the previous equation can be expressed in terms of the strain in the rotated coordinate system:

$$\mathbf{T}' = \mathbf{M}\mathbf{C}\mathbf{N}^{-1}\mathbf{E}' \quad (1.26)$$

Because

$$\mathbf{M}^T = \mathbf{N}^{-1}, \quad (1.27)$$

(Bond, 1943), the stiffness matrix in the rotated coordinate system is

$$\mathbf{C}' = \mathbf{M}\mathbf{C}\mathbf{M}^T \quad (1.28)$$

In some parts of this thesis, the orientation of an anisotropic rock is changed with respect to the Cartesian coordinate system using a coordinate transformation. The change is specified by the Euler angles, ϕ , θ , and ψ (see Auld, 1973, p. 81-82). Using equation 1.28 the first rotation is about the z axis by the amount $\phi = -\xi$ with

$$\mathbf{M}(\xi) = \begin{pmatrix} \cos^2 \xi & \sin^2 \xi & 0 & 0 & 0 & \sin 2\xi \\ \sin^2 \xi & \cos^2 \xi & 0 & 0 & 0 & -\sin 2\xi \\ 0 & 0 & 1 & 0 & 0 & 0 \\ 0 & 0 & 0 & \cos \xi & -\sin \xi & 0 \\ 0 & 0 & 0 & \sin \xi & \cos \xi & 0 \\ -\frac{1}{2} \sin 2\xi & \frac{1}{2} \sin 2\xi & 0 & 0 & 0 & \cos 2\xi \end{pmatrix}. \quad (1.29)$$

The second rotation is about the y axis by the amount $\theta = -\eta$ with

$$\mathbf{M}(\eta) = \begin{pmatrix} \cos^2 \eta & 0 & \sin^2 \eta & 0 & -\sin 2\eta & 0 \\ 0 & 1 & 0 & 0 & 0 & 0 \\ \sin^2 \eta & 0 & \cos^2 \eta & 0 & \sin 2\eta & 0 \\ 0 & 0 & 0 & \cos \eta & 0 & \sin \eta \\ \frac{1}{2} \sin 2\eta & 0 & -\frac{1}{2} \sin 2\eta & 0 & \cos 2\eta & 0 \\ 0 & 0 & 0 & -\sin \eta & 0 & \cos \xi \end{pmatrix}. \quad (1.30)$$

The third and final rotation is about the z axis by the amount $\psi = -\xi$ with $\mathbf{M}(\psi)$ given in equation 1.29.

1.3.3 Elastic Symmetry

Although the techniques developed in Chapters 2 and 3 can simulate wave propagation along a borehole when the solid has any type of anisotropy defined in the Cartesian coordinate system, only a few types are good models of actual rocks. In this section, elastic symmetry will be used to define what is meant by the type of anisotropy, and the different symmetries that are good models of rocks will be discussed.

The symmetry operations which are important in elasticity are reflection with respect to a plane and rotation about an axis by some angle (Love, 1892, section

104). (The symmetry operations that are used for crystals are more sophisticated, and curious readers may consult Phillips (1963, p. 2-8), Bhagavantam (1966, p. 35-64) and Buerger (1971, p. 20-51).) A medium has elastic symmetry if its strain energy function remains the same after a symmetry operation, and this situation occurs only when the stiffness matrix does not change during an operation (Love, 1892, section 105). Because an operation can be specified with direction cosines, the operation on the stiffness matrix can be described with equation 1.28:

$$\mathbf{C} = \mathbf{MCM}^T \quad . \quad (1.31)$$

(A exhaustive list of direction cosines, which are used to generate \mathbf{M} for the types of anisotropy found in crystals, is given by Auld (1973, p. 196-206).)

For an isotropic solid, every plane is a plane of symmetry, every axis is an axis of symmetry, and the angle of rotation about an axis can be any amount (Love, 1892, section 106). This solid has two independent elastic constants, and its stiffness matrix is

$$\begin{pmatrix} c_{11} & c_{13} & c_{13} & 0 & 0 & 0 \\ & c_{11} & c_{13} & 0 & 0 & 0 \\ & & c_{11} & 0 & 0 & 0 \\ & & & c_{44} & 0 & 0 \\ & & & & c_{44} & 0 \\ \text{symmetric} & & & & & c_{44} \end{pmatrix}$$

where $c_{11} = c_{13} + 2c_{44}$ (Nye, 1957, p. 141; Hearmon, 1961, p. 22-24; Fedorov, 1968, p. 33; Musgrave, 1970, p. 57; Auld, 1973, p. 363). In terms of the Lamé parameters, $\lambda = c_{13}$, $\mu = c_{44}$, and $\lambda + 2\mu = c_{11}$. Isotropic solids are often used to model the behavior of actual rocks, and consequently the solution of the wave equation is derived frequently for isotropic solids (see e.g., Bullen, 1963; Aki and Richards, 1980; Ben-Menahem and Singh, 1981; and White, 1983).

A transversely isotropic solid has one axis of symmetry which can have any amount of rotation and one plane of symmetry which is perpendicular to the axis (Love, 1892,

section 110). This solid has five independent elastic constants, and when this axis of symmetry is parallel to the z axis the stiffness matrix is

$$\begin{pmatrix} c_{11} & c_{12} & c_{13} & 0 & 0 & 0 \\ & c_{11} & c_{13} & 0 & 0 & 0 \\ & & c_{33} & 0 & 0 & 0 \\ & & & c_{44} & 0 & 0 \\ & & & & c_{44} & 0 \\ \text{symmetric} & & & & & c_{66} \end{pmatrix}$$

where $c_{12} = c_{11} - 2c_{66}$. Transverse isotropy is also called azimuthal isotropy, cross anisotropy, hexagonal anisotropy, and polar anisotropy. Transverse isotropy is used to model the elastic properties of sedimentary rocks (see e.g., Thomsen, 1986; Winterstein, 1986), of rocks with aligned fractures (see e.g., Crampin, 1984; Schoenberg and Douma, 1988), and of formations with beds which are thin compared to a wavelength of an elastic wave (see e.g., White and Angona, 1955; Backus, 1962).

An orthorhombic solid has three mutually perpendicular planes of symmetry (Love, 1892, section 110). When these planes are parallel to the coordinate planes, the stiffness matrix is

$$\begin{pmatrix} c_{11} & c_{12} & c_{13} & 0 & 0 & 0 \\ & c_{22} & c_{23} & 0 & 0 & 0 \\ & & c_{33} & 0 & 0 & 0 \\ & & & c_{44} & 0 & 0 \\ & & & & c_{55} & 0 \\ \text{symmetric} & & & & & c_{66} \end{pmatrix}.$$

which contains nine independent elastic constants. Orthorhombic anisotropy is called also orthotropic anisotropy. This type of anisotropy is appropriate for some rocks like granites (see e.g., Thill et al., 1973).

Other types of elastic symmetry apply to crystals (Love, 1892, sections 107-109; Nye, 1957, p 137-142; Hearmon, 1961, p. 17-21; Bhagavantam, 1966, p. 127-135;

Fedorov, 1969, p. 18-33; Musgrave, 1970, p. 40-57; Auld, 1973, p. 191-210, 360-362) and to curved materials like cylinders and spheres (Love, 1892, sections 110 and 114), but these particular symmetries are believed to be uncommon in the crust of the Earth. (A useful reference on the elastic moduli of crystals is the book by Simmons and Wang (1971).)

1.3.4 Plane Wave Propagation

In Chapter 3 the behavior of the normal modes propagating along a borehole in an anisotropic medium will be shown to be related to the phase velocity and polarization of a planar S -waves propagating in the same direction. Consequently, the behavior of these planar waves must be thoroughly understood before this chapter is read. In this section, the velocities and polarizations of the S -waves will be obtained by solving the wave equation, and these quantities will be studied for isotropic and anisotropic media which are representative of actual rocks.

The solution to the wave equation is found with a trial solution for the displacements:

$$\mathbf{u}(x, y, z, t) = \begin{pmatrix} A_x \\ A_y \\ A_z \end{pmatrix} e^{i[k(l_x x + l_y y + l_z z) - \omega t]} \quad (1.32)$$

where A_i is the magnitude of the displacement, k is the wavenumber, l_x , l_y , and l_z are direction cosines, ω is the frequency, and t is time. (Many researchers have used this method of solving the wave equation in anisotropic solids (Christoffel, 1877; Love, 1892, Section 208; Kelvin, 1904, p. 131-134; Mason, 1958, p. 368-369; Fedorov, 1968, p. 85-89; Landau and Lifschitz, 1970, p. 106-108; Musgrave, 1970, p. 83-84; Auld, 1973, p. 164-165).) First the strains are computed with equation 1.3, then the stresses are computed with equation 1.9, and finally the stresses and displacements are substituted in the wave equation (1.8) to yield

$$\left(\frac{1}{\rho} \Gamma_{ij} - \frac{\omega^2}{k^2} \delta_{ij} \right) A_i = 0 \quad (1.33)$$

which is called the Christoffel equation to honor the first researcher in this field. The Christoffel matrix, Γ , is real and symmetric, and its elements on the diagonal and in the upper triangle are

$$\begin{aligned}
\Gamma_{11} &= c_{11}l_x^2 + c_{66}l_y^2 + c_{55}l_z^2 + 2c_{56}l_y l_z + 2c_{15}l_z l_x + 2c_{16}l_x l_y \\
\Gamma_{22} &= c_{66}l_x^2 + c_{22}l_y^2 + c_{44}l_z^2 + 2c_{24}l_y l_z + 2c_{46}l_z l_x + 2c_{26}l_x l_y \\
\Gamma_{33} &= c_{55}l_x^2 + c_{44}l_y^2 + c_{33}l_z^2 + 2c_{34}l_y l_z + 2c_{35}l_z l_x + 2c_{45}l_x l_y \\
\Gamma_{12} &= c_{16}l_x^2 + c_{26}l_y^2 + c_{45}l_z^2 + (c_{46} + c_{25})l_y l_z + (c_{14} + c_{56})l_z l_x + \\
&\quad (c_{12} + c_{66})l_x l_y \\
\Gamma_{13} &= c_{15}l_x^2 + c_{46}l_y^2 + c_{35}l_z^2 + (c_{45} + c_{36})l_y l_z + (c_{13} + c_{55})l_z l_x + \\
&\quad (c_{14} + c_{56})l_x l_y \\
\Gamma_{23} &= c_{56}l_x^2 + c_{24}l_y^2 + c_{34}l_z^2 + (c_{44} + c_{23})l_y l_z + (c_{36} + c_{45})l_z l_x + \\
&\quad (c_{25} + c_{46})l_x l_y .
\end{aligned} \tag{1.34}$$

The Christoffel equation is an eigenvalue equation, and its three solutions correspond to the three types of plane waves: one P -wave and two S -waves. For each solution, the eigenvalue is the square of the phase velocity, and the eigenvector is the polarization of the displacements. Because the Christoffel matrix is the same for plane waves propagating along (l_x, l_y, l_z) and $(-l_x, -l_y, -l_z)$, the eigenvalues and eigenvectors calculated for both waves will be the same. Consequently the phase velocities and polarizations of waves propagating in opposite directions will be the same even if the medium has general anisotropy.

Although plane wave propagation in isotropic media is familiar to all seismologists, it will be reviewed here because it is very important. Phase velocities of both S -waves in any direction equal $\sqrt{c_{44}/\rho}$ (Auld, 1973, p. 168-169). The displacements are mutually perpendicular and perpendicular to the propagation direction. As an example, the phase velocities and polarizations of the S -waves propagating in the isotropic medium whose properties are listed in Table 1.2 were calculated (Figure 1-1). (In this table, ρ is the density.) An additional example is given by Auld (1973, p.

385-386).

The next medium is transversely isotropic, and without losing any generality the symmetry axis will be aligned with the z axis. The displacements for one S -wave, which is labeled S_2 , are always perpendicular to the propagation direction. The displacements for the other S -wave, which is labeled qS_1 , are not, in general, perpendicular to the propagation direction indicating that it is coupled to the P -wave. The phase velocities and polarizations of these waves have the same symmetry that the stiffness matrix does: these quantities have an axis of symmetry which can have any amount of rotation and a plane of symmetry which is perpendicular to the axis of symmetry. Because the medium has a high degree of symmetry, analytical expressions for the phase velocities of the waves exist (Auld, 1973, p. 390). Although these expressions are complicated functions of the propagation direction and the elastic moduli, these expressions simplify greatly in some special directions. The phase velocities of the S_2 -wave in the horizontal and vertical directions equal $\sqrt{c_{66}/\rho}$ and $\sqrt{c_{44}/\rho}$, respectively. Those for the qS_1 -wave in both directions equal $\sqrt{c_{44}/\rho}$. As an example, the phase velocities and polarizations of the S -waves propagating in a transversely isotropic medium whose properties are listed in Table 1.3 were computed (Figures 1-2 and 1-3). Additional examples of wave propagation in transversely isotropic media are given by White (1983, p. 38-45) and Helbig and Schoenberg (1987).

The last medium is orthorhombic, and without losing any generality the symmetry planes are aligned with the coordinate planes. The displacements for the S -waves are usually not perpendicular to the propagation direction indicating that they are, in general, coupled to the P -wave and to each other; for this reason the waves are labeled qS_1 and qS_2 . The phase velocities and polarizations have the same symmetry that the stiffness matrix has: these quantities have three mirror planes of symmetry. Because the medium has relatively little symmetry, no formulas for the phase velocities exist for an arbitrary propagation direction. However, formulas do exist for

propagation within the symmetry planes (Auld, 1973, p. 401-405). Although these formulas are complicated, they simplify greatly for propagation along the intersection of the symmetry planes (which are parallel to the coordinate axes). When the propagation direction is parallel to the x axis, the phase velocities of the waves are $\sqrt{c_{55}/\rho}$ and $\sqrt{c_{66}/\rho}$. Similarly, the velocities are $\sqrt{c_{44}/\rho}$ and $\sqrt{c_{66}/\rho}$ for propagation along the y axis and $\sqrt{c_{44}/\rho}$ and $\sqrt{c_{55}/\rho}$ along the z axis. As an example, the phase velocities and polarizations of the S -waves propagating in an orthorhombic medium, whose properties are listed in Table 1.4, were calculated (Figures 1-4, 1-5, and 1-6). Additional examples of wave propagation in crystals with this type of symmetry are given by Musgrave (1970, p. 117-123) and Auld (1973, p. 401-405).

1.3.5 Normal Modes Propagating along a Borehole

The formulation of the perturbation method in Chapter 2, the variational method in Chapter 3, and the inversion in Chapter 4 requires a thorough understanding of the behavior of the normal modes propagating along a fluid-filled borehole. In this section, the phase and group velocities, pressures, and displacements of the normal modes will be studied to acquire this understanding.

To study the normal modes propagating along a borehole, an appropriate mathematical model for the borehole environment must be developed. The model must include those features which have a large effect upon elastic wave propagation and must exclude those which have little effect. The actual conditions can be quite complicated. For example, the rock surrounding the borehole may consist of many layers which are permeable and attenuative, the fluid may be viscous, the borehole wall may be irregular, and the tool may have a very complicated internal shape (Figure 1-7a). In spite of these complications a mathematical model, which has been used successfully to approximate the most significant features of the waves, consists of a perfectly elastic fluid in a cylindrical borehole through a homogeneous, perfectly elastic, solid (Figure 1-7b and 1-7c). The fluid and solid extend to infinity along the axis of the

borehole, and the solid extends to infinity away from the borehole. In this section, the solid will be isotropic because an analytical solution to the wave equation exists for this case. The properties of the model are listed in Table 1.5.

The properties of the normal modes are determined from the dispersion equation, which is derived by solving the wave equation for cylindrical waves in the fluid and the solid and then by matching boundary conditions at the fluid-solid interface (see Appendix A). After the dispersion equation is solved, the displacements in the solid and the pressures in the fluid can be readily calculated. (In fact, other quantities like the stress and strain tensors can be calculated, but an adequate understanding of the normal modes can be obtained by studying the displacements and pressures.) The wavenumber and frequency are used to calculate the phase velocity. Although group velocity could be calculated numerically with the formula, $U = d\omega/dk_z$ (where ω is the frequency and k_z the wavenumber along the axis of the borehole), the perturbation method described in Chapter 2 is used because it is less susceptible to noise.

Phase and group velocities, pressures in the fluid, and displacements in the solid were computed for the normal modes which exist for the model whose parameters are listed in Table 1.5. An infinite number of modes exist, but only those at the lowest frequencies were computed and plotted (Figures 1-8 and 1-9). The numbering of the modes is based upon a convention established by Roever et al. (1974). The first number in the pair is the azimuthal order number, which describes the variation of the mode with azimuth. That is, the analytical expressions for the pressures and displacements (equations A.11 and A.43) contain either $\cos n\theta$ or $\sin n\theta$ where n is the azimuthal order number. The second number in the pair is the radial mode number, which describes the variation of the mode with radial distance. Several examples will be used to clarify what these numbers mean in terms of the pressures and displacements of the modes. This numbering scheme and the common names of the modes are summarized in Table 1.6.

The first mode whose azimuthal order number is 0 is called the tube wave. The

mode exists at all frequencies (Figures 1-8 and 1-9). Over a distance of one wavelength, the pressures and particle displacements oscillate in a well defined pattern (Figure 1-10). (In this and subsequent figures, the particle displacements, which are actually infinitesimal, are exaggerated enormously to make the components in the r and θ directions clearly visible. The component in the z direction is hard to discern due to the perspective of the illustration. Fortunately this component is not needed to understand the basic character of the modes.) At the beginning, the pressures and the displacements in the r and θ directions are zero. At $1/4$ wavelength, the pressure reaches its maximum positive value, and the displacements show that the borehole wall is dilated. At $1/2$ wavelength, the pressures and displacements in the r and θ directions are zero again. At $3/4$ wavelength the pressure reaches its maximum negative value, and the borehole wall is constricted. After one wavelength the pressures and displacements return to their initial, zero value. Because the pressures and displacements are the same at all azimuths, the azimuthal order number is 0. At either $1/4$ or $3/4$ wavelength the pressure is not zero at any point, and consequently the radial mode number is 0.

The next mode whose azimuthal order number is 0 is called the pseudo-Rayleigh wave. This wave only exists above approximately 8 kHz (Figures 1-9 and 1-8). This threshold, which is commonly called the cutoff frequency, depends upon the borehole radius and the properties of the fluid and solid. At the cutoff frequency the mode attains its highest phase velocity which equals the S -wave velocity of the solid. The displacements and pressures (Figure 1-11) show no azimuthal dependence making the azimuthal order number 0. At $1/4$ wavelength the pressure in the fluid is positive at the center and negative at the wall. Hence, the pressure is zero once between the center and the wall, making the radial mode number 1. An infinite number of higher order radial modes exist; the shapes of their dispersion curves are similar to that for the pseudo-Rayleigh wave; and the cutoff frequencies increase as the radial mode number increases (see e.g., the curve labeled (0,2) in Figures 1-8 and 1-9).

The first mode whose azimuthal order number is 1 is the flexural wave. Although the dispersion curve ends at about 2 kHz because solving the dispersion equation at lower frequencies is numerically difficult, the mode actually exists at all frequencies (Figures 1-8 and 1-9). The velocity of this mode does not exceed the S -wave velocity of the solid. Actually two modes exist having the same phase and group velocities (Figures 1-12 and 1-13). In mathematical terms, the two modes, which are orthogonal, are needed to form a complete set. In physical terms, a flexural wave in any arbitrary direction can be constructed by a linear superposition of these two modes. The two modes do not have any special orientation with respect to the solid because the solid is isotropic. Since the pressures and displacements vary according to either $\cos \theta$ or $\sin \theta$, the azimuthal order number is 1. Because the pressure at either $1/4$ wavelength or $3/4$ wavelength is not zero along an arbitrary line between the center and the borehole wall, the radial mode number is 0. An infinite number of higher order radial modes exists for this azimuthal order number, and the shapes of their dispersion curves are like that for the flexural wave (see e.g., the curve labeled (1,1) in Figures 1-8 and 1-9).

The first mode whose azimuthal order number is 2 is the screw wave. Its cutoff frequency is approximately 6 kHz, and its phase velocity does not exceed the S -wave velocity of the solid (Figure 1-8). Two modes with exactly the same phase and group velocities actually exist for the same reason that two flexural waves exist. Their orientation with respect to the solid is arbitrary because the medium is isotropic. Because the displacements and pressures vary according to either $\cos 2\theta$ or $\sin 2\theta$ (Figures 1-14 and 1-15), the azimuthal order number is 2. The radial mode number is zero for same reason that it is zero for the other waves. Again, an infinite number of higher order radial modes exist for this azimuthal order number (see e.g., the curve labeled (2,1) in Figures 1-8 and 1-9). The pattern of the displacements at the borehole wall suggests that the name for this mode is a misnomer.

Studying the normal modes at all azimuthal order numbers, all radial mode numbers, and all frequencies is unnecessary. The sources in modern logging tools (i.e.,

monopole, dipole, and quadrupole sources) only excite modes whose azimuthal order numbers are 0, 1, and 2. Because the sources have a limited frequency range, which extends from approximately 1 to 15 kHz, only the lower order radial modes are excited. Therefore the tube, pseudo-Rayleigh, flexural, and screw waves in the frequency range from 0 to 15 kHz deserve the most careful study. If the behavior of these modes at high frequencies is desired or if the behavior of the higher order modes is desired, then their general characteristics can be readily predicted from what is known about these lower order modes.

The properties of the normal modes depend strongly upon the S -wave velocity of the medium. First, the normal modes only exist when their phase velocity is lower than the S -wave velocity. Above this threshold, the modes radiate energy into the solid and consequently are called leaky modes. Second, the phase and group velocities are strongly affected by the S -wave velocity (see Cheng et al., 1982). Finally, the magnitude of the S -wave velocity relative to the acoustic velocity of the fluid determines what normal modes exist. When the S -wave velocity is larger, all of the normal modes from the previous example (Figures 1-8 and 1-9) exist. For this situation, the formation is described as being either fast or hard. When the S -wave velocity is lower, only the lowest order radial modes (e.g., (0,0), (1,0), (2,0), etc.) exist. For this situation, the formation is described as being either slow or soft.

Indices for stiffness tensor (ij or kl)	Index for stiffness matrix
xx	1
yy	2
zz	3
yz or zy	4
xz or zx	5
xy or yx	6

Table 1.1: Relations between indices in the stiffness tensor and stiffness matrix for Cartesian coordinates.

Quantity	Value
c_{11}	3.79×10^{10} Pa
c_{44}	1.51×10^{10} Pa
ρ	2140 kg/m ³

Table 1.2: Properties of the isotropic medium. These properties are similar to those of the Berea sandstone (Thomsen, 1986).

Quantity	Value
c_{11}	7.23×10^{10} Pa
c_{13}	2.06×10^{10} Pa
c_{33}	6.50×10^{10} Pa
c_{44}	2.21×10^{10} Pa
c_{66}	2.51×10^{10} Pa
ρ	2500 kg/m ³

Table 1.3: Properties of the transversely isotropic medium, which represents the Mesaverde shale (5496.5) (Thomsen, 1986). For this list of elastic constants, the symmetry axis is parallel to the z axis.

Quantity	Value
c_{11}	9.78×10^{10} Pa
c_{12}	1.95×10^{10} Pa
c_{13}	3.23×10^{10} Pa
c_{22}	9.09×10^{10} Pa
c_{23}	1.86×10^{10} Pa
c_{33}	8.17×10^{10} Pa
c_{44}	2.44×10^{10} Pa
c_{55}	2.00×10^{10} Pa
c_{66}	3.18×10^{10} Pa
ρ	2800 kg/m ³

Table 1.4: Properties of the orthorhombic medium. For this list of elastic constants, the symmetry planes are aligned with the coordinate planes. These properties were measured by J. Mendelson (1989, oral communication).

Quantity	Meaning	Value
c_{11}	elastic modulus for solid	3.79×10^{10} Pa
c_{44}	elastic modulus for solid	1.51×10^{10} Pa
ρ_2	density of solid	2140 kg/m ³
λ_1	incompressibility of fluid	0.225×10^{10} Pa
ρ_1	density of fluid	1000. kg/m ³
R	borehole radius	0.1016 m

Table 1.5: Model parameters used to calculated the normal modes. The properties of the solid are similar to those of the Berea sandstone (Thomsen, 1986).

Numerical Label	Common Name	Number of Modes
$(0,0)^\dagger$	tube wave	1
$(0,1)^\dagger$	pseudo-Rayleigh wave	1
$(0,2)^\dagger$	higher order pseudo-Rayleigh wave	1
\vdots	\vdots	\vdots
$(0,\infty)$	higher order pseudo-Rayleigh wave	1
$(1,0)^\dagger$	flexural wave	2
$(1,1)^\dagger$	higher order flexural wave	2
$(1,2)$	higher order flexural wave	2
\vdots	\vdots	\vdots
$(1,\infty)$	higher order flexural wave	2
$(2,0)^\dagger$	screw wave	2
$(2,1)^\dagger$	higher order screw wave	2
$(2,2)$	higher order screw wave	2
\vdots	\vdots	\vdots
$(2,\infty)$	higher order screw wave	2
$(3,0)^\dagger$	(none)	2
$(3,1)^\dagger$	(none)	2
$(3,2)$	(none)	2
\vdots	\vdots	\vdots
$(3,\infty)$	(none)	2
$(4,0)^\dagger$	(none)	2
$(4,1)$	(none)	2
$(4,2)$	(none)	2
\vdots	\vdots	\vdots
$(4,\infty)$	(none)	2
$(5,0)^\dagger$	(none)	2
$(5,1)$	(none)	2
$(5,2)$	(none)	2
\vdots	\vdots	\vdots
$(5,\infty)$	(none)	2
\vdots	\vdots	\vdots

Table 1.6: Normal modes that exist in the borehole model shown in Figure 1-7 when the formation is fast. The phase and group velocities of the modes marked with a dagger (\dagger) were calculated for the model, whose properties are listed in Table 1.5, and are shown in Figures 1-8 and 1-9, respectively.

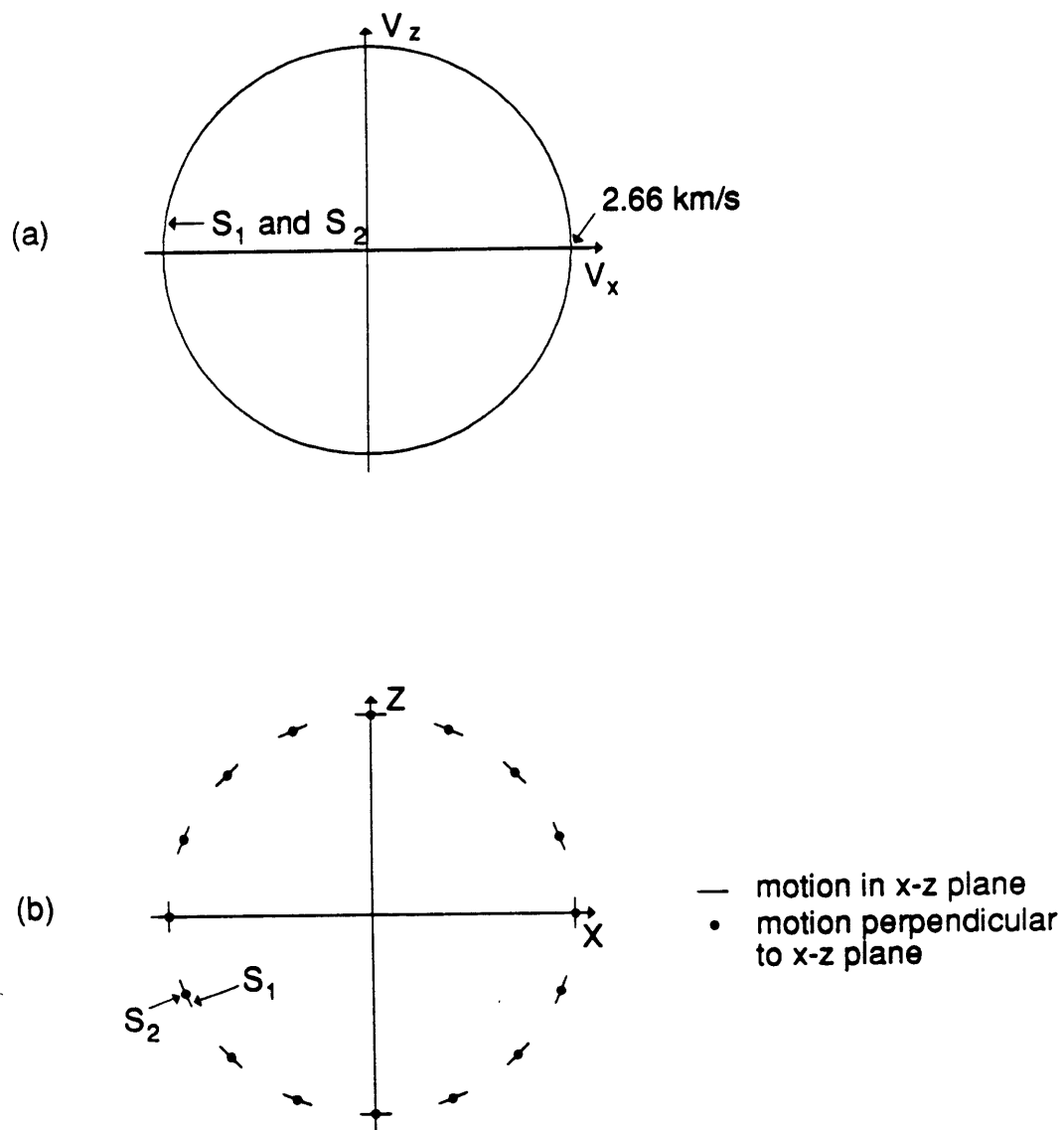


Figure 1-1: (a) Phase velocity surfaces and (b) polarizations for the two S -waves in the isotropic medium (Table 1.2).

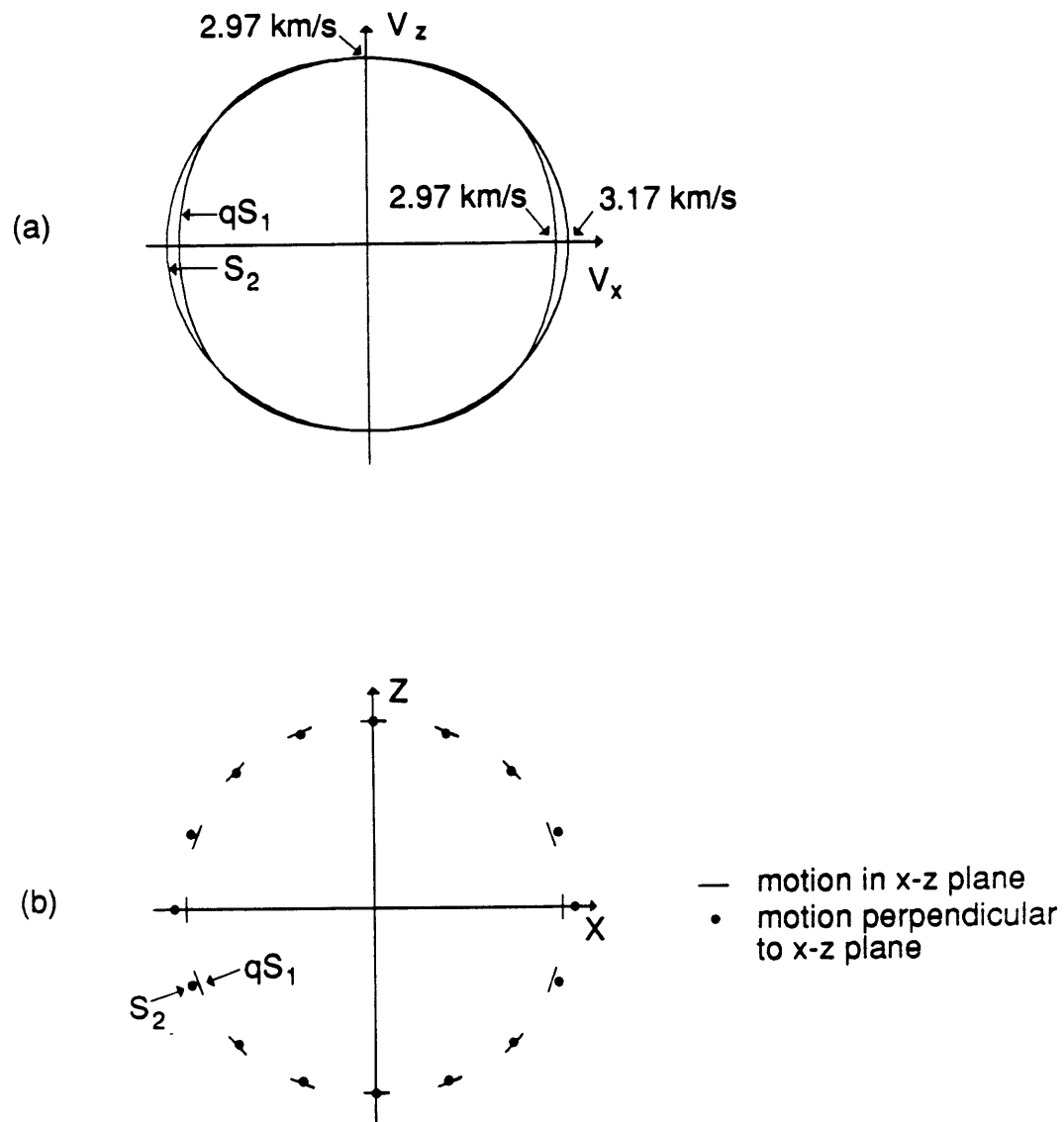


Figure 1-2: (a) Phase velocity surfaces and (b) polarizations in the x - z plane for the two S -waves in the transversely isotropic medium (Table 1.3).

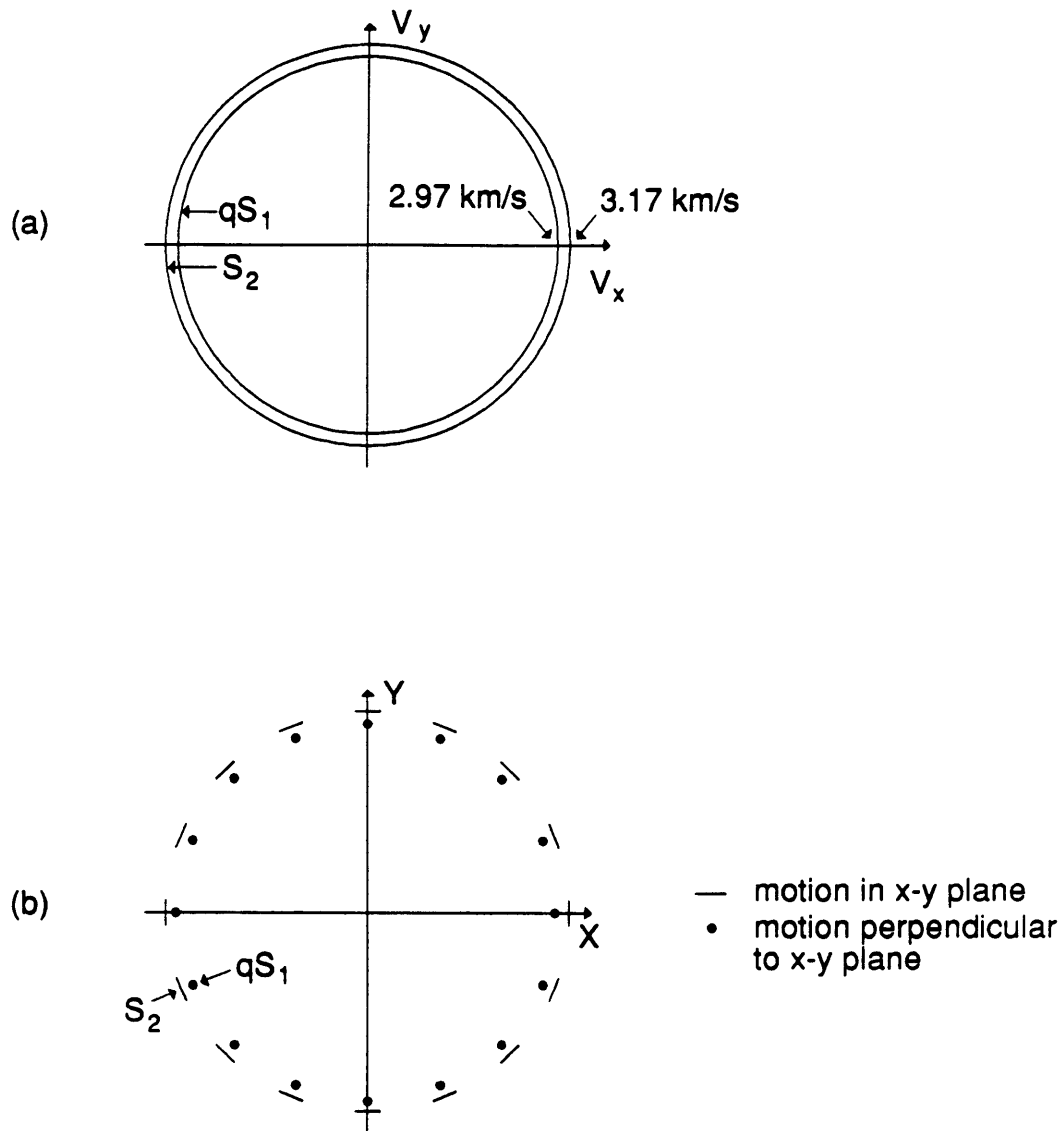


Figure 1-3: (a) Phase velocity surfaces and (b) polarizations in the x - y plane for the two S -waves in the transversely isotropic medium (Table 1.3).

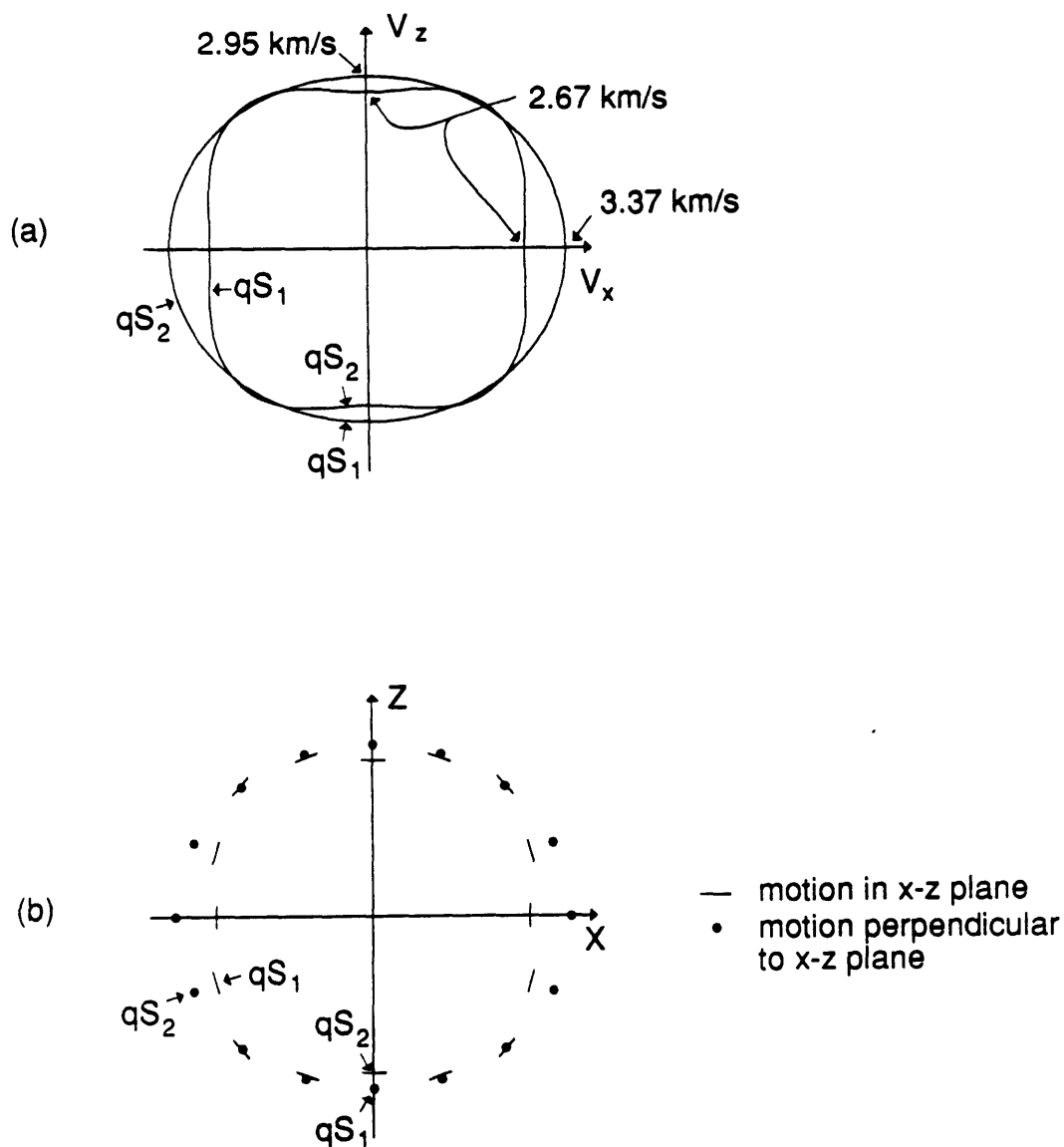


Figure 1-4: (a) Phase velocities and (b) polarizations in the $x-z$ plane for the two S -waves in the orthorhombic medium (Table 1.4). (The polarizations of the S -waves can be plotted in this manner because they are not coupled to each other for propagation in this plane.)

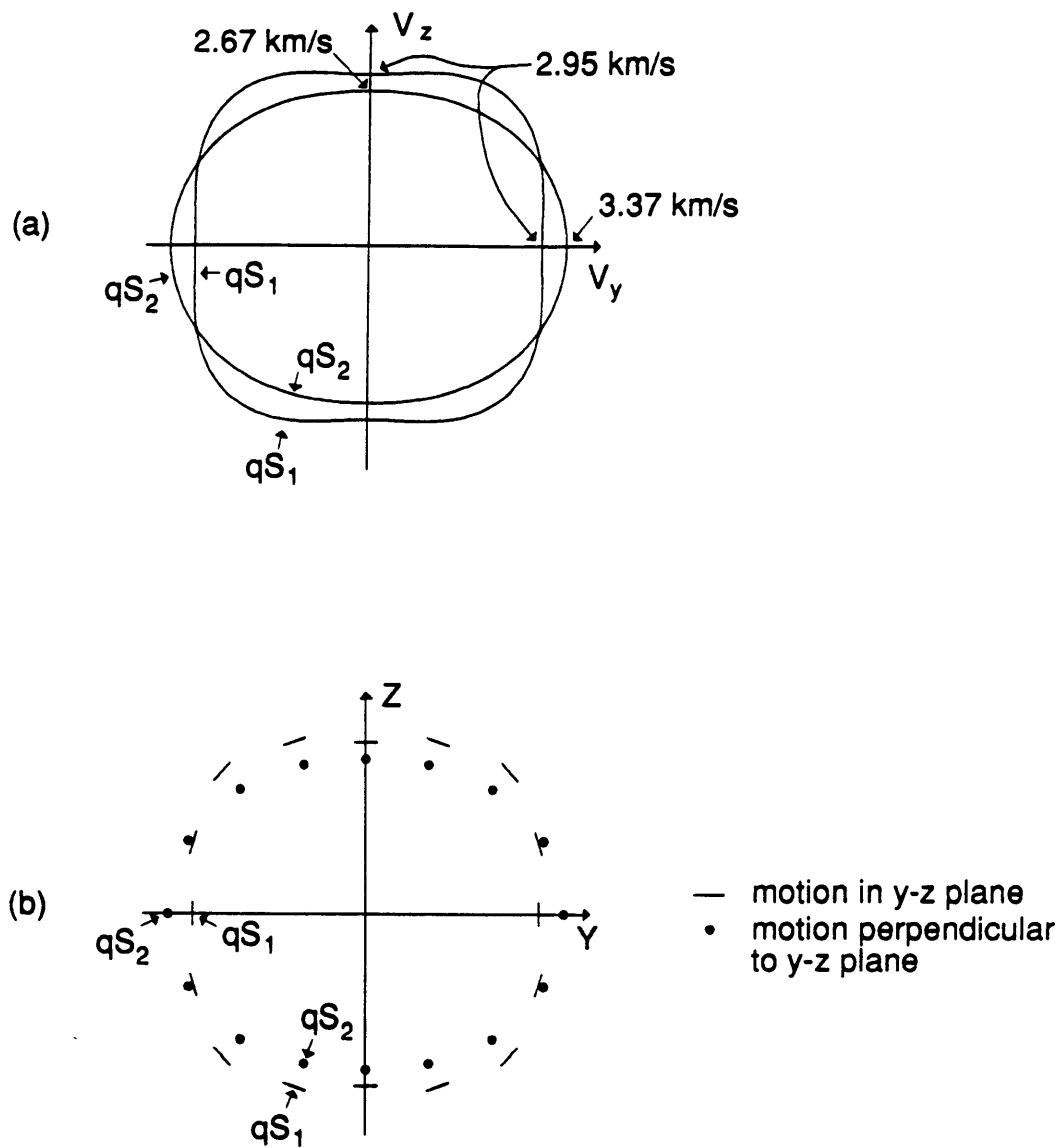


Figure 1-5: (a) Phase velocity surfaces and (b) polarizations in the y - z plane for the two S -waves in the orthorhombic medium (Table 1.4). (The polarizations of the S -waves can be plotted in this manner because they are not coupled to each other for propagation in this plane.)

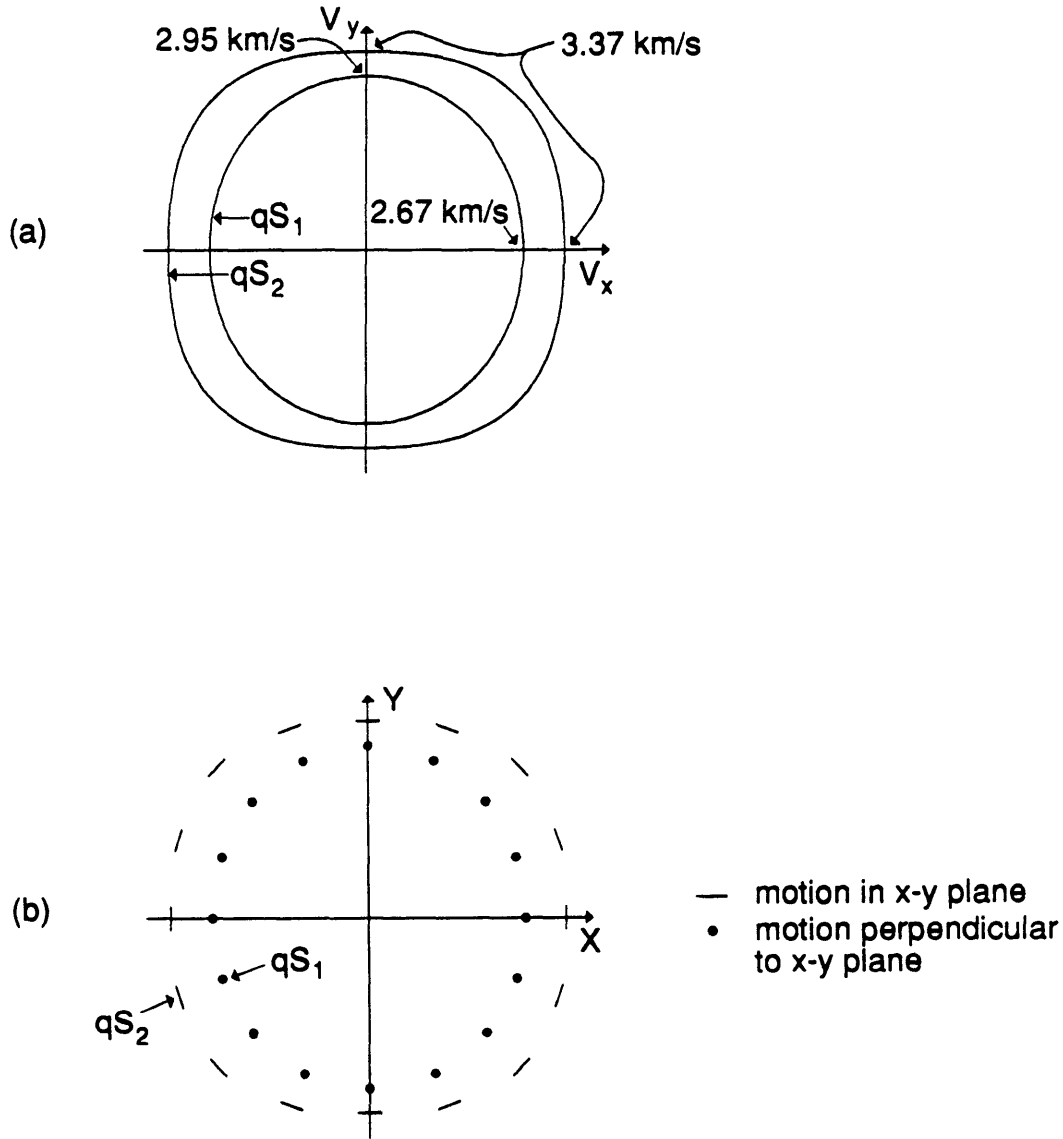


Figure 1-6: (a) Phase velocity surfaces and (b) polarizations in the x - y plane for the two S -waves in the orthorhombic medium (Table 1.4). (The polarizations of the S -waves can be plotted in this manner because they are not coupled to each other for propagation in this plane.)

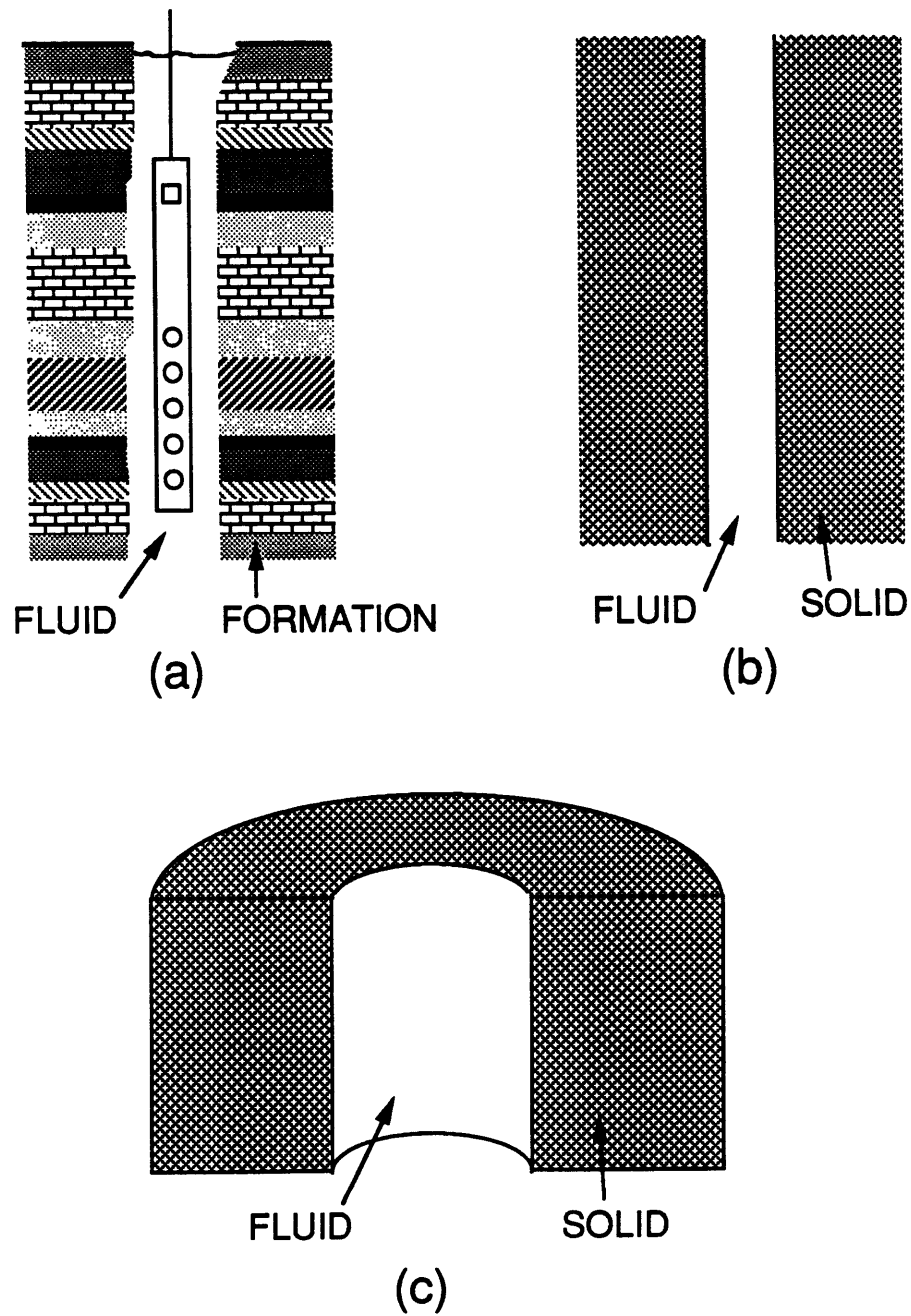


Figure 1-7: (a) Cross section showing some of the complicated features of the Earth and the borehole. (b) Mathematical model used to study wave propagation along the borehole. (c) Cutaway view of the model which clearly shows the geometry of the model.

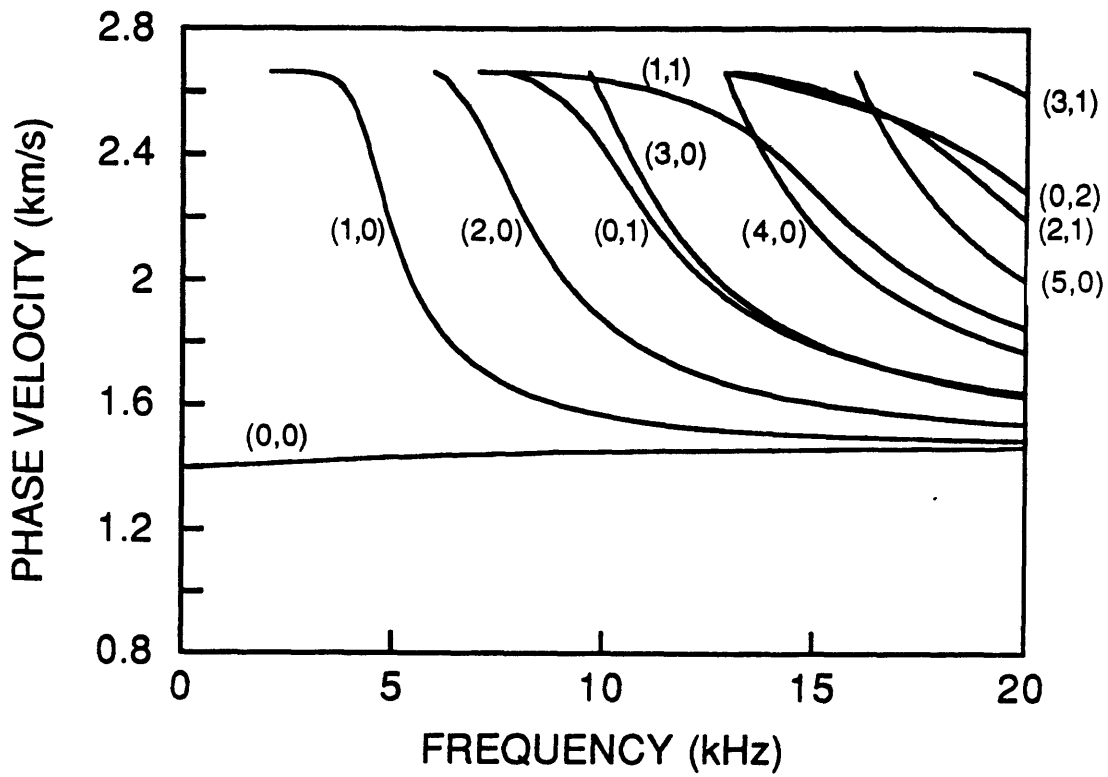


Figure 1-8: Phase velocities for the lowest order normal modes in the borehole model described in Table 1.5.

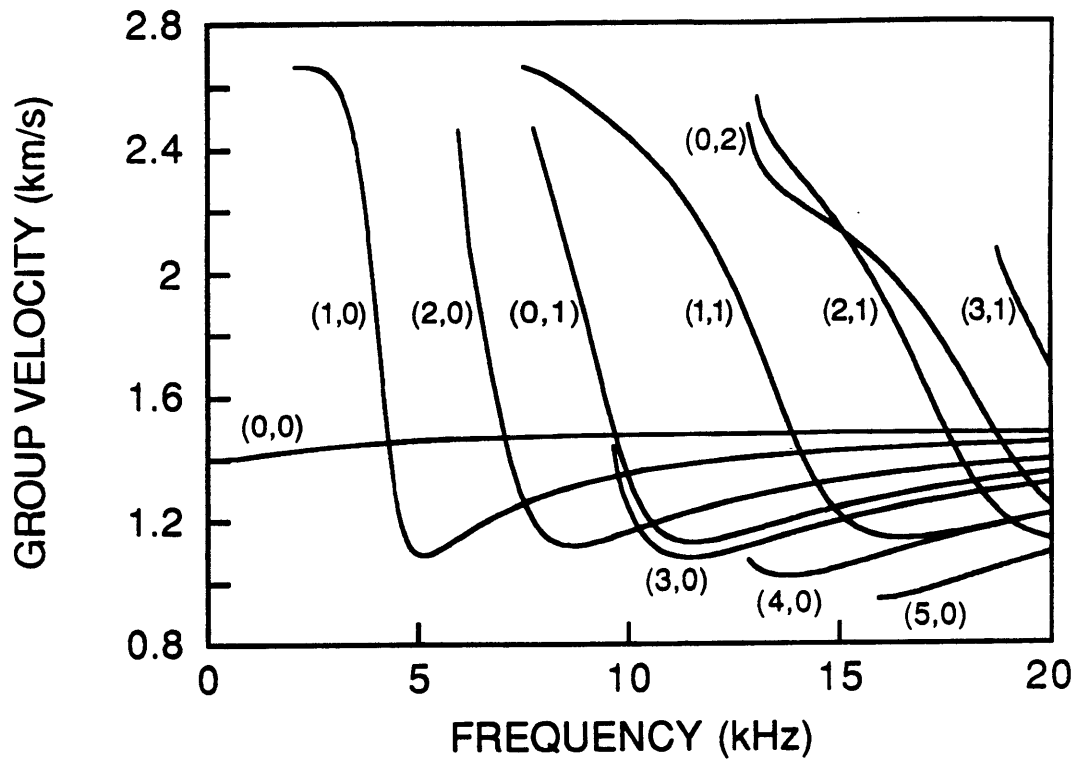


Figure 1-9: Group velocities for the lowest order normal modes in the borehole model described in Table 1.5.

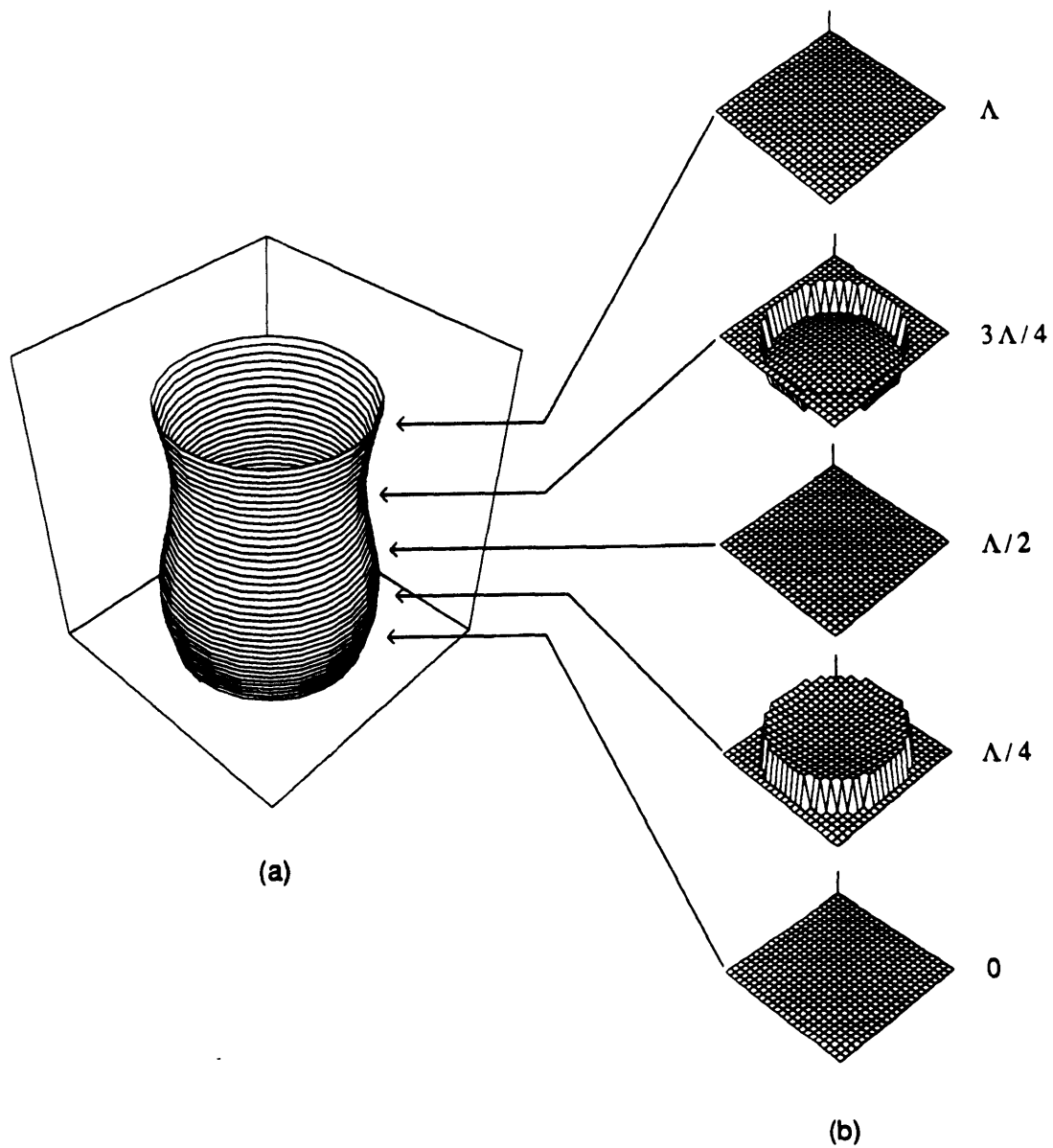


Figure 1-10: (a) Particle displacements for the tube wave at the borehole wall (in the solid and over one wavelength). (b) Corresponding pressures in the fluid. These displacements and pressures were computed for a borehole model with an isotropic, fast formation (Table 1.5).

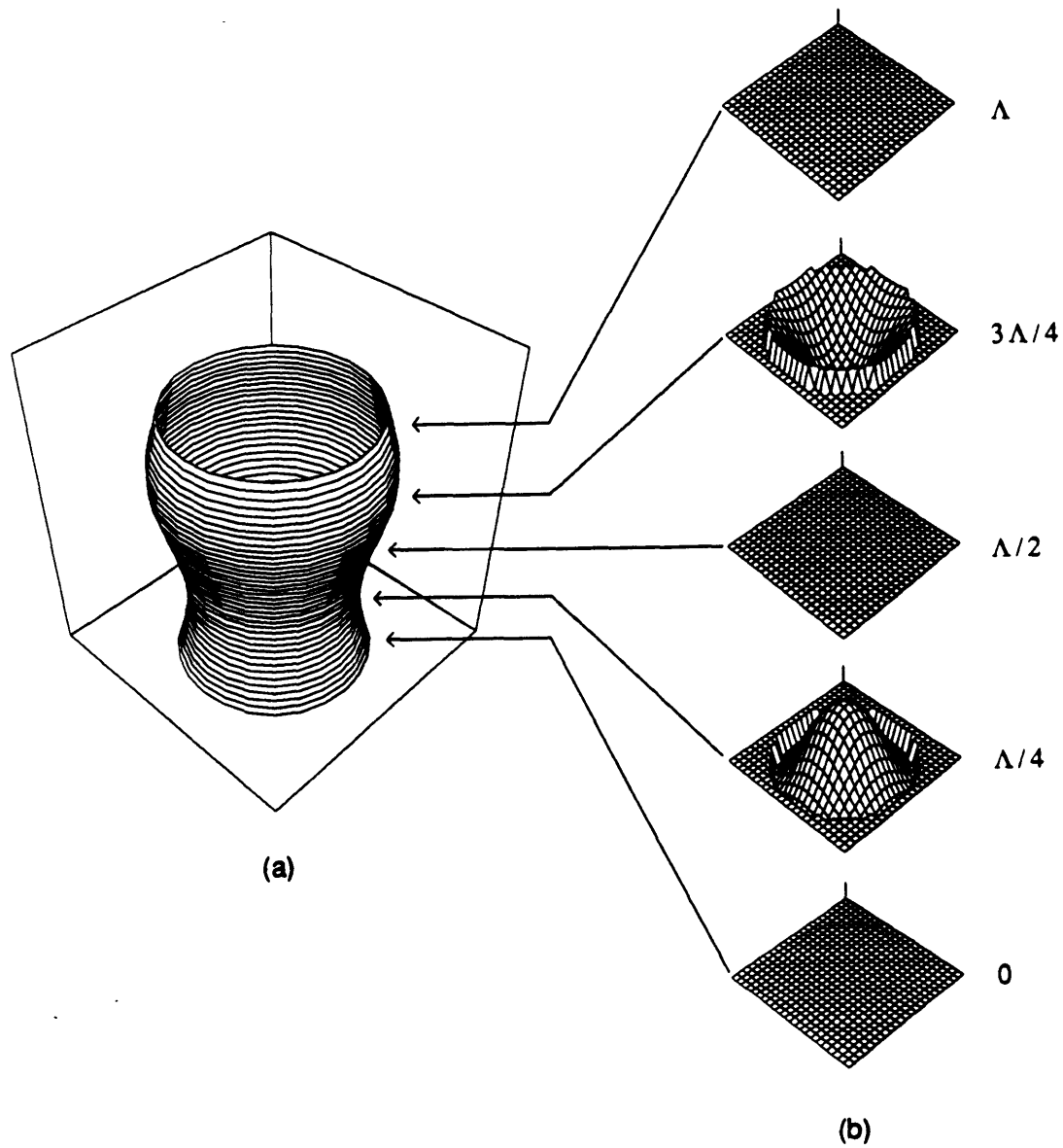


Figure 1-11: (a) Particle displacements for the pseudo-Rayleigh wave at the borehole wall (in the solid and over one wavelength). (b) Corresponding pressures in the fluid. These displacements and pressures were computed for a borehole model with an isotropic, fast formation (Table 1.5).

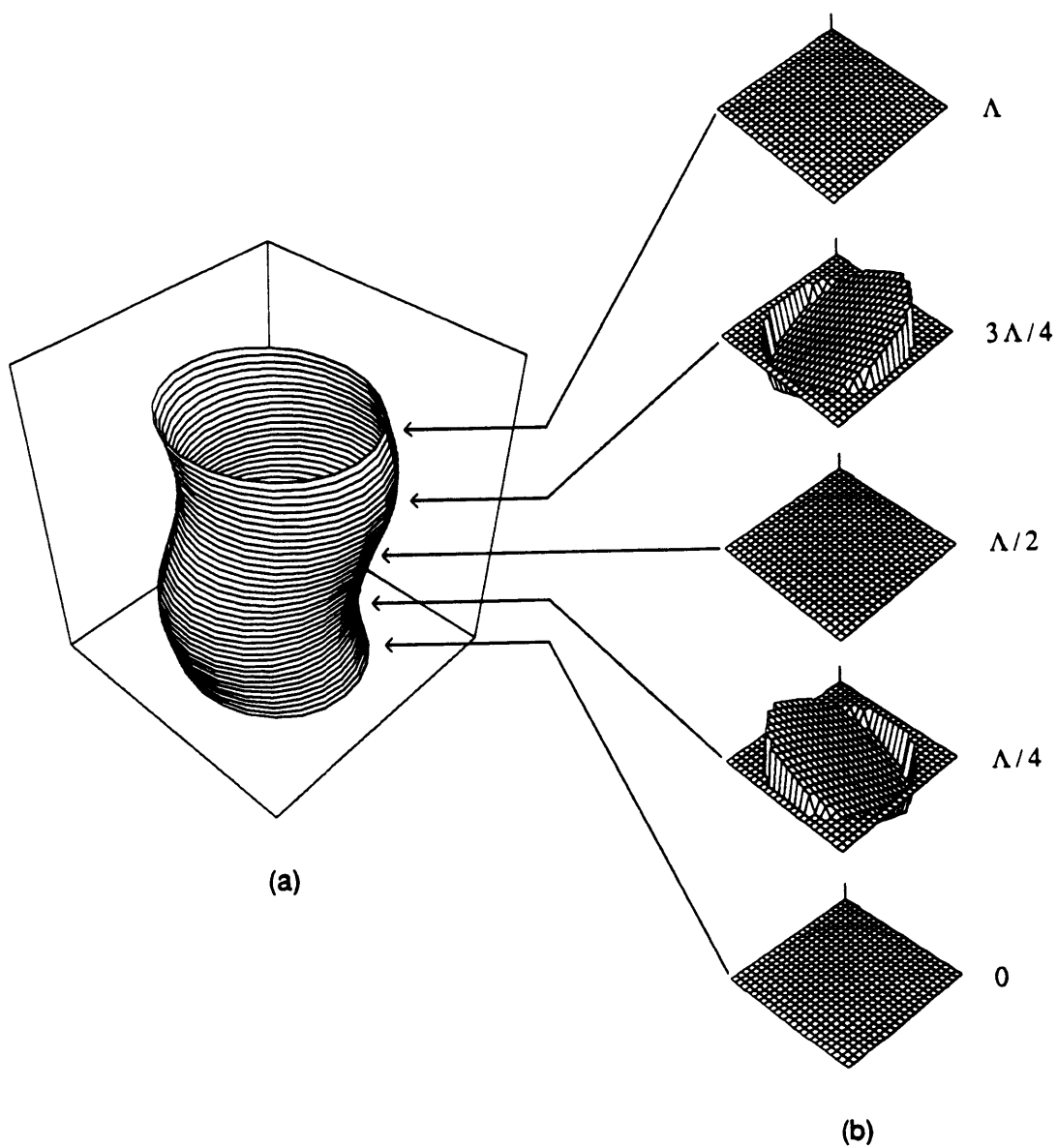


Figure 1-12: (a) Particle displacements for the first flexural wave at the borehole wall (in the solid and over one wavelength). (b) Corresponding pressures in the fluid. These displacements and pressures were computed for a borehole model with an isotropic, fast formation (Table 1.5).

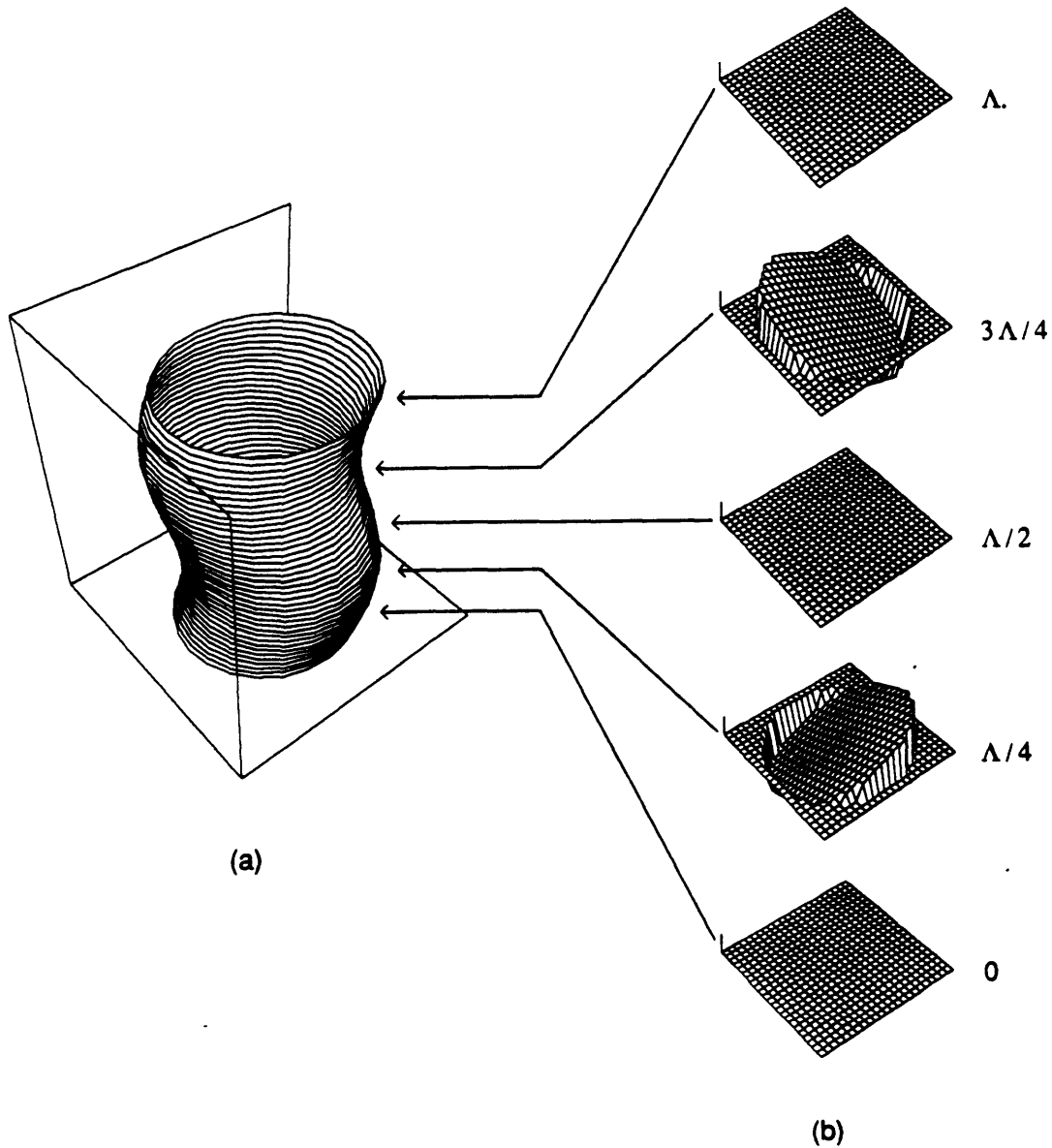


Figure 1-13: (a) Particle displacements for the second flexural wave at the borehole wall (in the solid and over one wavelength). (b) Corresponding pressures in the fluid. These displacements and pressures were computed for a borehole model with an isotropic, fast formation (Table 1.5). (Note that the perspective in this figure is different from that in Figure 1-12.)

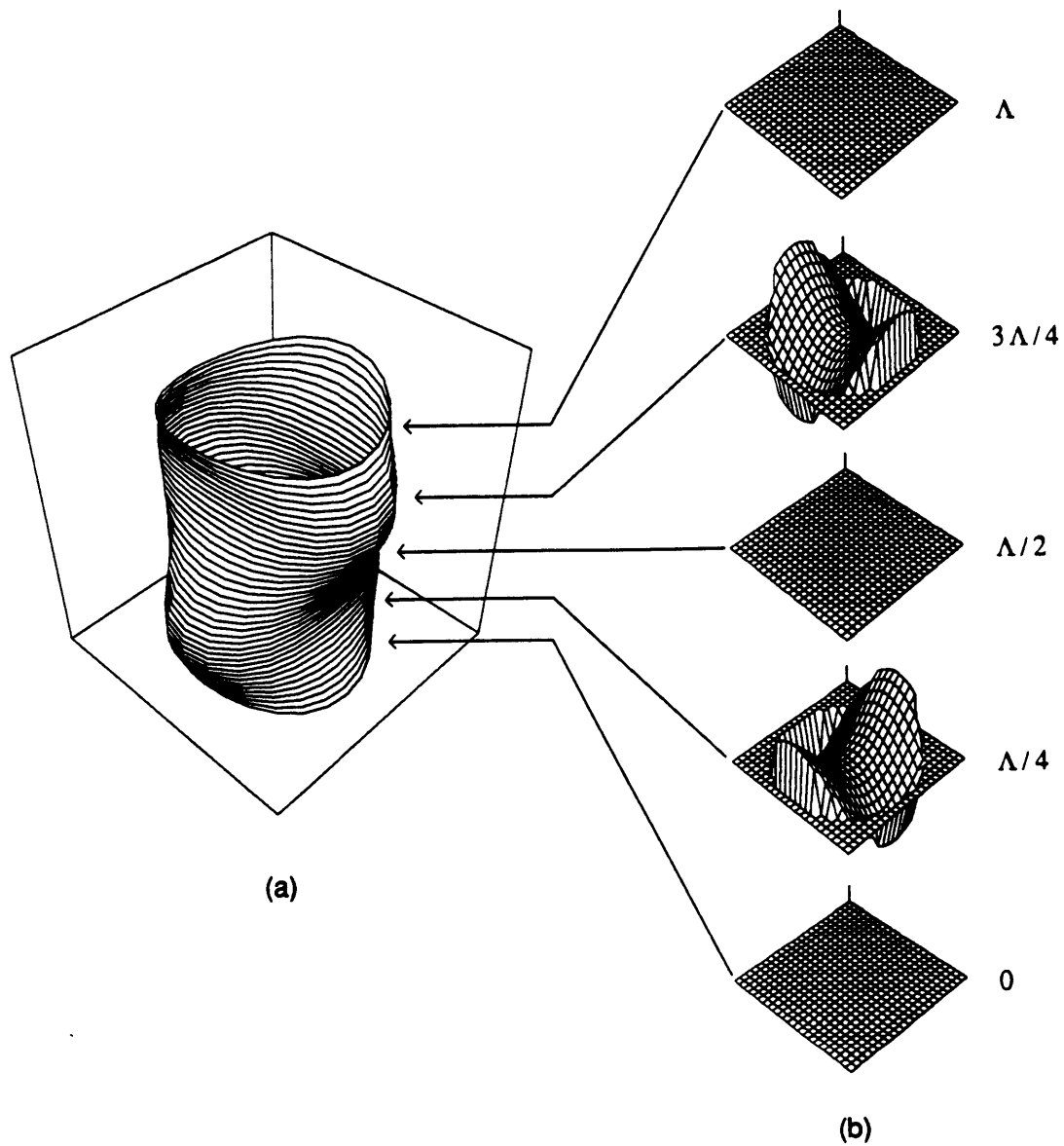


Figure 1-14: (a) Particle displacements for the first screw wave at the borehole wall (in the solid and over one wavelength). (b) Corresponding pressures in the fluid. These displacements and pressures were computed for a borehole model with an isotropic, fast formation (Table 1.5).

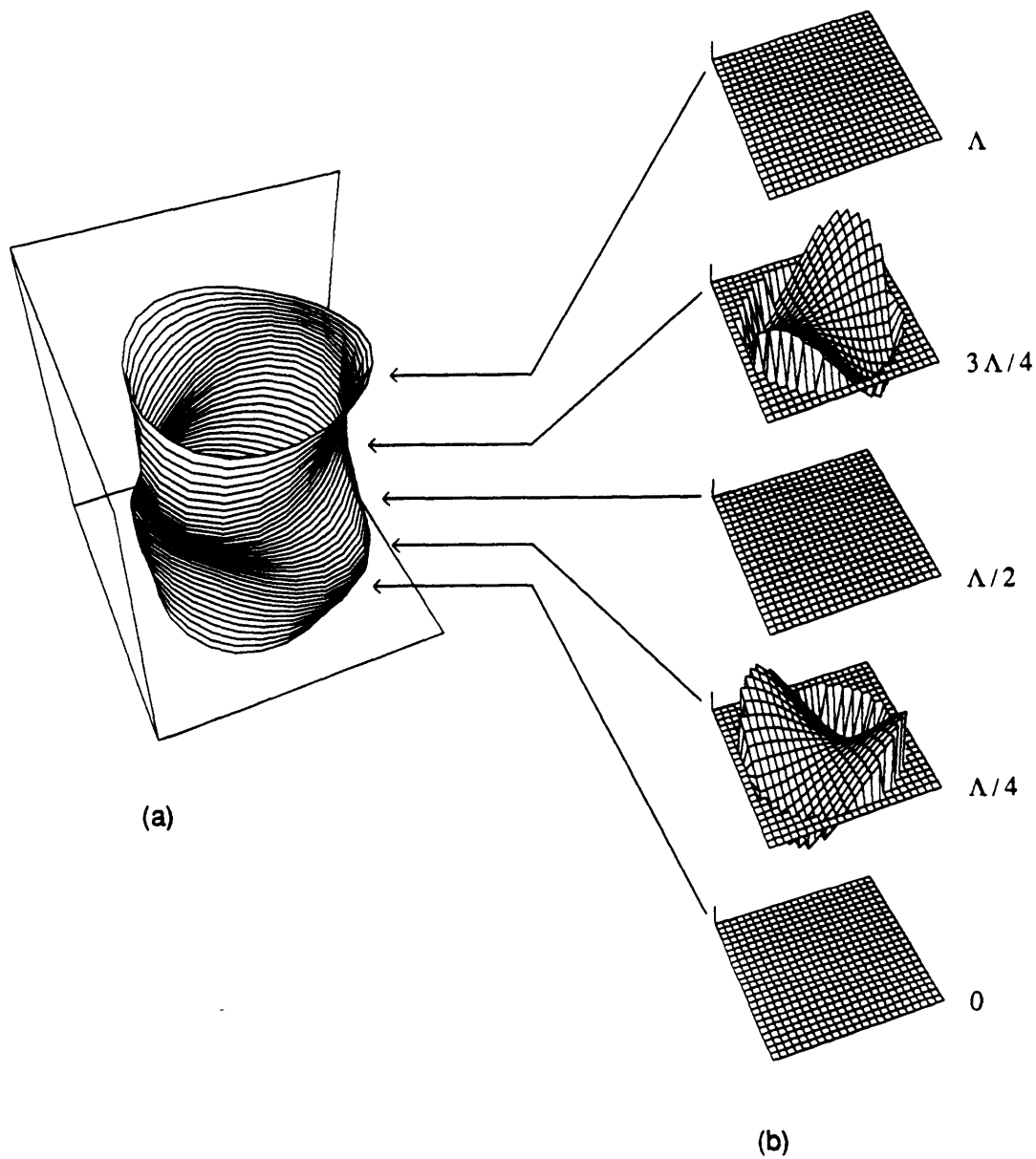


Figure 1-15: (a) Particle displacements for the second screw wave at the borehole wall (in the solid and over one wavelength). (b) Corresponding pressures in the fluid. These displacements and pressures were computed for a borehole model with an isotropic, fast formation (Table 1.5). (Note that the perspective in this figure is different from that in Figure 1-14.)

Chapter 2

Applications of Perturbation Theory to the Normal Modes

2.1 Introduction

In this chapter, four different applications of perturbation theory will be developed. These applications will be used in other chapters to study the normal modes.

The first application, which will be used in Chapter 3, is calculating the phase velocities of the modes when the formation has general anisotropy. Because analytical solutions do not exist for this case, an approximate technique like a perturbation method must be used. This method has not been used heretofore to study the normal modes in a borehole although Smith and Dahlen (1973) and Woodhouse and Dahlen (1978) used it to study surface waves and the normal modes of the Earth.

The second application, which will be used in Chapter 4, is calculating partial derivatives. The principal advantage of using a perturbation method is that the calculated derivatives are more accurate than those obtained by numerical differentiation. Cheng et al. (1982), Stevens and Day (1986), and Burns and Cheng (1987) used this approach to calculate derivatives for tube and pseudo-Rayleigh waves in isotropic formations. Here, this method is extended to all normal modes for either

isotropic or transversely isotropic formations.

The third application, which was used in Chapter 1, is calculating group velocity. The advantage of using this method is that it is more accurate than numerical differentiation. Toksöz et al. (1984) used this approach to calculate the group velocities of tube and pseudo-Rayleigh waves in isotropic formations. Here a method for calculating group velocities of all normal modes in either isotropic or transversely isotropic formations is developed.

The fourth application is calculating in the phase velocity of a normal mode propagating along a borehole with a slightly irregular cross section. Since many boreholes are slightly irregular, this issue must be addressed before the dispersion curves are used to estimate formation properties (see e.g., Chapter 4). Willen (1983) used a perturbation method to calculate seismograms generated by a monopole source in an elliptical borehole but did not report how the ellipticity affects the velocity dispersion. Nicoletis et al., (1990) determined how the ellipticity of a borehole affects the phase velocity of a tube wave at the zero frequency limit. In this chapter, a method of calculating the phase velocities of all normal modes at all frequencies when the borehole is slightly irregular is presented.

The chapter begins with the derivation of an equation which relates perturbations in frequency, wavenumber, elastic moduli, densities, and locations of interfaces. This equation is appropriate for a general model of the borehole. Then the perturbation equation is applied to the two-layer model which is used throughout this thesis, and formulas for the four different applications are derived. An example of each application is presented also.

2.2 Derivation of the Perturbation Equation

The derivation of the perturbation equation is based upon a mathematical model of the borehole environment. The model may consist of many layers, and each layer may

have any cross-sectional shape that remains the same along the axis of the borehole (Figure 2-1). Each fluid layer is perfectly elastic, and each solid layer is perfectly elastic and homogeneous. All layers extend to infinity along the axis of the borehole, and the outermost layer extends to infinity away from the axis of the borehole. From the entire model, only a volume element, V , having the shape of disk and a thickness of one wavelength, Λ , is needed because wave propagation in every element is the same. The surfaces between the layers, which are inside the volume element, are collectively designated Σ^i ; and the surfaces on the exterior Σ^e . The variables needed for the derivation are listed in Tables 2.1 for easy reference.

Because Hamilton's Principle (see e.g., Lanczos, 1970, p. 111-114; Goldstein, 1980, p. 35-37) is needed to derive the perturbation equation, it will be discussed first. This principle is based upon the Lagrangian energy density which is defined as the kinetic energy density minus the elastic strain energy density:

$$\mathcal{L} = \frac{1}{2}\rho\dot{u}_i\dot{u}_i - \frac{1}{2}u_{j,i}c_{ijkl}u_{l,k} \quad (2.1)$$

u_i is a displacement, \dot{u}_i and $u_{l,k}$ indicate differentiation with respect to time and space, c_{ijkl} is the stiffness tensor, and ρ is the density. \mathcal{L} is integrated over a volume element and one period, \mathcal{T} . (In a general derivation of Hamilton's Principle, the time integral has arbitrary limits, and the volume integral includes the entire model. Because the displacements, which will be chosen later, are expressed in the frequency-wavenumber domain, integration over one period and one wavelength greatly simplifies the mathematics. A similar approach was used by Aki and Richards (1980, p. 287) when they derived this principle for Love and Rayleigh waves.) Then this integral is perturbed with respect to the displacements.

$$\delta \int_t^{t+T} dt \int_V dV \mathcal{L} = \int_t^{t+T} dt \int_V dV (\rho\dot{u}_i\delta\dot{u}_i - \delta u_{j,i}c_{ijkl}u_{l,k}) \quad (2.2)$$

Gauss' theorem,

$$\begin{aligned} \int_V dV (\tau_{ji}\delta u_j)_{,i} = \\ \int_{\Sigma^i} dS (n_j\tau_{ji}\delta u_i|_{\text{inner side of } \Sigma^i} - n_j\tau_{ji}\delta u_i|_{\text{outer side of } \Sigma^i}) + \int_{\Sigma^e} dS n_j\tau_{ji}\delta u_i \quad , \end{aligned} \quad (2.3)$$

where τ_{ji} is the stress tensor and n_i is the normal to a surface, is used to transform the volume integral with the spatial derivatives. The divergence operator is applied to the integrand in the volume integral, and the terms are rearranged:

$$\begin{aligned} \int_V dV (c_{ijkl} \delta u_{j,i}) = \\ - \int_V dV \tau_{ji,j} u_i - \int_{\Sigma^i} dS [n_j \tau_{ji} \delta u_i]_-^+ + \int_{\Sigma^e} dS n_j \tau_{ji} \delta u_i \quad . \end{aligned} \quad (2.4)$$

Note the notation used for the integrand in the surface integral over Σ^i . After applying these changes and integrating the temporal derivatives by parts, the time integral of the Lagrangian energy is

$$\begin{aligned} \delta \int_t^{t+T} dt \int_V dV \mathcal{L} = \int_V dV \rho \dot{u}_i \delta u_i \Big|_t^{t+T} + \\ \int_t^{t+T} dt \left[- \int_V dV (\rho \ddot{u}_i - \tau_{ji,j}) \delta u_i + \int_{\Sigma^i} dS [n_j \tau_{ji} \delta u_i]_-^+ - \int_{\Sigma^e} dS n_j \tau_{ji} \delta u_i \right] \quad . \end{aligned} \quad (2.5)$$

By convention, the perturbed displacements are chosen to be zero at t and $t + T$ making the second volume integral zero. The third volume integral is zero if the displacements satisfy the equations of motion. The surface integrals account for the flux of energy through the internal and external surfaces of the volume element. The surface integral over Σ^i is zero if the stress and the perturbed displacements are periodic and satisfy the boundary conditions. The integral over Σ^e is zero if the stress is zero at infinite radius and the net flux through the end faces is zero. These conditions are satisfied for normal modes (e.g., tube, pseudo-Rayleigh, or flexural waves) but not leaky modes which radiate energy away from the center of the volume element making the surface integrals nonzero. In summary, Hamilton's Principle indicates that the time integral of the Lagrangian energy for a normal mode is stationary for perturbations in displacement which satisfy the boundary conditions and which are zero at t and $t + T$:

$$\delta \int_t^{t+T} dt \int_V dV \mathcal{L} = 0 \quad . \quad (2.6)$$

The value of the time integral of the Lagrangian energy is also needed to derive the perturbation equation. To find this value, multiply the equation of motion by u_i ,

and integrate this product over one period and one volume element. Apply the same integrations which were used to derive Hamilton's principle but in the reverse order:

$$\begin{aligned} \int_t^{t+T} dt \int_V dV (\rho \ddot{u}_i - \tau_{ji,j}) u_i = \\ \int_V dV \rho \dot{u}_i u_i \Big|_t^{t+T} - \int_t^{t+T} dt \int_V dV \left(\frac{1}{2} \rho \dot{u}_i \dot{u}_i - \frac{1}{2} u_{j,i} c_{ijkl} u_{l,k} \right) + \\ \int_t^{t+T} dt \left[\int_{\Sigma^i} dS [n_j \tau_{ji} u_i]_+^+ - \int_{\Sigma^e} dS n_j \tau_{ji} u_i \right] . \end{aligned} \quad (2.7)$$

Because the displacements are periodic, satisfy the equation of motion, and satisfy the boundary conditions; the first, second, fourth, and fifth integrals are zero. The result,

$$\int_t^{t+T} dt \int_V dV \mathcal{L} = 0 \quad , \quad (2.8)$$

indicates that the time integral of the Lagrangian energy is zero.

Perturbation theory will be used to relate changes in the elastic moduli, densities, locations of interfaces, frequency, and wavenumber. The mathematical formulation is similar to that used by Woodhouse and Dahlen (1978) and by Aki and Richards (1980, p. 286-292) and is based upon an idea first proposed by Rayleigh (1878, section 88). The Lagrangian energy density is considered a functional of the displacements, frequency (ω), wavenumber (k_z), elastic moduli, densities, and locations of interfaces (which are on Σ^i) and will be designated $\mathcal{L}(u_i, \omega, k_z, c_{ijkl}, \rho, \Sigma^i)$. For slight perturbations in the displacements, frequency, wavenumber, elastic moduli, densities, and locations of interfaces; the Lagrangian energy density is expressed as $\mathcal{L}^p(u_i + \delta u_i, \omega + \delta \omega, k_z + \delta k_z, c_{ijkl} + \delta c_{ijkl}, \rho + \delta \rho, \Sigma^i + \delta \Sigma^i)$. The derivation of the perturbation equation begins by integrating \mathcal{L}^p over one volume element and one period:

$$\begin{aligned} \int_t^{t+T} dt \int_V dV \mathcal{L}^p = \\ \int_t^{t+T} dt \left[\int_V dV \frac{1}{2} (\rho + \delta \rho) (\dot{u}_i + \delta \dot{u}_i + u_i \delta \omega) (\dot{u}_i + \delta \dot{u}_i + u_i \delta \omega) \right. \\ \left. - \int_V dV \frac{1}{2} (u_{j,i} + \delta u_{j,i} + \delta k_z e_{ij}) (c_{ijkl} + \delta c_{ijkl}) (u_{l,k} + \delta u_{l,k} + \delta k_z e_{kl}) \right] \end{aligned} \quad (2.9)$$

$$+ \int_{\Sigma^e} dS [-h\mathcal{L}]_-^+$$

where e_{ij} is the strain tensor. The perturbations in displacement ($\delta\dot{u}_i$, δu_j , and δu_l) and frequency ($\delta\omega$) are expressed explicitly. Because the displacements will be expressed in the wavenumber domain, the strains will contain expressions with k_z , and the perturbations in k_z can be expressed implicitly as $\delta_{k_z}e_{ij}$ and $\delta_{k_z}e_{kl}$. The surface integral accounts for the change in the Lagrangian energy due to the changes in the locations of the interfaces. (The location of each perturbed interface is specified by moving the original interface a distance, h , along its normal.) The expressions in the integrands are multiplied, and only terms with one perturbed variable are kept because terms with two or more perturbed variables are very small. Integration by parts is applied to the temporal derivatives and Gauss' theorem to the spatial derivatives.

$$\begin{aligned} \int_t^{t+T} dt \int_V dV \mathcal{L}^p = & \int_t^{t+T} dt \int_V dV \left(\frac{1}{2} \rho \dot{u}_i \dot{u}_i - \frac{1}{2} u_{j,i} c_{ijkl} u_{l,k} \right) + \int_V dV \rho \dot{u}_i \delta u_i \Big|_t^{t+T} \\ & \int_t^{t+T} dt \left[- \int_V dV (\rho \ddot{u}_i - \tau_{ji,j}) \delta u_i - \int_{\Sigma^e} dS n_j \tau_{ji} \delta u_i + \int_{\Sigma^e} dS [n_j \tau_{ji} \delta u_i]_-^+ \right. \\ & \quad + \int_{\Sigma^e} dS [-h\mathcal{L}]_-^+ - \int_V dV \delta_{k_z} e_{ij} c_{ijkl} e_{kl} + \int_V dV \rho \omega \delta \omega u_i u_i \\ & \quad \left. + \int_V dV \left(\frac{1}{2} \delta \rho \omega^2 u_i u_i - \frac{1}{2} e_{ij} \delta c_{ijkl} e_{kl} \right) \right] \end{aligned} \quad (2.10)$$

Equations 2.8 shows that the first and second integrals are zero. Hamilton's Principle shows that the integrals associated with the perturbations in displacement (i.e., the third, fourth, and fifth integrals) are, to first order, zero for the normal modes. The sixth integral is not zero because the locations of the interfaces have changed. In Appendix B, its integrand is manipulated to remove the unknown, δu_i , and the result is

$$[n_j \tau_{ji} \delta u_i]_-^+ = [-h n_i \tau_{ij} n_k u_{j,k} + h_{,i} u_i n_j n_k \tau_{kj}]_-^+ .$$

The first term on the right-hand side accounts for the change in the displacements between the original and the perturbed interfaces, and the second term for the change in the normal, $-h_{,i}$. With these simplifications, the final equation is

$$\begin{aligned} \int_t^{t+T} dt \left[\int_V dV \delta_{k_z} e_{ij} c_{ijkl} e_{kl} - \omega \delta \omega \int_V dV \rho u_i u_i \right] = \\ \int_t^{t+T} dt \left[- \int_{\Sigma^+} dS h [\mathcal{L} + n_i \tau_{ij} n_k u_{j,k}]_-^+ + \int_{\Sigma^+} dS h_{,i} [u_i n_j n_k \tau_{kj}]_-^+ \right. \\ \left. + \frac{\omega^2}{2} \int_V dV \delta \rho u_i u_i - \frac{1}{2} \int_V dV e_{ij} \delta c_{ijkl} e_{kl} \right] . \end{aligned} \quad (2.11)$$

The first and second integrals are associated with perturbations in the wavenumber and frequency, respectively. The third integral accounts for the change in the Lagrangian energy and displacements due to the changes in the locations of the interfaces, and the fourth for the changes in the normal to each interface. The fifth and sixth integrals account for perturbations in the densities and elastic moduli, respectively.

2.3 Applications

To use the perturbation equation to calculate partial derivatives, group velocity, etc., it must be applied to a specific model. The model must represent adequately the actual conditions in the borehole but must be simple to keep the mathematics simple. One model which meets these criteria consists of a fluid-filled, cylindrical borehole in a transversely isotropic solid with its symmetry axis parallel to the borehole (Figure 2-1). The density of the fluid is ρ_1 , and the incompressibility is λ_1 . The density of the solid is ρ_2 , and the elastic moduli are c_{11} , c_{33} , c_{13} , c_{44} , and c_{66} . (Although the perturbation equation was derived with tensor notation, the formulas will be derived with abbreviated subscript notation because computer code is written easily with it.) The borehole radius is R . These variables and also the variables in the formulas which will be derived in this section are listed in Table 2.2 for easy reference.

The displacements for this model (see Appendix A) are substituted into the integrals in equation 2.11, and the results are:

$$\int_t^{t+\mathcal{T}} dt \int_V dV \delta_{kz} e_{ij} c_{ijkl}^{TI} e_{kl} = \delta_{kz} \frac{\zeta \pi \Lambda \mathcal{T}}{4} I^{kz} \quad (2.12)$$

$$\int_t^{t+\mathcal{T}} dt \int_V dV \rho u_i u_i = \frac{\zeta \pi \Lambda \mathcal{T}}{4} I^\omega \quad (2.13)$$

$$\int_t^{t+\mathcal{T}} dt \int_V dV \delta \rho u_i u_i = \frac{\zeta \pi \Lambda \mathcal{T}}{4} (\delta \rho_1 I^{\rho_1} + \delta \rho_2 I^{\rho_2}) \quad (2.14)$$

$$\begin{aligned} \int_t^{t+\mathcal{T}} dt \int_V dV e_{ij} \delta c_{ijkl}^{TI} e_{kl} = & \frac{\zeta \pi \Lambda \mathcal{T}}{4} \left(\delta \lambda_1 I^{\lambda_1} + \delta c_{11}^{TI} I^{c_{11}^{TI}} + \right. \\ & \delta c_{33}^{TI} I^{c_{33}^{TI}} + \delta c_{13}^{TI} I^{c_{13}^{TI}} + \\ & \left. \delta c_{44}^{TI} I^{c_{44}^{TI}} + \delta c_{66}^{TI} I^{c_{66}^{TI}} \right) \end{aligned} \quad (2.15)$$

$$\int_t^{t+\mathcal{T}} dt \int_{\Sigma^i} dS h [\mathcal{L} + n_i \tau_{ij} n_k u_{j,k}]_-^+ = \frac{\Lambda \mathcal{T}}{4} I^{\Sigma^i, 1} \quad (2.16)$$

$$\int_t^{t+\mathcal{T}} dt \int_{\Sigma^i} dS h_{;i} [u_i n_j n_k \tau_{kj}]_-^+ = \frac{\Lambda \mathcal{T}}{4} I^{\Sigma^i, 2} \quad (2.17)$$

The integration over time yields $\mathcal{T}/2$. The volume integrals are computed in the circular cylindrical coordinate system with coordinates r , θ , and z . The integration over θ yields $\zeta \pi$. When the azimuthal order number is 0, $\zeta = 2$; otherwise $\zeta = 1$. The integration over z yields $\Lambda/2$. The integral over radius, which usually cannot be computed analytically, has the generic designation, I , and is listed in Appendix C. The surface integrals, which are over θ and z , can be computed analytically for simple perturbations in the location of the fluid-solid interface. When the perturbations only depend upon θ , the integration over z yields $\Lambda/2$. The integrals over θ are denoted $I^{\Sigma^i, 1}$ and $I^{\Sigma^i, 2}$ and are listed in Appendix C. Note that in equation 2.15 only the five elastic constants for the transversely isotropic solid, c_{IJ}^{TI} , are perturbed.

If the elastic moduli of the solid are perturbed to make it have general anisotropy, then a different expression for the integral involving these perturbations must be developed. The medium, to which the perturbations are made, is always chosen to be transversely isotropic rather than isotropic because the three additional elastic moduli of the transversely isotropic medium allow it to be closer to the general anisotropic

medium. Consequently the perturbations can be smaller, and the solution will be more accurate. The stiffness matrix for the anisotropic medium is written as a sum of transversely isotropic and perturbation parts: $[c_{IJ}] = [c_{IJ}^{TI}] + [\delta c_{IJ}]$. For the best results, the most amount of $[c_{IJ}]$ must be put into $[c_{IJ}^{TI}]$, and the least amount into $[\delta c_{IJ}]$. A simple, effective method of making this separation is to minimize the norm of $[\delta c_{IJ}]$, which only requires minimizing its largest eigenvalue (Strang, 1980, p. 286).

To compute the integral associated with the perturbations in the elastic moduli, the perturbation stiffness tensor which is defined in the Cartesian coordinate system must be transformed into the cylindrical coordinate system. The transformation is based upon this property: at a point in space, the components of a tensor in cylindrical coordinates equal the components of the equivalent tensor in Cartesian coordinates when the axes of the Cartesian and cylindrical coordinate systems are aligned (Malvern, 1969, p. 531). The transformation is performed with

$$[\delta c'_{IJ}] = [M][\delta c_{IJ}][M]^T, \quad (2.18)$$

where $[\delta c'_{IJ}]$ is the perturbation stiffness matrix at angle θ , $[\delta c_{IJ}]$ is the perturbation stiffness matrix at $\theta = 0$, and

$$[M] = \begin{bmatrix} \cos^2 \theta & \sin^2 \theta & 0 & 0 & 0 & \sin 2\theta \\ \sin^2 \theta & \cos^2 \theta & 0 & 0 & 0 & -\sin 2\theta \\ 0 & 0 & 1 & 0 & 0 & 0 \\ 0 & 0 & 0 & \cos \theta & -\sin \theta & 0 \\ 0 & 0 & 0 & \sin \theta & \cos \theta & 0 \\ -\frac{1}{2} \sin 2\theta & \frac{1}{2} \sin 2\theta & 0 & 0 & 0 & \cos 2\theta \end{bmatrix} \quad (2.19)$$

(Auld, 1973, p. 77). (This transformation is not applied to c_{IJ}^{TI} because it is the same at all azimuths.) The final integral, which pertains only to the solid, is

$$\int_t^{t+\mathcal{T}} dt \int_V dV e_{ij} \delta c_{ijkl} e_{kl} = \frac{\zeta \pi \Lambda \mathcal{T}}{4} I^{c_{IJ}} \quad (2.20)$$

where $I^{c_{IJ}}$ includes the perturbations in all elastic moduli and is given in Appendix C.

2.3.1 Phase Velocities for a Slightly Anisotropic Solid

Calculating the phase velocities of a normal mode when the solid has slight, general anisotropy requires four steps. First, the elastic moduli for the starting transversely isotropic model (whose symmetry axis is parallel to the borehole) are calculated. Second, at each frequency the phase velocity and wavenumber of the normal modes for the starting model are computed using equation A.46. An important point, which will be thoroughly discussed in Chapter 3, is that the mode in the transversely isotropic model must have the same orientation that the mode in the general anisotropic model has. Third, at each frequency the perturbation in the phase velocity, δv , is calculated. The formula to perform this calculation is derived by substituting equations 2.12 and 2.20 into 2.11 and ignoring the integrals associated with the other perturbations. The perturbation in phase velocity is calculated from δk_z using $\delta v = -v\delta k_z/k_z$ which is derived from $k_z v = \omega$ by assuming that ω is constant. The resulting equation is

$$\delta v = \frac{\omega}{2k_z^2} \frac{I^{c_{IJ}}}{I^{k_z}} \quad . \quad (2.21)$$

Fourth, the velocity corrections are added to the original dispersion curve for the transversely isotropic model.

Test results show that the predicted phase velocities are quite accurate. For the test, exact phase velocities were calculated for a model with transversely isotropic solid with its symmetry axis parallel to the borehole (Table 2.3). Then the isotropic part of the transversely isotropic stiffness matrix was determined. (For this test case only, c_{IJ}^T are the moduli for the isotropic solid, and δc_{IJ} are the perturbations which make the solid transversely isotropic.) After calculating the phase velocities for the isotropic model, velocity corrections, which account for the transverse isotropy, were computed with the perturbation method and were added to original phase velocities. In general, the predicted velocities are very close to the exact solutions, although slight errors occurred near the cutoff frequencies for the screw and pseudo-Rayleigh waves (Figures 2-2 and 2-3).

As an example of this application, the phase velocities of quasi-flexural waves in a model with an orthorhombic solid (Table 2.4) were calculated. In the starting model, the first flexural wave (# 1) is aligned with the polarization of the slow qS -wave whose wavenumber vector is parallel to the borehole; the second flexural wave (# 2) is aligned with polarization of the fast qS -wave whose wavenumber vector is parallel to the borehole. The predicted velocities of the two quasi-flexural waves are slightly different and are related to their orientation (Figure 2-4). (A thorough analysis of these modes is in Chapter 3). Above the phase velocity of the slow qS -wave (2.67 km/s), the velocities predicted with the perturbation method seem reasonable, but their accuracy is suspect. That is, modes whose phase velocities are greater than the phase velocity of the slow qS -wave are leaky which means that they radiate energy away from the borehole. Consequently the velocities of the leaky mode are being predicted with a normal mode which has very different displacements.

The perturbation method is appropriate for this problem because the perturbations in the elastic moduli are small. Many researchers currently believe that the azimuthal variations in S -wave velocity frequently range from 3 to 5%, and those in the P -wave velocity are even less (S. Crampin, 1988, oral communication; D. Corrigan, 1989, oral communication; D. F. Winterstein, 1989, oral communication). Since the anisotropy is small, the perturbations in the elastic moduli, $[\delta c_{IJ}]$, will be small, and the calculated phase velocities will be accurate.

2.3.2 Partial Derivatives

Partial derivatives for a transversely isotropic model (whose symmetry axis is parallel to the borehole) are calculated by relating perturbations in either the elastic moduli or densities to perturbations in either the frequency or wavenumber. For example, to calculate the partial derivative of the wavenumber with respect to an elastic modulus of the solid, equations 2.12 and 2.15 are substituted into equation 2.11. The integrals

associated with the other perturbations are ignored, and the equation is rearranged:

$$\frac{\delta k_z}{\delta c_{IJ}^{TI}} = -\frac{1}{2} \frac{I c_{IJ}^{TI}}{I k_z} \quad .$$

Comparing the effects that each elastic modulus has upon the wavenumber is done easily when the partial derivative is normalized:

$$\frac{c_{IJ}^{TI}}{k_z} \frac{\delta k_z}{\delta c_{IJ}^{TI}} = -\frac{c_{IJ}^{TI}}{2k_z} \frac{I c_{IJ}^{TI}}{I k_z} \quad .$$

This derivative is sometimes called the sensitivity. The other partial derivatives (Table 2.5) are derived in a similar manner.

As an example of this application, normalized partial derivatives for a tube wave (Figure 2-5) in a transversely isotropic model (Table 2.3) were calculated. The integration over radius was performed numerically using Gaussian quadrature and was terminated when the sum converged to four significant digits. A more extensive compilation of partial derivatives for models with fast, slow, and very slow formations is in Appendix E.

Some simple additions can be used to check the accuracy of the normalized partial derivatives. For example, the sum of the derivatives of the frequency with respect to the moduli are

$$\begin{aligned} S &= \frac{\lambda_1}{2\omega^2} \frac{I^{\lambda_1}}{I^\omega} + \frac{c_{11}^{TI}}{2\omega^2} \frac{I^{c_{11}^{TI}}}{I^\omega} + \dots + \frac{c_{66}^{TI}}{2\omega^2} \frac{I^{c_{66}^{TI}}}{I^\omega} \\ &= \frac{1}{2} \left[\frac{\zeta \pi \Lambda \mathcal{T} \omega^2 I^\omega}{8} \right]^{-1} \left[\frac{\zeta \pi \Lambda \mathcal{T}}{8} \left(\lambda_1 I^{\lambda_1} + c_{11}^{TI} I^{c_{11}^{TI}} + \dots + c_{66}^{TI} I^{c_{66}^{TI}} \right) \right] \quad . \end{aligned}$$

The expression within the first set of brackets is the time integral of the kinetic energy, and the expression within the second set is the time integral of the elastic strain energy. Because these energies are equal (see equation 2.8), the sum, S , must be $1/2$. Similarly, the sum of the normalized derivatives of the frequency with respect to the densities must be $-1/2$; the sum of the normalized derivatives of the wavenumber with respect to the elastic moduli times U_G/v (where U_G is the group velocity) must be $-1/2$; and the sum of the normalized derivatives of the wavenumber with respect

to the densities times U_G/v must be 1/2. (Equation 2.23 may be used to calculate U_G .)

When the formation is isotropic, the partial derivatives can be calculated readily with the previous equations because isotropy is a special case of transverse isotropy. Using the Lamé parameters, which are related to the elastic moduli via $c_{11}^{TI} = c_{33}^{TI} = \lambda_2 + 2\mu_2$, $c_{13}^{TI} = \lambda_2$, and $c_{44}^{TI} = c_{66}^{TI} = \mu_2$, equation 2.15 may be written:

$$\int_t^{t+\mathcal{T}} dt \int_V dV e_{ij} \delta c_{ijkl}^{TI} e_{kl} = \frac{\zeta \pi \Lambda \mathcal{T}}{4} \times \left[\delta \lambda_1 I^{\lambda_1} + \delta(\lambda_2 + 2\mu_2)(I^{c_{11}^{TI}} + I^{c_{33}^{TI}} + I^{c_{13}^{TI}}) + \delta \mu_2(I^{c_{44}^{TI}} + I^{c_{66}^{TI}} - 2I^{c_{13}^{TI}}) \right] . \quad (2.22)$$

Usually the derivative with respect to the formation P -wave velocity, α_2 , is desired and can be obtained with $2(\lambda_2 + 2\mu_2)/\delta(\lambda_2 + 2\mu_2) = \alpha_2/\delta\alpha_2$, which is derived from $\alpha_2^2 = (\lambda_2 + 2\mu_2)/\rho_2$. The derivative with respect to the formation S -wave velocity, β_2 , is obtained with $2\mu_2/\delta\mu_2 = \beta_2/\delta\beta_2$, which is derived from $\beta_2^2 = \mu_2/\rho_2$. Finally, the derivative with respect to the acoustic velocity of the fluid, α_1 , is obtained with $2\lambda_1/\delta\lambda_1 = \alpha_1/\delta\alpha_1$ which is derived from $\alpha_1^2 = \lambda_1/\rho_1$. (The 2 in these equations causes the normalized partial derivatives to sum to 1.) The normalized partial derivatives based upon these velocities are listed in Tables 2.6 and 2.7.

2.3.3 Group Velocities

Group velocity is calculated by relating perturbations in frequency and wavenumber. To derive the formula, equations 2.12 and 2.13 are substituted into equation 2.11, the other integrals are neglected, and the equation is rearranged:

$$U_G = \frac{\delta\omega}{\delta k_z} = \frac{1}{\omega} \frac{I^{k_z}}{I^\omega} . \quad (2.23)$$

As an example of this application, group velocities for tube and flexural waves in the transversely isotropic model (Table 2.3) were calculated (Figure 2-6). Additional examples are in Chapter 1.

2.3.4 Phase Velocities for a Slightly Irregular Borehole

Calculating the phase velocities of a normal mode when the borehole wall is slightly irregular requires four steps. First, a model with a cylindrical borehole, whose radius is close to the average radius of the irregular borehole, is selected. Second, at each frequency the phase velocity and wavenumber for the normal modes in the cylindrical model are computed using equation A.46. Third, at each frequency the perturbation in phase velocity is calculated. The formula to perform this calculation is derived by substituting equations 2.12, 2.16, and 2.17 into equation 2.11 and using $\delta v = -v\delta k_z/k_z$. The other integrals are neglected, and the equation is rearranged:

$$\delta v = \frac{\omega}{\zeta \pi k_z^2} \frac{I^{\Sigma',1} - I^{\Sigma',2}}{I^{k_z}} . \quad (2.24)$$

Fourth, these velocity corrections are added to the original dispersion curves. However, because the corrections are usually small, comparing the dispersion curves for the circular and irregular boreholes would not be worthwhile. Instead the corrections are displayed as the percent change in the phase velocity, $100\% \times \delta v/v$.

Test results indicate that the estimated phase velocities are accurate even for moderately large perturbations in the borehole wall. For the test, the solid was chosen to be isotropic (Table 2.8). Exact dispersion curves were computed for two cylindrical boreholes with radii, R and $R + \epsilon R$ where ϵ is a scaling parameter (Figure 2-7), and the difference between the velocities at each frequency is the exact perturbation. Equation 2.11 was used to estimate the same perturbations by changing the location of the borehole wall with $h(\theta) = \epsilon R$. When $\epsilon = 0.05$, the estimated and exact perturbations are nearly equal, but when ϵ is larger, say 0.10 or 0.20, the estimated perturbations are too large at moderate and high frequencies (Figure 2-8). This discrepancy for large values of ϵ is observed with the other normal modes also. Based upon these results, the maximum value of ϵ for which the perturbation method could give reasonably accurate results was judged to be 0.10.

As an example of this application, the velocity changes were calculated for a tube

wave in an elliptical borehole. The perturbation in the borehole wall is given by $h(\theta) = R\epsilon \cos^2(\theta - \phi)$ where $\epsilon = 0.10$ and $\phi = 45^\circ$ (Figure 2-9), and the properties of the model are listed in Table 2.8. The percent change in phase velocity at all frequencies is always less than 0.1% (Figure 2-10).

The perturbation method is appropriate for this problem because the irregularities in actual borehole walls are often small. For example, many boreholes have an elliptical shape for which ϵ is usually less than 0.03 or 0.04 (Figure 2-11) (R. Siegfried, 1988, oral communication). Therefore, the velocities predicted with the perturbation method will be accurate.

2.4 Summary

Using perturbation theory, an equation which relates first order perturbations in frequency, wavenumber, elastic moduli, densities, and locations of interfaces was derived. This equation applies to a general model which can have many fluid or solid layers with any cross-sectional shape. To develop some useful formulas, the perturbation equation was applied to the two-layer model which is used throughout this thesis. The inner layer is a fluid, and the outer layer is a transversely isotropic solid with its symmetry axis parallel to the borehole. Because analytical expressions for the displacements exist for this particular model, the terms in the perturbation equation simplify greatly. Formulas were derived to calculate (1) phase velocities for a model with slight, general anisotropy, (2) partial derivatives of either the wavenumber or frequency with respect to either an elastic modulus or density, (3) group velocity, and (4) phase velocities for a model with a slightly irregular borehole. These formulas are applicable also to models with an isotropic solid because it is a special case of a transversely isotropic solid. Furthermore, the formulas can be used for modes with any azimuthal order number or any radial mode number.

Variable	Meaning
ρ	density
c_{ijkl}	elastic modulus
u_i	displacement
e_{ij}	strain
τ_{ji}	stress
T_i	traction
k_z	wavenumber in z direction
Λ	wavelength
t	time
ω	frequency
\mathcal{T}	period of mode
Σ^i	interior surface
Σ^e	exterior surface
n_j	normal on Σ^i or Σ^e
h	perturbation to Σ^i along n_j
S	surface area
V	volume
\mathcal{L}	Lagrangian energy

Table 2.1: Variables needed to derive the perturbation equation.

Variable	Meaning
$r, \theta, \text{ and } z$	cylindrical coordinates
n	azimuthal order number
v	phase velocity
U_G	group velocity
α_1	acoustic velocity of fluid
α_2	P -wave velocity of an isotropic solid
β_2	S -wave velocity of an isotropic solid
λ_1	Lamé parameter for fluid
λ_2, μ_2	Lamé parameters for an isotropic solid
ρ_1	fluid density
ρ_2	solid density
c_{IJ}	elastic modulus in abbreviated subscript notation
c_{ijkl}^{TI} or c_{IJ}^{TI}	elastic modulus for a transversely isotropic solid with its symmetry axis parallel to the borehole
$[\delta c_{IJ}]$	perturbation stiffness matrix at $\theta = 0$
$[\delta c'_{IJ}]$	perturbation stiffness matrix at angle θ
$[M]$	rotation matrix for $[\delta c'_{IJ}]$
$u_r, u_\theta, \text{ and } u_z$	displacements in $r, \theta, \text{ and } z$ directions
$U_r, U_\theta, \text{ and } U_z$	Fourier transforms of $u_r, u_\theta, \text{ and } u_z$
$E_{rr}, E_{\theta\theta}, E_{zz}, \text{ etc.}$	Fourier transforms of strains
R	borehole radius
I^{k_z}	integral related to the perturbation of k_z
I^ω	integral related to the perturbation of ω
I^{ρ_1}	integral related to the perturbation of ρ_1
I^{ρ_2}	integral related to the perturbation of ρ_2
I^{λ_1}	integral related to the perturbation of λ_1
$I^{c_{IJ}^{TI}}$	integral related to the perturbation of c_{IJ}^{TI}
$I^{c_{IJ}}$	integral related to the perturbation of c_{IJ}
$I^{\Sigma^i,1}$ and $I^{\Sigma^i,2}$	integrals related to the perturbation of Σ^i
$I_{cc}, I_{ss}, \text{ and } I_{cs}$	additional integrals needed to compute $I^{\Sigma^i,1}$ and $I^{\Sigma^i,2}$
ζ	factor related to integral over θ
$d_{11}, d_{12}, d_{13}, \text{ etc.}$	additional terms needed to compute $I^{c_{IJ}}$
ϵ	scaling parameter in the analytical expressions for h

Table 2.2: Additional variables needed to derive formulas for partial derivatives, group velocity, etc.

Quantity	Value
c_{11}	3.126×10^{10} Pa
c_{13}	0.245×10^{10} Pa
c_{33}	2.249×10^{10} Pa
c_{44}	0.649×10^{10} Pa
c_{66}	0.882×10^{10} Pa
ρ_2	2075. kg/m ³
λ_1	0.225×10^{10} Pa
ρ_1	1000. kg/m ³
R	0.1016 m

Table 2.3: Properties of a transversely isotropic model for which the symmetry axis of the solid is parallel to the z axis. The properties of the solid are those of the Mesaverda shale 5496.5 (Thomsen, 1986).

Quantity	Value
c_{11}	9.78×10^{10} Pa
c_{12}	1.95×10^{10} Pa
c_{13}	3.23×10^{10} Pa
c_{22}	9.09×10^{10} Pa
c_{23}	1.86×10^{10} Pa
c_{33}	8.17×10^{10} Pa
c_{44}	2.44×10^{10} Pa
c_{55}	2.00×10^{10} Pa
c_{66}	3.18×10^{10} Pa
ρ_2	2800 kg/m ³
λ_1	0.225×10^{10} Pa
ρ_1	1000. kg/m ³
R	0.1016 m

Table 2.4: Properties of the orthorhombic model. The symmetry planes for the orthorhombic solid are parallel to the coordinate planes. The properties of the solid were measured by J. Mendelson (1989, oral communication).

Quantity	Normalized Partial Derivative of Wavenumber	Normalized Partial Derivative of Frequency
λ_1	$\frac{\lambda_1}{k_z} \frac{\delta k_z}{\delta \lambda_1} = -\frac{\lambda_1}{2k_z} \frac{I^{\lambda_1}}{I^{k_z}}$	$\frac{\lambda_1}{\omega} \frac{\delta \omega}{\delta \lambda_1} = \frac{\lambda_1}{2\omega^2} \frac{I^{\lambda_1}}{I^\omega}$
c_{IJ}^{TI}	$\frac{c_{IJ}^{TI}}{k_z} \frac{\delta k_z}{\delta c_{IJ}^{TI}} = -\frac{c_{IJ}^{TI}}{2k_z} \frac{I^{c_{IJ}^{TI}}}{I^{k_z}}$	$\frac{c_{IJ}^{TI}}{\omega} \frac{\delta \omega}{\delta c_{IJ}^{TI}} = \frac{c_{IJ}^{TI}}{2\omega^2} \frac{I^{c_{IJ}^{TI}}}{I^\omega}$
ρ_1	$\frac{\rho_1}{k_z} \frac{\delta k_z}{\delta \rho_1} = \frac{\rho_1 \omega^2}{2k_z} \frac{I^{\rho_1}}{I^{k_z}}$	$\frac{\rho_1}{\omega} \frac{\delta \omega}{\delta \rho_1} = -\frac{\rho_1}{2} \frac{I^{\rho_1}}{I^\omega}$
ρ_2	$\frac{\rho_2}{k_z} \frac{\delta k_z}{\delta \rho_2} = \frac{\rho_2 \omega^2}{2k_z} \frac{I^{\rho_2}}{I^{k_z}}$	$\frac{\rho_2}{\omega} \frac{\delta \omega}{\delta \rho_2} = -\frac{\rho_2}{2} \frac{I^{\rho_2}}{I^\omega}$

Table 2.5: Normalized partial derivatives for a transversely isotropic model with its symmetry axis parallel to the borehole.

Quantity	Normalized Partial Derivative of Wavenumber
α_1	$\frac{\alpha_1}{k_z} \frac{\delta k_z}{\delta \alpha_1} = -\frac{\lambda_1}{k_z} \frac{I^{\lambda_1}}{I^{k_z}}$
α_2	$\frac{\alpha_2}{k_z} \frac{\delta k_z}{\delta \alpha_1} = -\frac{\lambda_2 + 2\mu_2}{k_z} \frac{I^{c_{11}^{TI}} + I^{c_{33}^{TI}} + I^{c_{13}^{TI}}}{I^{k_z}}$
β_2	$\frac{\beta_2}{k_z} \frac{\delta k_z}{\delta \beta_2} = -\frac{\mu_2}{k_z} \frac{I^{c_{44}^{TI}} + I^{c_{66}^{TI}} - 2I^{c_{13}^{TI}}}{I^{k_z}}$

Table 2.6: Normalized partial derivatives of the wavenumber for an isotropic model.

Quantity	Normalized Partial Derivative of Frequency
α_1	$\frac{\alpha_1}{\omega} \frac{\delta \omega}{\delta \alpha_1} = \frac{\lambda_1}{\omega^2} \frac{I^{\lambda_1}}{I \omega}$
α_2	$\frac{\alpha_2}{\omega} \frac{\delta \omega}{\delta \alpha_2} = \frac{\lambda_2 + 2\mu_2}{\omega^2} \frac{I^{c_{11}^{TI}} + I^{c_{33}^{TI}} + I^{c_{13}^{TI}}}{I \omega}$
β_2	$\frac{\beta_2}{\omega} \frac{\delta \omega}{\delta \beta_2} = \frac{\mu_2}{\omega^2} \frac{I^{c_{44}^{TI}} + I^{c_{66}^{TI}} - 2I^{c_{13}^{TI}}}{I \omega}$

Table 2.7: Normalized partial derivatives of frequency for an isotropic model.

Quantity	Value
c_{11}	3.79×10^{10} Pa
c_{44}	1.51×10^{10} Pa
ρ_2	2140 kg/m ³
λ_1	0.225×10^{10} Pa
ρ_1	1000. kg/m ³
R	0.1016 m

Table 2.8: Properties of the isotropic model. The properties of the solid are like those of the Berea sandstone (Thomsen, 1986).

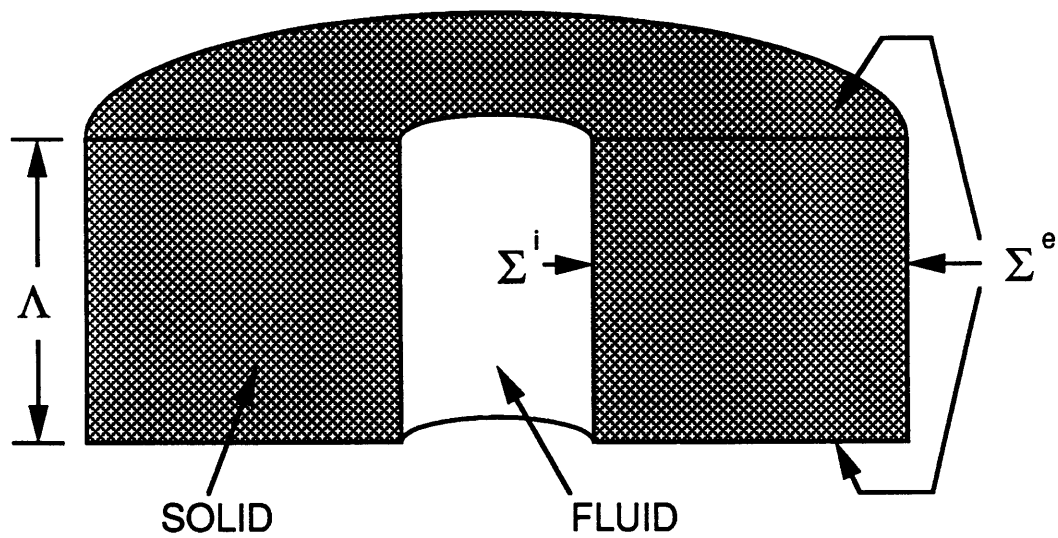


Figure 2-1: Cutaway view of the mathematical model used to derive the perturbation equation. Although the model may have many layers, this two-layer model was chosen to show clearly the important features.

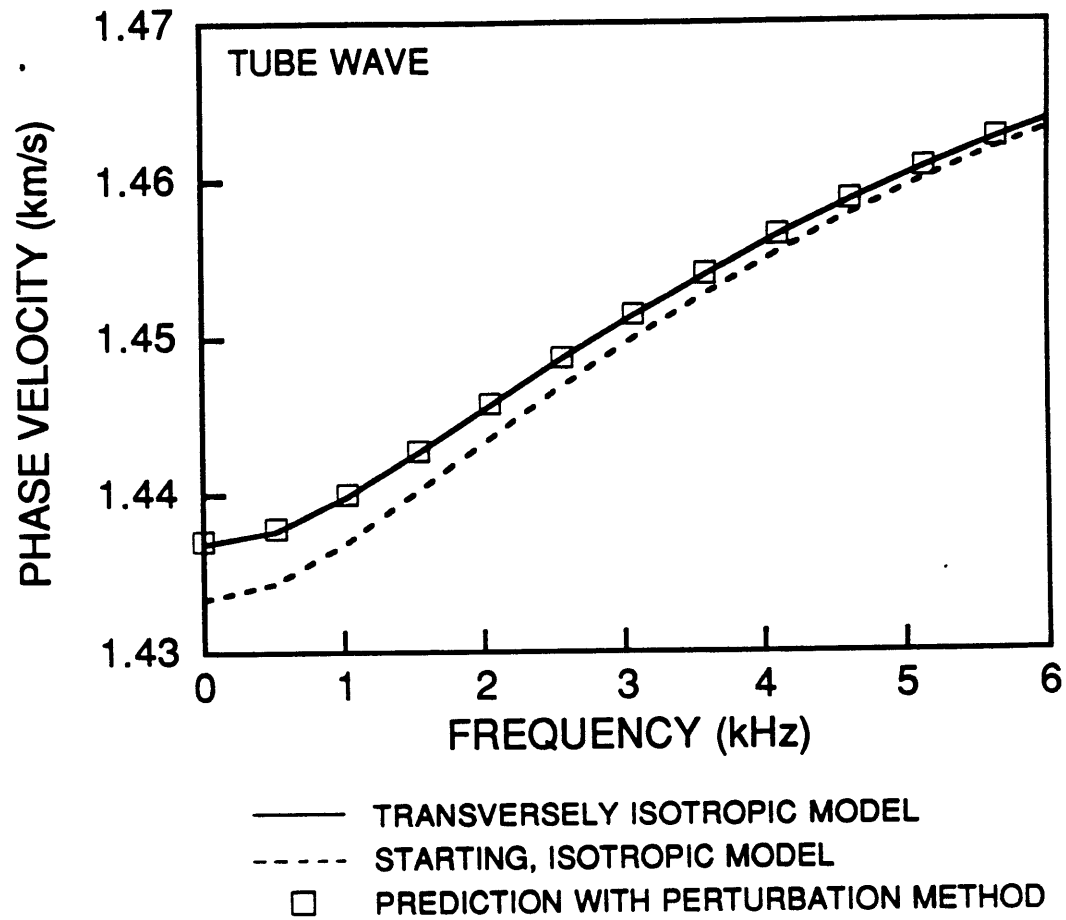


Figure 2-2: Accuracy of the phase velocities of the tube wave predicted by the perturbation method. Starting with an isotropic model this method is used to predict the phase velocities for the transversely isotropic model (Table 2.3) with the symmetry axis parallel to the borehole.

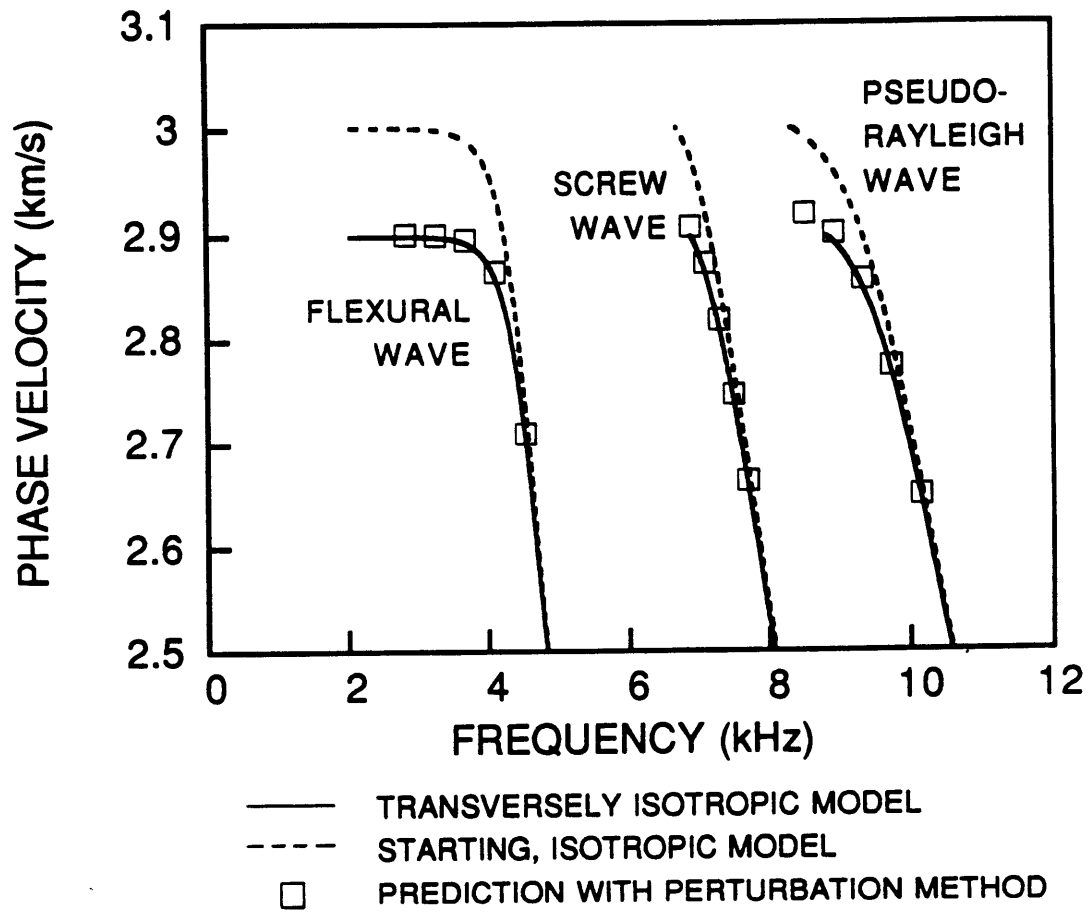


Figure 2-3: Accuracy of the phase velocities of the flexural, screw, and pseudo-Rayleigh waves predicted by the perturbation method. Starting with an isotropic model this method is used to predict the phase velocities for the transversely isotropic model (Table 2.3) with the symmetry axis parallel to the borehole.

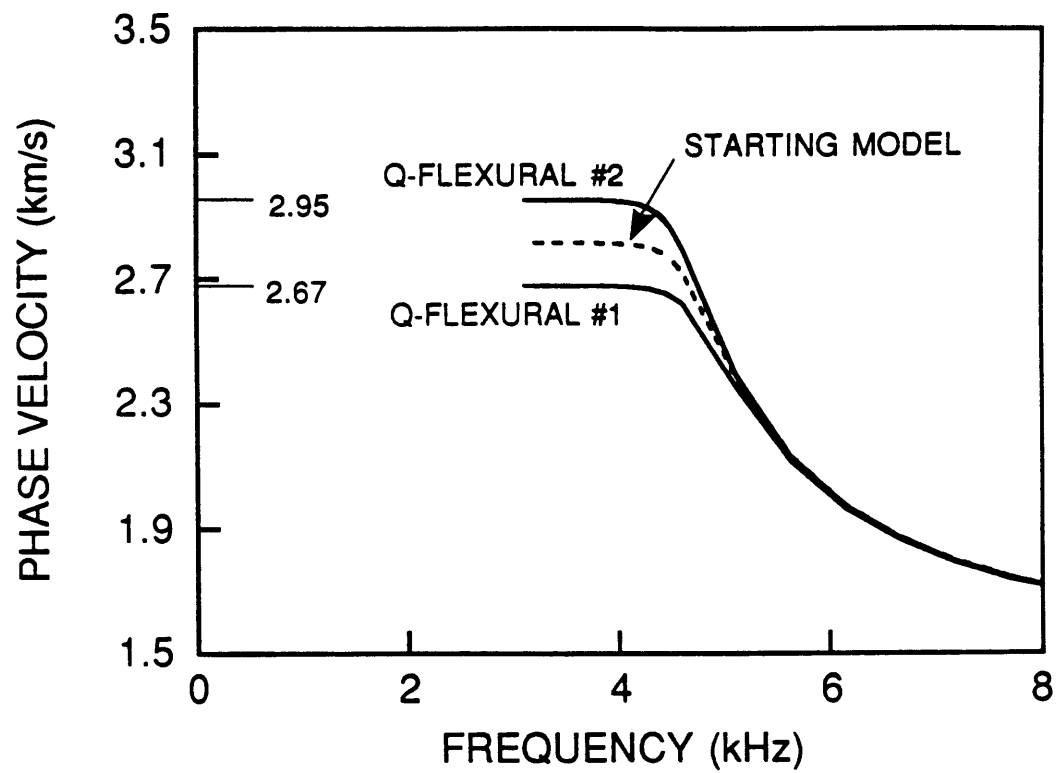


Figure 2-4: Phase velocities for the quasi-flexural waves in the orthorhombic model (Table 2.4) and in the starting model.

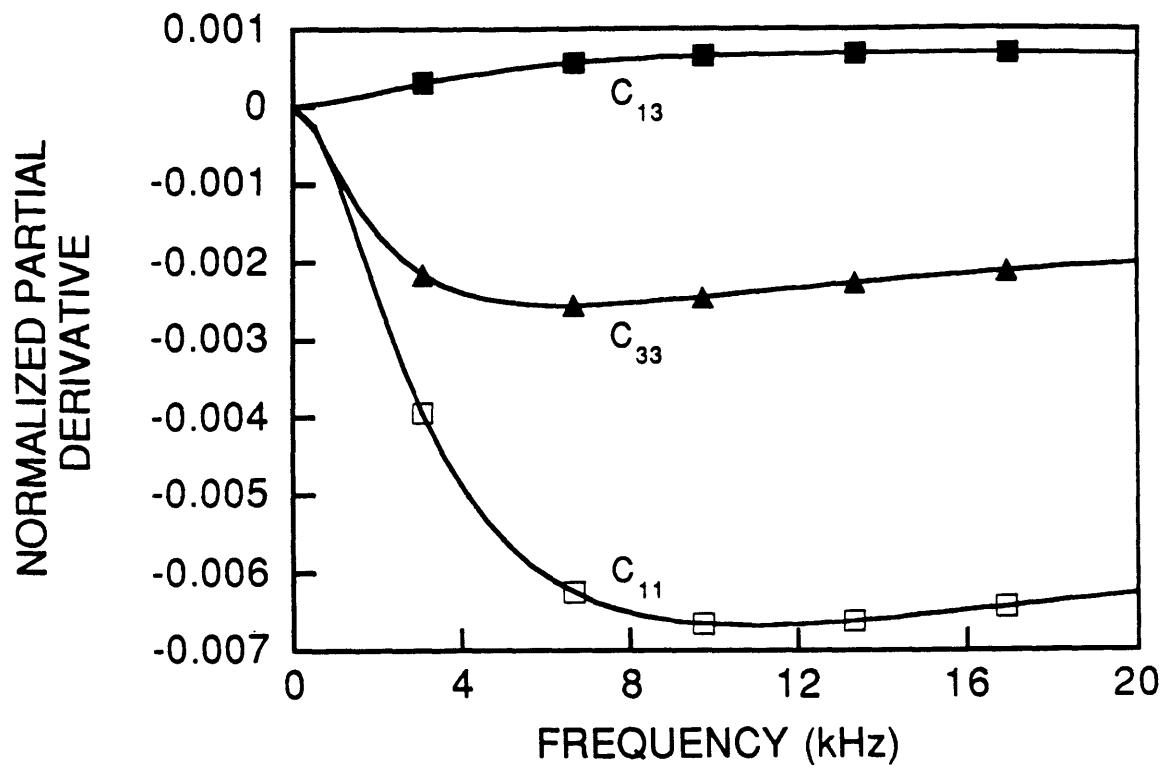


Figure 2-5: Normalized partial derivatives for the tube wave in the transversely isotropic model (Table 2.3).

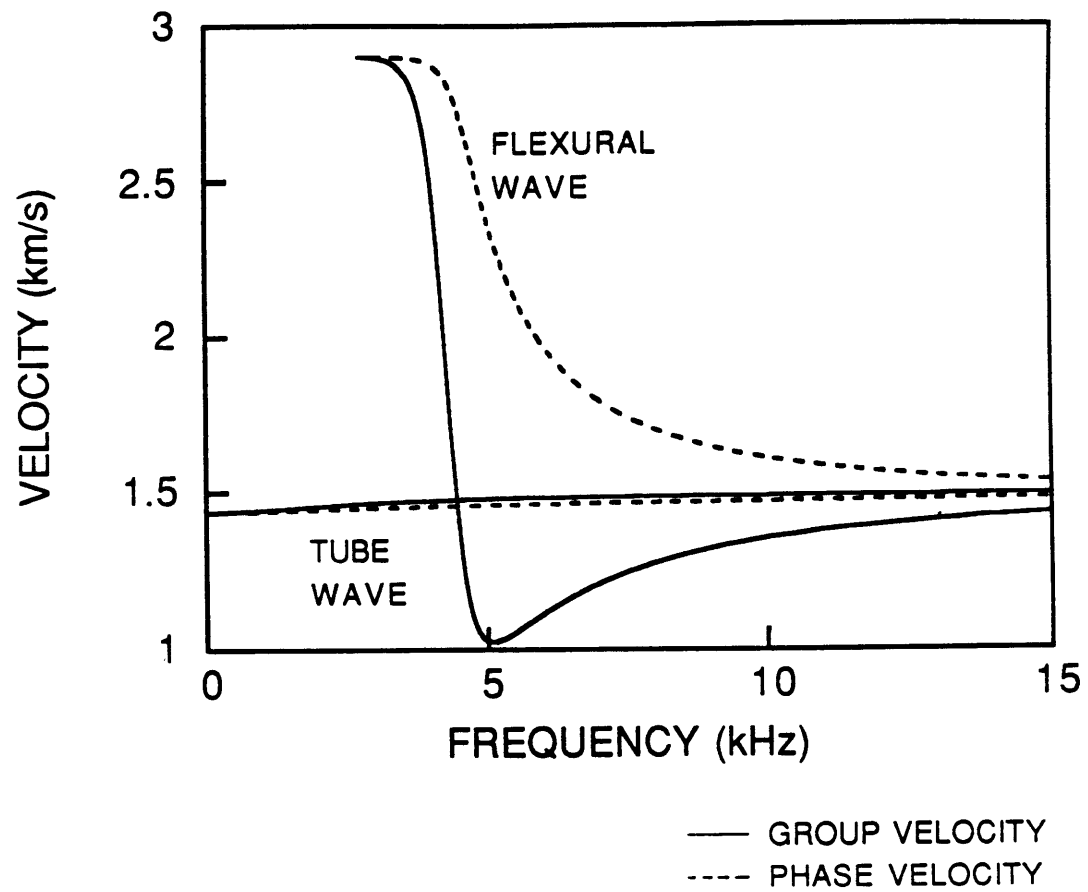


Figure 2-6: Phase and group velocities for tube and flexural waves in the transversely isotropic model (Table 2.3).

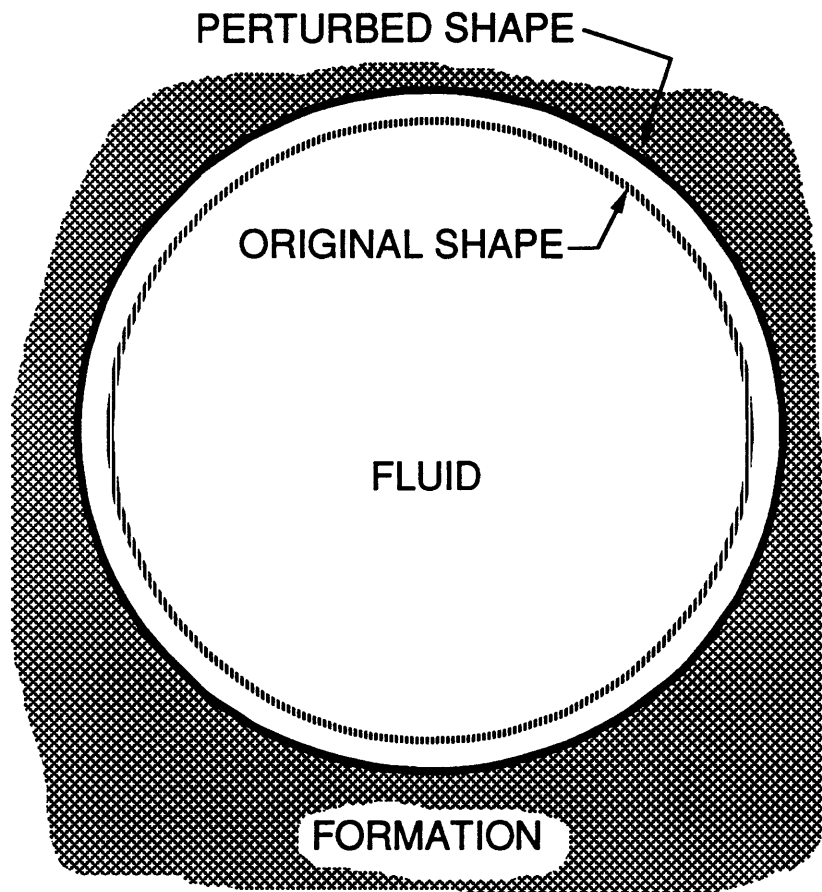


Figure 2-7: Cross sections of the original and perturbed cylindrical boreholes which are used to test the perturbation method. The properties of the isotropic model are listed in Table 2.8, and the velocity changes are in Figure 2-8

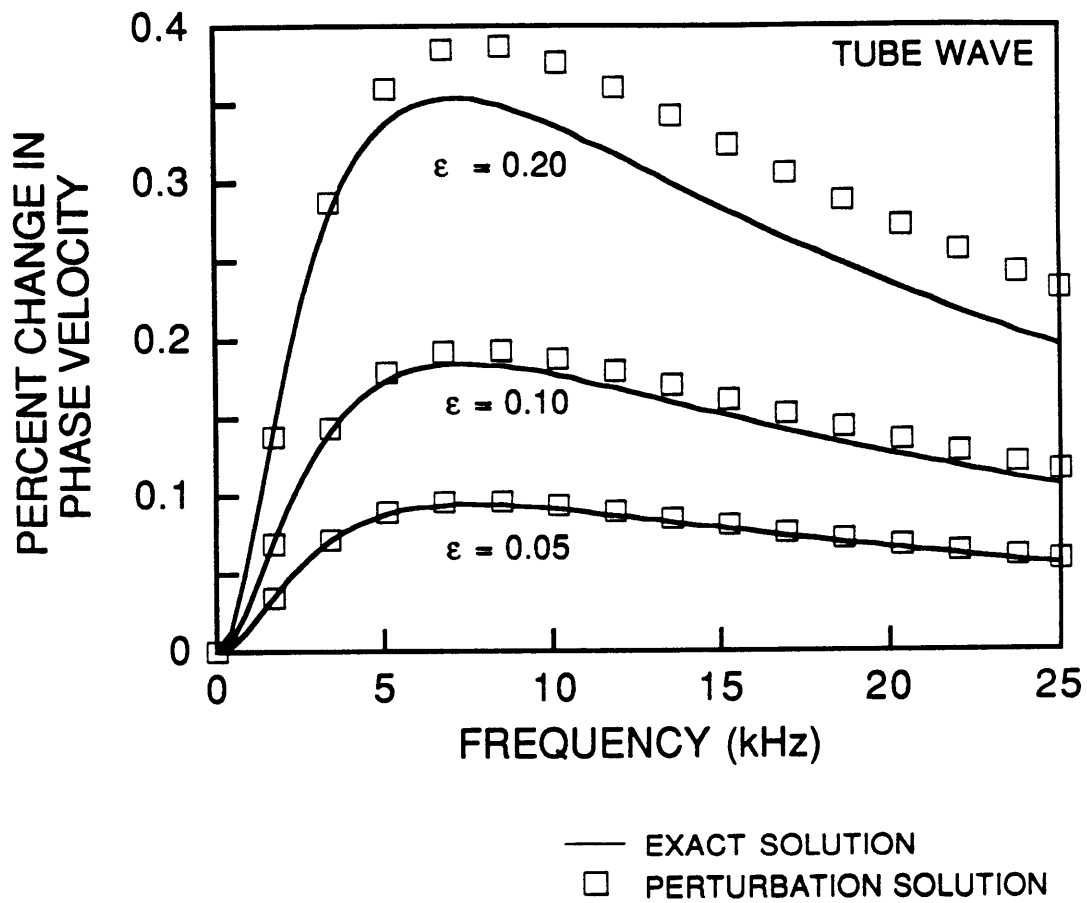


Figure 2-8: Accuracy of the velocity changes due to a change in borehole shape (Figure 2-7).

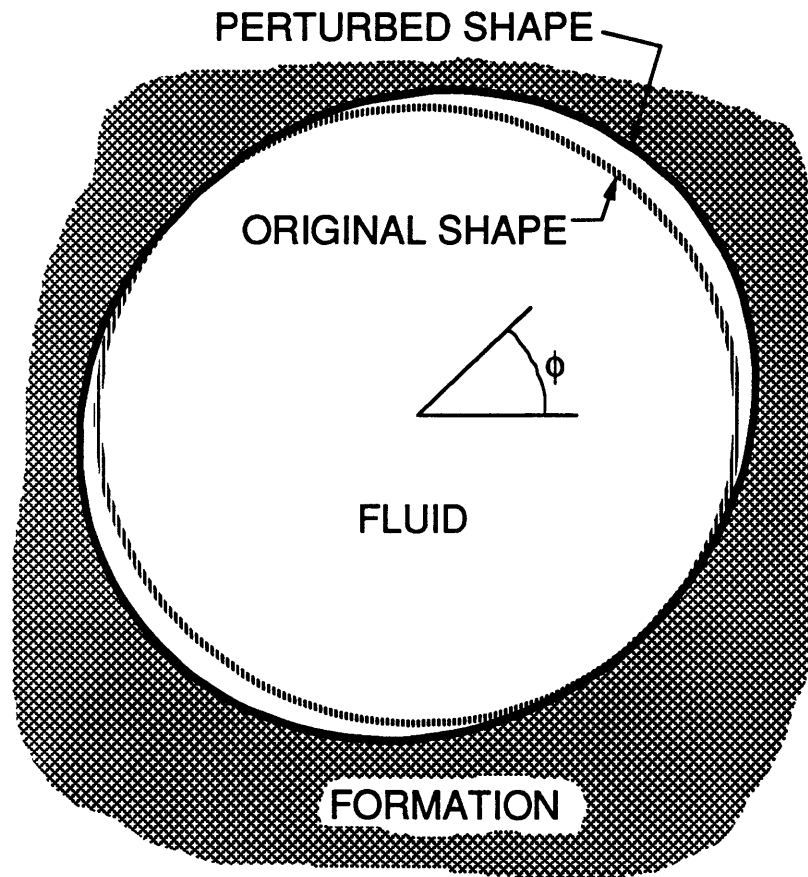


Figure 2-9: Cross sections of the cylindrical and elliptical boreholes. The properties of the model are listed in Table 2.8, and the velocity changes are presented in Figure 2-10.

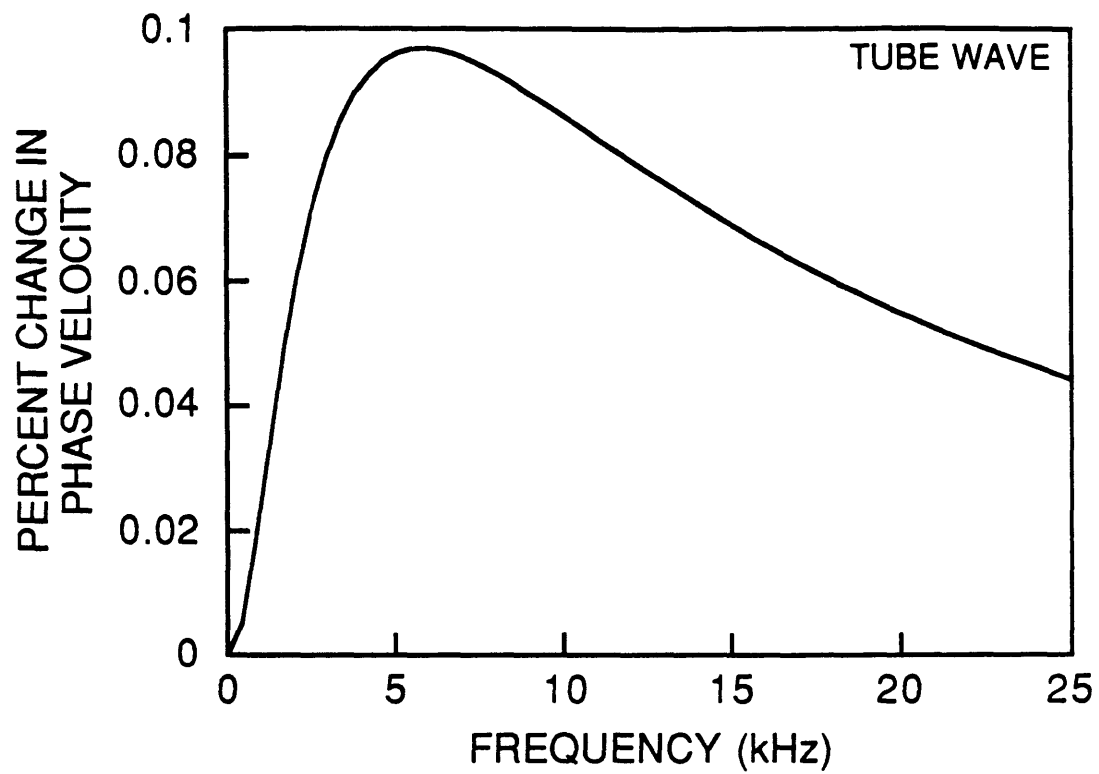


Figure 2-10: Change in the phase velocity of the tube wave due to an elliptical borehole wall (Figure 2-9).

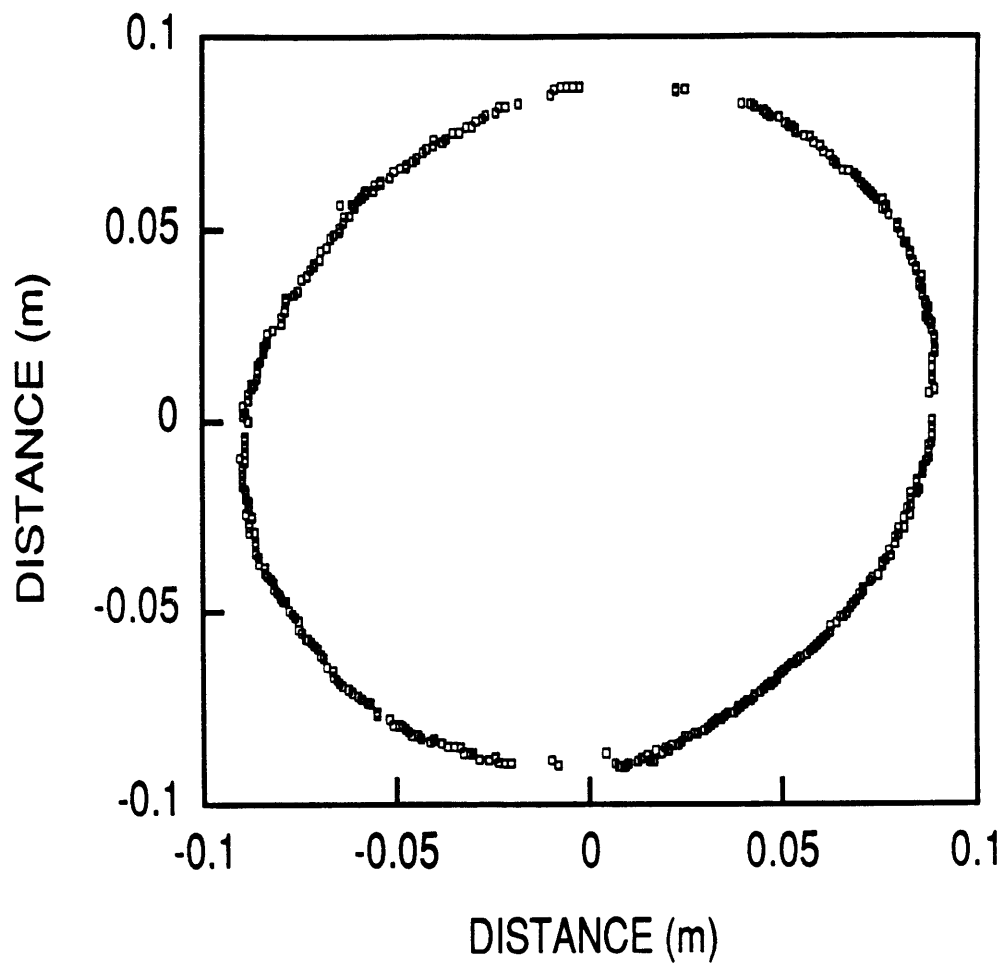


Figure 2-11: An elliptical borehole whose shape was determined with a borehole televiewer.

Chapter 3

Effects of Anisotropy upon the Normal Modes

3.1 Introduction

Because many geophysicists believe that the crust of the Earth is slightly anisotropic, several research groups have studied how it affects the waves generated during acoustic logging. Tongtaow (1980), White and Tongtaow (1981), Tongtaow (1982), Chan and Tsang (1983), and Schmitt (1989) focused on the special case of transversely isotropy with the symmetry axis aligned with the borehole. White and Tongtaow studied the waves generated by monopole and dipole sources and determined what affects the velocities and amplitudes of the refracted and guided waves. Chan and Tsang examined the amplitudes and velocities of the refracted waves in concentrically-layered, transversely isotropic formations. Schmitt studied the velocity dispersion curves, the attenuation curves, and the frequency-dependent sensitivities for the normal modes when the formation is transversely isotropic and permeable. Recently, some researchers have focused on transverse isotropy when the symmetry axis is perpendicular to the borehole. Leveille and Seriff (1989) determined the particle motion of the tube wave at the zero frequency limit, and they studied the horizontal dis-

placement on the inner wall of a finite length, cylindrical shell which has been excited by a horizontal point force. Nicoletis et al. (1990) determined the phase velocity and particle displacements of a tube wave at the zero frequency limit.

No complete investigation has been performed for wave propagation in a borehole when the formation is transversely isotropic and the symmetry axis is not aligned with the borehole or when the formation has more general anisotropy. Consequently this chapter is devoted to solving the wave equation and to studying the behavior of the normal modes for these complicated cases. The solution is derived in the frequency-wavenumber domain and is based upon a variational method which uses a combination of analytical expressions and finite elements. Although investigators in other disciplines have used a similar approach to solve the wave equation in anisotropic media (Nelson et al., 1971; Nelson, 1973; Huang and Dong, 1984; and Kausel, 1984), the solution for this problem is significantly more complicated for two reasons: (1) the wave equation must be solved for a cylindrical geometry when the anisotropy of the formation is defined in the Cartesian coordinate system, and (2) a fluid is present. With this solution, phase velocities, group velocities, and displacements are analyzed to determine how the anisotropy affects the normal modes.

Although only one problem is studied in this chapter, the variational method developed here can be readily adapted to study many problems. The mesh can be altered to model a borehole with a highly irregular cross section which might be caused, for example, by a breakout (see e.g., Zoback et al., 1985). Additional fluid and solid layers can be added to model a cased borehole, a borehole with a tool in the center, and even a borehole with a tool which is not in the center. Wave propagation in an infinite rod which is heterogeneous and anisotropic and which has an irregular cross section (a topic which is important to the engineering community (Redwood, 1960; Miklowitz, 1978; Thurston, 1978)) can be studied easily. Because these problems can be solved with minor modifications of the method developed here, this chapter should be interesting to a wide audience.

3.2 Method

This section is devoted to developing a solution to the wave equation for the situation which exists during acoustic logging. First a mathematical model of the borehole environment is developed; then a variational equation which describes wave propagation in the borehole is formulated; and finally the variational equation is solved with the finite element method. Since many variables are needed in this section, they are listed in Tables 3.1 and 3.2 for easy reference. All tensors are expressed with abbreviated subscript notation.

3.2.1 Formulation

The model for the borehole environment consists of a perfectly elastic fluid in a cylindrical borehole through a perfectly elastic, homogeneous solid (Figure 3-1). The fluid and solid extend to infinity along the axis of the borehole, and the solid extends to infinity away from the borehole. The z axis of the coordinate system is in the center of the borehole, and the borehole radius is R .

The usual approach to solving related problems in wave propagation involves developing the solution to the wave equation in each layer and then matching the continuity conditions at the interfaces between the layers (see e.g., Kennett, 1983, Chapter 2). Using this approach for the borehole model would require solving the wave equation in cylindrical coordinates for the solid whose anisotropy is defined in Cartesian coordinates (e.g., transverse isotropy with any orientation of the symmetry axis or orthorhombic anisotropy). Using the separation of variables technique (Appendix D), the propagation in the z direction may be described by $\exp(ik_z z)$ where k_z is the wavenumber in the z direction. However, the anisotropy prevents the solution from being separable in r and θ . To overcome this problem of inseparability, a variational method can be used.

The variational method is based upon Hamilton's Principle. This principle is

formulated with the Lagrangian energy which is defined as the kinetic energy of a system minus the potential energy of a system. In wave propagation problems, these energy terms are usually formulated with displacements (see e.g., Lysmer, 1970; Lysmer and Drake, 1972; Kausel and Roësset, 1981); however, when a fluid is present, the finite element solution to the variational equation works better when the energy terms for the fluid are formulated with a velocity potential, ϕ :

$$\nabla\phi = -\dot{\mathbf{u}} \quad (3.1)$$

where $\dot{\mathbf{u}}$ is the particle velocity (Everstine, 1981; Olsen and Bathe, 1985a). For this reason, the variational equation will be developed with three parts: one that pertains only to the fluid and is formulated with the velocity potential, another that pertains only to the solid and is formulated with displacements, and a third that involves the boundary conditions at the fluid-solid interface. (The reason that this third term is included in the variational equation will be presented later.)

For the fluid, the kinetic energy density is $\rho_1 \dot{\mathbf{u}}^T \dot{\mathbf{u}}/2$ where ρ_1 is the fluid density. Using equation 3.1, the kinetic energy is

$$\int_{V_1} dV \frac{1}{2} \rho_1 (\nabla\phi)^T \nabla\phi \quad (3.2)$$

where V_1 is the fluid volume. The potential energy density of the fluid is $\lambda_1 \Theta^2/2$ where λ_1 is the incompressibility and Θ is the dilatation (Bullen, 1963, p. 26). To express this energy density in terms of ϕ , several algebraic substitutions must be made. The dilatation is defined as

$$\Theta = \nabla \cdot \mathbf{u} \quad (3.3)$$

(Bullen, 1963, p. 17) and using equation 3.1 its temporal derivative is

$$\dot{\Theta} = -\nabla^2 \phi \quad (3.4)$$

Using the wave equation for the fluid,

$$\nabla^2 \phi = \frac{\rho_1}{\lambda_1} \ddot{\phi} \quad (3.5)$$

where λ_1/ρ_1 is the square of the velocity (Lamb, 1879, section 287), the dilatation is expressed in terms of the potential:

$$\Theta = -\frac{\rho_1}{\lambda_1}\dot{\phi} \quad . \quad (3.6)$$

Therefore, the potential energy of the fluid is

$$\int_{V_1} dV \frac{1}{2} \frac{\rho_1^2}{\lambda_1} \dot{\phi}^2 \quad . \quad (3.7)$$

For the solid, the kinetic energy is derived by integrating the kinetic energy density over the volume of the solid:

$$\int_{V_2} dV \frac{1}{2} \rho_2 \dot{\mathbf{u}}^T \dot{\mathbf{u}} \quad (3.8)$$

where ρ_2 is the density of the solid and V_2 is the volume. The potential energy is derived similarly:

$$\int_{V_2} dV \frac{1}{2} \mathbf{E}^T \mathbf{C} \mathbf{E} \quad (3.9)$$

where \mathbf{E} is the strain and \mathbf{C} is the stiffness matrix.

Two boundary conditions exist at the fluid-solid interface. First, the normal components of displacement in the fluid equal the normal components of displacement in the solid:

$$\mathbf{n} \cdot \mathbf{u}^{\text{fluid}} = \mathbf{n} \cdot \mathbf{u}^{\text{solid}} \quad (3.10)$$

where \mathbf{n} is the normal to the interface. Second, the traction that the fluid exerts on the solid is the negative of the traction that the solid exerts on the fluid:

$$\mathbf{T}^{\text{fluid}} = -\mathbf{T}^{\text{solid}} \quad , \quad (3.11)$$

and the tractions are normal to the interface:

$$\mathbf{T}^{\text{solid}} = \mathbf{n} \left[\mathbf{T}^{\text{solid}} \cdot \mathbf{n} \right] \quad (3.12)$$

$$\mathbf{T}^{\text{fluid}} = (-\mathbf{n}) \left[\mathbf{T}^{\text{fluid}} \cdot (-\mathbf{n}) \right] \quad . \quad (3.13)$$

Expressions for the work done at the fluid-solid interface are used to include these boundary conditions in the variational equation. The work done on the fluid by the solid is

$$\int_{\Sigma}^{\text{fluid}} dS \mathbf{T}^{\text{solid}} \cdot \mathbf{u}^{\text{fluid}} \quad (3.14)$$

where Σ is the surface. The integrand must be manipulated to include the boundary conditions and also must be expressed in terms of the velocity potential in the fluid and the displacements in the solid because these quantities will be perturbed to develop the variational equation. Substitute equation 3.12 and then equation 3.10 into the integrand:

$$\int_{\Sigma}^{\text{fluid}} dS \left[\mathbf{T}^{\text{solid}} \cdot \mathbf{n} \right] \mathbf{n} \cdot \mathbf{u}^{\text{solid}} \quad (3.15)$$

The normal component of traction can be expressed in terms of pressure using equation 3.11:

$$\begin{aligned} \mathbf{T}^{\text{solid}} \cdot \mathbf{n} &= -\mathbf{T}^{\text{fluid}} \cdot \mathbf{n} \\ &= -p \end{aligned} \quad (3.16)$$

The pressures is defined as

$$p = -\lambda_1 \Theta \quad (3.17)$$

(Bullen, 1963, p. 23) and can be expressed in terms of the potential using using equation 3.6:

$$p = \rho_1 \dot{\phi} \quad (3.18)$$

Combining equations 3.15, 3.16 and 3.18, the work done on the fluid at the interface is

$$- \int_{\Sigma}^{\text{fluid}} dS \rho_1 \dot{\phi} \mathbf{n} \cdot \mathbf{u}^{\text{solid}} \quad (3.19)$$

The derivation for the work done on the solid is very similar, and result is

$$\int_{\Sigma}^{\text{solid}} dS \rho_1 \dot{\phi} \mathbf{n} \cdot \mathbf{u}^{\text{solid}} \quad (3.20)$$

The Lagrangian energy for the entire model is formed from the energy terms for the fluid, solid, and fluid-solid interface:

$$\begin{aligned}
L = & \int_{V_1} dV \frac{1}{2} \rho_1 (\nabla \phi)^T \nabla \phi - \int_{V_1} dV \frac{1}{2} \frac{\rho_1^2}{\lambda_1} \dot{\phi}^2 + \\
& \int_{V_2} dV \frac{1}{2} \rho_2 \dot{\mathbf{u}}^T \dot{\mathbf{u}} - \int_{V_2} dV \frac{1}{2} \mathbf{E}^T \mathbf{C} \mathbf{E} - \\
& \int_{\Sigma}^{\text{fluid}} dS \rho_1 \dot{\phi} \mathbf{n} \cdot \mathbf{u}^{\text{solid}} + \int_{\Sigma}^{\text{solid}} dS \rho_1 \dot{\phi} \mathbf{n} \cdot \mathbf{u}^{\text{solid}} .
\end{aligned} \tag{3.21}$$

Notice that the net energy at the interface is zero. Hamilton's Principle states that the time integral of the Lagrangian energy is stationary for perturbations in the configuration of the system which satisfy the boundary conditions and which are specified at the initial and final times:

$$0 = \delta \int_{t_1}^{t_2} dt L \tag{3.22}$$

(see e.g., Lanczos, 1970, p. 111-114; Goldstein, 1980, p. 35-37). The initial and final times, t_1 and t_2 , are arbitrary. To find the variational equation which describes wave propagation, substitute equation 3.21 into equation 3.22:

$$\begin{aligned}
0 = & \int_{t_1}^{t_2} dt \left(\int_{V_1} dV \rho_1 (\nabla \delta \phi)^T \nabla \phi - \int_{V_1} dV \frac{\rho_1^2}{\lambda_1} \delta \dot{\phi} \dot{\phi} \right) + \\
& \int_{t_1}^{t_2} dt \left(\int_{V_2} dV \rho_2 \delta \dot{\mathbf{u}}^T \dot{\mathbf{u}} - \int_{V_2} dV \delta \mathbf{E}^T \mathbf{C} \mathbf{E} \right) + \\
& \int_{t_1}^{t_2} dt \left(- \int_{\Sigma}^{\text{fluid}} dS \rho_1 \delta \dot{\phi} \mathbf{n} \cdot \mathbf{u}^{\text{solid}} - \int_{\Sigma}^{\text{fluid}} dS \rho_1 \dot{\phi} \mathbf{n} \cdot \delta \mathbf{u}^{\text{solid}} \right) + \\
& \int_{t_1}^{t_2} dt \left(\int_{\Sigma}^{\text{solid}} dS \rho_1 \delta \dot{\phi} \mathbf{n} \cdot \mathbf{u}^{\text{solid}} + \int_{\Sigma}^{\text{solid}} dS \rho_1 \dot{\phi} \mathbf{n} \cdot \delta \mathbf{u}^{\text{solid}} \right) .
\end{aligned} \tag{3.23}$$

Note that $\delta \mathbf{E}$ refers to perturbations in displacement.

The second and third surface integrals are not needed in the finite element solution and will be shown to cancel. In the frequency domain, the sum of these two integrals is

$$i\omega \int_{\Sigma} dS \rho_1 \tilde{\phi} \mathbf{n} \cdot \delta \tilde{\mathbf{u}}^{\text{solid}} - i\omega \int_{\Sigma} dS \rho_1 \delta \tilde{\phi} \mathbf{n} \cdot \tilde{\mathbf{u}}^{\text{solid}} \tag{3.24}$$

where the labels “fluid” and “solid” have been dropped. The displacement at the interface is expressed in terms of the potential using equations 3.1 and 3.10:

$$\begin{aligned} \mathbf{n} \cdot \tilde{\mathbf{u}}^{\text{solid}} &= \mathbf{n} \cdot \tilde{\mathbf{u}}^{\text{fluid}} \\ &= \frac{1}{i\omega} \frac{\partial \tilde{\phi}}{\partial n} \end{aligned} \quad (3.25)$$

where $\partial/\partial n$ is the gradient in the normal direction. Substituting this expression into the sum of the integrals gives

$$\rho_1 \int_{\Sigma} dS \left(\tilde{\phi} \frac{\partial \delta \tilde{\phi}}{\partial n} - \delta \tilde{\phi} \frac{\partial \tilde{\phi}}{\partial n} \right) . \quad (3.26)$$

Greens second identity (Carrier and Pearson, 1976, p. 140) shows that this surface integral is

$$\begin{aligned} &\rho_1 \int_{V_1} dV \left(\tilde{\phi} \nabla^2 \delta \tilde{\phi} - \delta \tilde{\phi} \nabla^2 \tilde{\phi} \right) - \rho_1 \int_{\Sigma^1} dS \left(\tilde{\phi} \frac{\partial \delta \tilde{\phi}}{\partial n} - \delta \tilde{\phi} \frac{\partial \tilde{\phi}}{\partial n} \right) \\ &- \rho_1 \int_{\Sigma^2} dS \left(\tilde{\phi} \frac{\partial \delta \tilde{\phi}}{\partial n} - \delta \tilde{\phi} \frac{\partial \tilde{\phi}}{\partial n} \right) \end{aligned} \quad (3.27)$$

where Σ^1 and Σ^2 are the surfaces at $z = \infty$ and $z = -\infty$, respectively. (The volume, V_1 , has the shape of a right circular cylinder. The surface, Σ , is on the side of the cylinder, and the surfaces, Σ^1 and Σ^2 , are on the ends.) The surface integrals over Σ^1 and Σ^2 cancel by making the length of the cylinder an integral number of wavelengths. Using the wave equation (3.5) the volume integral is

$$\rho_1 \int_{V_1} dV \left(-\frac{\omega^2 \rho_1}{\lambda_1} \right) (\tilde{\phi} \delta \tilde{\phi} - \delta \tilde{\phi} \tilde{\phi}) \quad (3.28)$$

which equals zero. Therefore, the sum of the second and third surface integrals in equation 3.23 equals zero, and an analogous argument can be used to show that the sum of the first and fourth integrals also equals zero. Because both pairs of integrals contain the same information about the boundary conditions, only one pair is need. For reason, the first pair (i.e., the second and third surface integrals) are deleted from equation 3.23, but the second pair are retained.

The temporal derivatives of the perturbed quantities in the equation 3.23 are integrated by parts:

$$\begin{aligned}
0 = & \int_{t_1}^{t_2} dt \left(\int_{V_1} dV \rho_1 (\nabla \delta \phi)^T \nabla \phi + \int_{V_1} dV \frac{\rho_1^2}{\lambda_1} \delta \phi \ddot{\phi} \right) - \int_{V_1} dV \frac{\rho_1^2}{\lambda_1} \phi \delta \phi \Big|_{t_1}^{t_2} + \quad (3.29) \\
& \int_{t_1}^{t_2} dt \left(- \int_{V_2} dV \rho_2 \delta \mathbf{u}^T \ddot{\mathbf{u}} - \int_{V_2} dV \delta \mathbf{E}^T \mathbf{C} \mathbf{E} \right) + \int_{V_2} dV \rho_2 \delta \dot{\mathbf{u}}^T \delta \mathbf{u} \Big|_{t_1}^{t_2} + \\
& \int_{t_1}^{t_2} dt \left(\int_{\Sigma}^{\text{fluid}} dS \rho_1 \delta \phi \mathbf{n} \cdot \dot{\mathbf{u}}^{\text{solid}} + \int_{\Sigma}^{\text{solid}} dS \rho_1 \dot{\phi} \mathbf{n} \cdot \delta \mathbf{u}^{\text{solid}} \right) - \\
& \int_{\Sigma}^{\text{fluid}} dS \rho_1 \delta \phi \mathbf{n} \cdot \mathbf{u}^{\text{solid}} \Big|_{t_1}^{t_2} .
\end{aligned}$$

By convention, the perturbations in the configuration of the system (i.e., the potentials and the displacements) at t_1 and t_2 are zero: $\delta \phi(t_1) = \delta \phi(t_2) = 0$ and $\delta \mathbf{u}(t_1) = \delta \mathbf{u}(t_2) = 0$. With these simplifications, the final equation, which is called the variational equation, is

$$\begin{aligned}
0 = & \int_{t_1}^{t_2} dt \left(\int_{V_1} dV \rho_1 (\nabla \delta \phi)^T \nabla \phi + \int_{V_1} dV \frac{\rho_1^2}{\lambda_1} \delta \phi \ddot{\phi} - \right. \quad (3.30) \\
& \int_{V_2} dV \rho_2 \delta \mathbf{u}^T \ddot{\mathbf{u}} - \int_{V_2} dV \delta \mathbf{E}^T \mathbf{C} \mathbf{E} + \\
& \left. \int_{\Sigma}^{\text{fluid}} dS \rho_1 \delta \phi \mathbf{n} \cdot \dot{\mathbf{u}}^{\text{solid}} + \int_{\Sigma}^{\text{solid}} dS \rho_1 \dot{\phi} \mathbf{n} \cdot \delta \mathbf{u}^{\text{solid}} \right) .
\end{aligned}$$

3.2.2 Solution

Discretization with Finite Elements

To solve the variational equation, expressions for the velocity potential, displacement, and strain must be developed. Because the wave equation is separable in z , propagation in this direction is described with $\exp(\imath k_z z)$ (see Appendix D). The wave equation is not separable in r and θ , and the finite element method is used to describe the velocity potentials and displacements in this plane. The horizontal plane is divided into small regions called elements, and the elements collectively form what is called the mesh (Figure 3-2). As a result of this discretization, the variational

equation includes sums over the volumes of all elements and the surfaces between the elements at the fluid-solid interface:

$$\begin{aligned}
0 = \int_{t_1}^{t_2} dt & \left[\sum_{m=1}^M \left(\int_{V_1^{(m)}} dV^{(m)} \rho_1^{(m)} (\nabla \delta \phi^{(m)})^T \nabla \phi^{(m)} + \right. \\
& \left. \int_{V_1^{(m)}} dV^{(m)} \frac{\rho_1^{(m)2}}{\lambda_1^{(m)}} \delta \phi^{(m)} \ddot{\phi}^{(m)} \right) - \\
& \sum_{n=1}^N \left(\int_{V_2^{(n)}} dV^{(n)} \rho_2^{(n)} \delta \mathbf{u}^{(n)T} \ddot{\mathbf{u}}^{(n)} + \int_{V_2^{(n)}} dV^{(n)} \delta \mathbf{E}^{(n)T} \mathbf{C}^{(n)} \mathbf{E}^{(n)} \right) + \\
& \sum_{q=1}^Q \left(\int_{\Sigma^{(q)}}^{\text{fluid}} dS^{(q)} \rho_1^{(q)} \delta \phi^{(q)} \mathbf{n}^{(q)} \cdot \dot{\mathbf{u}}^{(q)\text{solid}} + \right. \\
& \left. \int_{\Sigma^{(q)}}^{\text{solid}} dS^{(q)} \rho_1^{(q)} \dot{\phi}^{(q)} \mathbf{n}^{(q)} \cdot \delta \mathbf{u}^{(q)\text{solid}} \right) \Bigg] .
\end{aligned} \tag{3.31}$$

where M , N , and Q are the numbers of fluid, solid, and interface elements, respectively, and m , n , and q are the associated indices. To solve this equation, expressions for the velocity potential, displacements, and strains must be developed for the finite elements.

Expressions for Velocity Potential, Displacement, and Strain

For a fluid element (Figure 3-3), the potentials are assigned at nine preselected points which are called nodes. (The potentials at these nodes are actually unknown at this stage and are calculated later.) The potential at a point within the element is calculated by interpolation. The interpolating functions for this wave propagation problem were chosen to be quadratic polynomials in x and y (Bathe, 1982, p. 200) because this order polynomial can approximate a reasonably complicated function without too much algebra. The potential at (x, y) within element m is a linear combination of the nine interpolating functions for the nine nodes:

$$\phi^{(m)}(x, y, z, t) = \frac{1}{2\pi} \int_{-\infty}^{\infty} dk_z \mathbf{h}^{(m)}(x, y) \mathbf{\Phi}^{(m)}(k_z, t) e^{ik_z z} \tag{3.32}$$

where $\mathbf{h}^{(m)}(x, y)$ is a row vector whose nine elements are the interpolation functions:

$$\mathbf{h}^{(m)}(x, y) = \left(h_1^{(m)}(x, y) \quad h_2^{(m)}(x, y) \quad \cdots \quad h_9^{(m)}(x, y) \right) ,$$

and $\Phi^{(m)}(k_z, t)$ is a column vector with the nodal potentials:

$$\Phi^{(m)}(k_z, t) = \begin{pmatrix} \Phi_1^{(m)}(k_z, t) \\ \Phi_2^{(m)}(k_z, t) \\ \vdots \\ \Phi_9^{(m)}(k_z, t) \end{pmatrix}.$$

Note that Cartesian coordinates are used because the finite element method is actually easier to implement with them than with circular cylindrical coordinates. The fluid elements in the center of the mesh have six nodes (Figure 3-4), and the interpolating functions are also quadratic (Bathe, 1982, p. 230). The potential within this type of element is expressed with an equation like equation 3.32 except that $\mathbf{h}^{(m)}(x, y)$ and $\Phi^{(m)}(k_z, t)$ only have six entries.

For a solid element, the three components of displacements are assigned at the nine nodes. The displacements at (x, y) within element n are

$$\mathbf{u}^{(n)}(x, y, z, t) = \frac{1}{2\pi} \int_{-\infty}^{\infty} dk_z \mathbf{H}^{(n)}(x, y) \mathbf{U}^{(n)}(k_z, t) e^{ik_z z} \quad (3.33)$$

where $\mathbf{H}^{(n)}(x, y)$ is 3×27 matrix:

$$\mathbf{H}^{(n)}(x, y) = \begin{pmatrix} h_1^{(n)}(x, y) & 0 & 0 \\ \vdots & \vdots & \vdots \\ h_9^{(n)}(x, y) & 0 & 0 \\ 0 & h_1^{(n)}(x, y) & 0 \\ \vdots & \vdots & \vdots \\ 0 & h_9^{(n)}(x, y) & 0 \\ 0 & 0 & h_1^{(n)}(x, y) \\ \vdots & \vdots & \vdots \\ 0 & 0 & h_9^{(n)}(x, y) \end{pmatrix}^T$$

and $\mathbf{U}^{(n)}(k_z, t)$ is a column vector with 27 elements:

$$\mathbf{U}^{(n)}(k_z, t) = \begin{pmatrix} U_{1x}^{(n)}(k_z, t) \\ \vdots \\ U_{9x}^{(n)}(k_z, t) \\ U_{1y}^{(n)}(k_z, t) \\ \vdots \\ U_{9y}^{(n)}(k_z, t) \\ U_{1z}^{(n)}(k_z, t) \\ \vdots \\ U_{9z}^{(n)}(k_z, t) \end{pmatrix}.$$

The expression for the displacements in the outermost elements is slightly different. Because their outer edges are located at infinite radius where the displacements are zero, nodes 1, 2, and 5 are not needed. Consequently $\mathbf{U}(k_z, t)$ has 18 elements, and $\mathbf{H}(x, y)$ is now a 3×18 matrix.

The strain at (x, y) within a solid element with nine nodes is

$$\mathbf{E}^{(n)}(x, y, z, t) = \frac{1}{2\pi} \int_{-\infty}^{\infty} dk_z \left(\mathbf{B}_0^{(n)}(x, y) + \imath k_z \mathbf{B}_1^{(n)}(x, y) \right) \mathbf{U}^{(n)}(k_z, t) e^{\imath k_z z} \quad . \quad (3.34)$$

$\mathbf{B}_0^{(n)}(x, y)$ accounts for differentiation in the x and y directions, and its size is 6×27 :

$$\mathbf{B}_0^{(n)}(x, y) = \begin{pmatrix} h_{1,x}^{(n)}(x, y) & 0 & 0 & 0 & 0 & h_{1,y}^{(n)}(x, y) \\ \vdots & \vdots & \vdots & \vdots & \vdots & \vdots \\ h_{9,x}^{(n)}(x, y) & 0 & 0 & 0 & 0 & h_{9,y}^{(n)}(x, y) \\ 0 & h_{1,y}^{(n)}(x, y) & 0 & 0 & 0 & h_{1,x}^{(n)}(x, y) \\ \vdots & \vdots & \vdots & \vdots & \vdots & \vdots \\ 0 & h_{9,y}^{(n)}(x, y) & 0 & 0 & 0 & h_{9,x}^{(n)}(x, y) \\ 0 & 0 & 0 & h_{1,y}^{(n)}(x, y) & h_{1,x}^{(n)}(x, y) & 0 \\ \vdots & \vdots & \vdots & \vdots & \vdots & \vdots \\ 0 & 0 & 0 & h_{9,y}^{(n)}(x, y) & h_{9,x}^{(n)}(x, y) & 0 \end{pmatrix}^T.$$

$\mathbf{B}_1^{(n)}(x, y)$ accounts for differentiation in the z direction, and its size is also 6×27 :

$$\mathbf{B}_1^{(n)}(x, y) = \begin{pmatrix} 0 & 0 & 0 & 0 & h_1^{(n)}(x, y) & 0 \\ \vdots & \vdots & \vdots & \vdots & \vdots & \vdots \\ 0 & 0 & 0 & 0 & h_9^{(n)}(x, y) & 0 \\ 0 & 0 & 0 & h_1^{(n)}(x, y) & 0 & 0 \\ \vdots & \vdots & \vdots & \vdots & \vdots & \vdots \\ 0 & 0 & 0 & h_9^{(n)}(x, y) & 0 & 0 \\ 0 & 0 & h_1^{(n)}(x, y) & 0 & 0 & 0 \\ \vdots & \vdots & \vdots & \vdots & \vdots & \vdots \\ 0 & 0 & h_9^{(n)}(x, y) & 0 & 0 & 0 \end{pmatrix}^T .$$

For the outermost elements, $\mathbf{B}_0^{(n)}(x, y)$ and $\mathbf{B}_1^{(n)}(x, y)$ are both 6×18 because nodes 1, 2, and 5 are not included in the expression for the strain.

Along the fluid-solid interface, special elements are used (Figure 3-5). Locations within an element are specified by the distance along the interface, l . The potential at l in element q is

$$\phi^{(q)}(l, z, t) = \frac{1}{2\pi} \int_{-\infty}^{\infty} dk_z \mathbf{h}_I^{(q)}(l) \mathbf{\Phi}^{(q)}(k_z, t) e^{ik_z z} . \quad (3.35)$$

$\mathbf{h}_I^{(q)}(l)$ is a row vector,

$$\mathbf{h}_I^{(q)}(l) = \begin{pmatrix} h_{I1}^{(q)}(l) & h_{I2}^{(q)}(l) & h_{I3}^{(q)}(l) \end{pmatrix} ,$$

whose elements are interpolating functions developed from quadratic polynomials in l (Bathe, 1982, p. 199): $\mathbf{\Phi}^{(q)}(k_z, t)$ is a column vector whose elements are the potentials at the three nodes:

$$\mathbf{\Phi}^{(q)}(k_z, t) = \begin{pmatrix} \Phi_1^{(q)}(k_z, t) \\ \Phi_2^{(q)}(k_z, t) \\ \Phi_3^{(q)}(k_z, t) \end{pmatrix} .$$

The normal displacement at l in element q is

$$\mathbf{n} \cdot \mathbf{u}^{(q)\text{solid}}(l, z, t) = \frac{1}{2\pi} \int_{-\infty}^{\infty} dk_z \mathbf{H}_I^{(q)}(l) \mathbf{U}^{(q)}(k_z, t) e^{ik_z z} \quad (3.36)$$

where $\mathbf{U}^{(q)}(k_z, t)$ is a column vector whose elements are the components of the displacements at the three nodes:

$$\mathbf{U}^{(q)}(k_z, t) = \begin{pmatrix} U_{1x}^{(q)}(k_z, t) \\ U_{2x}^{(q)}(k_z, t) \\ U_{3x}^{(q)}(k_z, t) \\ U_{1y}^{(q)}(k_z, t) \\ U_{2y}^{(q)}(k_z, t) \\ U_{3y}^{(q)}(k_z, t) \end{pmatrix}.$$

The normal on the interface for node i is $(\cos \theta_i, \sin \theta_i)$ where θ_i is the angle that the normal makes with a line parallel to the x axis. $\mathbf{H}_I^{(q)}(l)$ is a row vector consisting of the interpolation functions and the appropriate components of the normal:

$$\mathbf{H}_I^{(q)}(l) = \begin{pmatrix} h_{I1}^{(q)}(l) \cos \theta_1 \\ h_{I2}^{(q)}(l) \cos \theta_2 \\ h_{I3}^{(q)}(l) \cos \theta_3 \\ h_{I1}^{(q)}(l) \sin \theta_1 \\ h_{I2}^{(q)}(l) \sin \theta_2 \\ h_{I3}^{(q)}(l) \sin \theta_3 \end{pmatrix}^T.$$

Note that $\mathbf{U}^{(q)}(k_z, t)$ does not contain any components of the displacements in the z direction because the normal to Σ is always perpendicular to the z direction.

Integrals in the Discretized Variational Equation

To show how the integrals in the discretized variational equation are derived, the integral associated with the potential energy of the fluid will be derived in detail. Because the derivations for the other integrals are nearly identical, only the final results are presented.

The derivation of the integral associated with the potential energy of the entire fluid begins by computing the related integral for a fluid element. Equation 3.32 is

substituted into this integral:

$$\begin{aligned} \int_{V_1^{(m)}} dV^{(m)} \frac{\rho_1^{(m)2}}{\lambda_1^{(m)}} \delta\phi^{(m)} \ddot{\phi}^{(m)} = \\ \int dx \int dy \int_{-\infty}^{\infty} dz \frac{\rho_1^{(m)2}}{\lambda_1^{(m)}} \frac{1}{2\pi} \int_{-\infty}^{\infty} dk'_z \left[\mathbf{h}^{(m)}(x, y) \delta\mathbf{\Phi}^{(m)}(k'_z, t) \right]^T e^{ik'_z z} \\ \times \frac{1}{2\pi} \int_{-\infty}^{\infty} dk_z \mathbf{h}^{(m)}(x, y) \ddot{\mathbf{\Phi}}^{(m)}(k_z, t) e^{ik_z z} \end{aligned} \quad (3.37)$$

where the integrals over x and y only pertain to the domain of the element. The order in which the integrations are performed is changed:

$$\begin{aligned} \int_{V_1^{(m)}} dV^{(m)} \frac{\rho_1^{(m)2}}{\lambda_1^{(m)}} \delta\phi^{(m)} \ddot{\phi}^{(m)} = \frac{1}{(2\pi)^2} \int_{-\infty}^{\infty} dk_z \int_{-\infty}^{\infty} dk'_z \\ \times \delta\mathbf{\Phi}^{(m)T}(k'_z, t) \int dx \int dy \frac{\rho_1^{(m)2}}{\lambda_1^{(m)}} \mathbf{h}^{(m)T}(x, y) \mathbf{h}^{(m)}(x, y) \ddot{\mathbf{\Phi}}^{(m)}(k_z, t) \int_{-\infty}^{\infty} dz e^{i(k_z + k'_z)z} . \end{aligned} \quad (3.38)$$

To perform the integration over x and y , coordinates within the elements are calculated using the same interpolations functions which are used to calculate the potential. The result which is obtained with Gauss-Legendre quadrature (Bathe, 1982, p. 277-278) is a real, symmetric matrix:

$$\mathbf{M}_F^{(m)} = \int dx \int dy \frac{\rho_1^{(m)2}}{\lambda_1^{(m)}} \mathbf{h}^{(m)T}(x, y) \mathbf{h}^{(m)}(x, y) . \quad (3.39)$$

The integral over z yields the Dirac delta function: $2\pi\delta(k_z + k'_z)$ (Mathews and Walker, 1970, p. 102). The integral over k'_z is performed, and using the property that $\mathbf{\Phi}^{(m)}(-k_z, t) = \mathbf{\Phi}^{(m)*}(k_z, t)$ (Lathi, 1965, p. 111) the result is

$$\int_{V_1^{(m)}} dV^{(m)} \frac{\rho_1^{(m)2}}{\lambda_1^{(m)}} \delta\phi^{(m)} \ddot{\phi}^{(m)} = \frac{1}{2\pi} \int_{-\infty}^{\infty} dk_z \delta\mathbf{\Phi}^{(m)H}(k_z, t) \mathbf{M}_F^{(m)} \ddot{\mathbf{\Phi}}^{(m)}(k_z, t) . \quad (3.40)$$

The vectors, $\mathbf{\Phi}^{(m)}(k_z, t)$, and matrices, $\mathbf{M}_F^{(m)}$, for all elements are combined to form one vector, $\mathbf{\Phi}(k_z, t)$ and one matrix, \mathbf{M}_F , for the entire model (Bathe, 1982, p. 124-125, 702-706). The final expression for the integral associated with the potential energy is

$$\sum_{m=1}^M \int_{V_1^{(m)}} dV^{(m)} \frac{\rho_1^{(m)2}}{\lambda_1^{(m)}} \delta\phi^{(m)} \ddot{\phi}^{(m)} = \frac{1}{2\pi} \int_{-\infty}^{\infty} dk_z \delta\mathbf{\Phi}^H(k_z, t) \mathbf{M}_F \ddot{\mathbf{\Phi}}(k_z, t) . \quad (3.41)$$

The integral associated with the kinetic energy of the fluid is calculated in a similar manner using equation 3.32:

$$\begin{aligned} \sum_{m=1}^M \int_{V_1^{(m)}} dV^{(m)} \rho_1^{(m)} (\nabla \delta \phi^{(m)})^T \nabla \phi^{(m)} = \\ \frac{1}{2\pi} \int_{-\infty}^{\infty} dk_z \delta \Phi^H(k_z, t) \left(\mathbf{K}_{0F} + k_z^2 \mathbf{K}_{2F} \right) \Phi(k_z, t) \end{aligned} \quad (3.42)$$

where

$$\begin{aligned} \mathbf{K}_{0F}^{(m)} &= \int dx \int dy \rho_1 \left[\mathbf{h}_{,x}^{(m)T}(x, y) \mathbf{h}_{,x}^{(m)}(x, y) + \mathbf{h}_{,y}^{(m)T}(x, y) \mathbf{h}_{,y}^{(m)}(x, y) \right] \\ \mathbf{K}_{2F}^{(m)} &= \int dx \int dy \rho_1 \mathbf{h}^{(m)T}(x, y) \mathbf{h}^{(m)}(x, y) \end{aligned} \quad (3.43)$$

Matrices \mathbf{K}_{0F} and \mathbf{K}_{2F} are real and symmetric.

The integral associated with the potential energy of the solid is calculated with equation 3.34:

$$\begin{aligned} \sum_{n=1}^N \int_{V_2^{(n)}} dV^{(n)} \delta \mathbf{E}^{(n)T} \mathbf{C}^{(n)} \mathbf{E}^{(n)} = \\ \frac{1}{2\pi} \int_{-\infty}^{\infty} dk_z \delta \mathbf{U}^H(k_z, t) \left(\mathbf{K}_{0S} + i k_z \mathbf{K}_{1S} + k_z^2 \mathbf{K}_{2S} \right) \mathbf{U}(k_z, t) \end{aligned} \quad (3.44)$$

where

$$\begin{aligned} \mathbf{K}_{0S}^{(n)} &= \int dx \int dy \mathbf{B}_0^{(n)T}(x, y) \mathbf{C}^{(n)} \mathbf{B}_0^{(n)}(x, y) \\ \mathbf{K}_{1S}^{(n)} &= \int dx \int dy \left[\mathbf{B}_0^{(n)T}(x, y) \mathbf{C}^{(n)} \mathbf{B}_1^{(n)}(x, y) - \right. \\ &\quad \left. \mathbf{B}_1^{(n)T}(x, y) \mathbf{C}^{(n)} \mathbf{B}_0^{(n)}(x, y) \right] \\ \mathbf{K}_{2S}^{(n)} &= \int dx \int dy \mathbf{B}_1^{(n)T}(x, y) \mathbf{C}^{(n)} \mathbf{B}_1^{(n)}(x, y) \end{aligned} \quad (3.45)$$

Matrices \mathbf{K}_{0S} and \mathbf{K}_{2S} are real and symmetric; Matrix \mathbf{K}_{1S} is real and antisymmetric. For the outermost elements which extend to infinity in the radial direction, the integration over x and y is performed using the coordinate interpolation scheme given by Olsen and Bathe (1985b).

The integral associated with the kinetic energy of a solid element is calculated with equation 3.33:

$$\sum_{n=1}^N \int_{V_2^{(n)}} dV^{(n)} \rho_2^{(n)} \delta \mathbf{u}^{(n)T} \ddot{\mathbf{u}}^{(n)} = \frac{1}{2\pi} \int_{-\infty}^{\infty} dk_z \delta \mathbf{U}^H(k_z, t) \mathbf{M}_S \ddot{\mathbf{U}}(k_z, t) \quad (3.46)$$

where

$$\mathbf{M}_S^{(n)} = \int dx \int dy \rho_2 \mathbf{H}^{(n)T}(x, y) \mathbf{H}^{(n)}(x, y) \quad . \quad (3.47)$$

Matrix \mathbf{M}_S is real and symmetric. Again, the coordinate interpolation scheme by Olsen and Bathe (Olsen, 1985b) is used for the integration over x and y for the outermost elements.

The integral associated with the work done on the fluid at the fluid-solid interface is computed with equations 3.35 and 3.36:

$$\sum_{q=1}^Q \int_{\Sigma^{(q)}}^{\text{fluid}} dS^{(q)} \rho_1^{(q)} \delta \phi^{(q)} \mathbf{n}^{(q)} \cdot \dot{\mathbf{u}}^{(q)\text{solid}} = \frac{1}{2\pi} \int_{-\infty}^{\infty} dk_z \delta \Phi^H(k_z, t) \mathbf{F} \dot{\mathbf{U}}(k_z, t) \quad (3.48)$$

where

$$\mathbf{F}^{(q)} = \int dl \rho_1 \mathbf{h}_I^{(q)T}(l) \mathbf{H}_I^{(q)}(l) \quad . \quad (3.49)$$

Matrix \mathbf{F} is real.

The integral associated with the work done on the solid at the fluid-solid interface is computed also with equations 3.35 and 3.36:

$$\sum_{q=1}^Q \int_{\Sigma^{(q)}}^{\text{solid}} dS^{(q)} \rho_1^{(q)} \dot{\phi}^{(q)} \mathbf{n}^{(q)} \cdot \delta \mathbf{u}^{(q)\text{solid}} = \frac{1}{2\pi} \int_{-\infty}^{\infty} dk_z \delta \mathbf{U}^H(k_z, t) \mathbf{F}^T \dot{\Phi}(k_z, t) \quad . \quad (3.50)$$

Wave Equation

The solution to the variational equation is obtained by substituting equations 3.41, 3.42, 3.44, 3.46, 3.48, and 3.50 into equation 3.31, and the resulting equation is

$$0 = \int_{t_1}^{t_2} \frac{1}{2\pi} \int_{-\infty}^{\infty} dk_z \delta \mathbf{Y}^H \left[\left(\mathbf{A}_0 + k_z \mathbf{A}_1 + k_z^2 \mathbf{A}_2 \right) \mathbf{V} + \mathbf{D}_1 \dot{\mathbf{V}} + \mathbf{D}_2 \ddot{\mathbf{V}} \right] \quad (3.51)$$

where

$$\mathbf{Y} = \begin{pmatrix} \Phi(k_z, t) \\ \mathbf{U}(k_z, t) \end{pmatrix}$$

$$\mathbf{V} = \begin{pmatrix} \Phi(k_z, t) \\ -\mathbf{U}(k_z, t) \end{pmatrix}$$

$$\begin{aligned}
\mathbf{A}_0 &= \begin{pmatrix} \mathbf{K}_{0F} & \mathbf{0} \\ \mathbf{0} & \mathbf{K}_{0S} \end{pmatrix} \\
\mathbf{A}_1 &= \begin{pmatrix} \mathbf{0} & \mathbf{0} \\ \mathbf{0} & \imath \mathbf{K}_{1S} \end{pmatrix} \\
\mathbf{A}_2 &= \begin{pmatrix} \mathbf{K}_{2F} & \mathbf{0} \\ \mathbf{0} & \mathbf{K}_{2S} \end{pmatrix} \\
\mathbf{D}_1 &= \begin{pmatrix} \mathbf{0} & -\mathbf{F} \\ \mathbf{F}^T & \mathbf{0} \end{pmatrix} \\
\mathbf{D}_2 &= \begin{pmatrix} \mathbf{M}_F & \mathbf{0} \\ \mathbf{0} & \mathbf{M}_S \end{pmatrix} .
\end{aligned} \tag{3.52}$$

For arbitrary perturbations, $\delta \mathbf{Y}$, the integral will be zero when

$$(\mathbf{A}_0 + k_z \mathbf{A}_1 + k_z^2 \mathbf{A}_2) \mathbf{V} + \mathbf{D}_1 \dot{\mathbf{V}} + \mathbf{D}_2 \ddot{\mathbf{V}} = \mathbf{0} , \tag{3.53}$$

and this equation is called the wave equation. In the frequency-wavenumber domain the wave equation is

$$(\mathbf{A}'_0 + k_z \mathbf{A}_1 + k_z^2 \mathbf{A}_2) \tilde{\mathbf{V}} = \mathbf{0} \tag{3.54}$$

where

$$\begin{aligned}
\tilde{\mathbf{V}} &= \begin{pmatrix} \Phi(k_z, \omega) \\ -\mathbf{U}(k_z, \omega) \end{pmatrix} \\
\mathbf{A}'_0 &= \begin{pmatrix} \mathbf{K}_{0F} - \omega^2 \mathbf{M}_F & \imath \omega \mathbf{F} \\ -\imath \omega \mathbf{F}^T & \mathbf{K}_{0S} - \omega^2 \mathbf{M}_S \end{pmatrix} .
\end{aligned} \tag{3.55}$$

Matrices \mathbf{A}'_0 and \mathbf{A}_1 are Hermitian, and \mathbf{A}_2 is real and symmetric.

Equation 3.54 is a quadratic eigenvalue problem — the eigenvalue is k_z , and the eigenvector is $\tilde{\mathbf{V}}$. The eigenvalues and eigenvectors are calculated using an algorithm developed by Chen and Taylor (1988), which has been modified for complex, Hermitian matrices. Each eigenvalue-eigenvector pair applies to one normal mode. The

phase velocity, v , of the mode is calculated with $v = \omega/k_z$. The pressures in the fluid elements are calculated with equations 3.18 and 3.32. The displacements in the solid elements are calculated with equation 3.33.

After the wave equation is solved, the group velocity can be readily calculated using only matrix multiplication. To derive the formula, equation 3.54 is differentiated with respect to k_z and multiplied on the left by $\tilde{\mathbf{V}}^H$. The equation is then solved for $\partial\omega/\partial k_z$, the group velocity:

$$U_G(k_z, \omega) = \frac{\partial\omega}{\partial k_z} = \frac{\tilde{\mathbf{V}}^H [\mathbf{A}_1 + 2k_z \mathbf{A}_2] \tilde{\mathbf{V}}}{\tilde{\mathbf{V}}^H \begin{pmatrix} 2\omega \mathbf{M}_F & -i\mathbf{F} \\ i\mathbf{F}^T & 2\omega \mathbf{M}_S \end{pmatrix} \tilde{\mathbf{V}}} . \quad (3.56)$$

3.2.3 Discussion of the Method

In this finite element solution to the variational equation, some but not all of the boundary conditions between contiguous elements in the fluid and solid are satisfied. In the solid, two elements having a common boundary will share three nodes, and therefore both elements will have the same displacements at these nodes and along the boundary. However, the elements will not have the same traction along the boundary although the tractions will be approximately equal when the mesh is properly selected. Similarly, in the fluid the velocity potential between contiguous elements is continuous, but the displacements are not. A more sophisticated variational equation could be developed to satisfy all boundary conditions between elements, but it is not needed because the current method gives accurate results.

All of the boundary conditions at the fluid-solid interface are satisfied by including them in the variational equation. Without these terms the fluid would not be coupled to the solid, and two sets of solutions to the eigenvalue problem would be obtained: one would pertain to wave propagation along a fluid cylinder and the other to propagation along an empty borehole.

The eigenvalue problem actually has four related solutions. The most previously

stated solution for a normal mode may be represented by the combination: $\omega, k_z, \tilde{\mathbf{V}}$. The solution for another mode propagating in the same direction is the combination: $-\omega, -k_z, \tilde{\mathbf{V}}^*$, and this result may be verified by manipulating equation 3.54. The solutions for the modes propagating in the opposite direction are $\omega, -k_z, \tilde{\mathbf{Y}}$ and $-\omega, k_z, \tilde{\mathbf{Y}}^*$ where

$$\tilde{\mathbf{Y}} = \begin{pmatrix} \Phi(k_z, \omega) \\ \mathbf{U}(k_z, \omega) \end{pmatrix} . \quad (3.57)$$

These multiple solutions indicate that the phase velocities of the modes propagating in opposite directions along the borehole are equal, even if the solid has completely general anisotropy. Although this fact may seem surprising, plane waves demonstrate similar behavior: in an anisotropic medium the phase velocities of two plane waves propagating in opposite directions (which are defined by the orientation of the wavenumber vector) are always equal (see Chapter 1).

Two features of the variation equation make it amenable to a finite element solution. First, because the motion in the fluid is described in terms of a velocity potential instead of displacements, spurious modes do not develop (Wiggins, 1976; Hamdi and Ousset, 1978; Everstine, 1981; Buland and Gilbert, 1984; Olsen and Bathe, 1985a). This potential-based method has the added advantage that it needs far fewer equations than the displacement-based method. Second, the variational equation is formulated in terms of first spatial derivatives and not the second spatial derivatives which are in the wave equation (see e.g., Aki and Richards, 1980, p. 19). Consequently the potential and displacements calculated with this variational method approximate well the exact the values of these quantities, a point which will be demonstrated later. For the strains and stresses, which involve first derivatives, the match between values obtained with the variational method and the exact values is not as good (see Carrier and Pearson, 1976, p. 175).

The combined use of analytical and numerical expressions for the velocity potential and displacement has two very important advantages. First, because the pressures

and displacements for the modes are expressed in the frequency-wavenumber domain using $\exp[i(k_z z - \omega t)]$, some properties of their behavior like velocity dispersion can be easily studied. Second, using $\exp(ik_z z)$ to simulate wave propagation in the z direction greatly reduces the size of the problem. If this analytical expression were not used, then a three-dimensional mesh would have to be established. Since the memory requirements for the two-dimensional mesh are quite large, the memory requirements for the three-dimensional mesh would be enormous. Concomitantly the number of computations would increase greatly. These two factors suggest that trying to solve the variational equation using a three-dimension mesh might exceed the capabilities of current computers.

An important issue in the finite element method is designing the mesh. The mesh must have enough elements in the right locations to allow reasonably accurate wavenumbers, pressures, and displacements to be calculated. At the same time, the mesh must have as few elements as possible to minimize the amount of computation and memory needed to solve the wave equation. The selected mesh (Figure 3-2) satisfied these two criteria for the tube, pseudo-Rayleigh, flexural, and screw waves, which are the normal modes commonly encountered in acoustic logging. The mesh is very dense in the radial direction near the borehole wall because the pressures and displacements for the modes change rapidly here. The density is only high enough for the lower order radial modes; the higher order radial modes have even more rapid changes and would require more elements. Because the pressures and displacements change slowly away from the borehole wall, the mesh density is lower there. As the radial distance increases (beyond the borehole wall) the displacements for normal modes diminish and eventually go to zero at infinity. The outermost elements (Figure 3-2) model this behavior well; however, these elements cannot model the leaky modes which have oscillatory displacements. The mesh density in the azimuthal direction is just high enough to obtain accurate results for the tube and pseudo-Rayleigh waves which do not change with azimuth, for the flexural wave which changes according

to $\cos \theta$, and for the screw wave which changes according to $\cos 2\theta$. Obtaining good results for a mode with a higher azimuthal order number would require more elements.

This variational method has been extensively tested, and the results are very accurate. Consider a model with an isotropic, fast formation (Table 3.3) and another with an isotropic, slow formation (Table 3.4) because exact solutions for the phase and group velocities, pressures, and displacements exist (see Appendix A and Chapter 2). The phase and group velocities calculated with the variational method are almost always within 0.1% of their exact values (Figures 3-6, 3-7, 3-8, and 3-9). Similarly the pressures and displacements calculated with the variational method match the exact solutions (Figures 3-10, 3-11, 3-12, and 3-13).

3.3 Results

Although the behavior of the modes could be studied for many types of anisotropy, only those types which are prevalent in the Earth should be considered. Field data, laboratory data, and mathematical modeling indicate that two types are important. Transverse isotropy is a good model for (1) sedimentary rocks like shales which contain aligned clay minerals (Thomsen, 1986; Winterstein, 1986), (2) formations which consist of many beds that are thin relative to the wavelength of an elastic wave (Backus, 1962; White, 1955), and (3) rocks with aligned microfractures (Crampin, 1984). Orthorhombic anisotropy is a good model for some igneous and metamorphic rocks whose microcracks and minerals are aligned (Thill et al., 1973).

Acutal logging conditions can be simulated using different orientations of the anisotropy with respect to the borehole. If the formation is transversely isotropic, for example, this orientation is expressed by the angle between the symmetry axis of the formation and the borehole. When this angle is zero, three situations are modeled: a vertical borehole through horizontally lying shales or thin beds, a deviated borehole through a tilted shales or thin beds (where the angle of deviation equals the angle

of tilt), and a horizontal borehole through a formation with aligned microcracks (for which the major axis of the microcracks is vertical). When this angle is small, three situations are modeled: a vertical borehole through a tilted shales or thin beds, a deviated borehole through horizontal shales or thin beds, and a deviated borehole through tilted shales or thin beds (where the angle of deviation does not equal the angle of tilt). And when this angle equals 90° , two situations are modeled: a horizontal borehole through a horizontal formation and a vertical borehole through a formation with aligned microcracks (for which the major axis of the microcracks is vertical). In addition to the examples presented here, many others obviously exist.

In this section, normal mode propagation in transversely isotropic and orthorhombic models are studied with the variational method. The accuracy of the phase velocities is checked using the perturbation method that is developed in Chapter 2. Using the formula, $U_G = v \left[1 - \frac{\omega}{v} \frac{dv}{d\omega} \right]^{-1}$, (where v is the phase velocity computed with the perturbation method) the accuracy of the group velocities is checked.

3.3.1 Transversely Isotropic Models

Because the behavior of the the normal modes in the transversely isotropic models is closely related to planar qS -wave propagation, these waves will be discussed first. The properties of the solid are listed in Table 3.5. The waves propagating parallel to the symmetry axis have the same phase velocity, 2.97 km/s (Figure 3-14a). Although the polarizations for this particular propagation direction are often decomposed into the orientations shown in Figure 3-14b, the orientations are actually arbitrary. The waves propagating at an angle with respect to the symmetry axis have different phase velocities and different polarizations with unique orientations. For example, when the propagation direction is 20° with respect to the symmetry axis, the phase velocities are 2.99 km/s and 3.03 km/s. The polarization of the slower wave is perpendicular to the a - b plane, and that for the faster wave is in this plane. When the propagation direction is 90° with respect to the symmetry axis, the phase velocities are 2.97 km/s

and 3.17 km/s. The polarization of the faster wave is perpendicular to the a - b plane, and that for the slower wave is in this plane.

First, normal modes were computed when the symmetry axis was parallel to the borehole. The properties of the borehole model are listed in Table 3.5. The shapes of the phase and group velocity curves (Figures 3-15 and 3-16) are like those for an isotropic model. The phase velocities do not exceed 2.97 km/s which equals the phase velocities of the two S -waves propagating parallel to the symmetry axis (Figure 3-14). The characteristics of the displacements and pressures are identical to those for an isotropic model and consequently are not plotted. The orientations of the two flexural waves and two screw waves are arbitrary just as the polarizations of the two S -waves propagating parallel to the symmetry axis are arbitrary.

When the symmetry axis is tilted 20° and 90° with respect to the borehole, small but significant changes occur in the phase and group velocities. (The modes are labeled with the same name used for isotropic models except that the prefix, quasi or q , is attached.) The general shapes of the dispersion curves are the same as those when the symmetry axis is aligned with the borehole (Figures 3-17, 3-18, 3-19, 3-20, 3-21, 3-22, 3-23, and 3-24). When the symmetry axis is tilted 20° , the phase velocities of the normal modes never exceed 2.99 km/s, the phase velocity of the slowest qS -wave whose wavenumber vector is parallel to the borehole. An analogous result applies when the symmetry axis is tilted 90° . In both cases, the quasi-flexural and quasi-screw waves have different phase and group velocities (Figures 3-25, 3-26, 3-27, 3-28); the differences are large at low frequencies but small at high frequencies. Near the limiting qS -wave velocity, the difference between the phase velocities for the quasi-flexural waves is greater than the difference between the phase velocities for the quasi-screw waves.

The most obvious effect of the anisotropy is the alignment of the quasi-flexural and quasi-screw waves. (Because the general characteristics of the displacements for the 20° and 90° models are similar, only the displacements for the 20° model are plotted.)

For the slow quasi-flexural wave, the particle displacements in the plane perpendicular to the borehole, when viewed together, are aligned with the polarization of the slow qS -wave whose wavenumber vector is parallel to the borehole (Figure 3-29). For the fast quasi-flexural wave, the particle displacements in the plane perpendicular to the borehole, when viewed together, are aligned with the polarization of the fast qS -wave (Figure 3-30). For the slow quasi-screw wave, the particle displacements in the plane perpendicular to the borehole, when viewed together, are aligned along two mutually perpendicular directions which are rotated 45° with respect to the polarizations of the slow and fast qS -waves (Figure 3-31). For the fast quasi-screw wave, the particle displacements in the plane perpendicular to the borehole, when viewed together, are aligned along two mutually perpendicular directions which are parallel to the polarizations of the qS -waves (Figure 3-32). The quasi-tube and quasi-pseudo-Rayleigh waves show no obvious alignment with respect to the qS -waves (Figures 3-33 and 3-34). The anisotropy makes the displacements for each wave truly different from those that would exist if the solid were isotropic or transversely isotropic with its symmetry axis parallel to the borehole. However, these changes are so small that they are not discernible in Figures 3-29, 3-30, 3-31, 3-32, 3-33, and 3-34, and consequently a valid generalization is that the displacements are very similar to those which exist when the medium is isotropic or transversely isotropic with its symmetry axis parallel to the borehole.

3.3.2 Orthorhombic Model

For the orthorhombic model (Table 3.6) only one orientation of the borehole was studied: the borehole is parallel to the intersection of two symmetry planes. The phase velocities of the two qS -waves which propagate parallel to the borehole are 2.67 km/s and 2.95 km/s (Figure 3-35a), and their polarizations are mutually perpendicular (Figure 3-35b).

The phase and group velocities of the normal modes (Figures 3-36, 3-37, 3-

38, and 3-37) are like those in the transversely isotropic models when the symmetry axis is tilted with respect to the borehole. The phase and group velocities do not exceed 2.67 km/s, the phase velocity of the slow qS -wave whose wavenumber vector is parallel to the borehole. The two quasi-flexural waves have different phase and group velocities, and the differences are large at low frequencies but small at high frequencies (Figures 3-40 and 3-42). The two quasi-screw waves behave similarly (Figures 3-41 and 3-42). Near the limiting qS -wave velocity, the difference between the phase velocities of the quasi-flexural waves is greater than that for the quasi-screw waves.

The displacements are also like those in the transversely isotropic models when the symmetry axis is tilted with respect to the borehole. (For this reason, they are not plotted.) For the slow quasi-flexural wave, the particle displacements in the plane perpendicular to the borehole, when viewed together, are aligned with the polarizations of the slow qS -wave whose wavenumber vector is parallel to the borehole. For the fast quasi-flexural wave, the particle displacements in the plane perpendicular to the borehole, when viewed together, are aligned with the polarization of the fast qS -wave. For slow quasi-screw wave, the particle displacements in the plane perpendicular to the borehole, when viewed together, are aligned along two mutually perpendicular directions which are rotated 45° with respect to the polarizations of the slow and fast qS -waves. For the fast quasi-screw wave, the particle displacements in the plane perpendicular to the borehole, when viewed together, are aligned along two mutually perpendicular directions which are parallel with the polarizations of the two qS -waves. Due to the anisotropy the displacements are different from those that would exist if the solid were isotropic or transversely isotropic with its symmetry axis parallel to the borehole, but the differences are small.

3.3.3 Discussion of the Results

The differences in the phase and group velocities of the quasi-flexural and quasi-screw waves are correlated with the differences between the phase velocities of the qS -waves whose wavenumber vectors are parallel to the axis of the borehole. This result suggests that phase velocity surface can be used to predict the relative differences in the velocities of these two modes. For example, when the velocity surface shows that the differences between the two qS -waves are zero, the quasi-flexural waves will have the same phase and group velocities. When the surface shows a large difference, the two quasi-flexural waves will have a correspondingly large difference in their phase and group velocities. Using this property, the general behavior of the normal modes for virtually any model can be readily predicted.

Two features of the quasi-flexural waves make them suitable for detecting the anisotropy of the solid: the horizontal motion and phase velocity of each wave is correlated with the polarization and phase velocity, respectively, of the related qS -wave propagating along the borehole. The feature associated with the phase velocity requires some comment. The fact that the phase velocity of the faster quasi-flexural wave does not exceed phase velocity of the slowest qS -wave propagating along the borehole only applies to the normal mode portion of this wave. Above this threshold, the mode will become leaky meaning that it will propagate energy in the form of elastic waves into the solid. At low frequencies the phase velocity of this leaky mode is expected to approach the phase velocity of the faster qS -wave propagating parallel to the borehole. (This hypothesis was not be tested here because the solution to the wave equation was not formulated in a manner that the leaky modes could be studied.) If this hypothesis is correct, then the differences between the phase and group velocities of these waves at low frequencies will be substantial.

The other normal modes are not well suited for detecting the anisotropy of the solid. The quasi-screw waves cannot be used to distinguish between the polarizations of the fast and slow qS -waves propagating along the axis of the borehole, and the

differences in the phase and group velocities of these two modes are quite small. The motion and phase velocities of the quasi-tube and quasi-pseudo-Rayleigh waves are only slightly affected by the anisotropy.

Although the quasi-flexural waves can be used to detect the qS -wave anisotropy in the direction of the borehole, this mode as well as the other normal modes cannot be used to completely characterize the anisotropy. The waves in the transversely isotropic model with the symmetry axis tilted 20° are very similar to the corresponding waves in the model whose axis is tilted 90° . Therefore, a reasonable hypothesis is that the waves cannot be used to determine the orientation of the symmetry axis of any transversely isotropic model. (The only exception to this statement exists when the symmetry axis is parallel to the borehole: the phase and group velocities of the two flexural and two screw waves are identical.) In addition, the behavior of the waves in the transversely isotropic models with the tilted symmetry axes and the orthorhombic model are very similar. Therefore, a reasonable hypothesis is that the waves cannot distinguish between transverse isotropy and orthorhombic anisotropy and, moreover, between other types of anisotropy like monoclinic and triclinic anisotropy.

3.4 Summary and Conclusions

A variational method was developed to calculate wavenumbers, pressures, and displacements for normal modes propagating along a fluid-filled borehole through an anisotropic medium. The implementation uses an analytical expression, $\exp(\imath k_z z)$, to describe wave propagation along the borehole and finite element expressions to describe propagation in the plane perpendicular to the borehole. This approach has two advantages: it reduces the size of the problem to the extent that current computers can perform the calculations, and it allows the modes to be expressed in the frequency-wavenumber domain where their modal behavior can be studied. For isotropic models, the phase and group velocities, pressures, and displacements

calculated with this variational method matched exact solutions.

The investigation of the behavior of the normal modes in anisotropic models was limited to two cases: a transversely isotropic model for which the borehole had several different orientations with respect to the symmetry axis and an orthorhombic model for which the borehole was parallel to the intersection of two symmetry planes. These two cases were chosen because they adequately represent many logging situations. For these anisotropic models the phase and group velocities calculated with the variational method match those calculated with a completely independent method based upon perturbation theory.

The normal modes in these anisotropic models show several effects which do not exist when the solid is isotropic or transversely isotropic with its symmetry axis parallel to the borehole:

1. The phase velocities for the quasi-pseudo-Rayleigh, both quasi-flexural, and both quasi-screw waves do not exceed the phase velocity of the slowest qS -wave. (The phase velocities of the leaky modes, which were not investigated in this chapter, will exceed this threshold.)
2. The two quasi-flexural waves have different phase and group velocities; the differences are greatest at low frequencies and diminish as the frequency increases. In general, the two quasi-screw waves behave similarly.
3. The greater the difference between the phase velocities of the qS -waves, the greater the difference between the phase velocities of the quasi-flexural waves at all frequencies. The two quasi-screw waves behave similarly.
4. Near the limiting qS -wave velocity, the difference between the phase velocities for the two quasi-flexural waves is greater than that for the two quasi-screw waves.
5. For the slow quasi-flexural wave, the particle displacements in the plane perpendicular to the borehole, when viewed together, are aligned with the polarization

of the slow qS -wave.

6. For the fast quasi-flexural wave, the particle displacements in the plane perpendicular to the borehole, when viewed together, are aligned with the polarization of the fast qS -wave.
7. For the slow quasi-screw wave, the particle displacements in the plane perpendicular to the borehole, when viewed together, are aligned along two mutually perpendicular directions which are rotated 45° with respect to the polarizations of both qS -waves.
8. For the fast quasi-screw wave, the particle displacements in the plane perpendicular to the borehole, when viewed together, are aligned along two mutually perpendicular directions which are parallel with the polarizations of both qS -waves.

(In this list, the qS -waves refer to the plane waves whose wavenumber vectors are parallel to the borehole.) Despite these significant effects, the general characteristics of the phase velocities, group velocities, and displacements are similar (but not identical) to those that would exist if the solid were isotropic or transversely isotropic with its symmetry axis parallel to the borehole. This result is expected because the solid is only slightly anisotropic.

Region	Meaning	Variable
fluid	volume	V_1
	density	ρ_1
	incompressibility	λ_1
	velocity potential	ϕ
	dilatation	Θ
solid	volume	V_2
	density	ρ_2
	stiffness matrix	\mathbf{C}
	strain vector	\mathbf{E}
fluid-solid interface	surface	Σ
	normal vector	\mathbf{n}
	traction	\mathbf{T}
general	cylindrical coordinates	r, θ, z
	Cartesian coordinates	x, y, z
	displacement	\mathbf{u}
	time	t
	wavenumber for z direction	k_z
	frequency	ω
	phase velocity	v
	group velocity	U_G
	pressure	p
	borehole radius	R
	surface area	S
	volume	V
	Lagrangian energy	L

Table 3.1: Variables needed to formulate the variational equations and other miscellaneous variables.

Region	Meaning	Variable
fluid (element m)	interpolating functions velocity potential at nodes stiffness matrices mass matrix	$h_i^{(m)}(x, y)$ or $\mathbf{h}^{(m)}(x, y)$ $\Phi_i^{(m)}(k_z, t)$ or $\Phi^{(m)}(k_z, t)$ $\mathbf{K}_{0F}^{(m)}, \mathbf{K}_{2F}^{(m)}$ $\mathbf{M}_F^{(m)}$
fluid (all elements)	velocity potential stiffness matrices mass matrix	$\Phi(k_z, t)$ $\mathbf{K}_{0F}, \mathbf{K}_{2F}$ \mathbf{M}_F
solid (element n)	interpolating functions strain matrix for x and y directions strain matrix for z directions displacement at nodes stiffness matrices mass matrix	$h_i^{(n)}(x, y)$ or $\mathbf{H}^{(n)}(x, y)$ $\mathbf{B}_0^{(n)}(x, y)$ $\mathbf{B}_1^{(n)}(x, y)$ $U_{ix}^{(n)}(k_z, t), U_{iy}^{(n)}(k_z, t),$ $U_{iz}^{(n)}(k_z, t)$ or $\mathbf{U}^{(n)}(k_z, t)$ $\mathbf{K}_{0S}^{(n)}, \mathbf{K}_{1S}^{(n)}, \mathbf{K}_{2S}^{(n)}$ $\mathbf{M}_S^{(n)}$
solid (all elements)	displacement stiffness matrices mass matrix	$\mathbf{U}(k_z, t)$ $\mathbf{K}_{0S}, \mathbf{K}_{1S}, \mathbf{K}_{2S}$ \mathbf{M}_S
fluid-solid interface (element q)	distance along Σ angle between \mathbf{n} and Σ at node i interpolating functions interpolating matrix for fluid interpolating matrix for solid coupling matrix	l $\theta_i^{(q)}$ $h_{Ii}^{(q)}(l)$ $\mathbf{h}_I^{(q)}(l)$ $\mathbf{H}_I^{(q)}(l)$ $\mathbf{F}^{(q)}$
fluid-solid interface (all elements)	coupling matrix	\mathbf{F}
general	number of fluid elements number of solid elements number of interface elements vector and matrices in wave equation	M N Q $\mathbf{Y}, \mathbf{V}, \tilde{\mathbf{Y}}, \tilde{\mathbf{V}}, \mathbf{A}_0, \mathbf{A}_1,$ $\mathbf{A}_2, \mathbf{A}'_0, \mathbf{D}_1, \mathbf{D}_2$

Table 3.2: Additional variables needed for the finite element solution to the variational equation.

Quantity	Value
c_{11}	3.79×10^{10} Pa
c_{44}	1.51×10^{10} Pa
ρ_2	2140 kg/m ³
λ_1	0.225×10^{10} Pa
ρ_1	1000. kg/m ³
R	0.1016 m

Table 3.3: Properties of the isotropic model with the a formation. The properties of the solid are like those for the Berea sandstone (Thomsen, 1986).

Quantity	Value
c_{11}	0.998×10^{10} Pa
c_{44}	0.117×10^{10} Pa
ρ_2	2250kg/m ³
λ_1	0.225×10^{10} Pa
ρ_1	1000. kg/m ³
R	0.1016 m

Table 3.4: Properties of the isotropic model with a slow formation.

Quantity	Value
c_{11}	7.23×10^{10} Pa
c_{13}	2.06×10^{10} Pa
c_{33}	6.50×10^{10} Pa
c_{44}	2.21×10^{10} Pa
c_{66}	2.51×10^{10} Pa
ρ_2	2500 kg/m ³
λ_1	0.225×10^{10} Pa
ρ_1	1000. kg/m ³
R	0.1016 m

Table 3.5: Properties of the transversely isotropic model. For this list of elastic constants, the symmetry axis is parallel to the z axis. The properties of the solid are like those for the Mesaverda shale (5496.5) (Thomsen, 1986).

Quantity	Value
c_{11}	$9.78 \times 10^{10} \text{ Pa}$
c_{12}	$1.95 \times 10^{10} \text{ Pa}$
c_{13}	$3.23 \times 10^{10} \text{ Pa}$
c_{22}	$9.09 \times 10^{10} \text{ Pa}$
c_{23}	$1.86 \times 10^{10} \text{ Pa}$
c_{33}	$8.17 \times 10^{10} \text{ Pa}$
c_{44}	$2.44 \times 10^{10} \text{ Pa}$
c_{55}	$2.00 \times 10^{10} \text{ Pa}$
c_{66}	$3.18 \times 10^{10} \text{ Pa}$
ρ_2	2800 kg/m^3
λ_1	$0.225 \times 10^{10} \text{ Pa}$
ρ_1	$1000. \text{ kg/m}^3$
R	0.1016 m

Table 3.6: Properties of the orthorhombic model. The symmetry planes for the orthorhombic solid are parallel to the coordinate planes. The properties of the solid were measured by J. Mendelson (1989, oral communication).

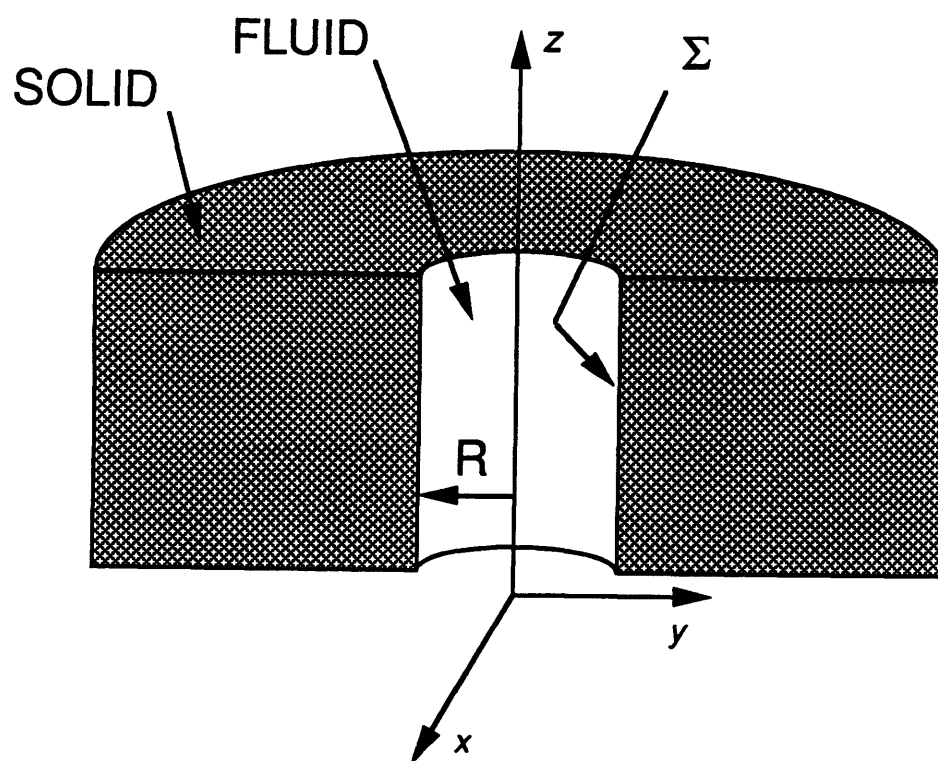


Figure 3-1: Cutaway view of the mathematical model.

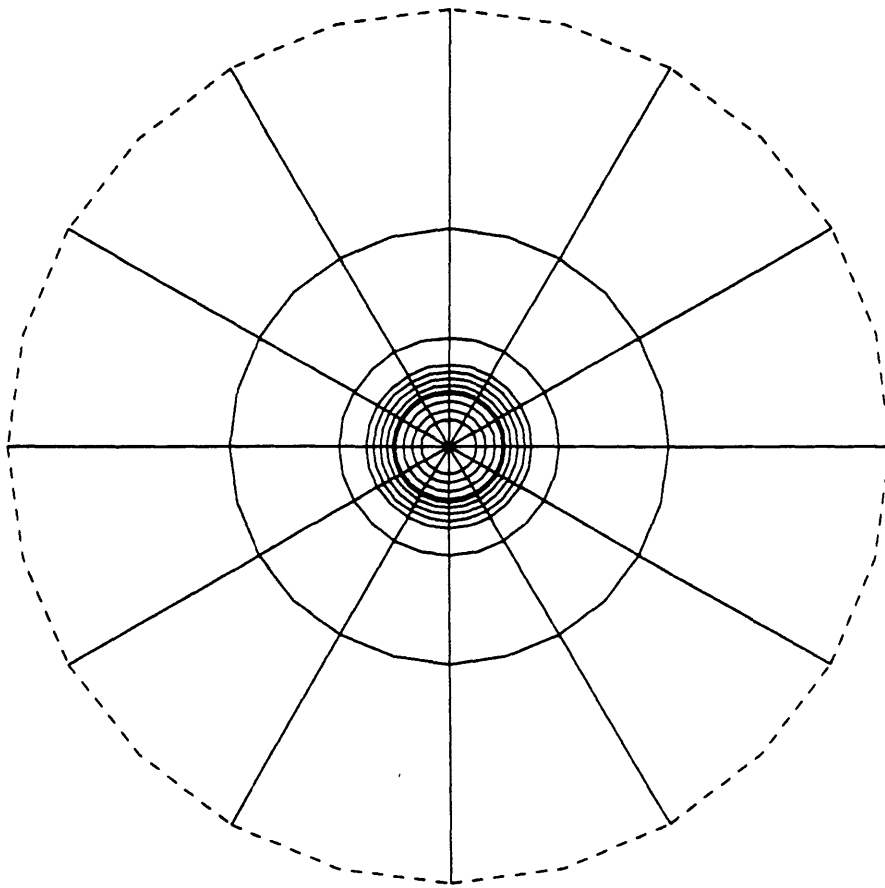


Figure 3-2: Finite element mesh. The location of the fluid-solid interface is shown by the dark line. The outermost elements actually extend to infinity which is symbolized by the dashed line.

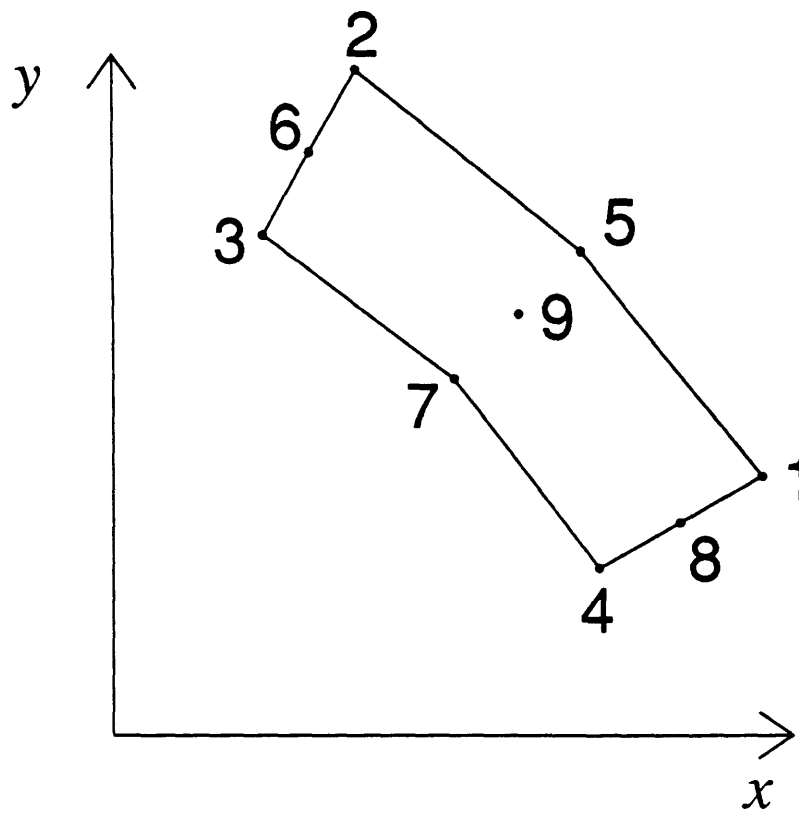


Figure 3-3: A two dimensional element with nine nodes. This type of element is used in the fluid and solid regions.

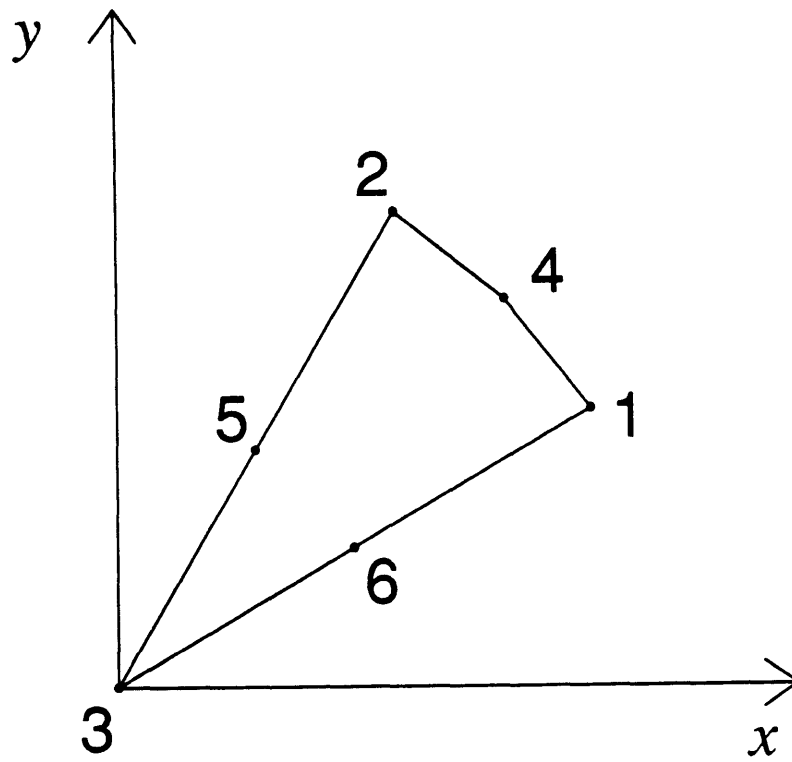


Figure 3-4: A two dimensional element with six nodes. This type of element is used only in the center of the mesh.

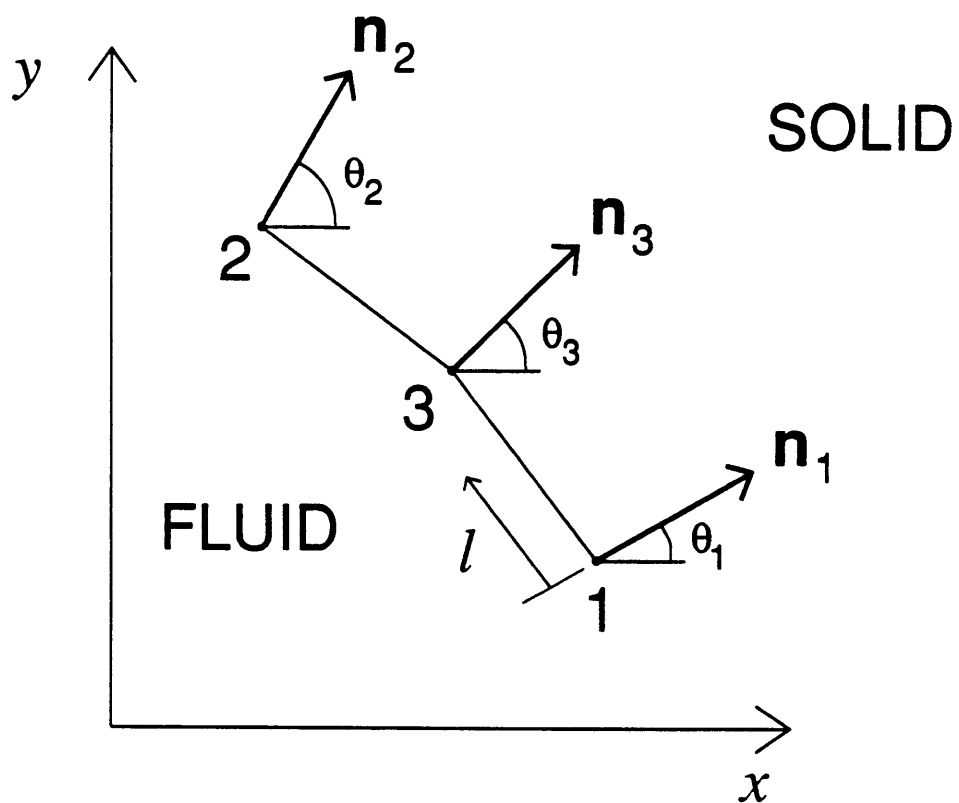


Figure 3-5: An interface element. This element has three nodes, and distances along the element are specified by l .

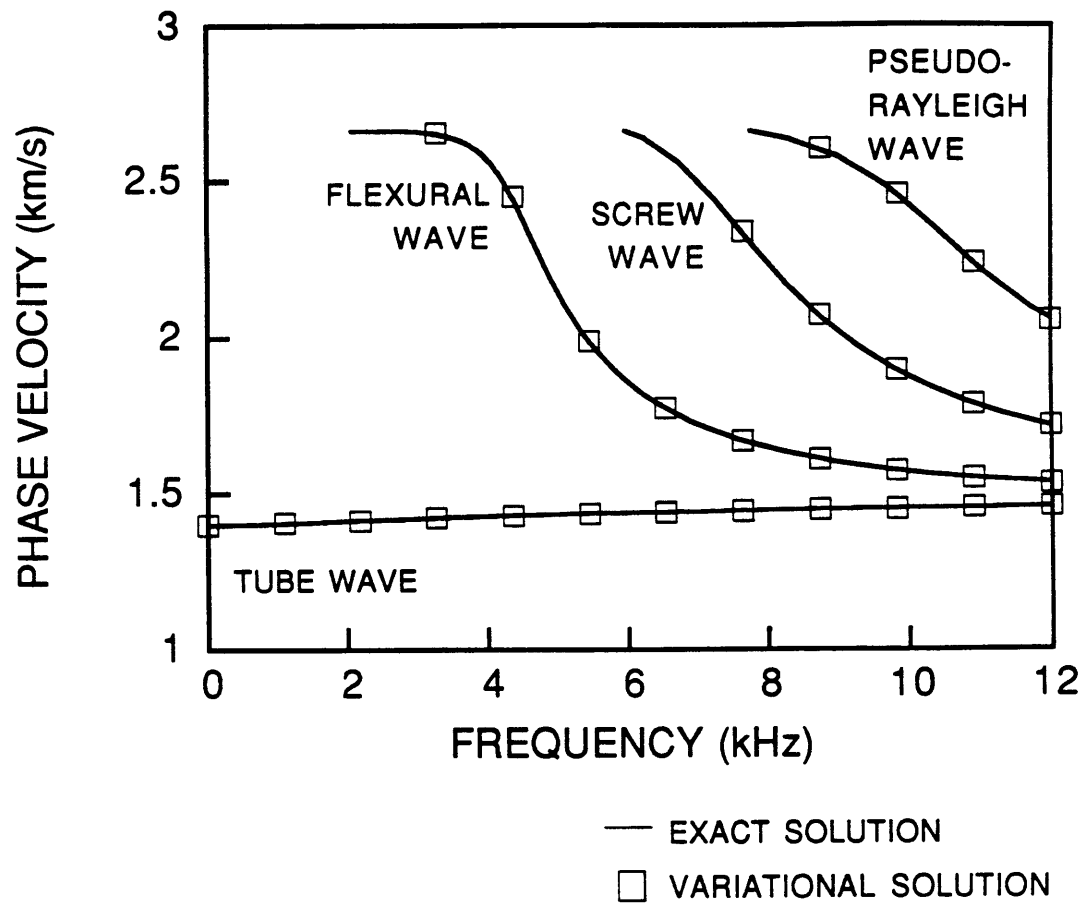


Figure 3-6: Accuracy of the phase velocities calculated with the variational method. The model has an isotropic, fast formation (Table 3.3).

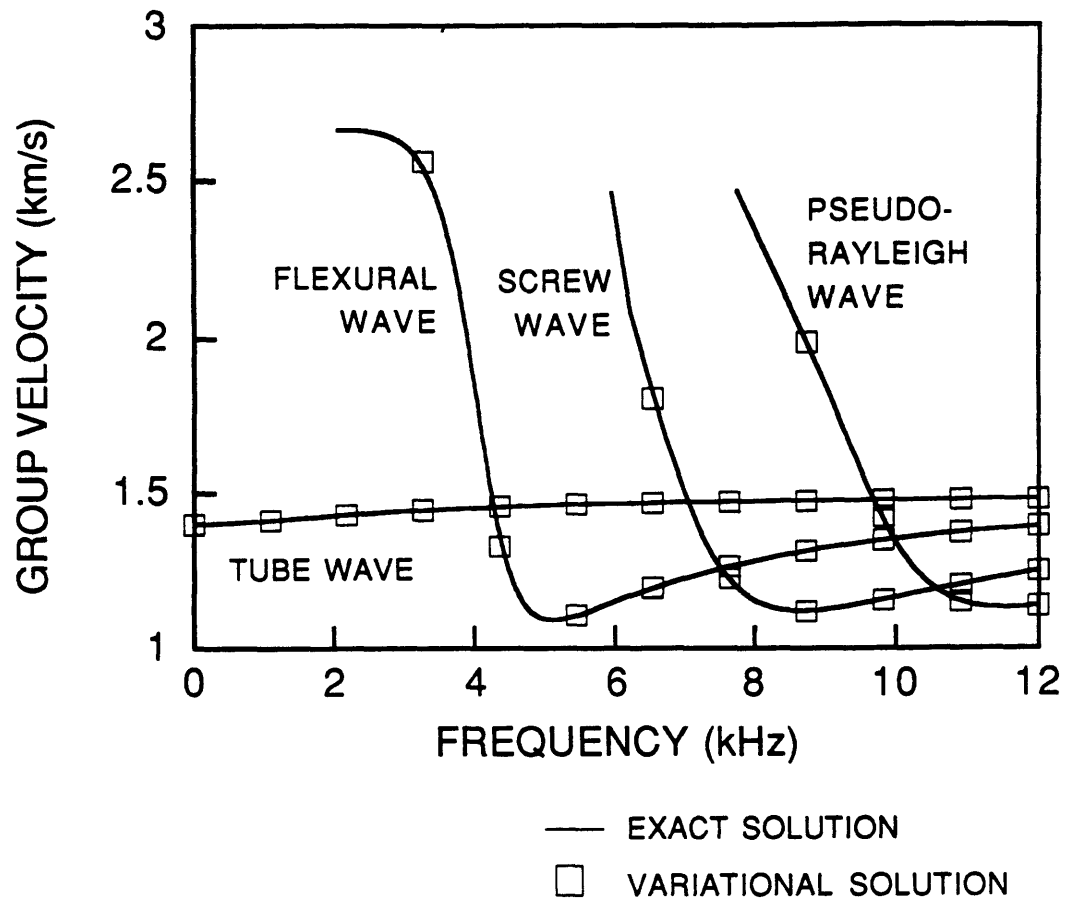


Figure 3-7: Accuracy of the group velocities calculated with the variational method. The model has an isotropic, fast formation (Table 3.3).

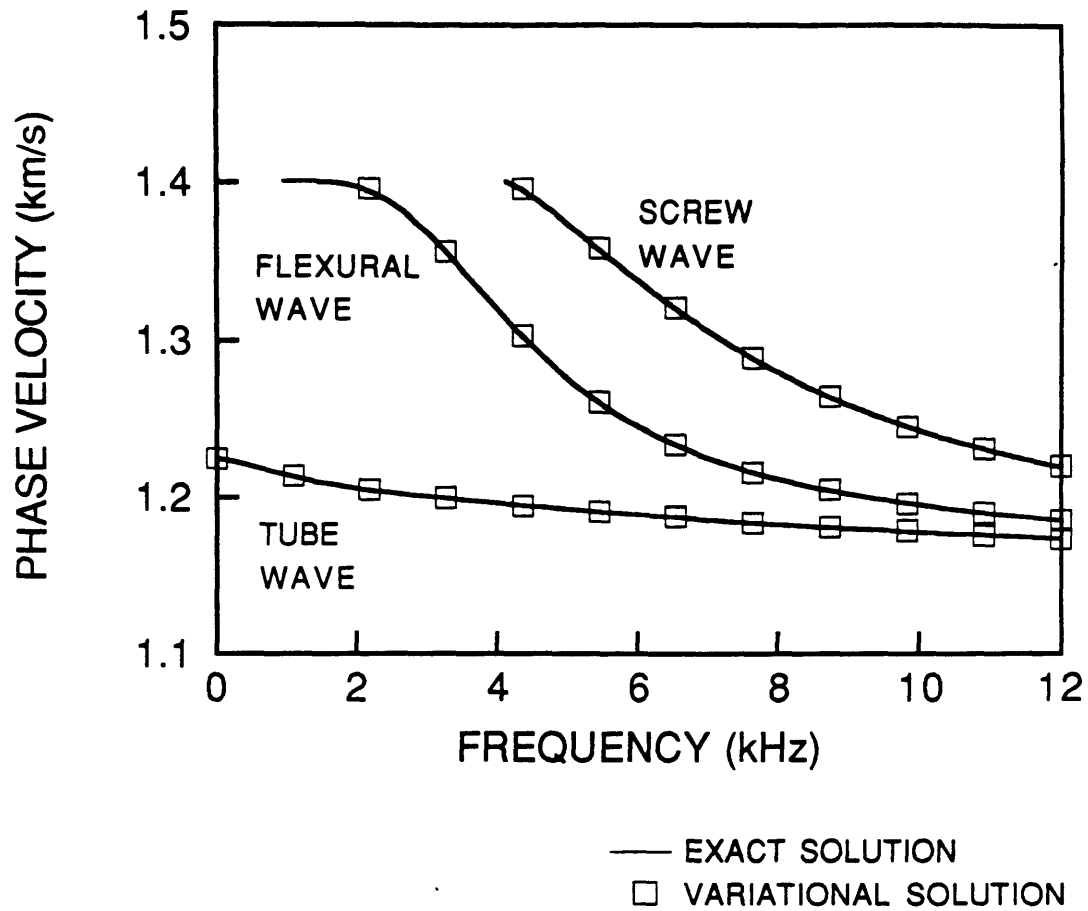


Figure 3-8: Accuracy of the phase velocities calculated with the variational method. The model has an isotropic, slow formation (Table 3.4).

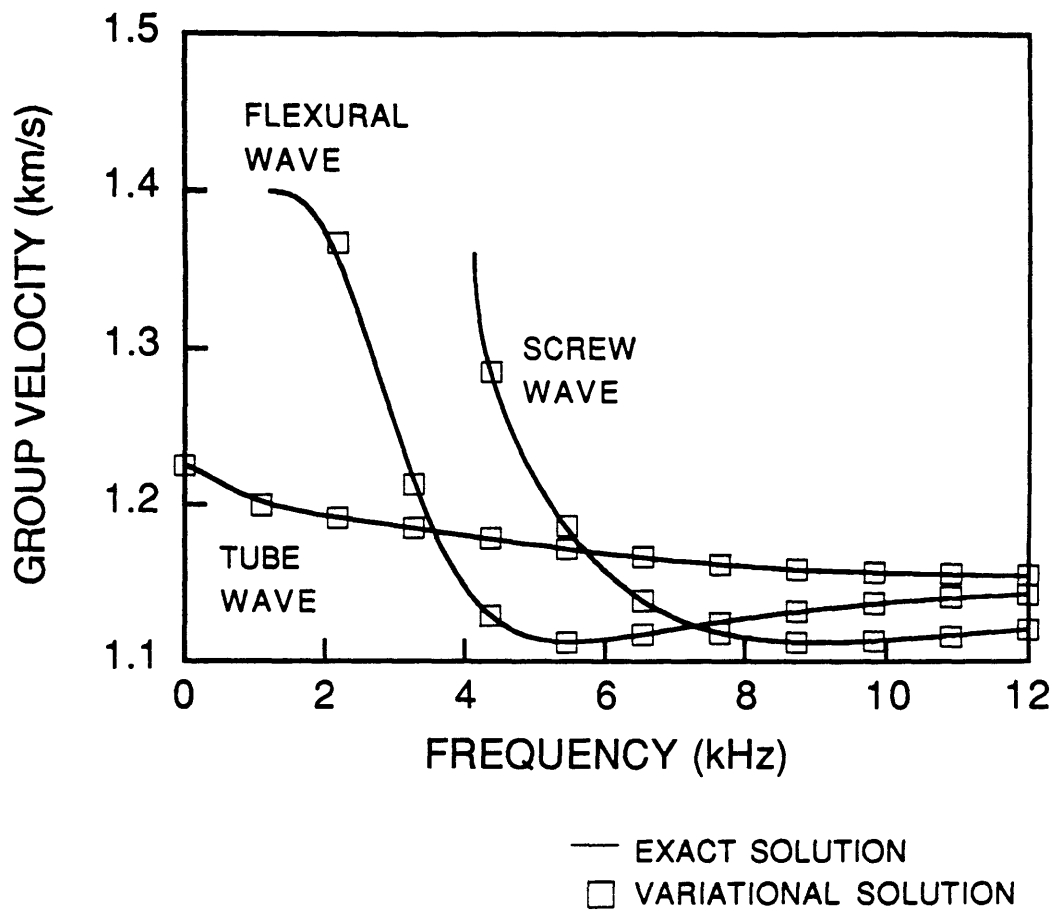


Figure 3-9: Accuracy of the group velocities calculated with the variational method. The model has an isotropic, slow formation (Table 3.4).

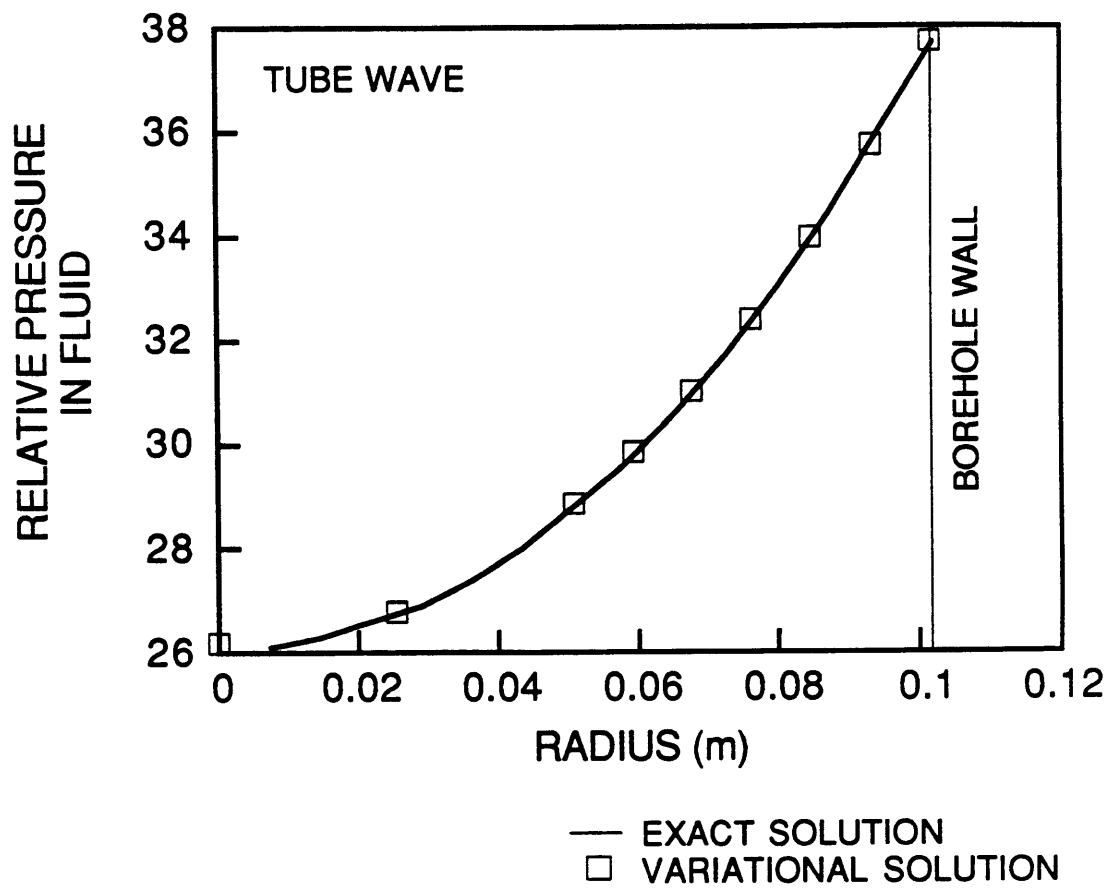


Figure 3-10: Accuracy of the pressures for the tube calculated with the variational method. The model has an isotropic, fast formation (Table 3.3).

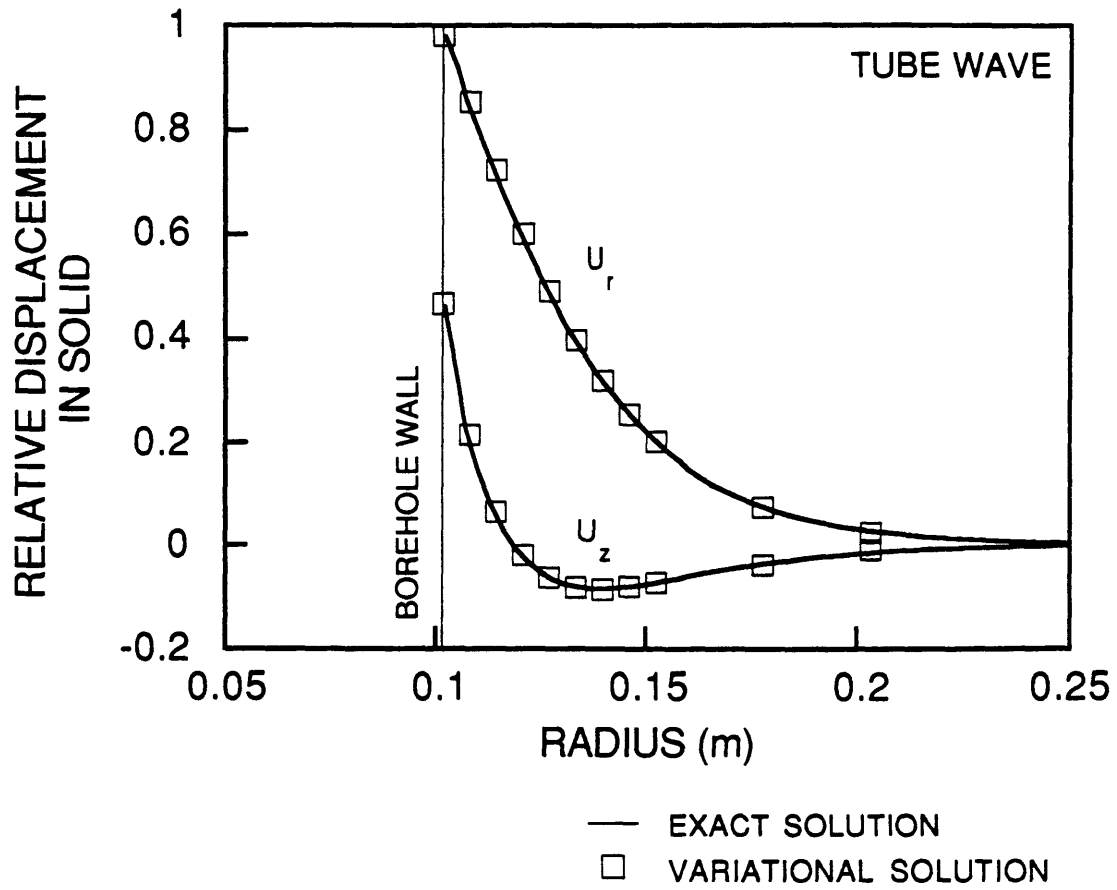


Figure 3-11: Accuracy of the displacements for the tube wave calculated with the variational method. The model has an isotropic, fast formation (Table 3.3).

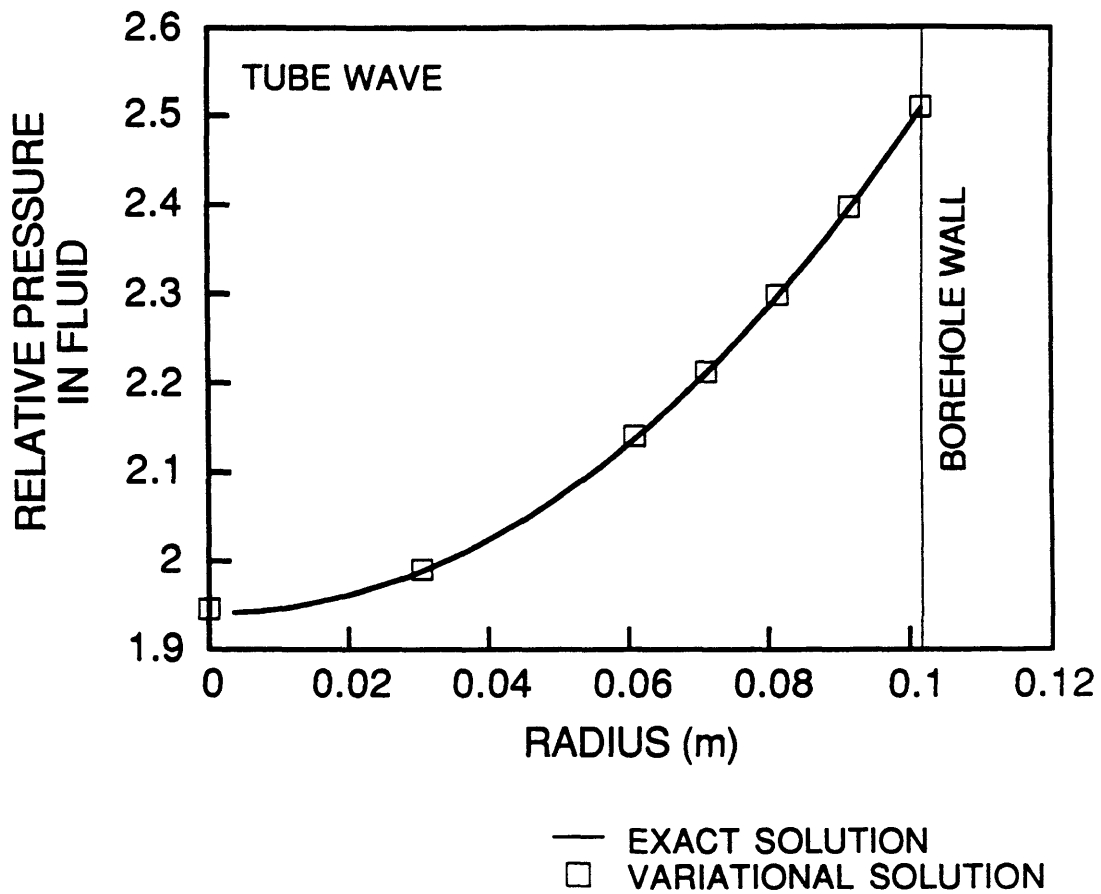


Figure 3-12: Accuracy of the pressures for the tube calculated with the variational method. The model has an isotropic, slow formation (Table 3.4).

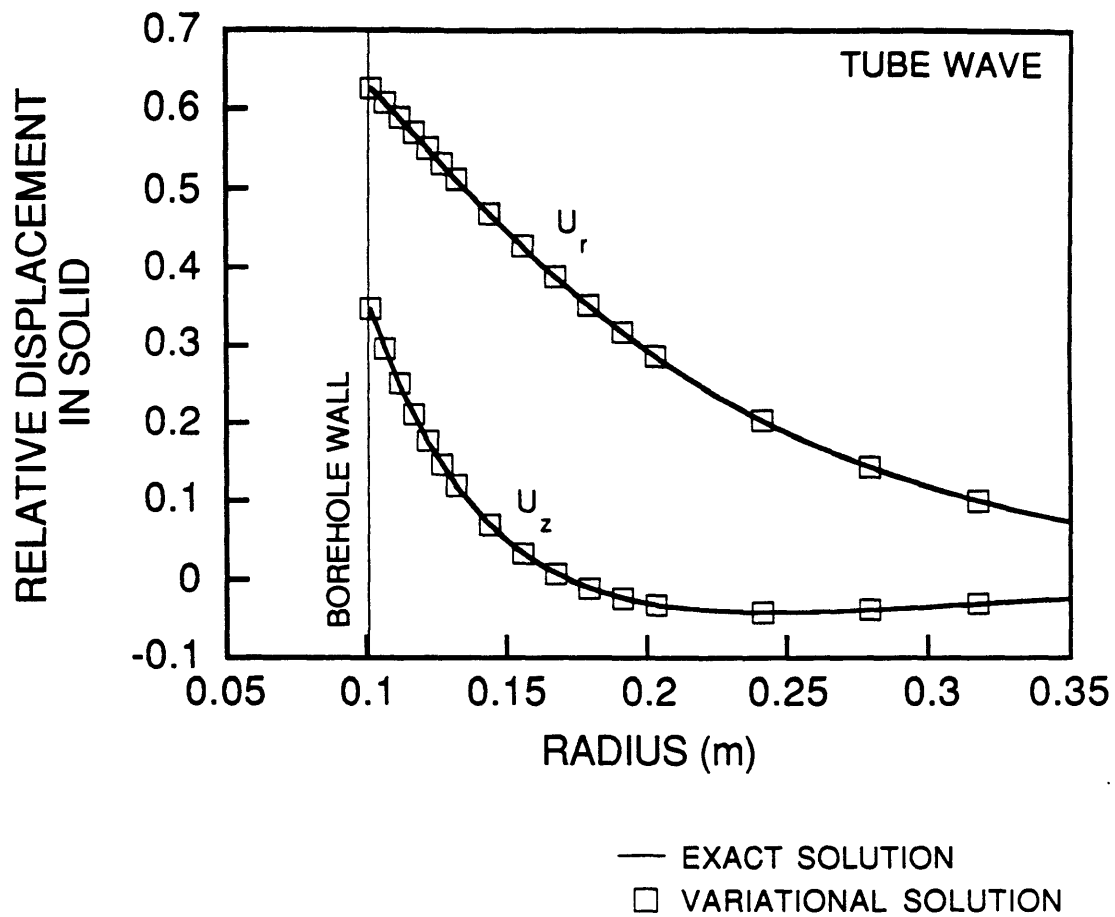


Figure 3-13: Accuracy of the displacements for the tube wave calculated with the variational method. The model has an isotropic, slow formation (Table 3.4).

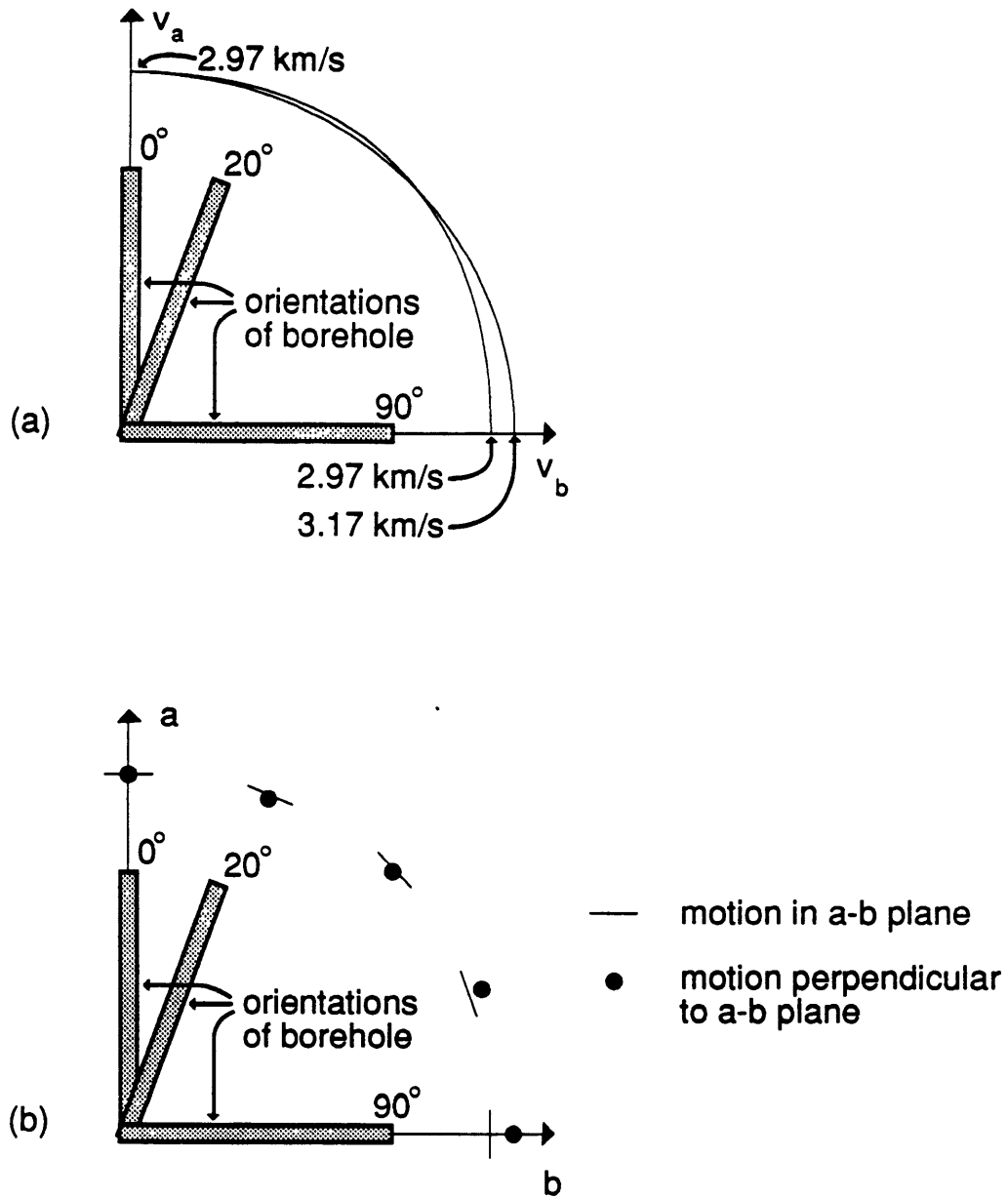


Figure 3-14: (a) Phase velocity surfaces and (b) polarizations for the qS -waves in the transversely isotropic model (Table 3.5). Axis a is parallel to the symmetry axis, and axis b is perpendicular to a and in an arbitrary direction.

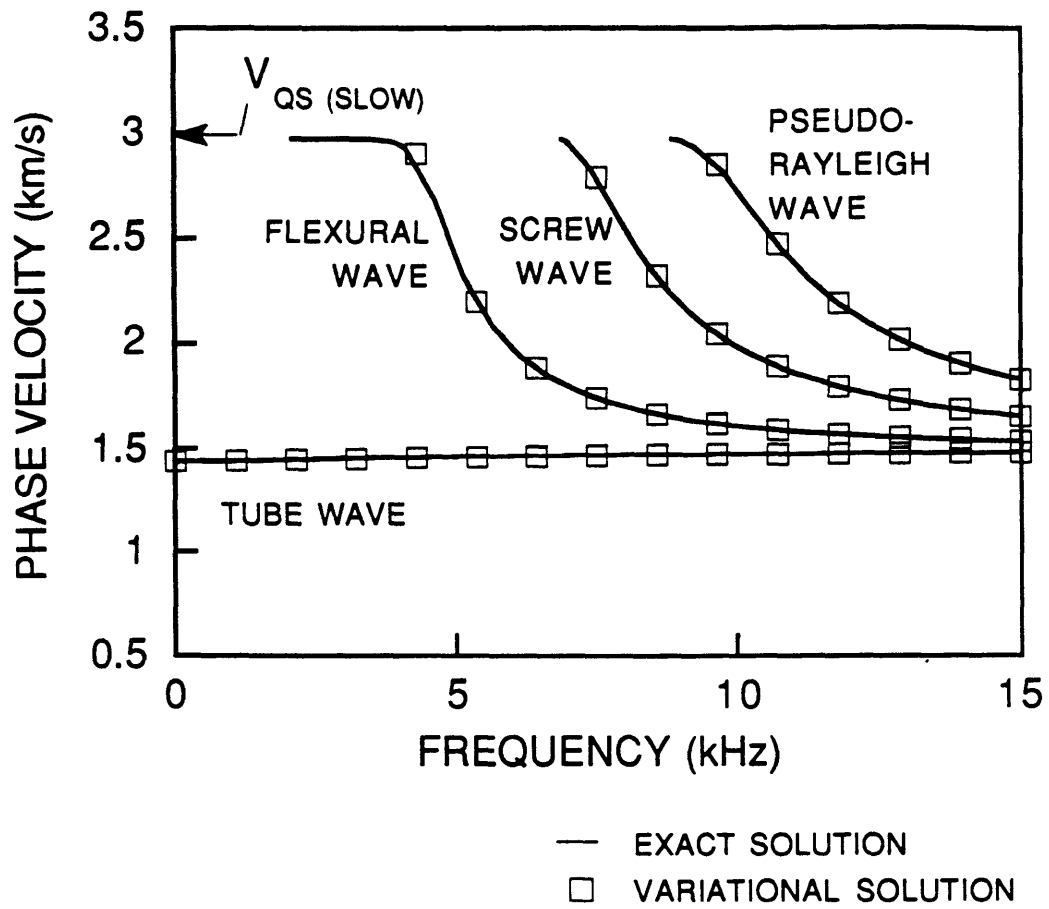


Figure 3-15: Phase velocities for the normal modes in the transversely isotropic model (Table 3.5) when the symmetry axis is parallel to the borehole.

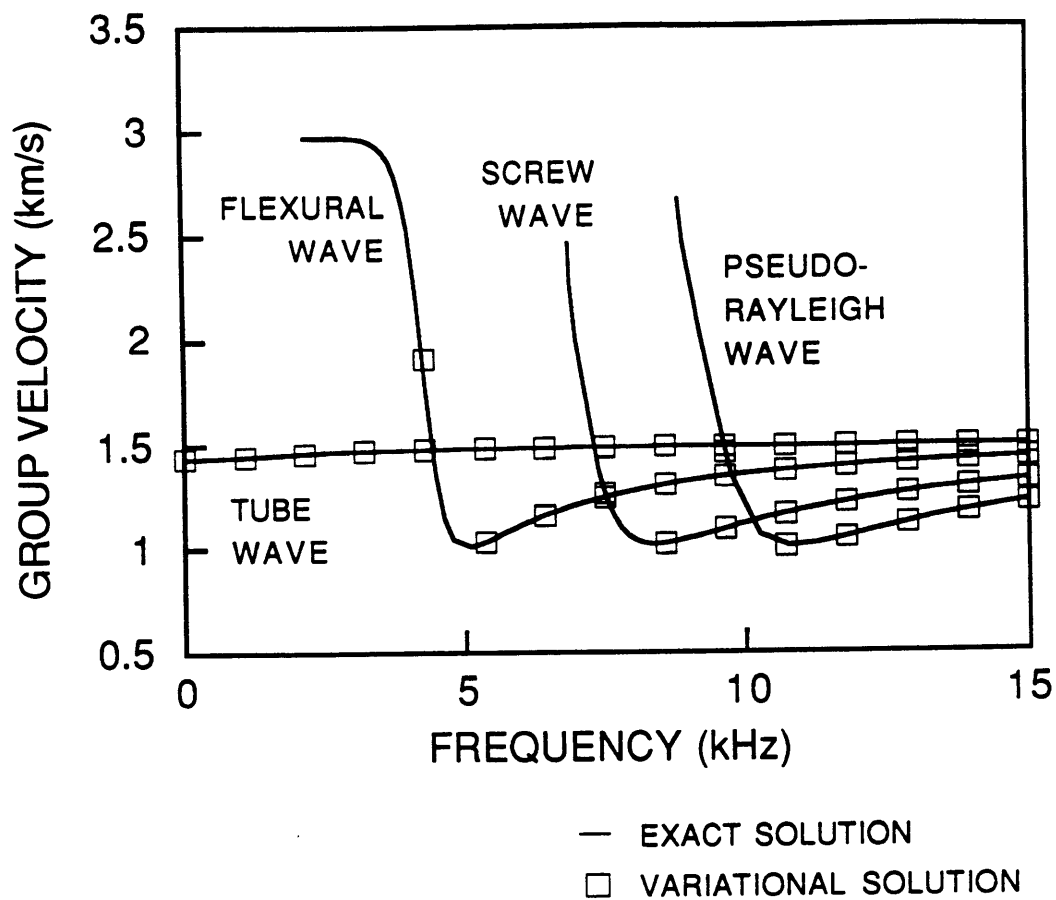


Figure 3-16: Group velocities for the normal modes in the transversely isotropic model (Table 3.5) when the symmetry axis is parallel to the borehole.

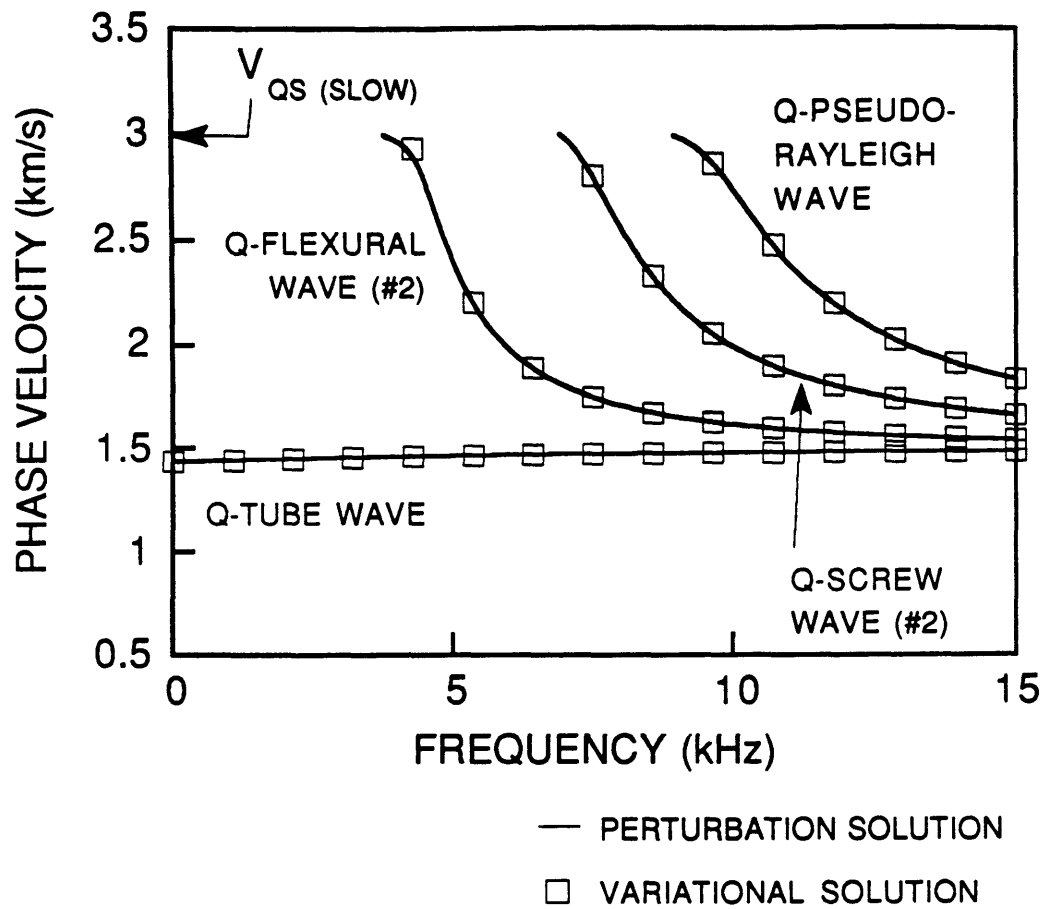


Figure 3-17: Phase velocities of the normal modes in the transversely isotropic model (Table 3.5) when its symmetry axis is tilted 20° with respect to the borehole. See also Figure 3-18.

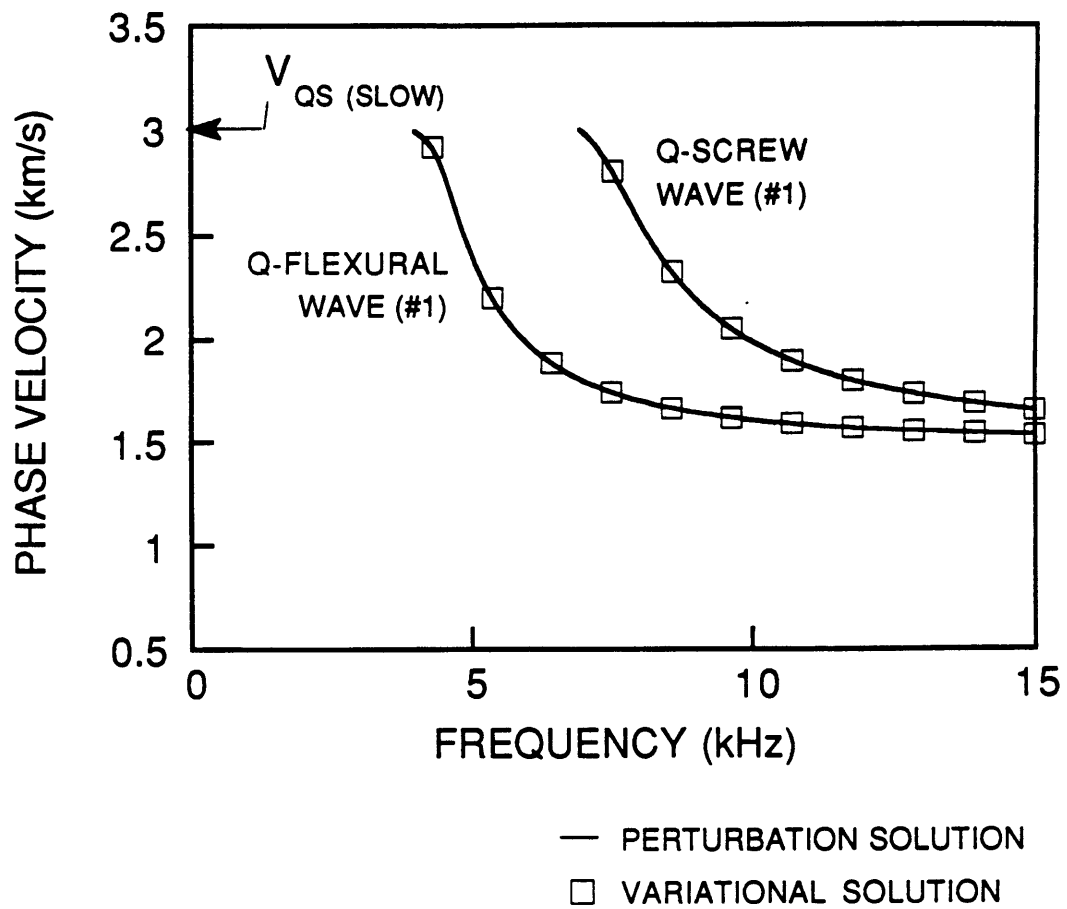


Figure 3-18: Phase velocities of the normal modes in the transversely isotropic model (Table 3.5) when its symmetry axis is tilted 20° with respect to the borehole. See also Figure 3-17.

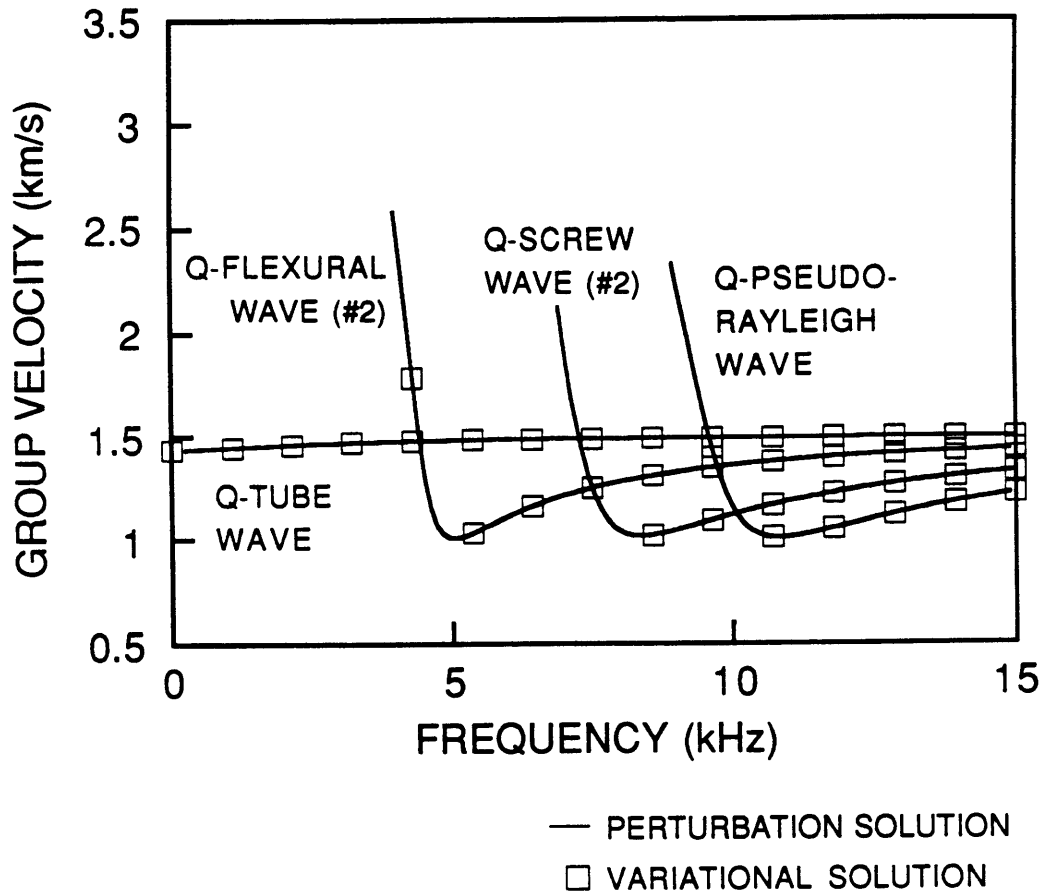


Figure 3-19: Group velocities of the normal modes in the transversely isotropic model (Table 3.5) when its symmetry axis is tilted 20° with respect to the borehole. See also Figure 3-20.

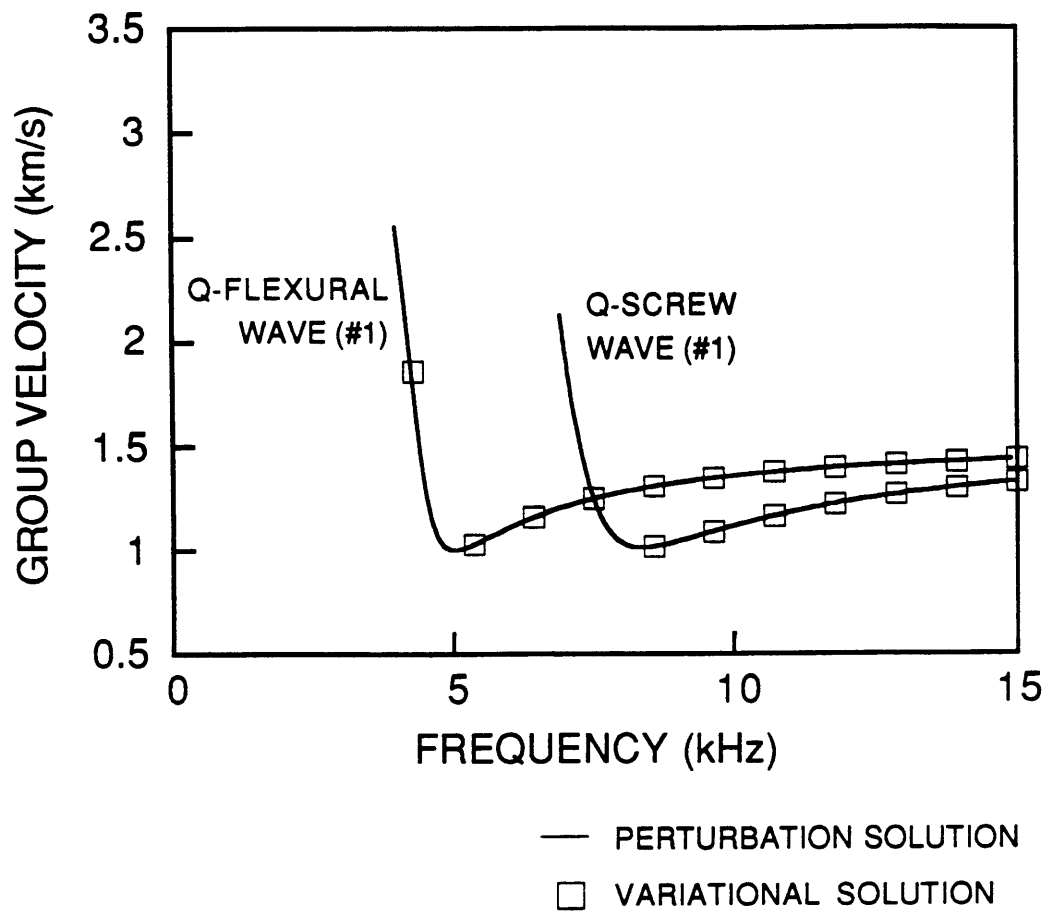


Figure 3-20: Group velocities of the normal modes in the transversely isotropic model (Table 3.5) when its symmetry axis is tilted 20° with respect to the borehole. See also Figure 3-19.

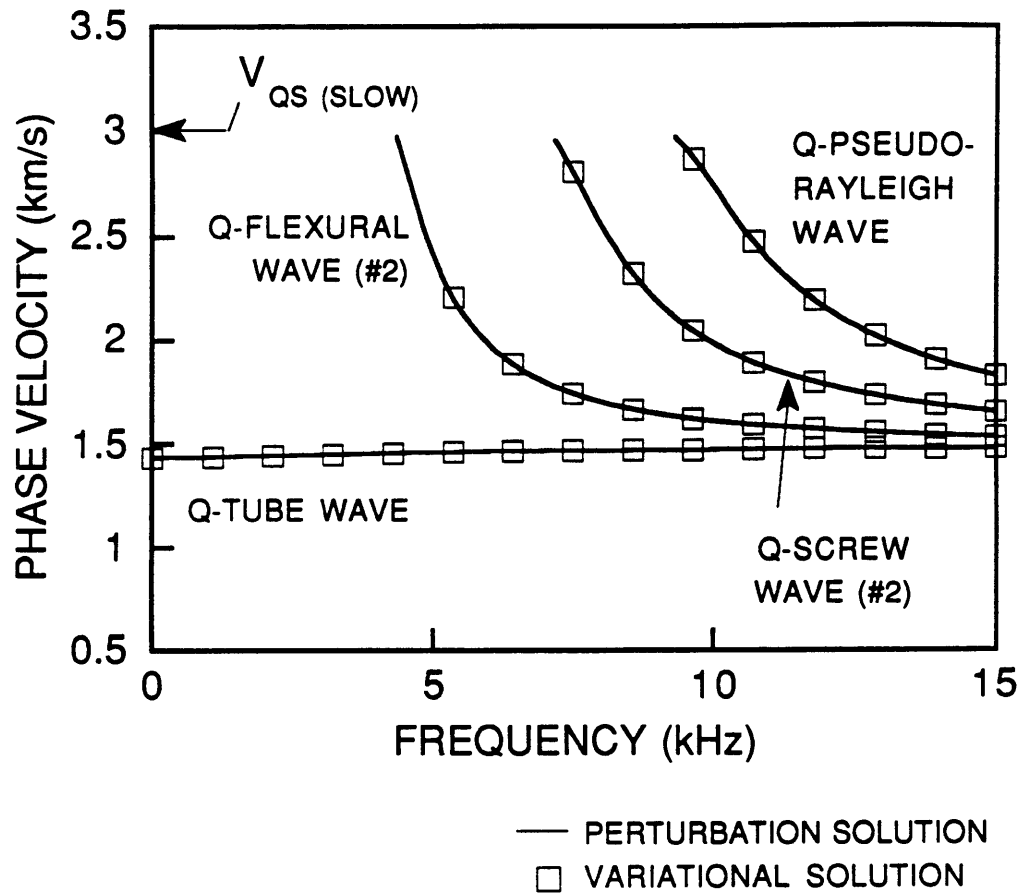


Figure 3-21: Phase velocities of the normal modes in the transversely isotropic model (Table 3.5) when its symmetry axis is tilted 90° with respect to the borehole. See also Figure 3-22.

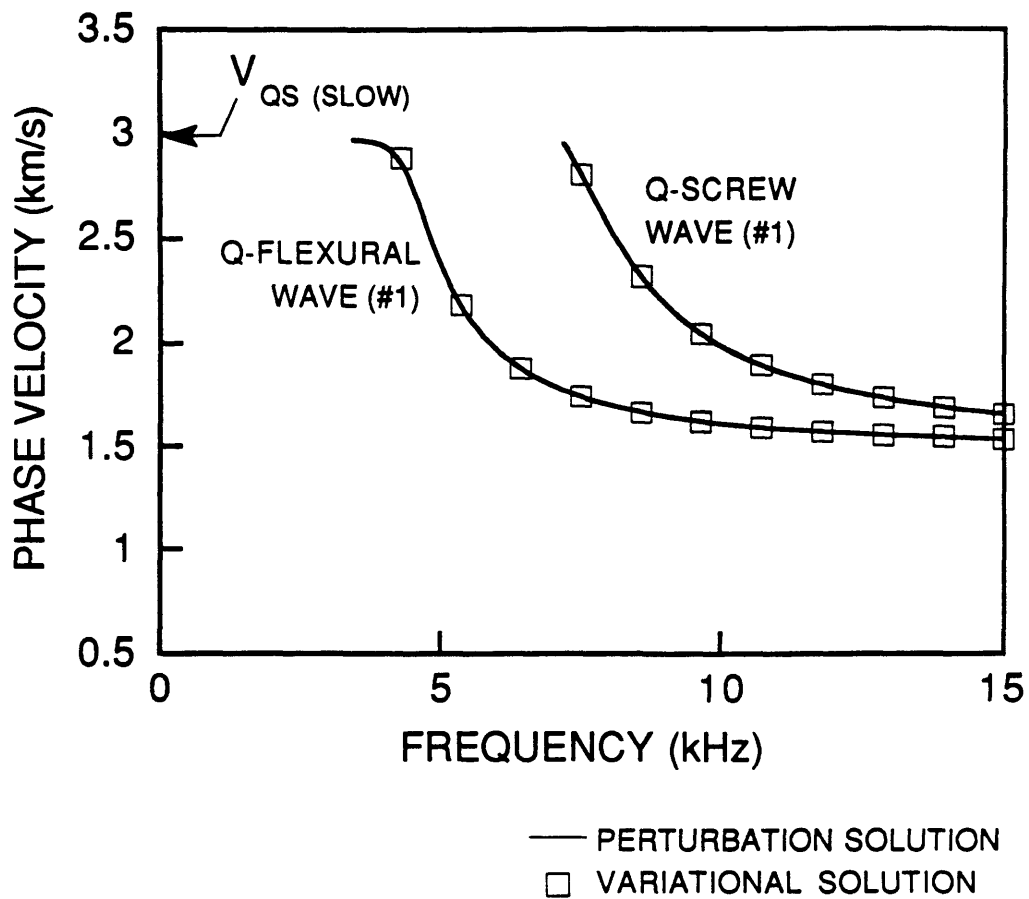


Figure 3-22: Phase velocities of the normal modes in the transversely isotropic model (Table 3.5) when its symmetry axis is tilted 90° with respect to the borehole. See also Figure 3-21.

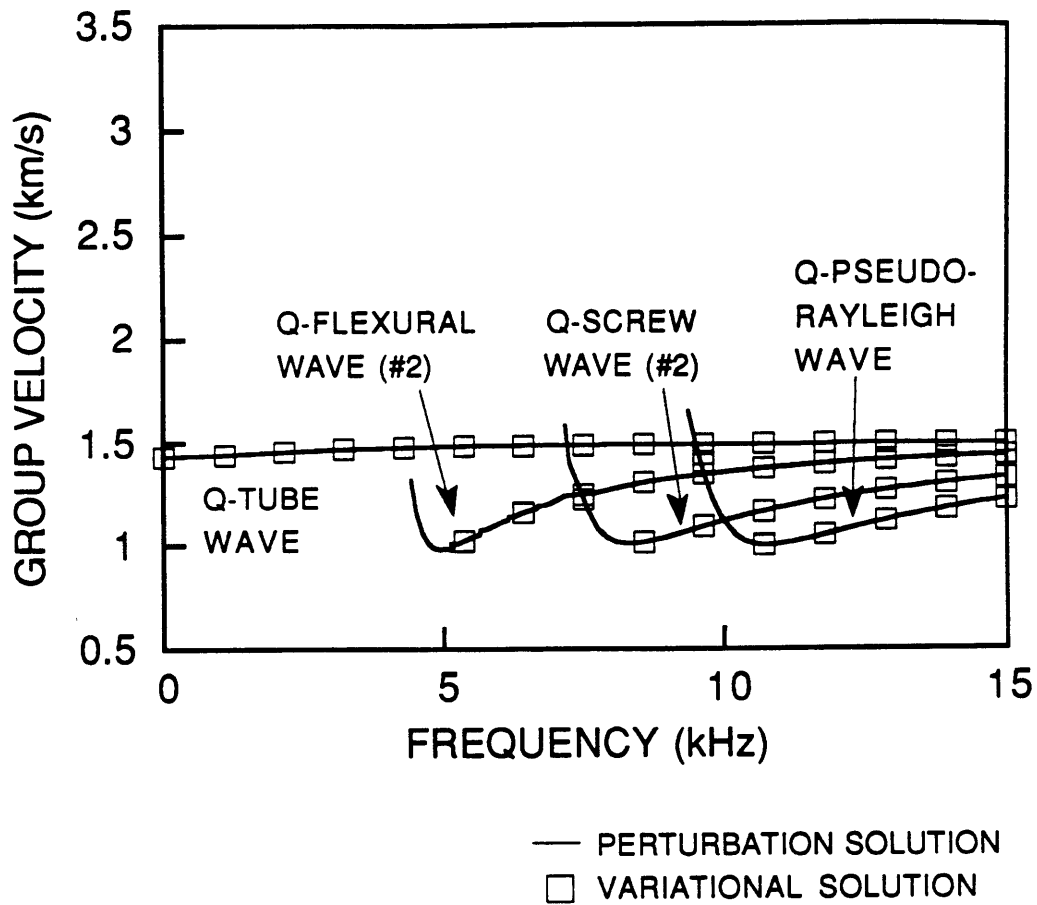


Figure 3-23: Group velocities of the normal modes in the transversely isotropic model (Table 3.5) when its symmetry axis is tilted 90° with respect to the borehole. See also Figure 3-24.

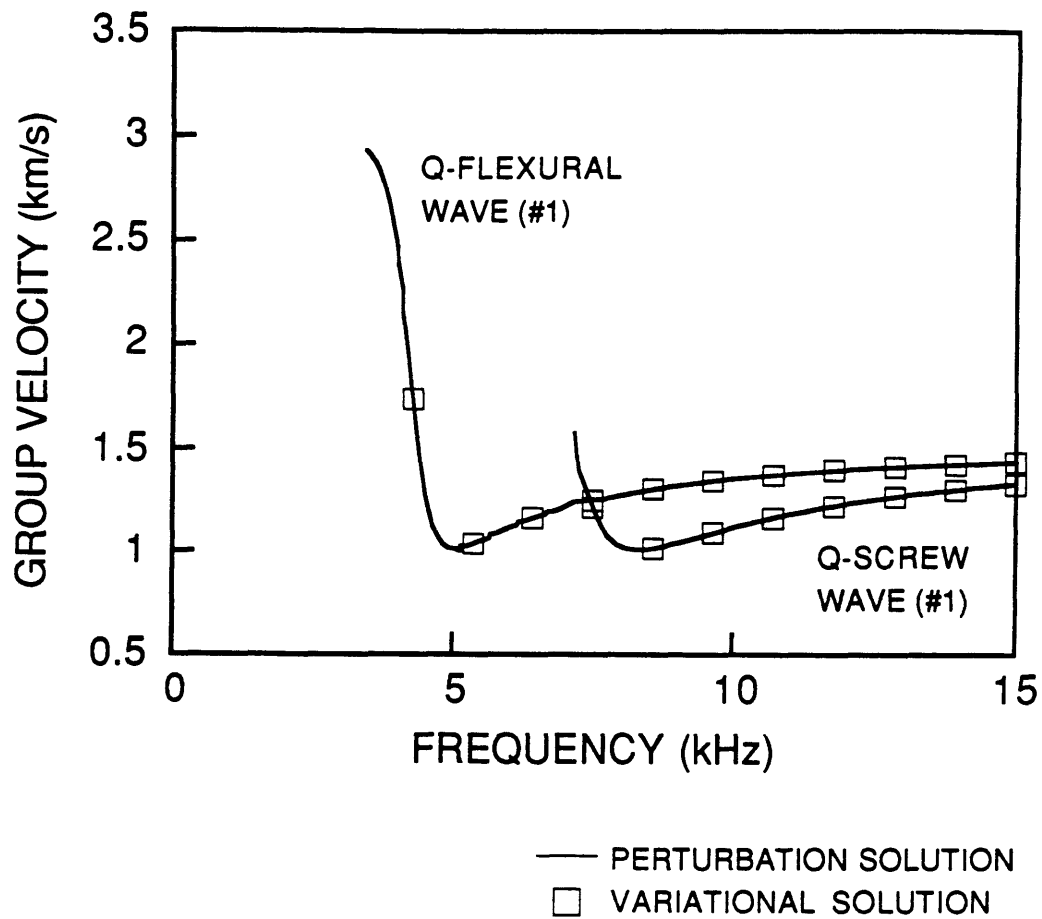


Figure 3-24: Group velocities of the normal modes in the transversely isotropic model (Table 3.5) when its symmetry axis is tilted 90° with respect to the borehole. See also Figure 3-23.

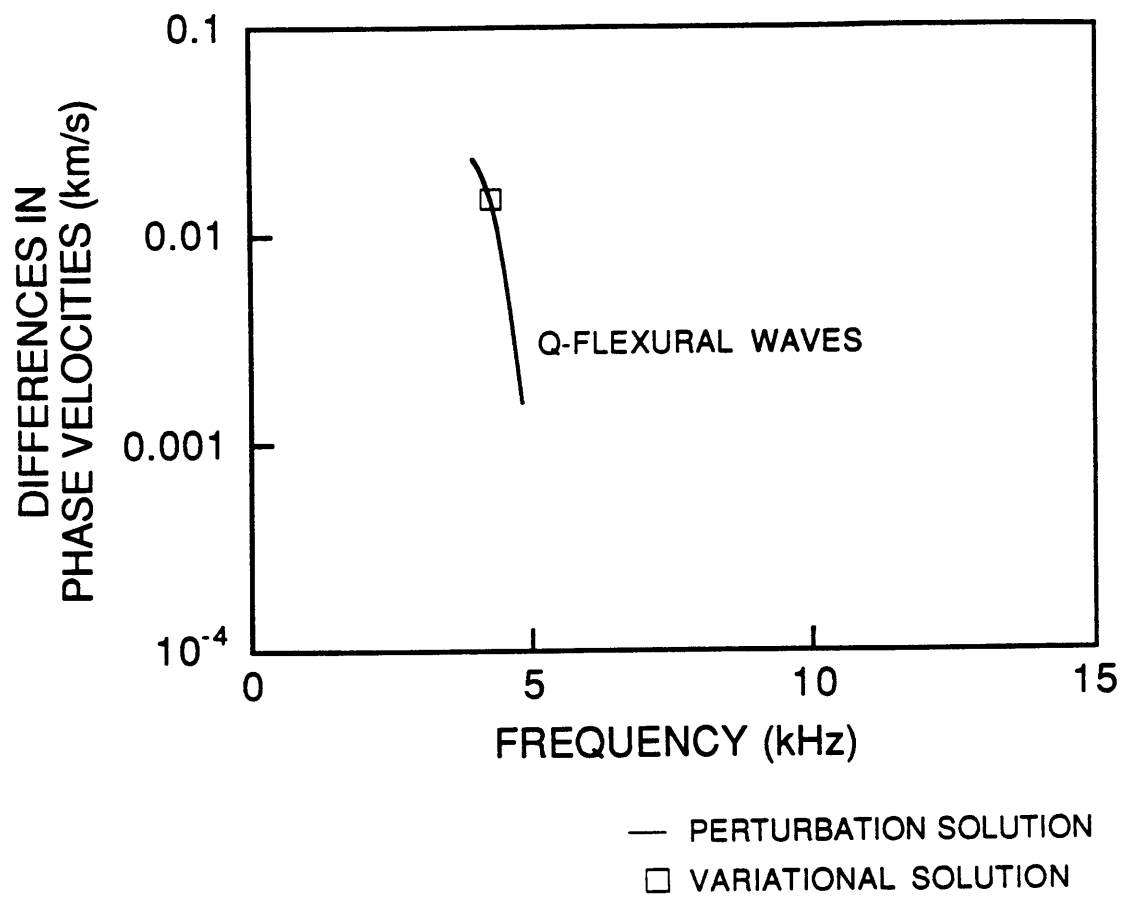


Figure 3-25: Differences between the phase velocities of the quasi-flexural waves (Figure 3-17 and 3-18) in the transversely isotropic model (Table 3.5) when its symmetry axis is tilted 20° with respect to the borehole. (When differences less than about 0.001 km/s become inaccurate, they are not plotted.)

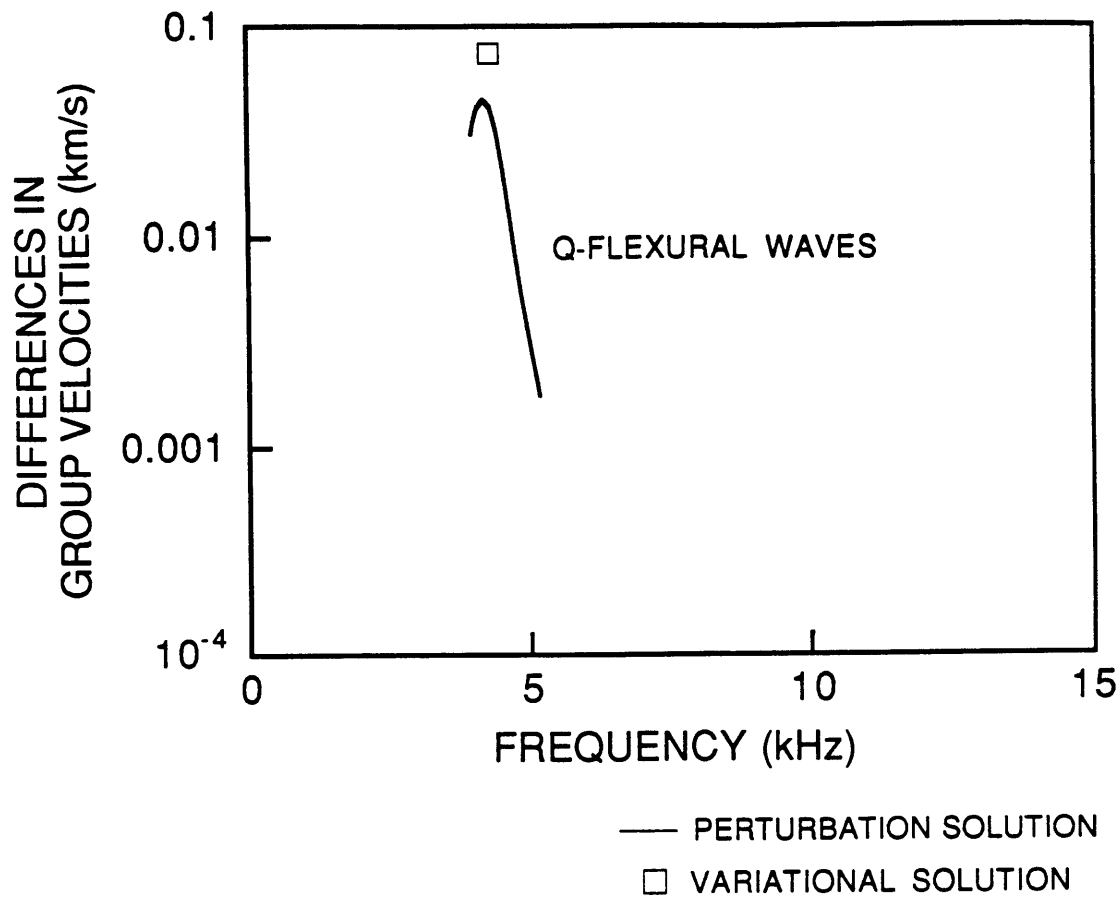


Figure 3-26: Differences between the group velocities of the quasi-flexural waves (Figure 3-19 and 3-20) in the transversely isotropic model (Table 3.5) when its symmetry axis is tilted 20° with respect to the borehole. (When differences less than about 0.001 km/s become inaccurate, they are not plotted.) The discrepancy between the perturbation and variational solutions is due to numerical inaccuracies.

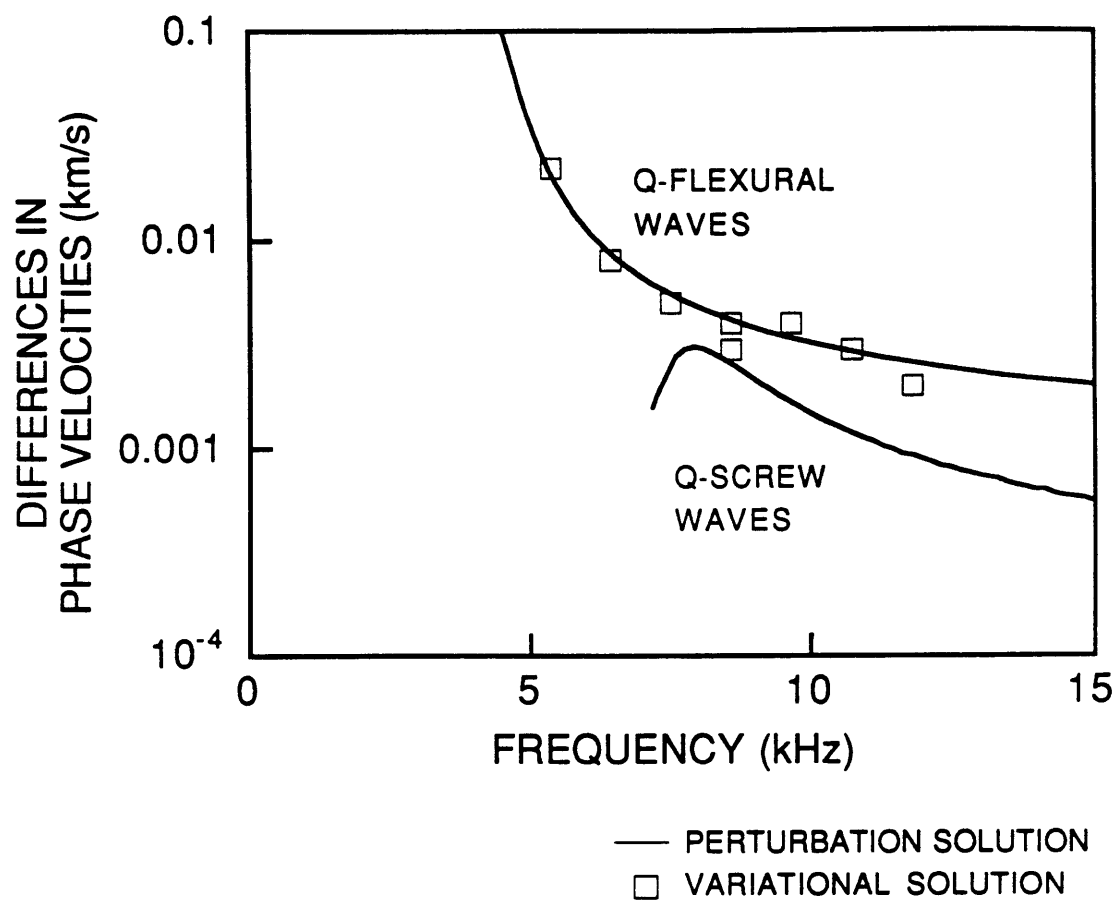


Figure 3-27: Differences between the phase velocities of the quasi-flexural waves and quasi-screw waves (Figure 3-21 and 3-22) in the transversely isotropic model (Table 3.5) when its symmetry axis is tilted 90° with respect to the borehole. (When differences less than about 0.001 km/s become inaccurate, they are not plotted.)

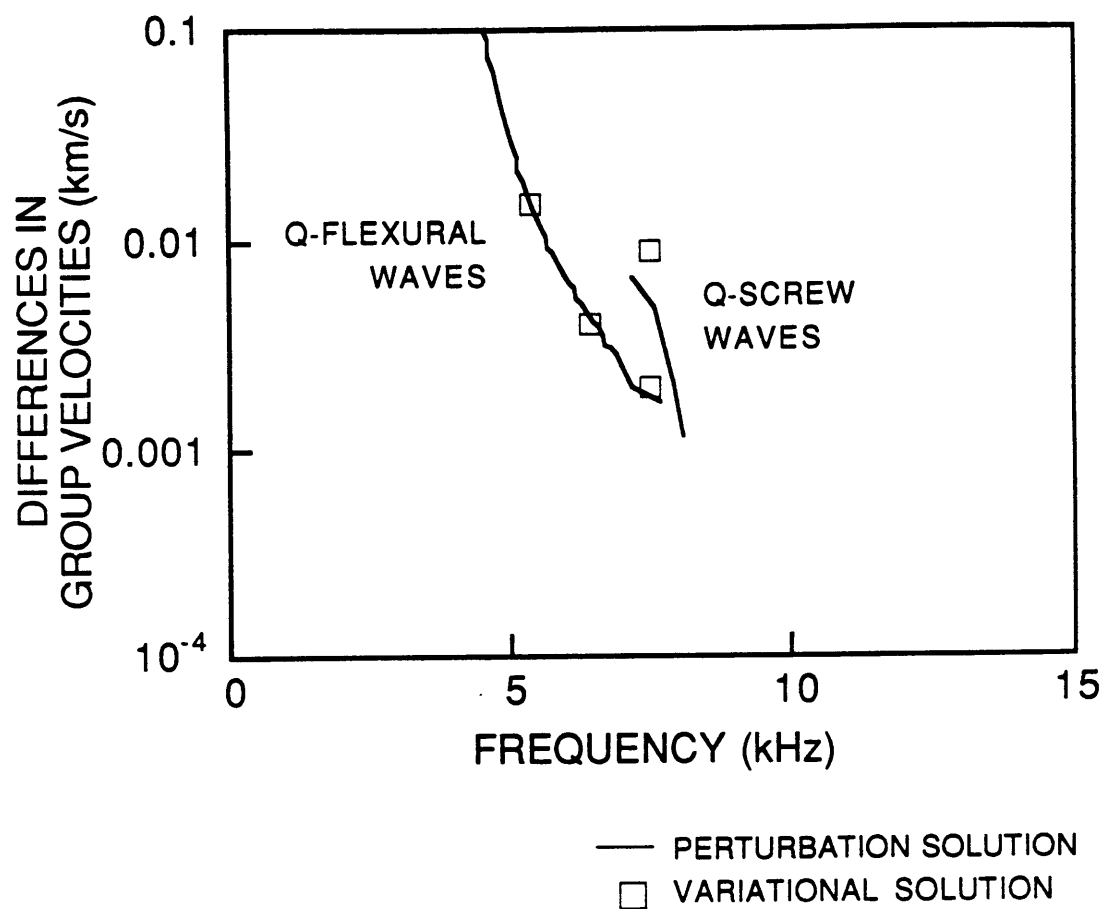


Figure 3-28: Differences between the group velocities of the quasi-flexural waves and quasi-screw waves (Figure 3-23 and 3-24) in the transversely isotropic model (Table 3.5) when its symmetry axis is tilted 90° with respect to the borehole. (When differences less than about 0.001 km/s become inaccurate, they are not plotted.)

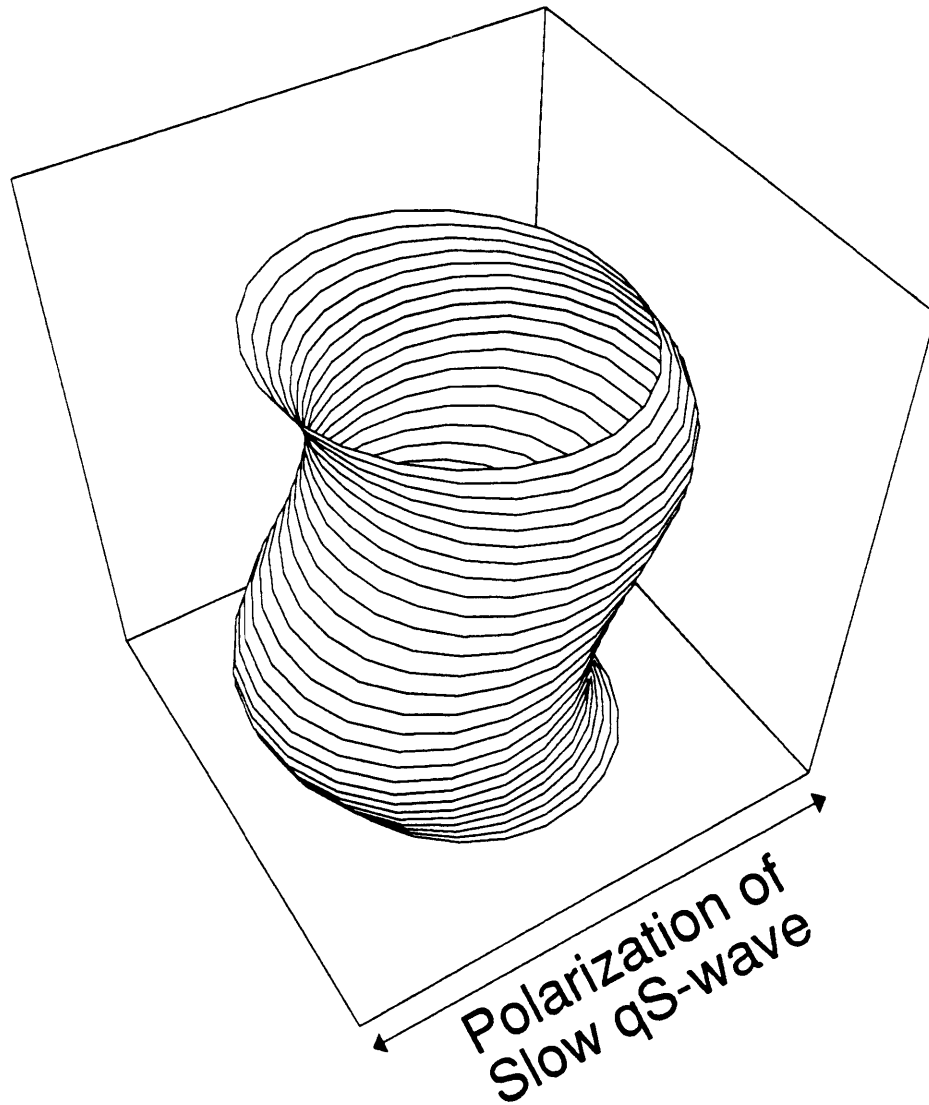


Figure 3-29: Particle displacements in the r , θ , and z directions for the slow quasi-flexural wave (# 1) at the borehole wall (in the solid and over one wavelength). These displacements were computed for the transversely isotropic model (Table 3.5) whose symmetry axis is tilted 20° . Due to the perspective, the displacements in the z direction are difficult to discern.

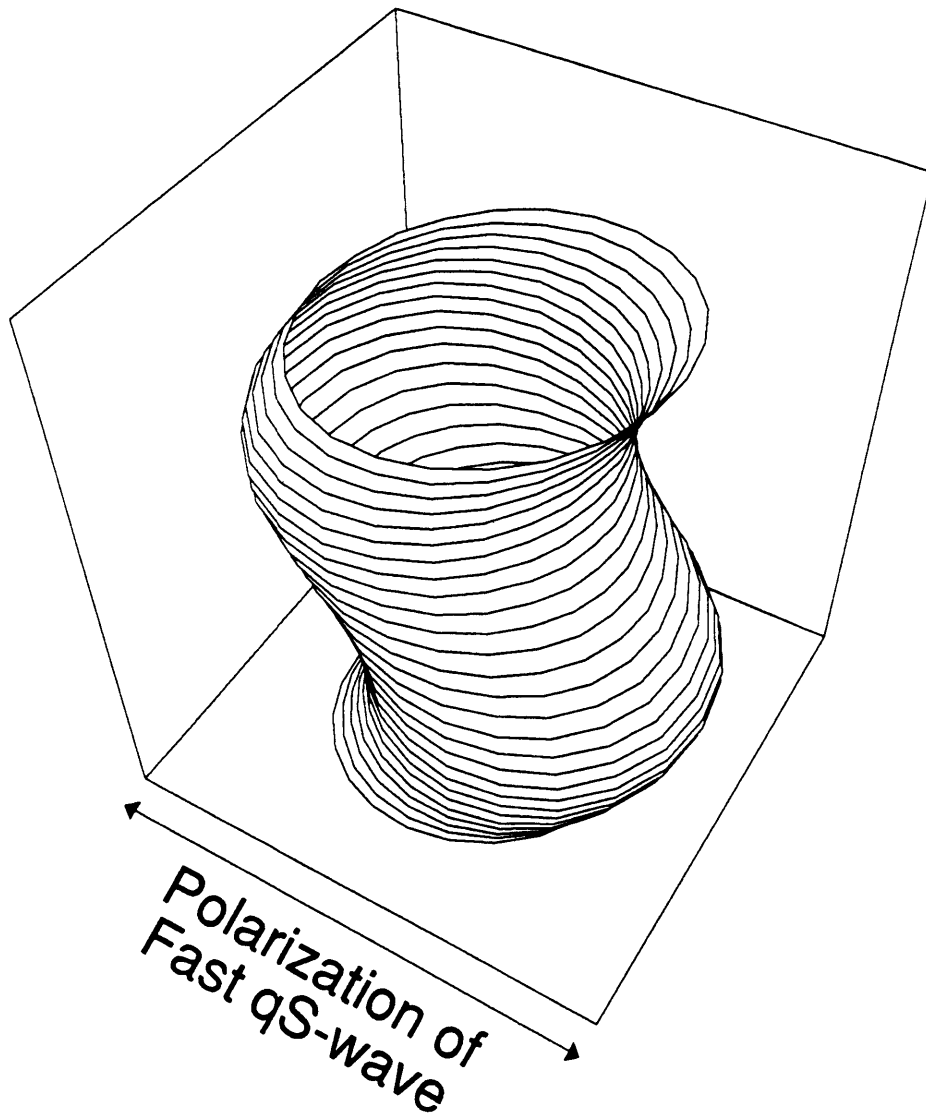


Figure 3-30: Particle displacements in the r , θ , and z directions for the fast quasi-flexural wave (# 2) at the borehole wall (in the solid and over one wavelength). These displacements were computed for the transversely isotropic model (Table 3.5) whose symmetry axis is tilted 20° . Due to the perspective, the displacements in the z direction are difficult to discern.

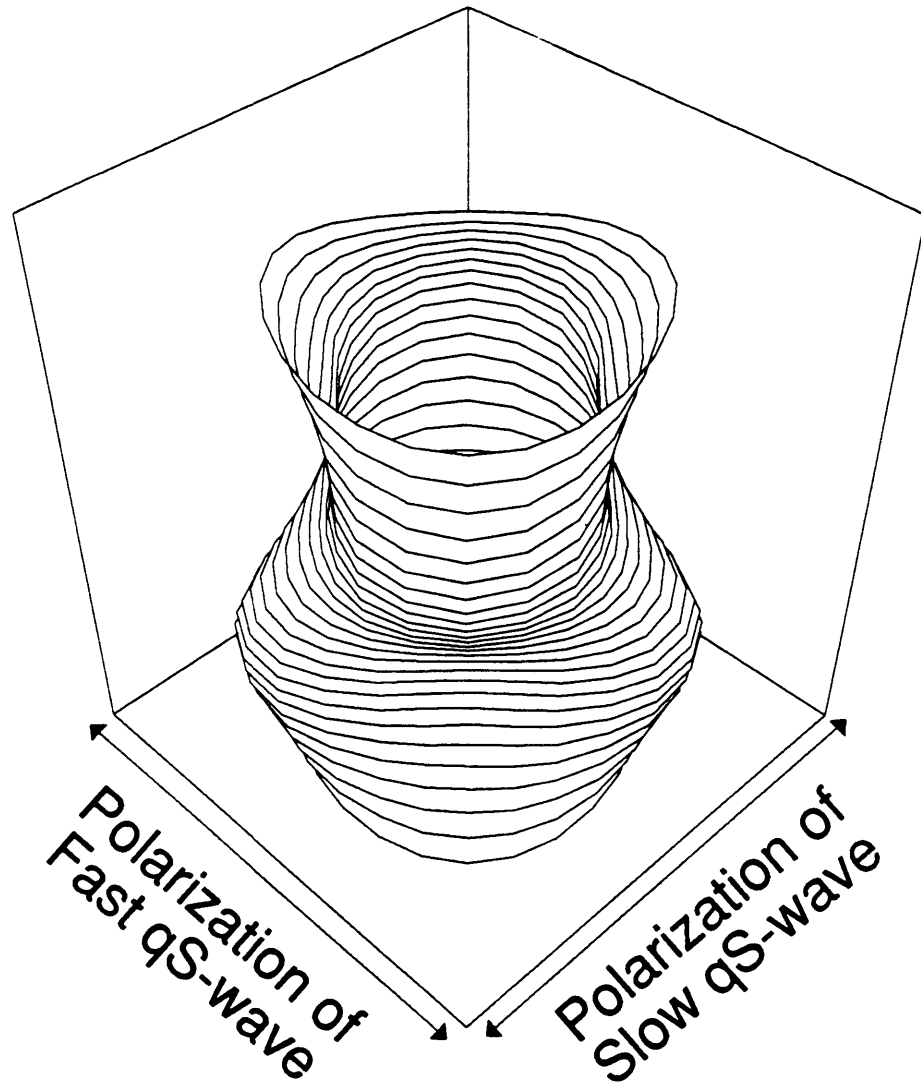


Figure 3-31: Particle displacements in the r , θ , and z directions for the slow quasi-screw wave (# 1) at the borehole wall (in the solid and over one wavelength). These displacements were computed for the transversely isotropic model (Table 3.5) whose symmetry axis is tilted 20° . Due to the perspective, the displacements in the z direction are difficult to discern.

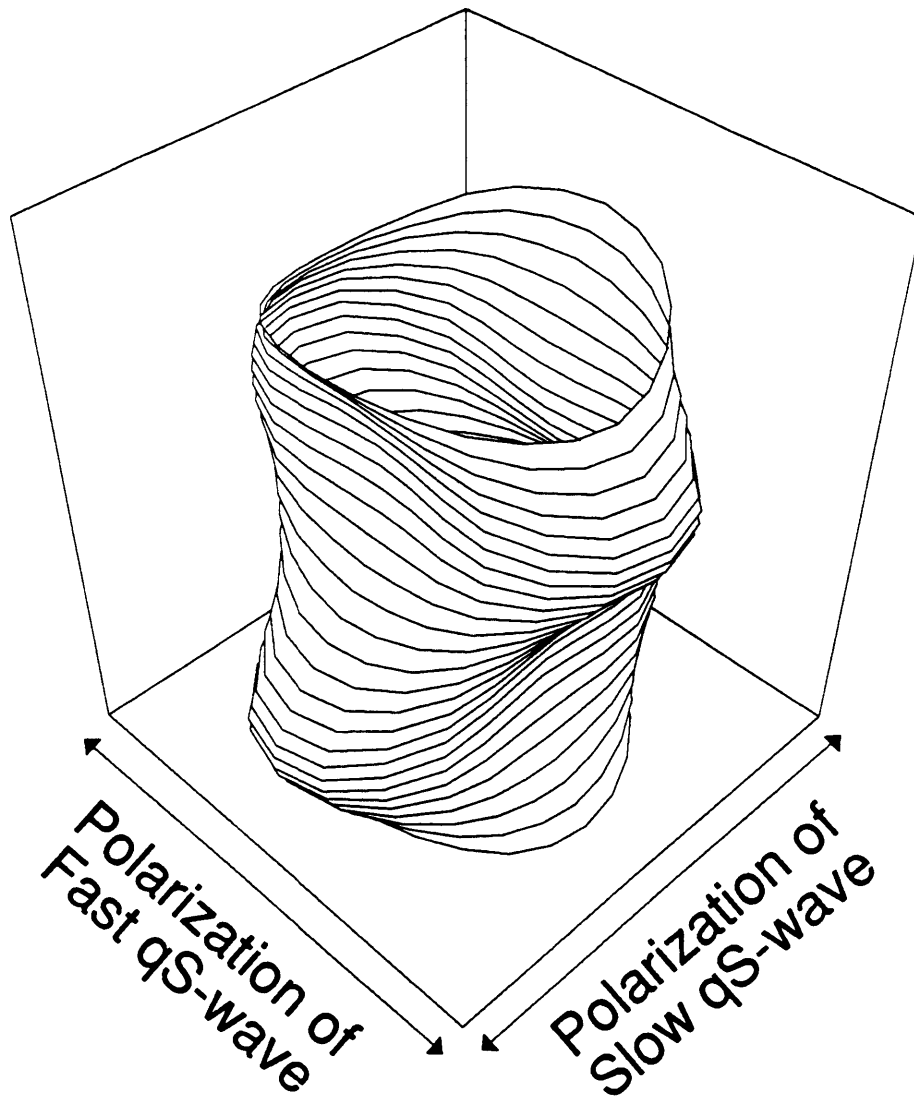


Figure 3-32: Particle displacements in the r , θ , and z directions for the fast quasi-screw wave (# 2) at the borehole wall (in the solid and over one wavelength). These displacements were computed for the transversely isotropic model (Table 3.5) whose symmetry axis is tilted 20° . Due to the perspective, the displacements in the z direction are difficult to discern.

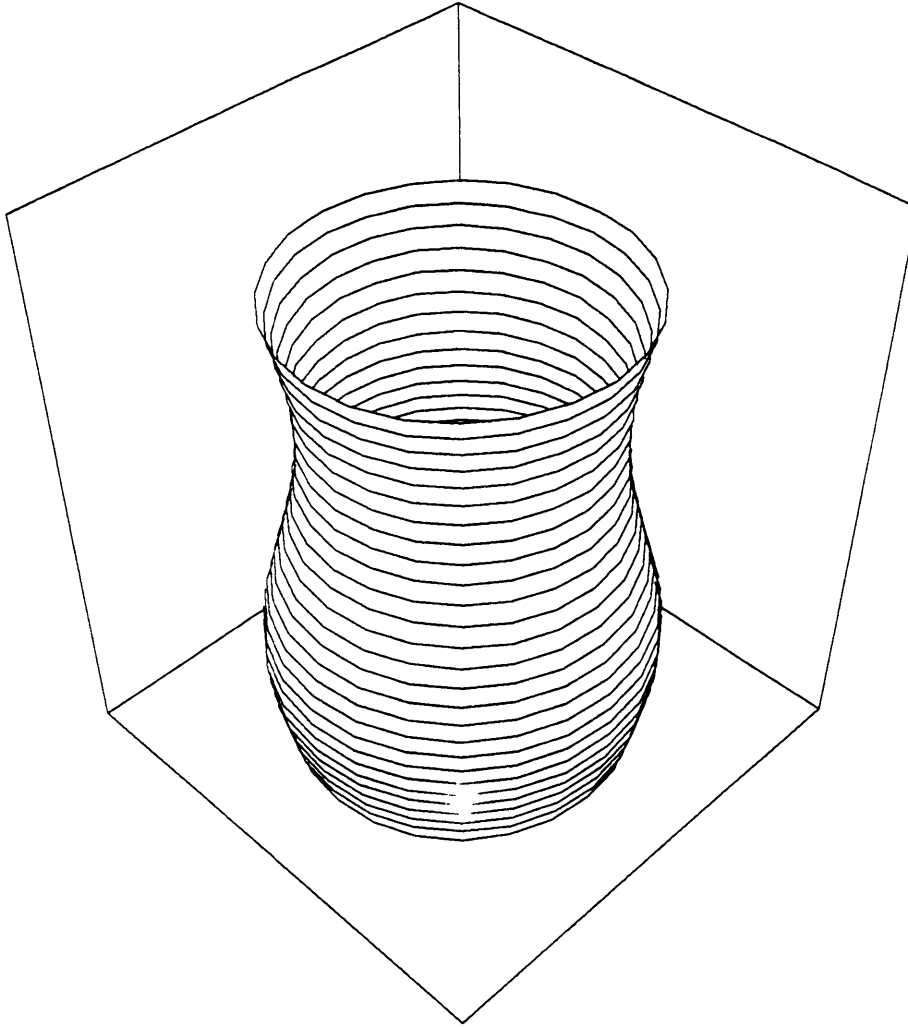


Figure 3-33: Particle displacements in the r , θ , and z directions for the quasi-tube wave at the borehole wall (in the solid and over one wavelength). These displacements were computed for the transversely isotropic model (Table 3.5) whose symmetry axis is tilted 20° . Due to the perspective, the displacements in the z direction are difficult to discern.

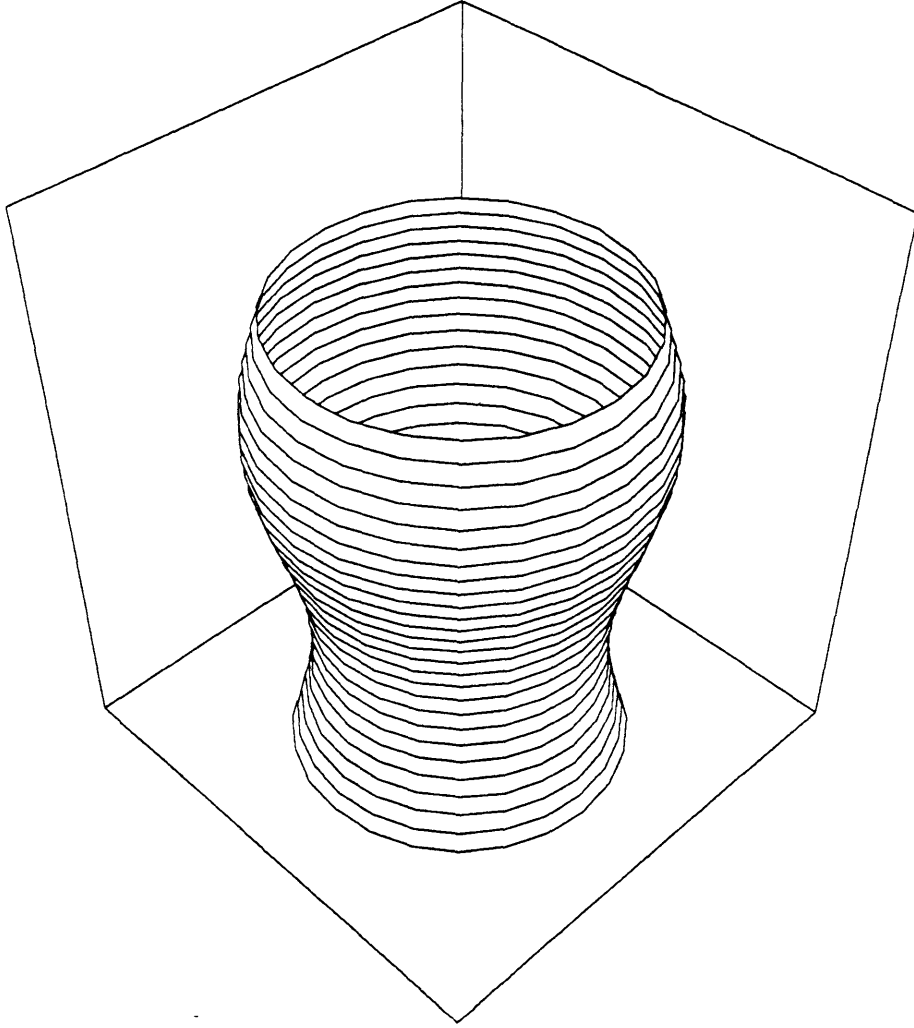


Figure 3-34: Particle displacements in the r , θ , and z directions for the quasi-pseudo-Rayleigh wave at the borehole wall (in the solid and over one wavelength). These displacements were computed for the transversely isotropic model (Table 3.5) whose symmetry axis is tilted 20° . Due to the perspective, the displacements in the z direction are difficult to discern.

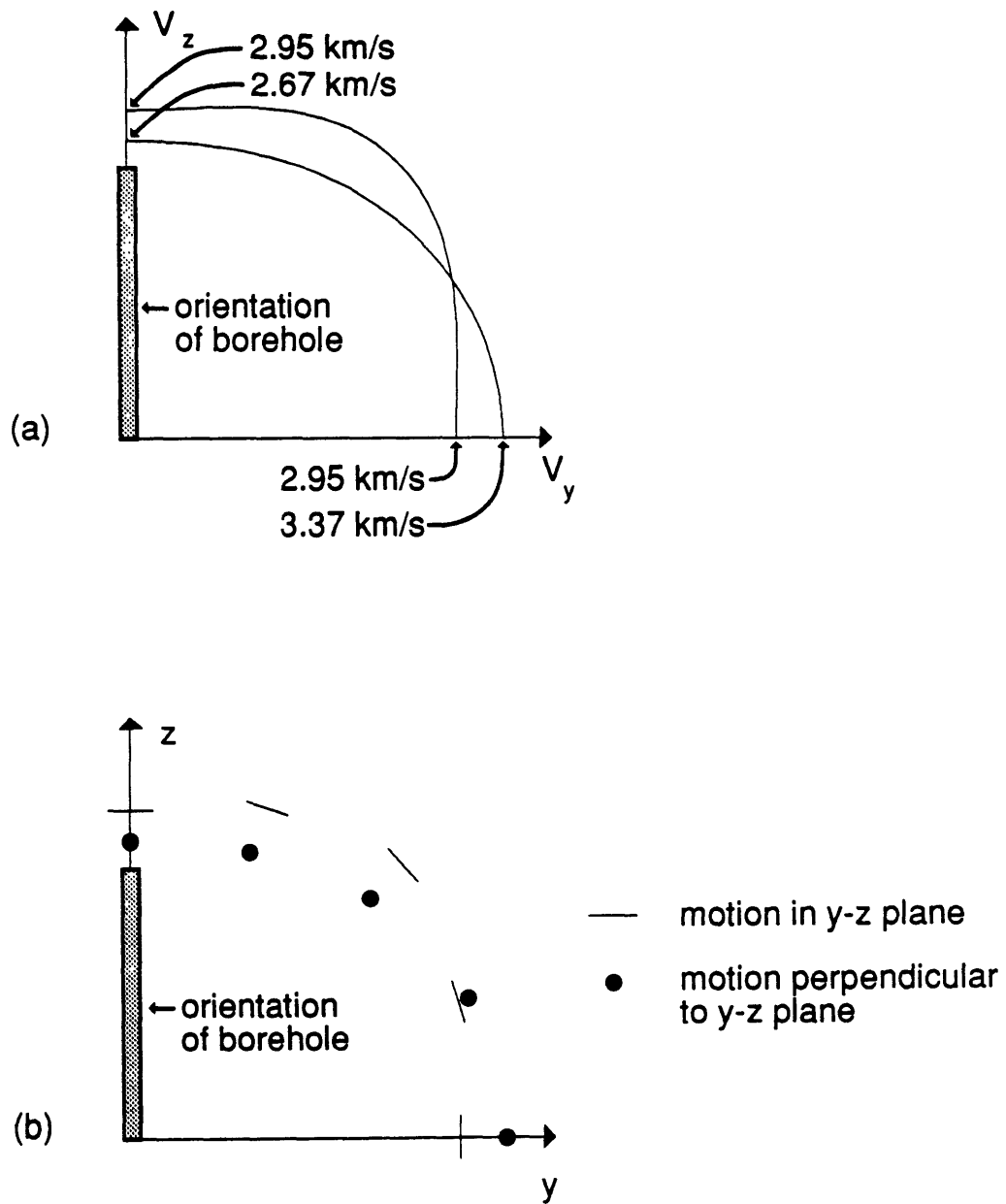


Figure 3-35: (a) Phase velocity surfaces and (b) polarizations for the qS-waves in the y - z symmetry plane of the orthorhombic model (Table 3.6).

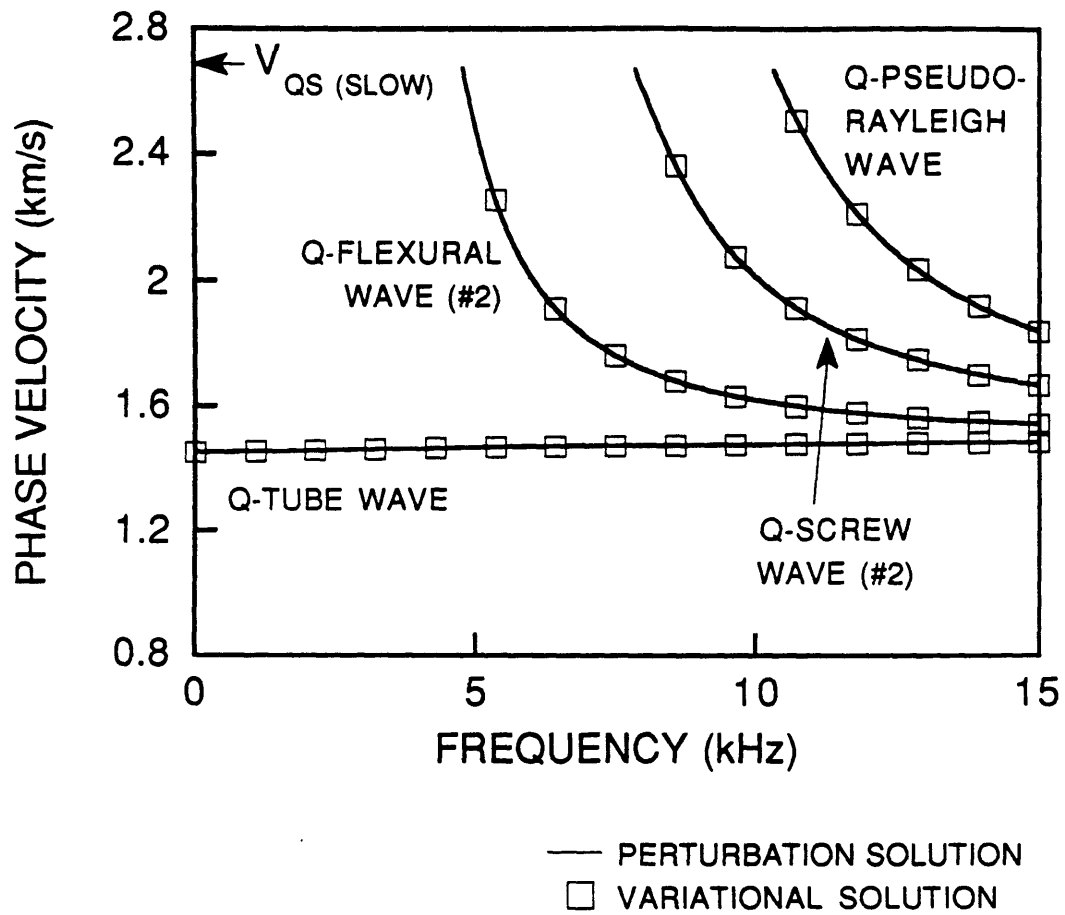


Figure 3-36: Phase velocities of the normal modes in the orthorhombic model (Table 3.6) See also Figure 3-37.

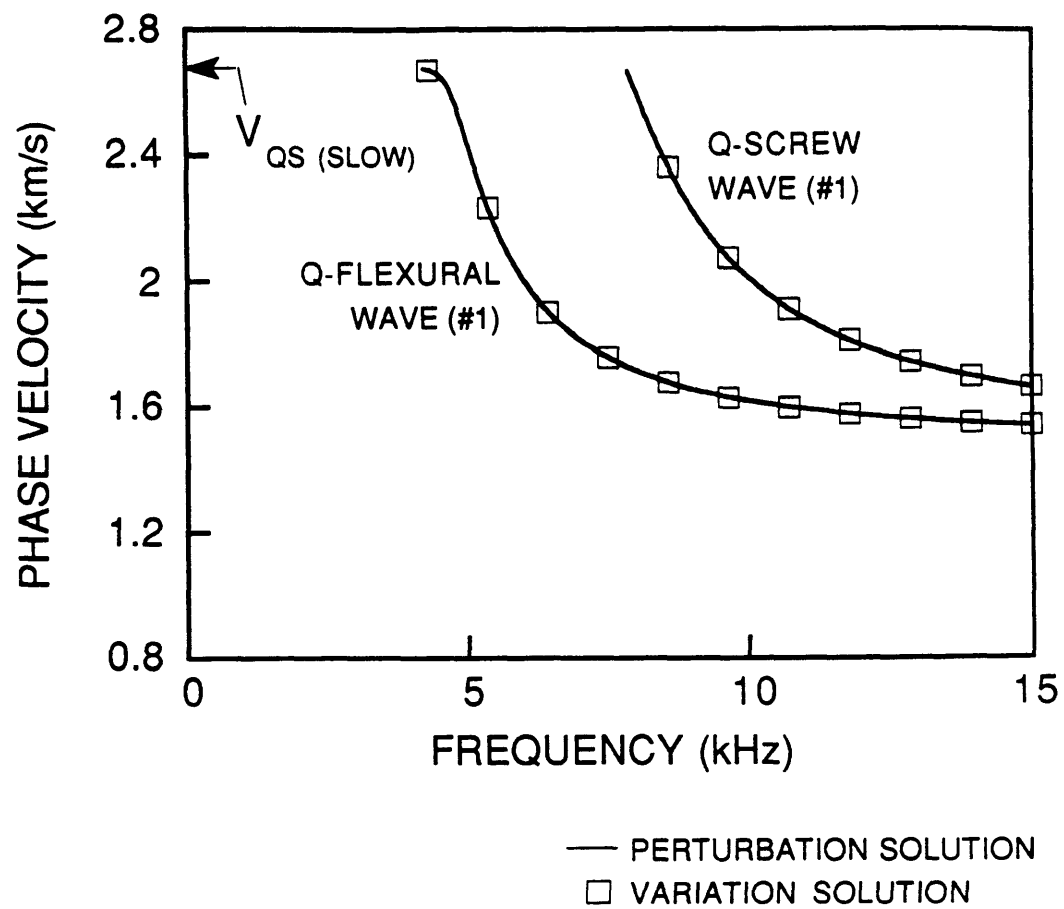


Figure 3-37: Phase velocities of the normal modes in the orthorhombic model (Table 3.6) See also Figure 3-36.

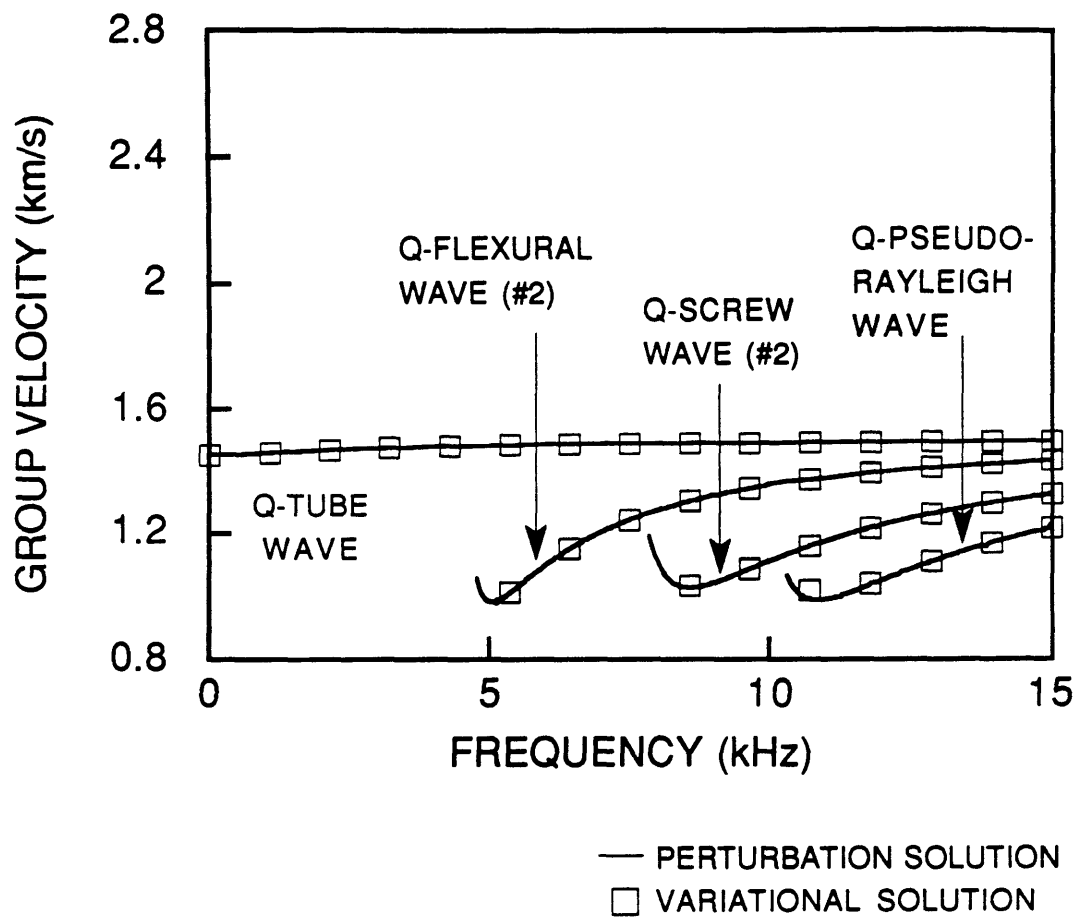


Figure 3-38: Group velocities of the normal modes in the orthorhombic model (Table 3.6). See also Figure 3-39.

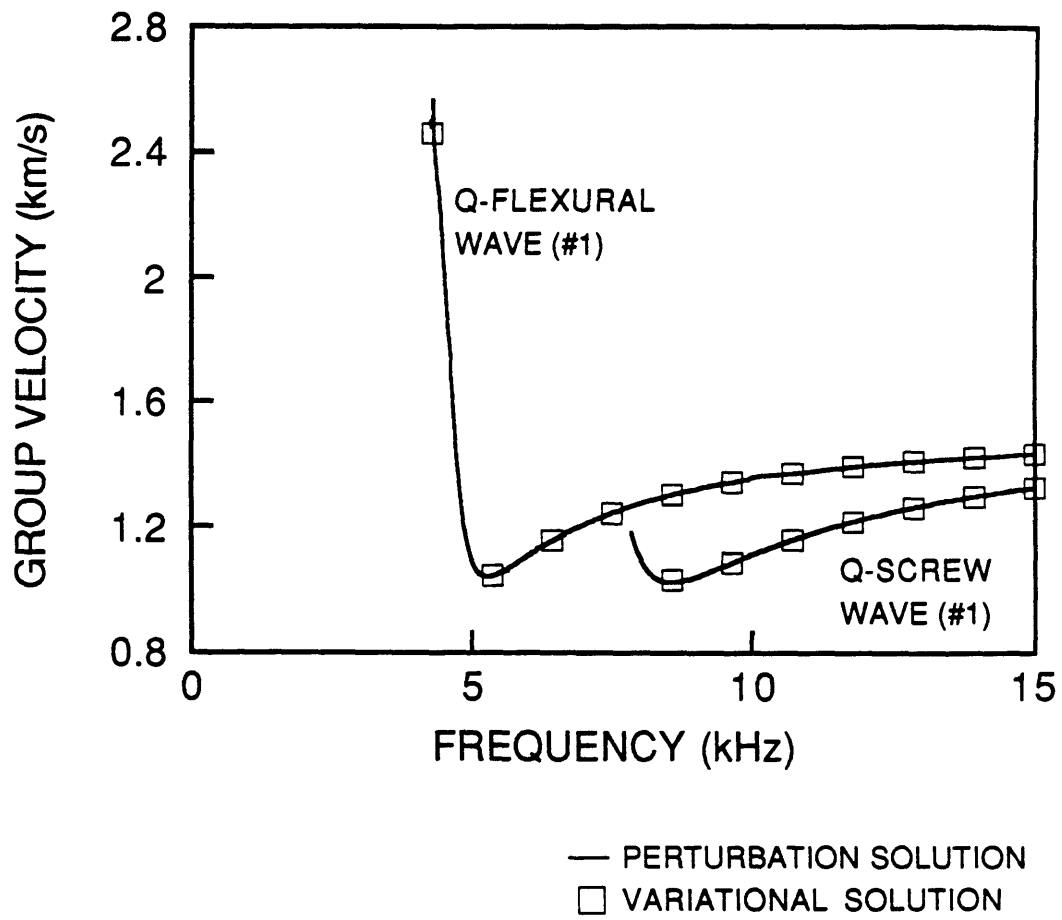


Figure 3-39: Group velocities of the normal modes in the orthorhombic model (Table 3.6). See also Figure 3-38.

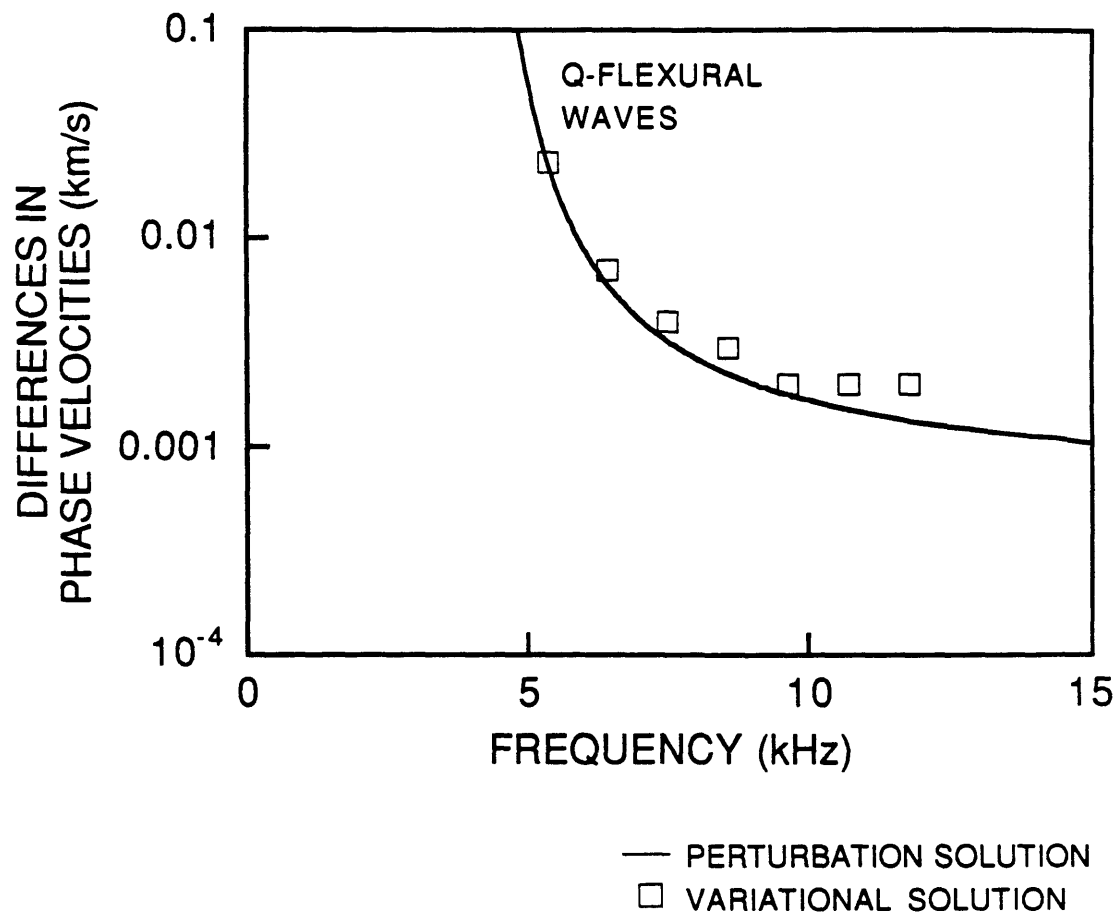


Figure 3-40: Differences between the phase velocities of the quasi-flexural waves (Figure 3-36 and 3-37) in the orthorhombic model (Table 3.6). (When differences less than about 0.001 km/s become inaccurate, they are not plotted.)

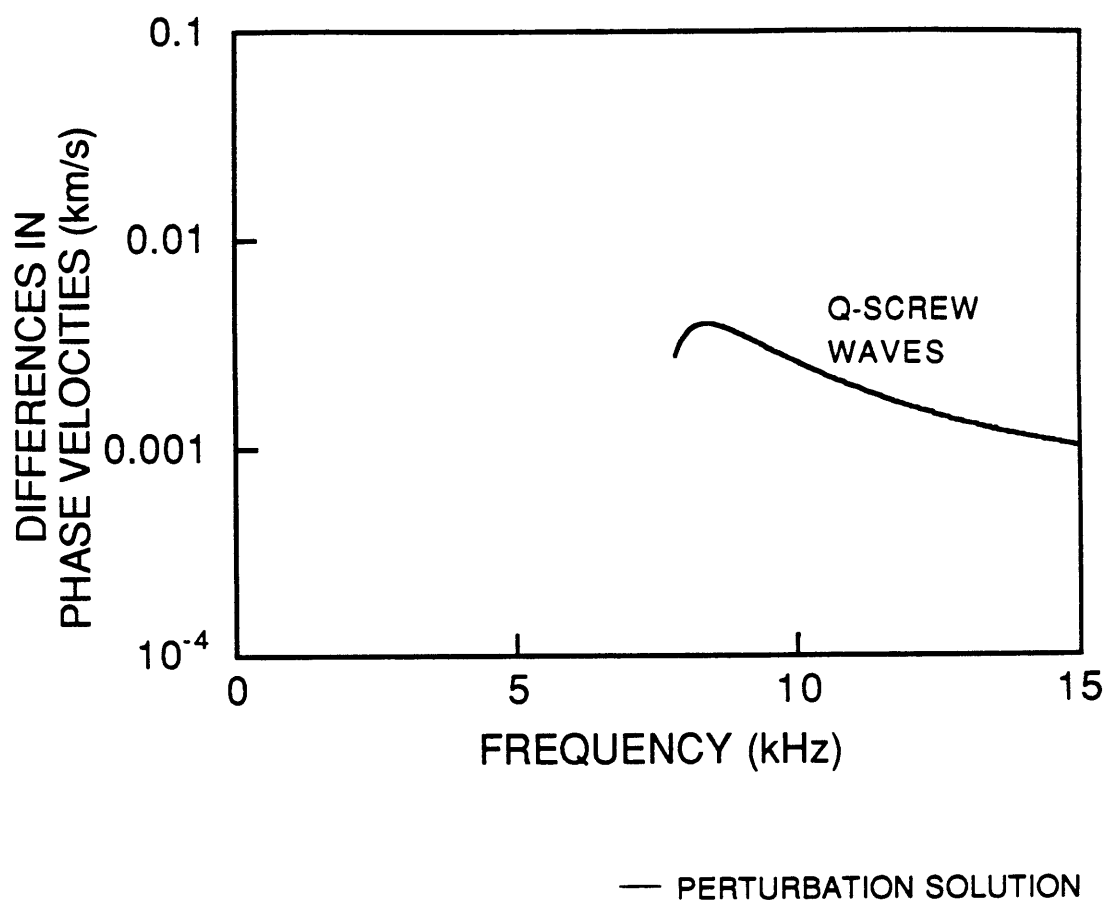


Figure 3-41: Differences between the phase velocities of the quasi-screw waves (Figures 3-36 and 3-37) in the orthorhombic model (Table 3.6). (When differences less than about 0.001 km/s become inaccurate, they are not plotted.)

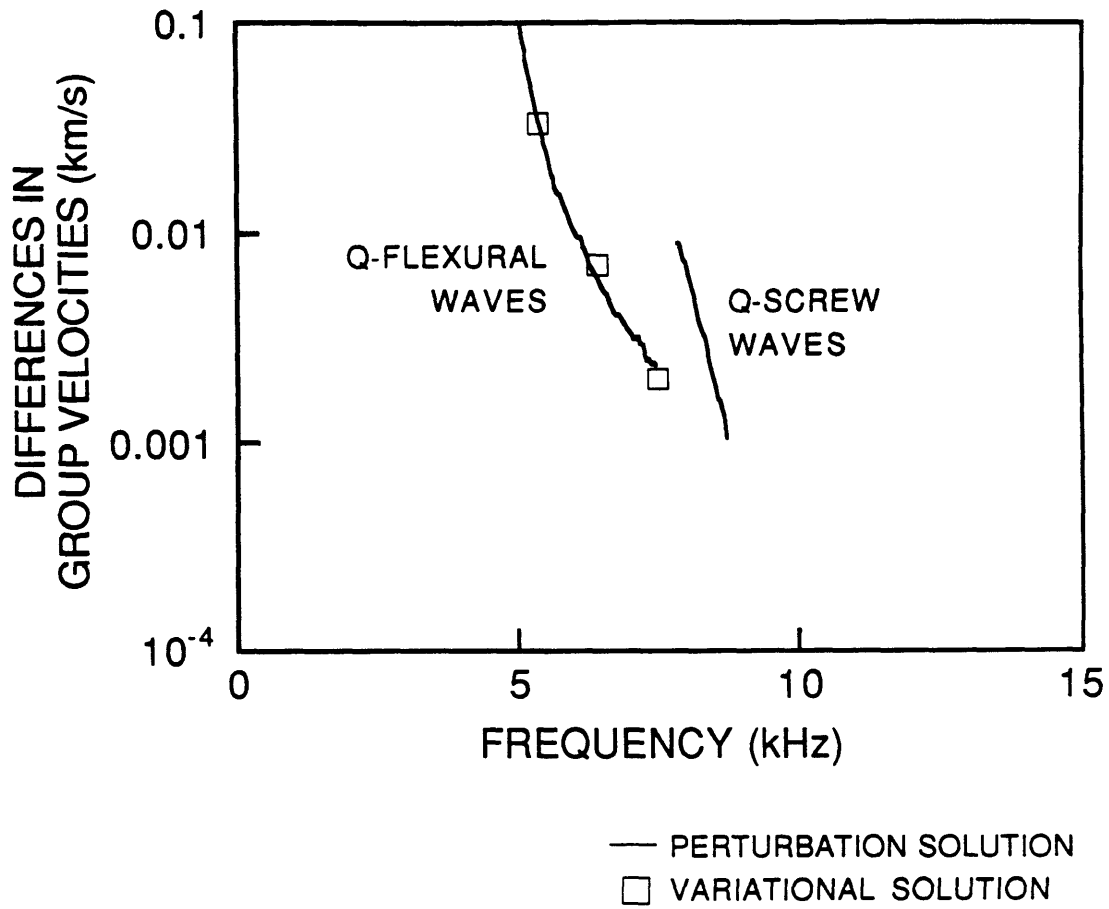


Figure 3-42: Differences between the group velocities of the quasi-flexural waves and quasi-screw waves (Figures 3-38 and 3-39) in the orthorhombic model (Table 3.6). (When differences less than about 0.001 km/s become inaccurate, they are not plotted.)

Chapter 4

Estimating a Shear Modulus of a Transversely Isotropic Formation

4.1 Introduction

In sedimentary basins, transverse isotropy with a vertical symmetry axis is the largest component of anisotropy. Field measurements indicate that in these formations the velocity of a horizontally polarized *S*-wave can be 10 to 30% higher in the horizontal direction than in the vertical direction (White et. al., 1983; Winterstein, 1986). In contrast, azimuthal variations in *S*-wave velocity generally range from 3 to 5%, and those in *P*-wave velocity are even less (S. Crampin, 1988, oral communication; D. Corrigan, 1989, oral communication; D. F. Winterstein, 1989, oral communication). In these basins, many boreholes are vertical, and consequently transverse isotropy with a symmetry axis parallel to the borehole is the largest component of anisotropy which must be considered when borehole seismic data like acoustic logging data is interpreted.

An important question in the analysis and interpretation of acoustic logging data is: can it be used to estimate the elastic properties of a transversely isotropic formation? In this situation, the velocities of the refracted *P*- and *S*-waves are $\sqrt{c_{33}/\rho}$ and

$\sqrt{c_{44}/\rho}$, respectively (White and Tongtaow, 1981; Chan and Tsang, 1983). Consequently, if the formation density is known, then the refracted waves can be used to estimate c_{33} and c_{44} . The velocity of the flexural wave is $\sqrt{c_{44}/\rho}$, and can be used to estimate c_{44} in a similar manner (Tongtaow, 1982). White and Tongtaow (1981) also developed a formula which relates the velocity of the tube wave at the zero frequency limit to c_{66} , but when data at low frequencies (i.e., less than about 200 Hz) are unavailable this formula cannot be used.

In this chapter, a method is developed to estimate c_{66} of a transversely isotropic formation (with its symmetry axis parallel to the borehole) using the wavenumbers from the tube wave. These wavenumbers are shown to be moderately sensitive to c_{66} over a wide range of frequencies for most transversely isotropic formations, and this sensitivity is the basis of the inversion. A robust procedure for the inversion is developed, and its performance is evaluated using synthetic data from fast and slow formations. Furthermore, the inversion is applied to field data to determine if the transverse isotropy of actual formations can be detected.

4.2 Method

The inversion is based upon a mathematical model of the borehole environment (Figure 4-1). The fluid is perfectly elastic, its incompressibility is λ_1 , and its density is ρ_1 . The borehole wall is perfectly round, and its radius is R . The formation is perfectly elastic and homogeneous. Because the formation is transversely isotropic with its symmetry axis parallel to the borehole, its elastic properties are specified by only five moduli: c_{11} , c_{13} , c_{33} , c_{44} , and c_{66} which are written in abbreviated subscript notation (see Chapter 1). The density of the formation is ρ_2 .

The procedure by which c_{66} is estimated is based upon a cost function that has three terms. The first term contributes information about the data, the second about the original estimate of c_{66} , and the third about the physical constraints on c_{66} . These

three terms will now be developed.

The first term in the cost function requires that the wavenumbers predicted by the forward model closely match the observed wavenumbers. Array processing of seismograms from multi-receiver tools is used to estimate the wavenumber, amplitude, attenuation, and phase of each guided wave at all frequencies (Parks et al., 1983; McClellan, 1986; Ellefsen et al., 1989). The estimated wavenumbers are arranged in a vector denoted \mathbf{d}_{obs} . Because the amplitude estimates indicate the accuracy of the wavenumber estimates, they are used to develop the data covariance matrix, \mathbf{C}_D . The matrix is diagonal because all wavenumber estimates are assumed to be independent. Wavenumbers for the current forward model are calculated with the dispersion equation (A.46). These predicted wavenumbers are arranged in a vector denoted $\mathbf{g}(m)$, where m represents the current estimate of c_{66} . In terms of probability theory, the relationship between the observed and predicted wavenumbers may be expressed by the normal density function:

$$f_D(m) = K_1 \exp \left[-\frac{1}{2}(\mathbf{d}_{obs} - \mathbf{g}(m))^T \mathbf{C}_D^{-1} (\mathbf{d}_{obs} - \mathbf{g}(m)) \right] \quad (4.1)$$

where K_1 is a normalizing constant. Maximizing the probability density function is equivalent to minimizing the negative of its exponent,

$$\frac{1}{2}(\mathbf{d}_{obs} - \mathbf{g}(m))^T \mathbf{C}_D^{-1} (\mathbf{d}_{obs} - \mathbf{g}(m)) \quad , \quad (4.2)$$

which will be the first term in the cost function.

The second term in the cost function requires that c_{66} , which is estimated during the inversion, be close to the initial estimate of its value. A cross-plot of c_{44} and c_{66} , which is based upon laboratory and field measurements of transversely isotropic rocks, indicates that when c_{44} is known the range of acceptable values for c_{66} is well defined (Figure 4-2). Consequently the cross-plot is used to estimate the most-likely value of c_{66} (which is used for the initial value of c_{66} in the inversion, m_o) and the standard deviation of c_{66} (σ_m). The relationship between m_o and the model parameter

predicted by the inversion, m , may be expressed by the normal density function:

$$f_M(m) = K_2 \exp \left[-\frac{1}{2}(m - m_o)(\sigma_M^2)^{-1}(m - m_o) \right] \quad (4.3)$$

where K_2 is a normalizing constant. Maximizing this density function is equivalent to minimizing the negative of its exponent,

$$\frac{1}{2}(m - m_o)(\sigma_M^2)^{-1}(m - m_o) \quad , \quad (4.4)$$

which will be the second term in the cost function.

The third term in the cost function requires that the elastic moduli be physically possible. The elastic strain energy density, $\frac{1}{2}e_I c_{IJ} e_J$, is always positive for any nonzero strain, e_I . Hence, the matrix of elastic moduli, c_{IJ} , must be positive definite. For a transversely isotropic medium, this requirement is met when

$$c_{11} - |c_{11} - 2c_{66}| > 0 \quad , \quad (4.5)$$

$$(c_{11} - c_{66})c_{33} - c_{13}^2 > 0 \quad , \quad (4.6)$$

and

$$c_{44} > 0 \quad (4.7)$$

(Auld, 1973, p. 147-149). Only the first two equations are needed for the inversion. They are written symbolically as $h_i(m) > 0$ (where i is an equation index) and are used to develop penalty functions,

$$\psi_i = \frac{\alpha_i}{h_i(m)} \quad , \quad (4.8)$$

where α_i is a small, positive constant (Bard, 1974, p. 141-145). The penalty functions are written in vector form as Ψ , and the inner product,

$$\Psi^T \Psi \quad , \quad (4.9)$$

is the third term in the cost function. For almost all values of c_{66} , this term is negligibly small. As c_{66} approaches the region in which either equation 4.5 or equation 4.6 is not satisfied, this term becomes very large and significantly increases the cost function.

The cost function used by the inversion combines the expressions in 4.2, 4.4, and 4.9:

$$\begin{aligned} \Phi(m) = & \frac{1}{2}(\mathbf{d}_{obs} - \mathbf{g}(m))^T \mathbf{C}_D^{-1}(\mathbf{d}_{obs} - \mathbf{g}(m)) + \\ & \frac{1}{2}(m - m_o)(\sigma_M^2)^{-1}(m - m_o) + \mathbf{\Psi}^T \mathbf{\Psi} \quad . \end{aligned} \quad (4.10)$$

This cost function is minimized with respect to m to find the best choice for c_{66} using a Levenburg-Marquardt algorithm which has been developed for nonlinear, least-squares problems (Moré, 1978; Moré et al., 1980). The Jacobian matrix, which is required for this algorithm, is calculated using the perturbation method which was developed in Chapter 2. Because the costs associated with the constraints are virtually zero for most reasonable values for c_{66} , the optimization is similar to the maximum likelihood inversion (Aki and Richards, 1980, p. 690-692).

To evaluate the estimate for c_{66} , its final standard deviation is compared to its initial standard deviation. If the deviation has been significantly reduced, then c_{66} is well resolved. The final standard deviation is the square root of the final model variance,

$$\sigma_{M'}^2 = [\mathbf{G}^T \mathbf{C}_D^{-1} \mathbf{G} + (\sigma_M^2)^{-1}]^{-1} \quad (4.11)$$

(Tarantola, 1987, p. 196-198) where $G_{ij} = \partial g_i / \partial m_j$. This formula is only approximate because the problem is nonlinear.

4.3 Results and Discussion

4.3.1 Sensitivity of the Data to the Elastic Moduli

To properly perform an inversion, the sensitivity of the wavenumbers to the different elastic moduli must be determined. This sensitivity can be expressed quantitatively with the normalized partial derivative of the wavenumber with respect to an elastic modulus of the formation, c_{IJ}^{TI} :

$$\frac{c_{IJ}^{TI}}{k_z} \frac{\partial k_z}{\partial c_{IJ}^{TI}} \quad .$$

Similarly, the sensitivity associated with the incompressibility of the fluid is

$$\frac{\lambda_1}{k_z} \frac{\partial k_z}{\partial \lambda_1} \quad .$$

The sensitivities were calculated for the normal modes in fast, slow, and very slow formations (Tables 4.1, 4.2, and 4.3) using the perturbation method described in Chapter 2. In Appendix E, the sensitivities of all normal modes are examined to demonstrate that the best data for estimating c_{66} come from the low frequency portion of the tube wave. The sensitivities for this part of the tube wave will be discussed here in the context of the inversion.

In many respects, the sensitivities for the fast and slow formations (Figures 4-3, 4-4, 4-5, and 4-6) are similar. The wavenumbers are more sensitive to λ_1 than they are to c_{66} , and therefore λ_1 must be accurately known before c_{66} can be estimated. The wavenumbers are insensitive to c_{11} and c_{13} , and consequently using any reasonable value for these unknown moduli will not adversely affect the inversion. Because the data are insensitive to c_{33} and only moderately sensitive to c_{44} near 5 kHz, inaccurate values for these moduli, which are determined from the refracted waves and the flexural wave, will not affect the estimate of c_{66} much.

The sensitivities for the non-leaky tube wave in the very slow formation (Figures 4-7 and 4-8) are very different from those in the previous two examples. In general, the wavenumbers are very sensitive to c_{44} , moderately sensitive to c_{11} , c_{13} , c_{33} , and c_{66} , and insensitive to λ_1 . Because the sensitivities for c_{11} and c_{13} are roughly equal to that for c_{66} and because c_{11} and c_{13} are unknown, c_{66} cannot be estimated.

An important issue is knowing when c_{66} can be reliably estimated. To this end, examine the sensitivities for the fast, slow, and very slow formations (Figures 4-3, 4-5, 4-7, and Figures 4-4, 4-6, 4-8 in these orders). The sensitivities for λ_1 generally decrease, and the sensitivities for c_{11} , c_{13} , c_{33} , and c_{44} increase. The sensitivity of c_{66} does not change as much between the three formations as the sensitivities of the other moduli do. To accurately estimate c_{66} , the sensitivities for c_{11} and c_{13} , which are not precisely known, must be small compared to the sensitivity of c_{66} . As a rule

of thumb, this situation occurs when the velocity of the vertically propagating S -wave is greater than or approximately equal to the acoustic velocity of the fluid.

4.3.2 Testing the Inversion with Synthetic Data

The inversion for c_{66} was tested first with synthetic data calculated for the model with the fast formation (Table 4.1). Synthetic seismograms (Figure 4-9) were processed to extract the wavenumber and amplitude estimates for the tube wave (Figures 4-10 and 4-11). Then values for the elastic moduli of the formation were selected. Values for c_{33} and c_{44} were determined from the refracted P - and S -waves, respectively. (Although the refracted P -wave is not evident in Figure 4-9, it can be seen if the amplitudes are increased.) Values for c_{11} and c_{13} were determined from cross-plots of the elastic moduli of transversely isotropic rocks (Figures 4-12 and 4-13). The starting value for c_{66} and its standard deviation, 0.35×10^{10} Pa, were estimated from the cross-plot with c_{44} (Figure 4-2). The formation density, fluid density, fluid incompressibility, and borehole radius were set to their correct values because they can be measured in field situations. All of the model parameters used in the inversion are summarized in Table 4.1. Only data below 4 kHz were used because at higher frequencies the data become slightly sensitive to c_{44} which is never exactly known. For this inversion, the cost function is dominated by the term associated with the data (Figure 4-14) indicating that the estimated value for c_{66} depends almost entirely upon the data and not upon the initial estimate of its value or the constraints. The cost surface (Figure 4-15) has no local minima over the range of values which c_{66} might have, and hence convergence to the global minimum is guaranteed. The estimated value for c_{66} is 0.92×10^{10} Pa which differs from the correct value by only 0.04×10^{10} Pa. c_{66} is moderately well resolved: the final standard deviation is 0.29×10^{10} Pa, which is smaller than the initial standard deviation (0.35×10^{10} Pa).

Then the inversion was tested with synthetic data calculated for the model with the slow formation (Table 4.2). The generation of synthetic seismograms, array pro-

cessing, and inversion followed the same procedures used the fast formation. The model parameters for the inversion are listed in Table 4.2. The standard deviation was estimated from Figure 4-2 to be 0.35×10^{10} Pa. Because the cost function is dominated by the term associated with the data (Figure 4-16), the estimated value for c_{66} depends upon the data and not on the initial estimate or the constraints. Because the cost surface has no local minima (Figure 4-17), convergence to a global minimum is guaranteed. The estimated value for c_{66} is 1.10×10^{10} Pa which differs from the correct value by 0.05×10^{10} Pa. Again c_{66} is moderately well resolved because the standard deviation was reduced from 0.35×10^{10} Pa to 0.18×10^{10} Pa

For both inversions, the exact value of c_{66} was not estimated. This inaccuracy may be due to errors introduced into the inversion by the approximate values which were chosen for c_{11} , c_{13} , c_{33} , and c_{44} (Tables 4.1 and 4.2). Nonetheless, each estimated value for c_{66} is within 5% of its correct value.

4.3.3 Field Data

The inversion was applied to field data to determine if it could detect the anisotropy in actual formations. The acoustic logging tool had 12 receivers which were spaced 0.152 m apart and 2 sources. Therefore, two sets of 12 seismograms were recorded at each depth. In addition to the acoustic logging data, shear wave logs, gamma ray logs, induction logs, etc. were recorded and were very valuable in performing the inversion. Drill cores from several zones in the well were brought to the surface, and the permeabilities of the cores were measured.

To determine the incompressibility of the fluid, seismograms from a zone with a very slow formation (Figure 4-18) were processed to calculate the phase velocities of the leaky P -wave (Figure 4-19). These phase velocities asymptotically approach the acoustic velocity of the fluid. Judging from this dispersion curve, the acoustic velocity of the fluid is approximately 1.54 km/s. Because the fluid density is 1.10×10^3 kg/m³, the fluid incompressibility is approximately 0.261×10^{10} Pa.

Because the logging tool affects the tube wave, the inversion must be modified. The most direct method of accounting for its effects is to develop a new mathematical model and then derive a new dispersion equation. The tool near the receivers consists a steel cable, 12 transducers mounted on the cable, a layer of oil which surrounds the cable and the transducers, and a rubber housing. Incorporating these features in the mathematical model would be difficult, and the resulting dispersion equation would be complicated. An alternative method of accounting for the tool is based on the fact that at low frequencies the tool causes a uniform shift in the phase velocities of the tube wave (Cheng and Toksöz, 1981). An equivalent result could be obtained by scaling the wavenumbers. The results of some numerical experiments indicated that the errors introduced by this scaling are very small. The main advantages of this method are that it is simple and that the original mathematical model and dispersion equation can be used.

To determine the best scaling, a two-step process was used. First, wavenumbers were calculated by processing seismograms from a formation which had low permeability (i.e., 26 to 33 mD) and low gamma ray emissions (i.e., 75 to 95 GAPI units). Low permeability (i.e., less than about 100 mD) is important because permeability can affect the velocity dispersion of the tube wave (Cheng et al., 1987). The low emissions indicate that few clay minerals are present, and because these minerals are a major cause of transverse isotropy their small concentration suggests that the formation is mostly isotropic. Second, several inversions for c_{66} were performed using different scaling factors for the wavenumbers. Because the formation is assumed to be isotropic, c_{66} must match c_{44} , and the scaling factor that gave this result is 0.94.

The field logs were used to find a zone where c_{66} could be accurately estimated. In the selected zone, the borehole wall is smooth (Figure 4-20), which reduces the scattering of the waves and makes the processing results more accurate. The difference between the drill bit size and the measured diameter is small indicating that shale hydration is not a severe problem. Between 230 and 258 m, the gamma ray emission

is high (Figure 4-21) due to the radioactive decay of thorium (Figure 4-22) but not uranium (Figure 4-22) or potassium (Figure 4-23). These measurements indicate that the rock contains many clay minerals and consequently may be transversely isotropic. The vertical S -wave velocity is high (Figure 4-24) indicating that (if the formation is transversely isotropic) the tube wave will be more sensitive to c_{66} than the other elastic moduli. The density corrections are small (Figure 4-25) indicating that the density measurements are reliable. The permeability of the rock ranges from 0.1 to 10^4 mD (Figure 4-26) and will have a significant effect upon the accuracy of the estimates for c_{66} . The acoustic logging data show no reflections (Figure 4-27) indicating that the elastic properties of contiguous beds are similar and that large fractures are not present.

Between 225 and 246 m, the wavenumbers for the tube wave were calculated by combining the data from both sources. That is, the wavenumbers were calculated from 2 data sets, each of which contained 12 seismograms from the 12 receivers. A few inaccurate wavenumber estimates were obtained, and these were deleted before the inversion was performed. The model parameters (i.e., c_{11} , c_{13} , c_{33} , c_{44} , a starting value for c_{66} , σ_M , ρ_2 , and R) were determined from the logs (Figures 4-20, 4-24, and 4-25) and cross plots (Figures 4-2, 4-12 and 4-13). c_{66} was determined at 133 depths (Figure 4-28). These estimates are an average of the actual values of c_{66} over the distance spanned by the receiving array of the acoustic logging tool. That is, each estimate is obtained from the data recorded by the 12 receivers which span 1.68 m. Because the actual value of c_{66} probably changes over this interval, the estimated value is just an average. In general, between successive depths the estimates change only slightly because the logging tool only moves one-twelfth of the length of the array. That is, the intervals spanned by the receiving array between successive depths overlap by 1.52 m, and therefore the estimated values for c_{66} should be nearly equal. A few values for c_{66} are anomalous and are caused by inaccurate wavenumber estimates.

Above 235 m and below 244 m, most estimates for c_{66} are much lower than the

corresponding values for c_{44} . This property is not common of transversely isotropic rocks (see Thomsen, 1986). A possible cause of this unusual result is the high permeabilities (i.e. from 350 mD to greater than 10^4 mD) (Figure 4-26) which decrease the phase velocity of the tube wave from what it would be if the permeabilities were much lower. Because the borehole model does not account for this effect, the inversion selects low values of c_{66} to match the data.

Between 235 and 244 m, all estimates for c_{66} (except a few outliers) are higher than the corresponding values for c_{44} , and this property is typical of transversely isotropic rocks (see Thomsen, 1986). In this zone the tube wave velocity is virtually unaffected by the permeability because it is low (i.e., less than 110 mD) (Figure 4-26). The values of c_{44} and c_{66} are correlated: high or low values of c_{66} are associated with high or low values of c_{44} , respectively. Another way of studying the anisotropy is to examine the percent difference between the velocities of horizontally propagating S -waves with horizontal and vertical polarizations (v_{SH} and v_{SV} , respectively):

$$\frac{v_{SH} - v_{SV}}{v_{SV}} \times 100\%$$

which is called the S -wave anisotropy. To compute a useful log based upon this quantity, the anomalous values of c_{66} were deleted, the percentage was computed at each depth, and the results were smoothed to remove spurious values. The log (Figure 4-29) shows that the S -wave anisotropy ranges from 5 to 20%.

4.4 Conclusions

Sensitivities, which are normalized partial derivatives, indicate how the wavenumbers for the tube wave are affected by the elastic moduli of the fluid and the formation. At low frequencies the wavenumbers for the tube wave in fast and slow formations are very sensitive to λ_1 and moderately sensitive to c_{66} . Therefore, an accurate value for λ_1 must be obtained before a value for c_{66} is estimated. The wavenumbers are insensitive to c_{11} , c_{13} , c_{33} at all frequencies, and are only moderately sensitive to

c_{44} near 5 kHz. Consequently, the inversion for c_{66} will not be adversely affected if slightly inaccurate values for these moduli are picked. In very slow formations, the wavenumbers for the tube wave are as sensitive to the unknown moduli, c_{11} and c_{13} as they are to c_{66} . Hence c_{66} cannot be estimated for very slow formations. A useful rule of thumb is that c_{66} should be estimated only when the vertical S -wave velocity is greater than or nearly equal to the acoustic velocity of the fluid.

The inversion for c_{66} is based upon a cost function which combines information about the wavenumbers, the expected values for c_{66} , and the physical constraints on its value. The cost function is minimized using a robust method. When the inversion was applied to synthetic data from fast and slow formations, the estimates for c_{66} were within 5% of their correct values and were moderately well resolved. When the inversion was applied to field data, the estimates for c_{66} were significantly higher than the values for c_{44} in the zone with low permeability and high clay content. The percentage of S -wave anisotropy ranged from 5 to 20%.

Quantity	Value	Value used for Inversion
c_{11}	3.126×10^{10} Pa	3.0×10^{10} Pa
c_{13}	0.345×10^{10} Pa	1.1×10^{10} Pa
c_{33}	2.249×10^{10} Pa	2.1×10^{10} Pa
c_{44}	0.649×10^{10} Pa	0.64×10^{10} Pa
c_{66}	0.882×10^{10} Pa	1.0×10^{10} Pa
ρ_2	2075. kg/m ³	2075. kg/m ³
λ_1	0.225×10^{10} Pa	0.225×10^{10} Pa
ρ_1	1000. kg/m ³	1000. kg/m ³
R	0.1016 m	0.1016 m

Table 4.1: Parameters for the borehole model with a fast formation representing the Green River shale (Thomsen, 1986) and the parameters used in the inversion.

Quantity	Value	Value used for Inversion
c_{11}	3.395×10^{10} Pa	3.0×10^{10} Pa
c_{13}	1.058×10^{10} Pa	1.2×10^{10} Pa
c_{33}	2.248×10^{10} Pa	2.2×10^{10} Pa
c_{44}	0.537×10^{10} Pa	0.51×10^{10} Pa
c_{66}	1.053×10^{10} Pa	0.70×10^{10} Pa
ρ_2	2420. kg/m ³	2420. kg/m ³
λ_1	0.225×10^{10} Pa	0.225×10^{10} Pa
ρ_1	1000. kg/m ³	1000. kg/m ³
R	0.1016 m	0.1016 m

Table 4.2: Parameters for the borehole model with a slow formation representing shale (5000) (Thomsen, 1986) and the parameters used in the inversion.

Quantity	Value
c_{11}	$1.387 \times 10^{10} \text{ Pa}$
c_{13}	$0.803 \times 10^{10} \text{ Pa}$
c_{33}	$0.998 \times 10^{10} \text{ Pa}$
c_{44}	$0.177 \times 10^{10} \text{ Pa}$
c_{66}	$0.283 \times 10^{10} \text{ Pa}$
ρ_2	$2250. \text{ kg/m}^3$
λ_1	$0.225 \times 10^{10} \text{ Pa}$
ρ_1	$1000. \text{ kg/m}^3$
R	0.1016 m

Table 4.3: Parameters for the borehole model with a very slow formation representing the Pierre shale (Thomsen, 1986).

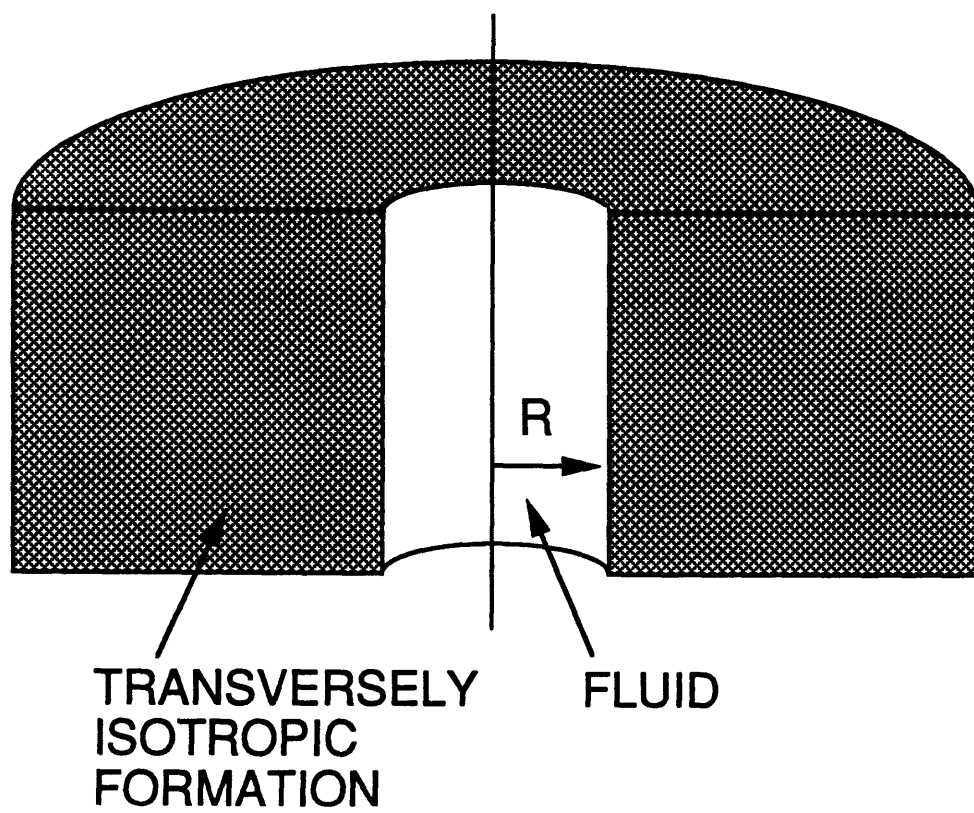


Figure 4-1: Mathematical model used for the inversion.

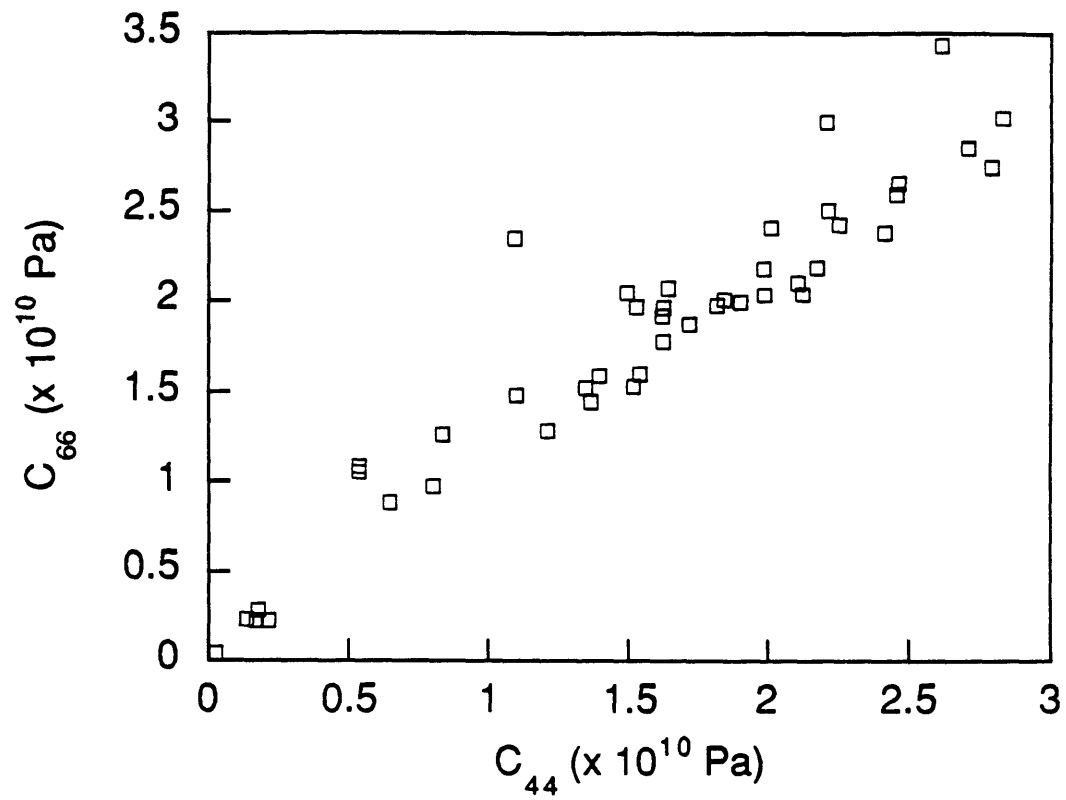


Figure 4-2: Cross-plot used to determine the most-likely value of c_{66} and its standard deviation. The data are from the list of elastic moduli of transversely isotropic rocks compiled by Thomsen (1986).

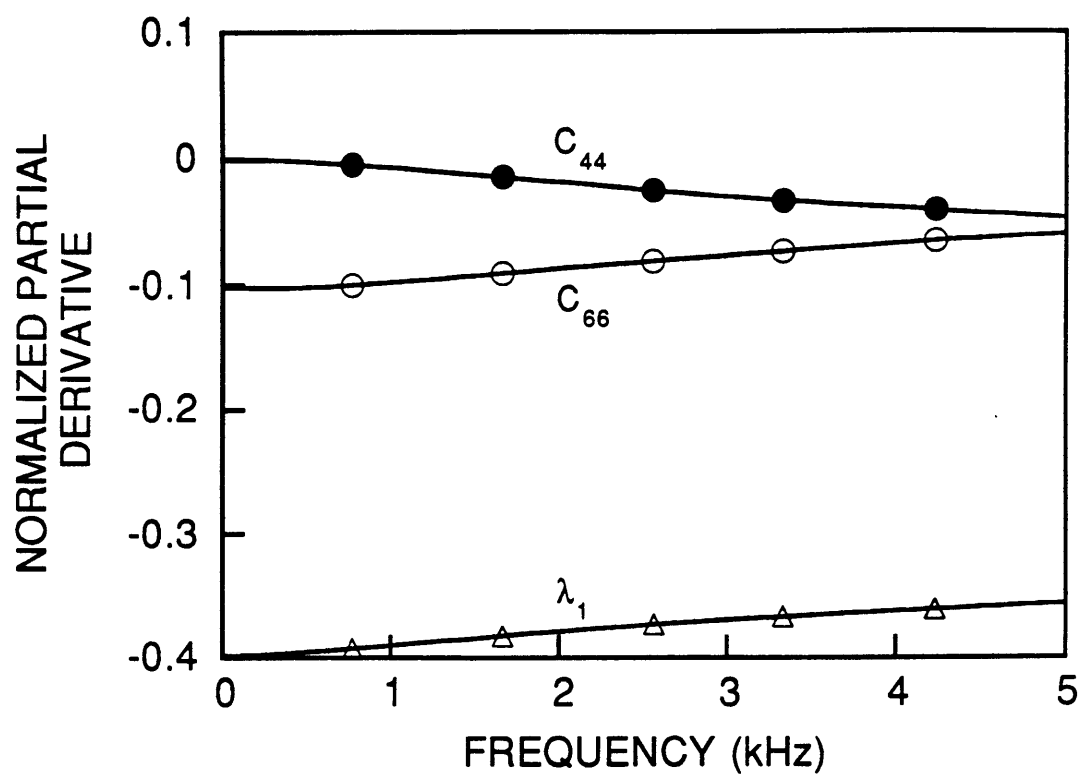


Figure 4-3: Sensitivities for the tube wave in the model with the fast formation (Table 4.1). See also Figure 4-4.

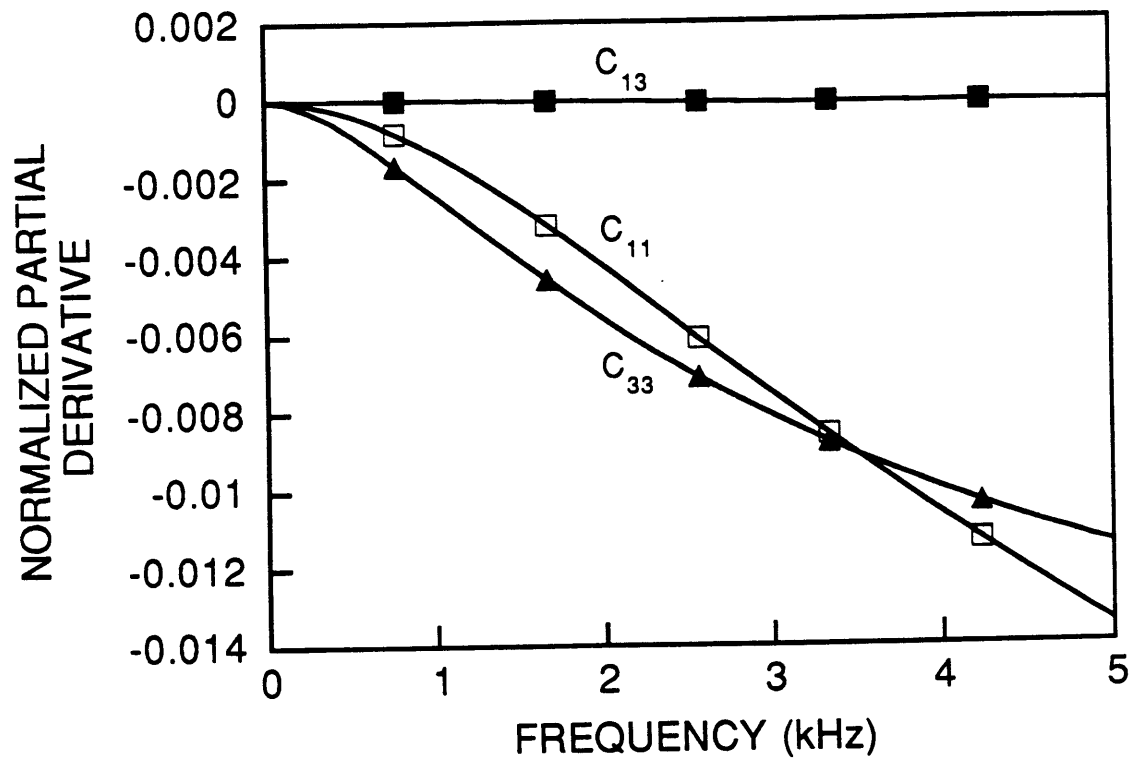


Figure 4-4: Sensitivities for the tube wave in the model with the fast formation (Table 4.1). See also Figure 4-3.

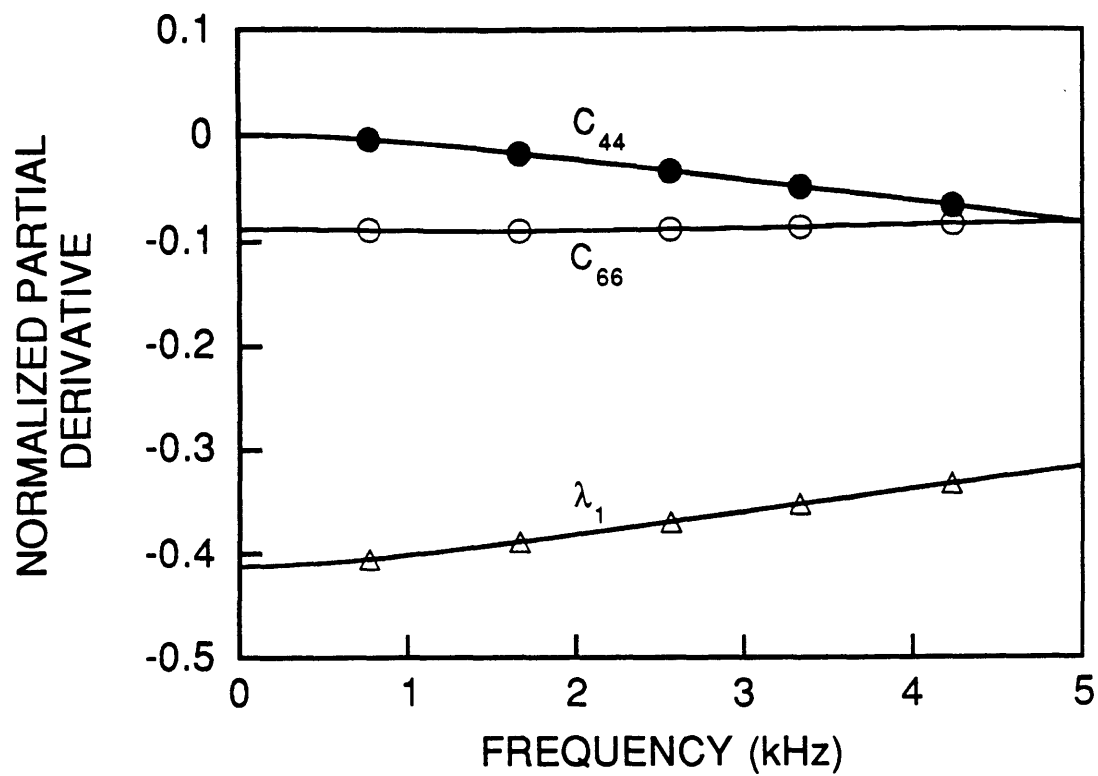


Figure 4-5: Sensitivities for the tube wave in the model with the slow formation (Table 4.2). See also Figure 4-6.

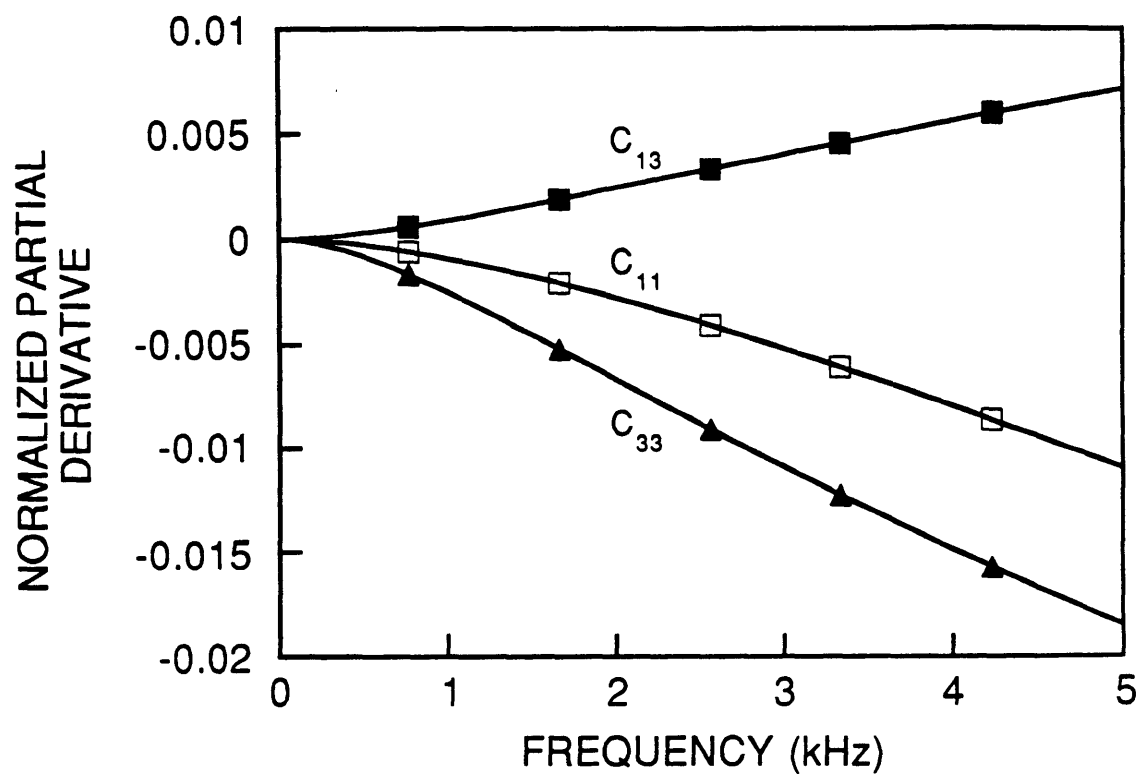


Figure 4-6: Sensitivities for the tube wave in the model with the slow formation (Table 4.2). See also Figure 4-5.

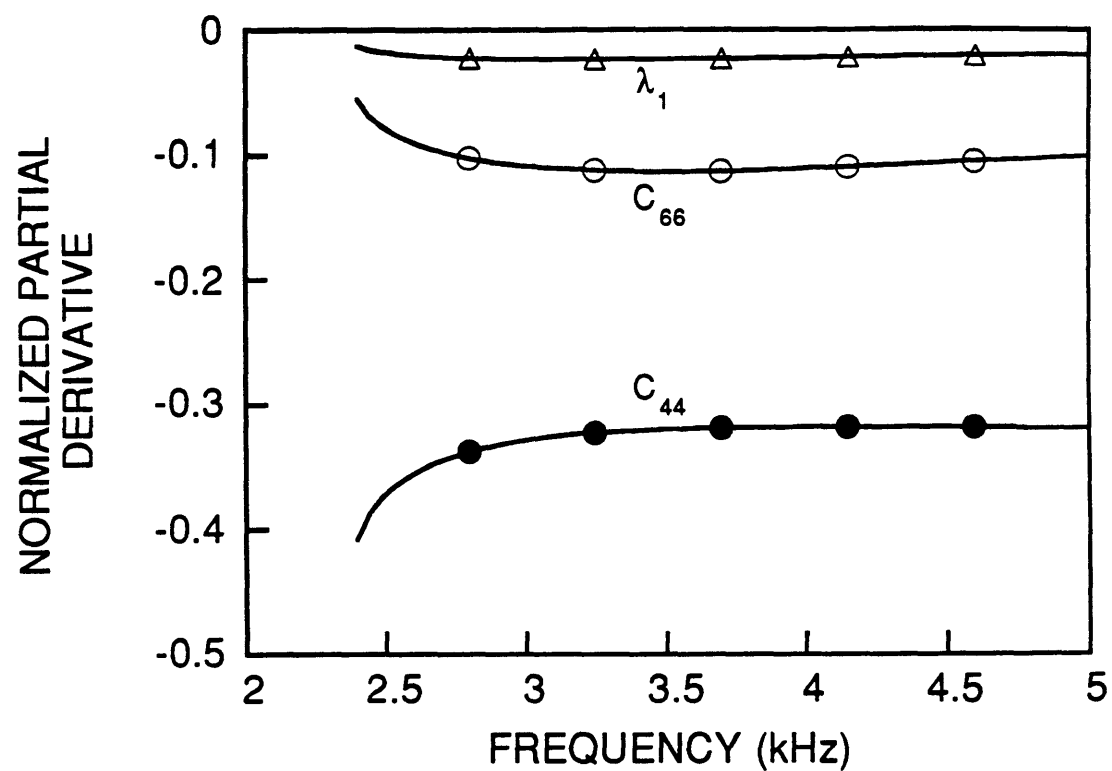


Figure 4-7: Sensitivities for the tube wave in the model with the very slow formation (Table 4.3). See also Figure 4-8.

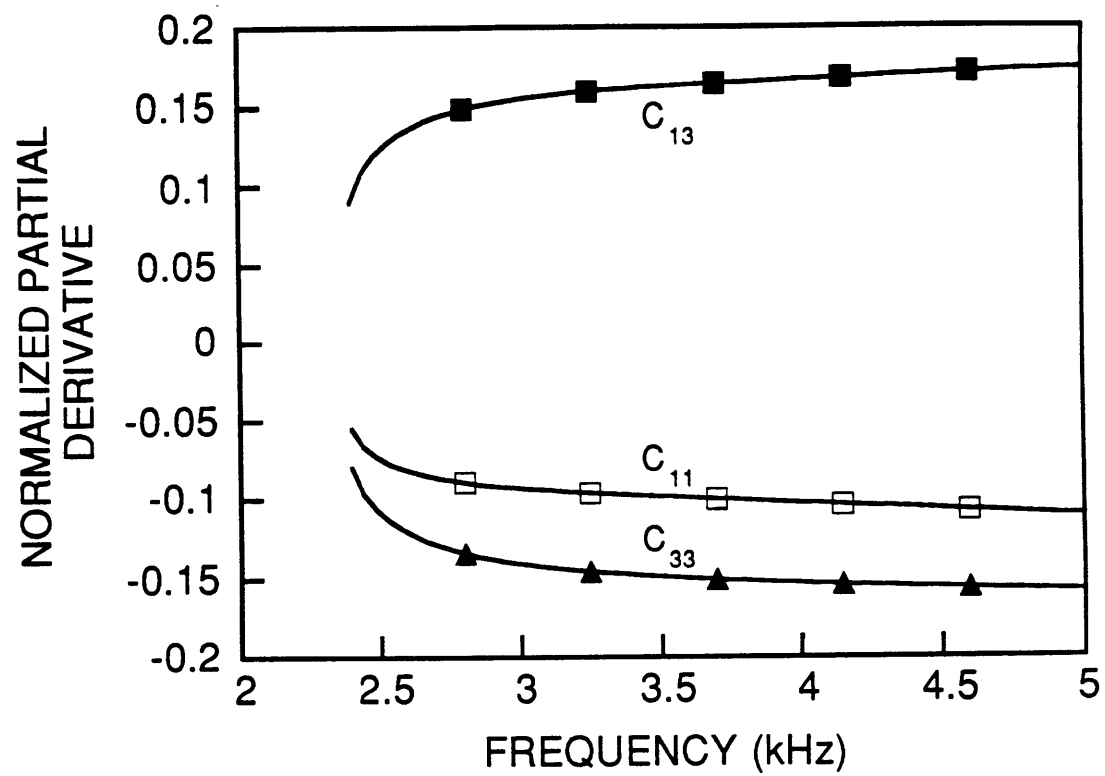


Figure 4-8: Sensitivities for the tube wave in the model with the very slow formation (Table 4.3). See also Figure 4-7.

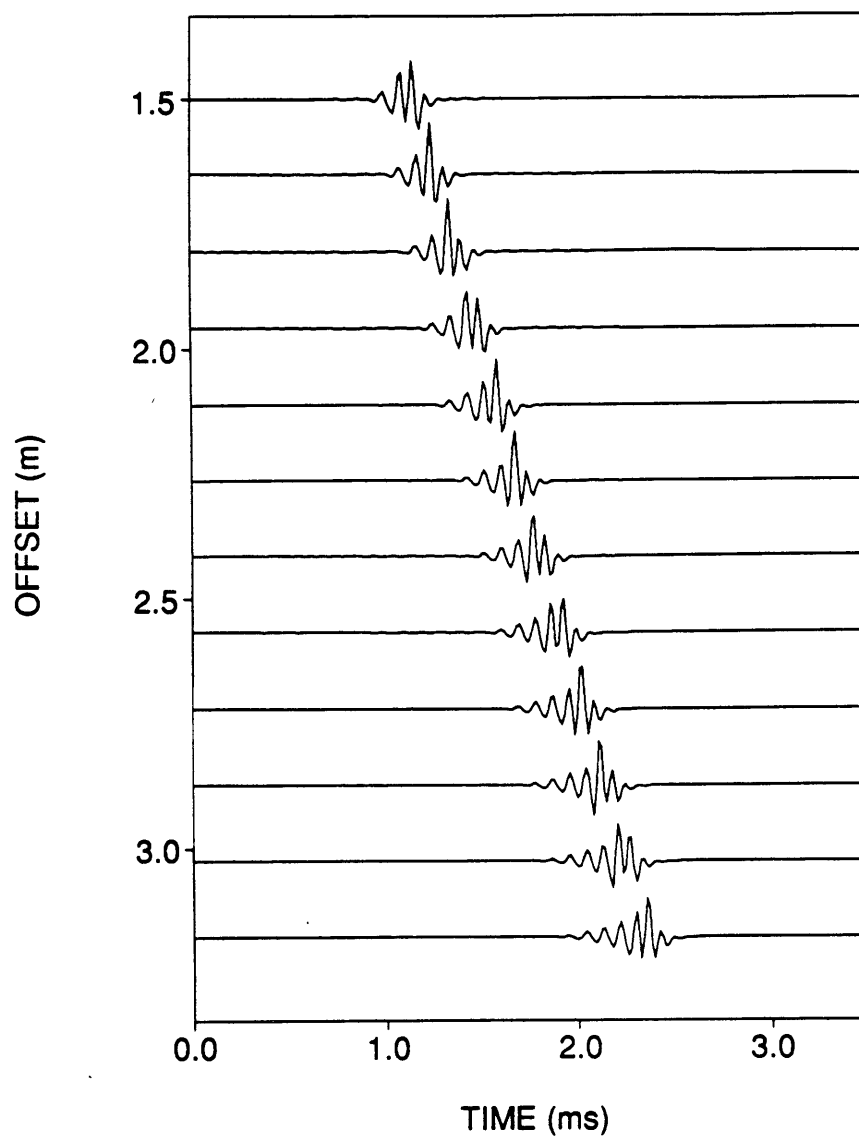


Figure 4-9: Synthetic seismograms for the model with the fast formation (Table 4.1).

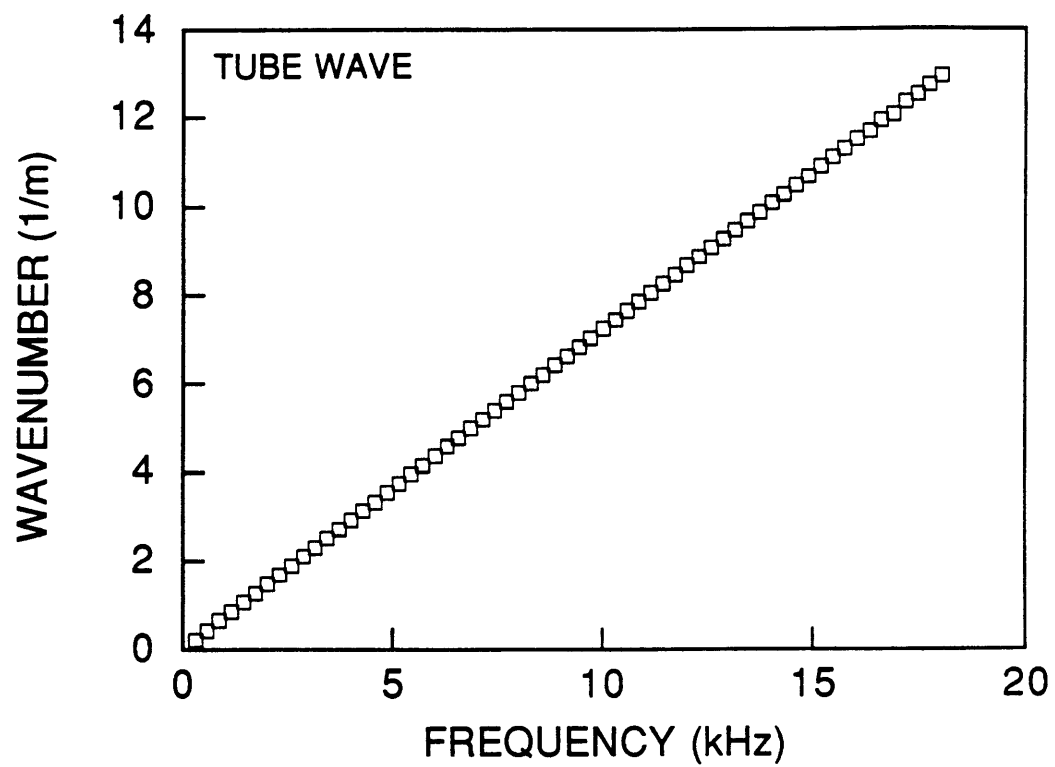


Figure 4-10: Wavenumber estimates for the tube wave obtained by processing the synthetic seismograms for the fast formation (Figure 4-9).

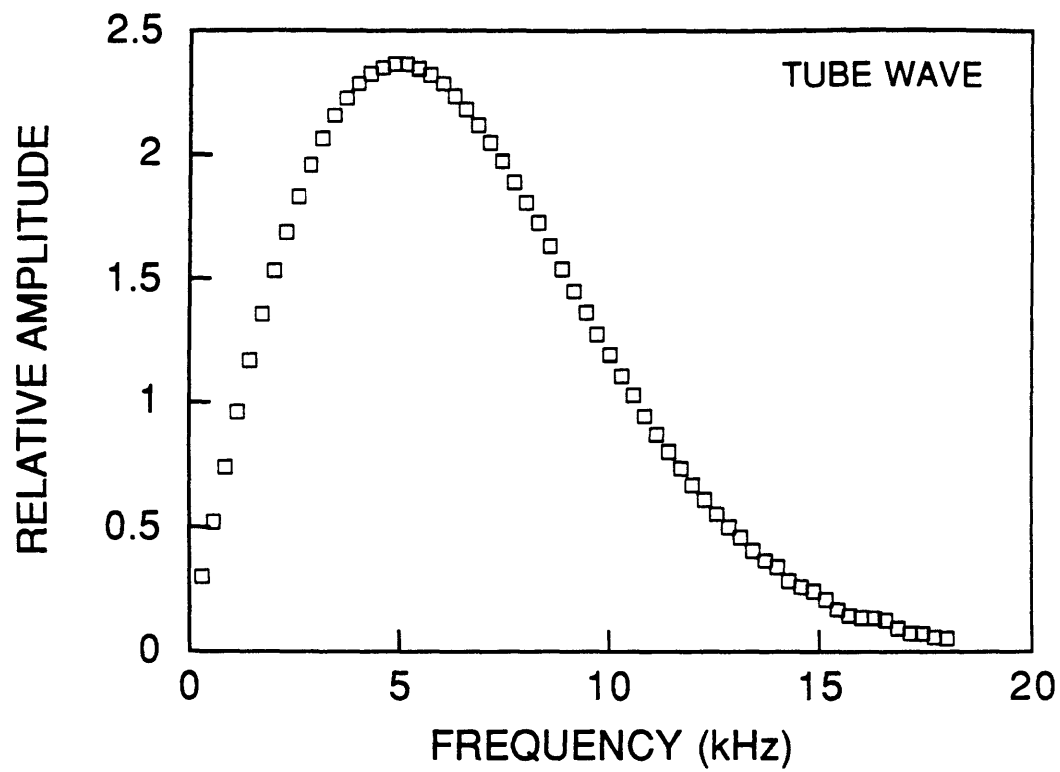


Figure 4-11: Amplitude estimates for the tube wave obtained by processing the synthetic seismograms for the fast formation (Figure 4-9).

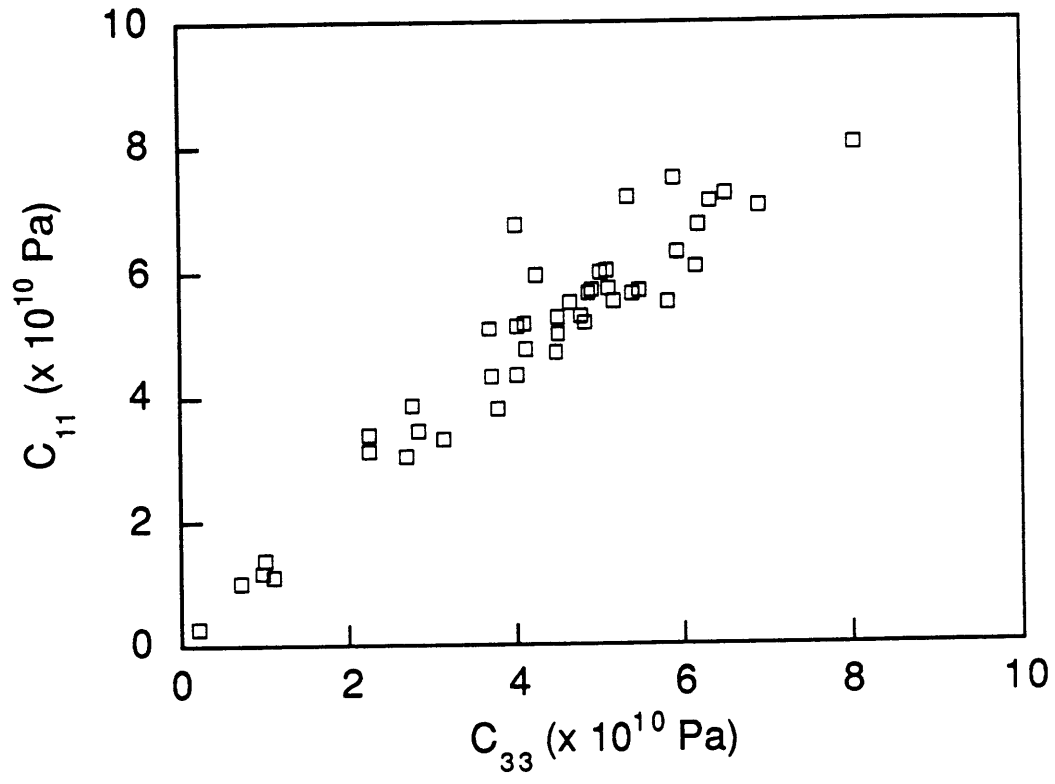


Figure 4-12: Cross-plot used to determine a reasonable value for c_{11} . The data are from the list of elastic moduli of transversely isotropic rocks compiled by Thomsen (1986).

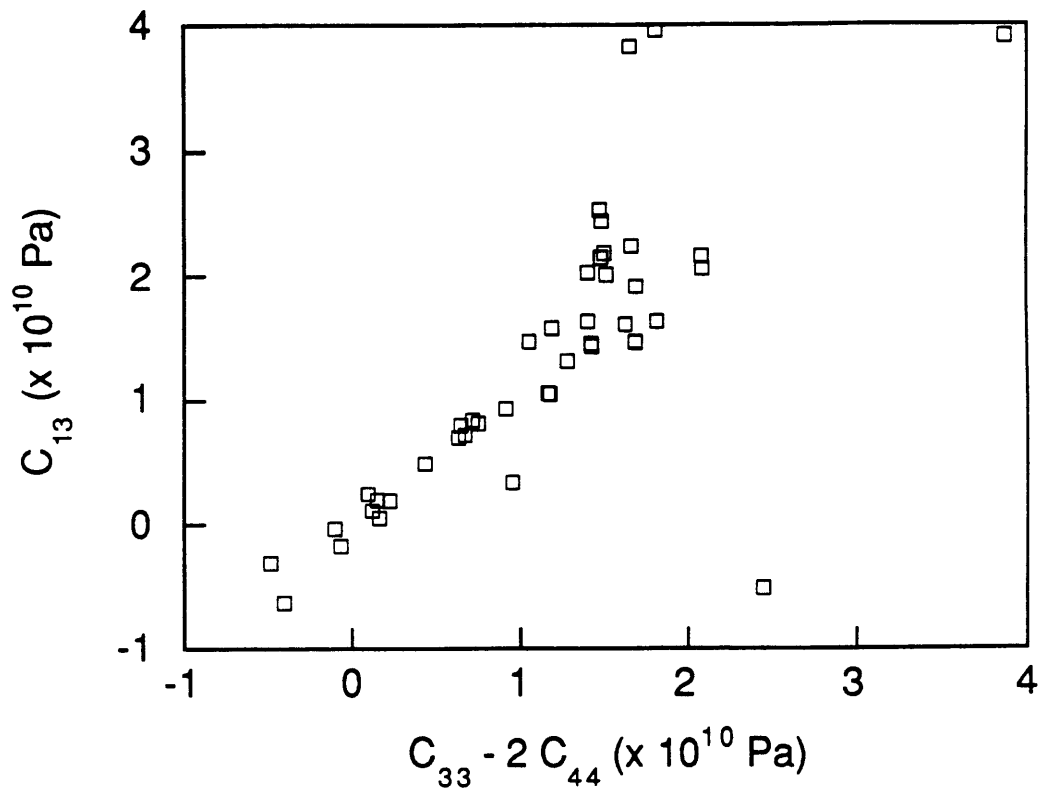


Figure 4-13: Cross-plot used to determine a reasonable value for c_{13} . (Note that c_{13} depends strongly on the linear combination, $c_{33} - 2c_{44}$. To understand this result, assume for a moment that the rock is isotropic. The elastic moduli in terms of the Lamé parameters are $c_{11} = c_{33} = \lambda + 2\mu$, $c_{13} = \lambda$, and $c_{44} = c_{66} = \mu$. When a rock is only slightly anisotropic, $c_{33} - 2c_{44}$ is close to c_{13} .) The data are from the list of elastic moduli of transversely isotropic rocks compiled by Thomsen (1986).

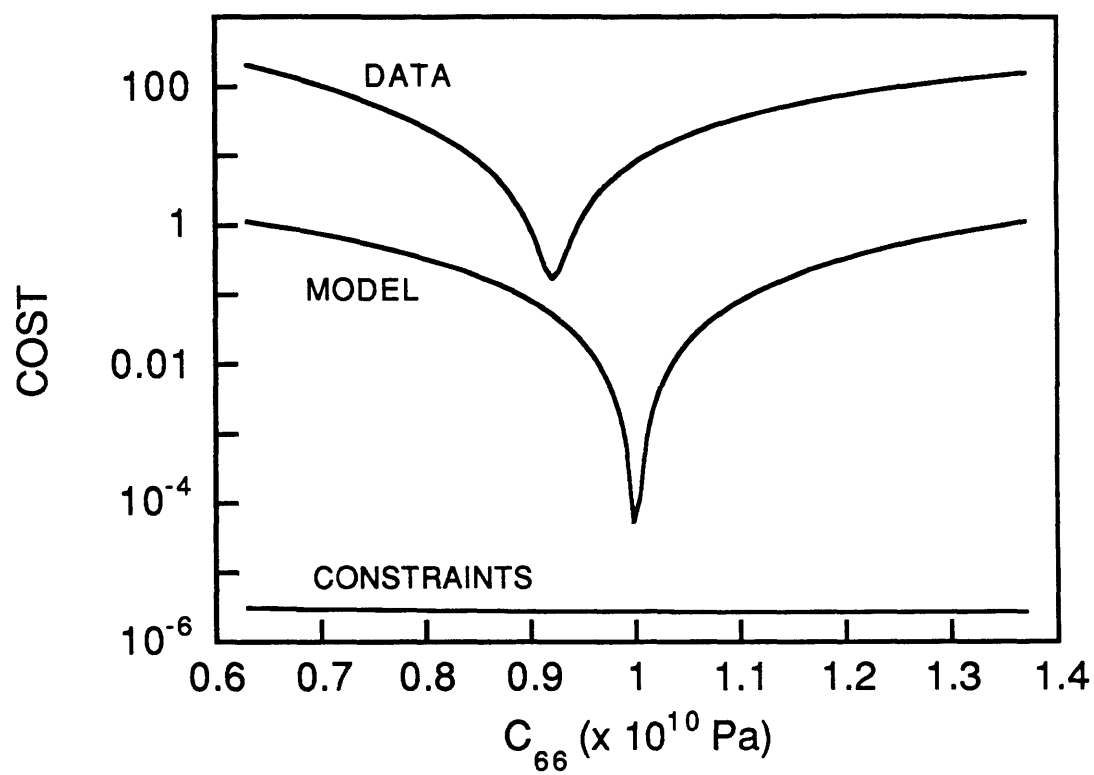


Figure 4-14: Terms in the cost function used to estimate c_{66} in the fast formation.

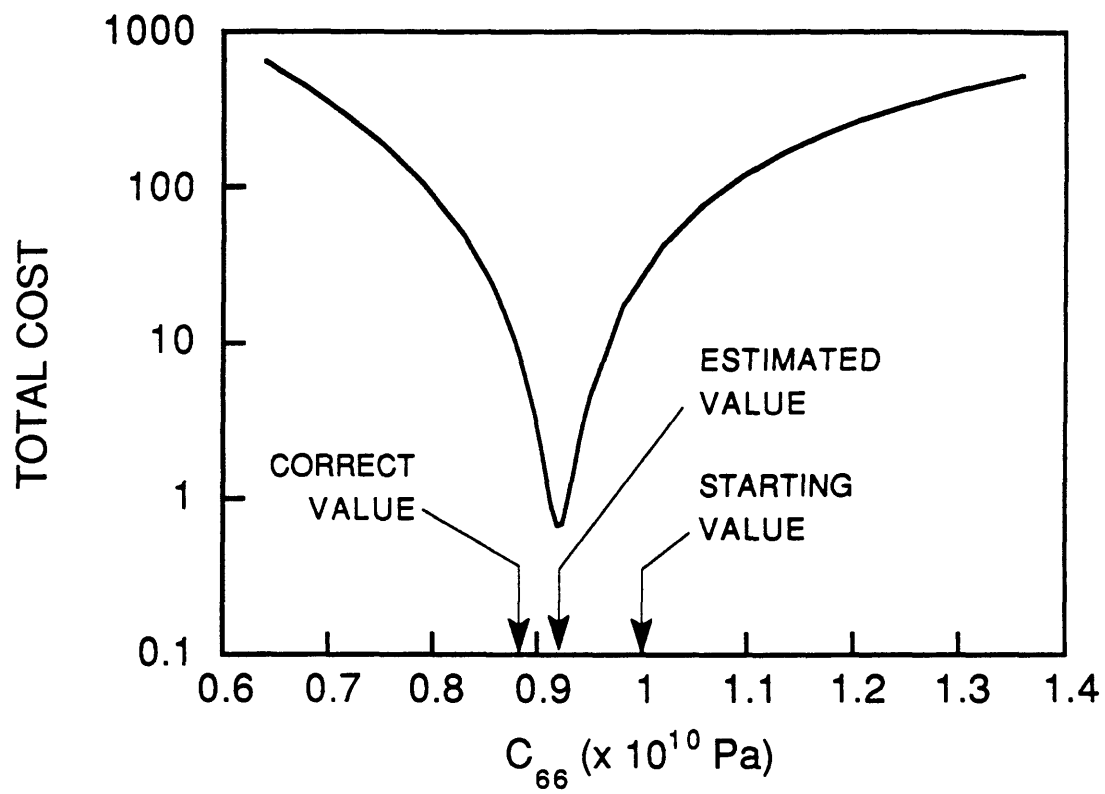


Figure 4-15: Cost surface for the estimation of c_{66} in the fast formation.

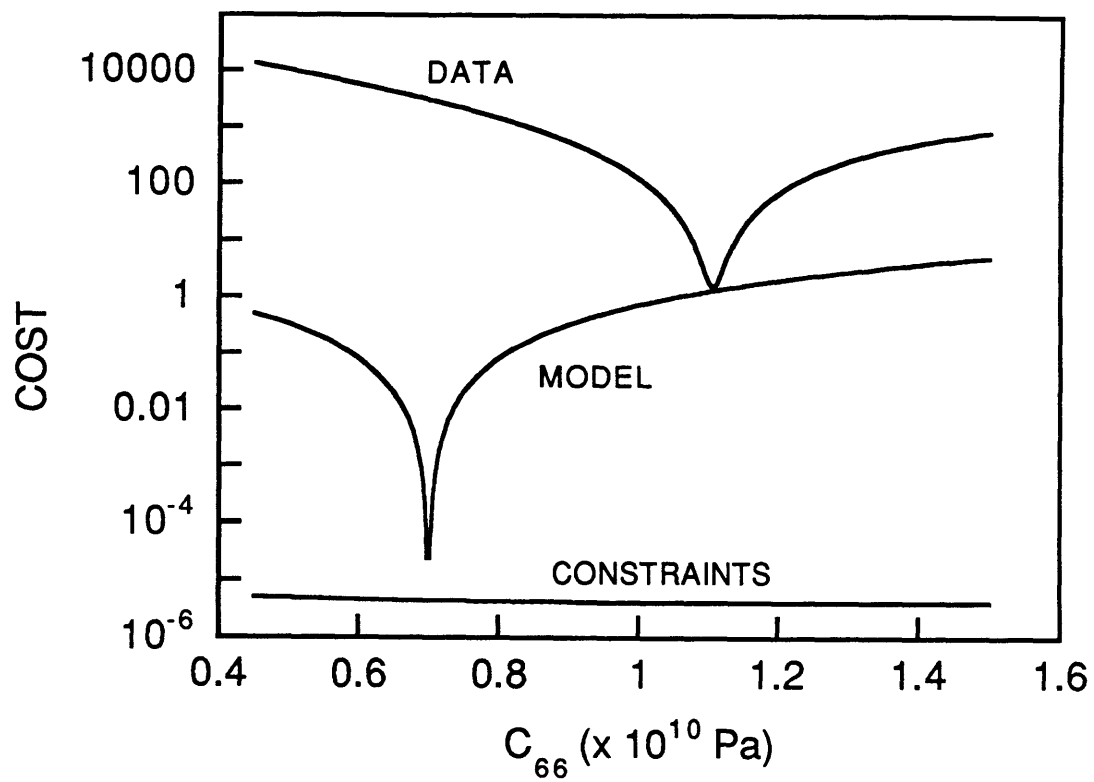


Figure 4-16: Terms in the cost function used to estimate c_{66} in the slow formation.

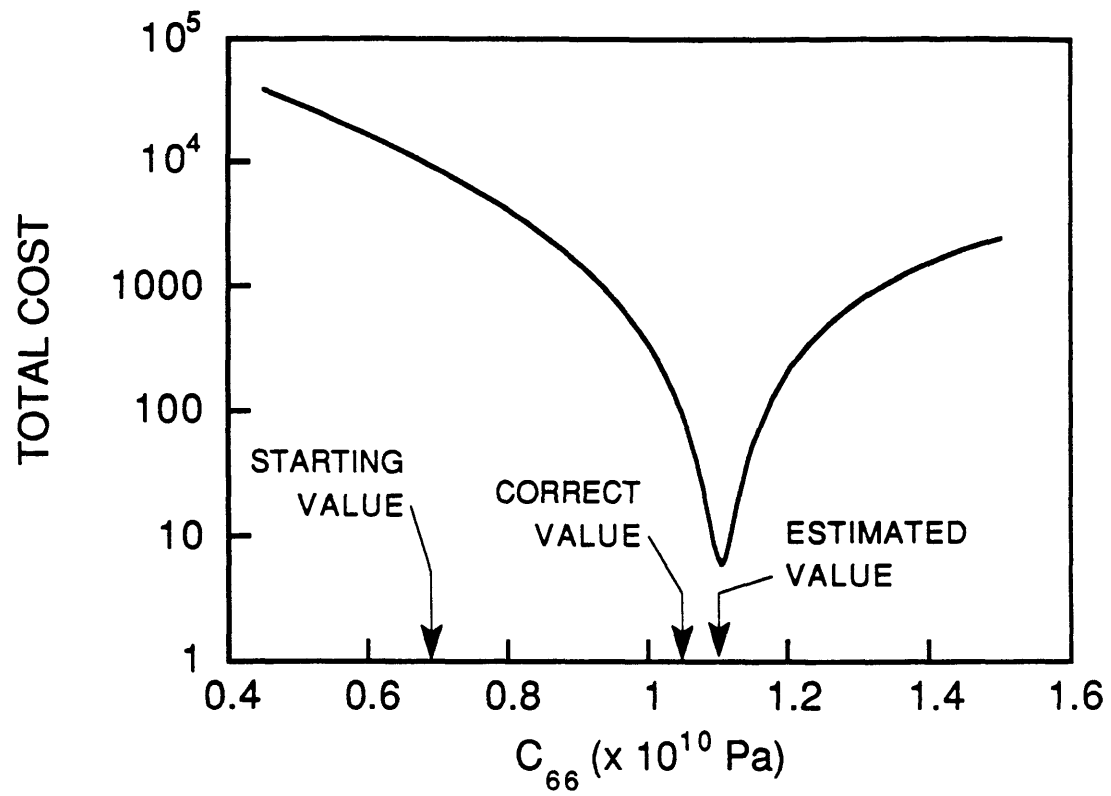


Figure 4-17: Cost surface for the estimation of c_{66} in the slow formation.

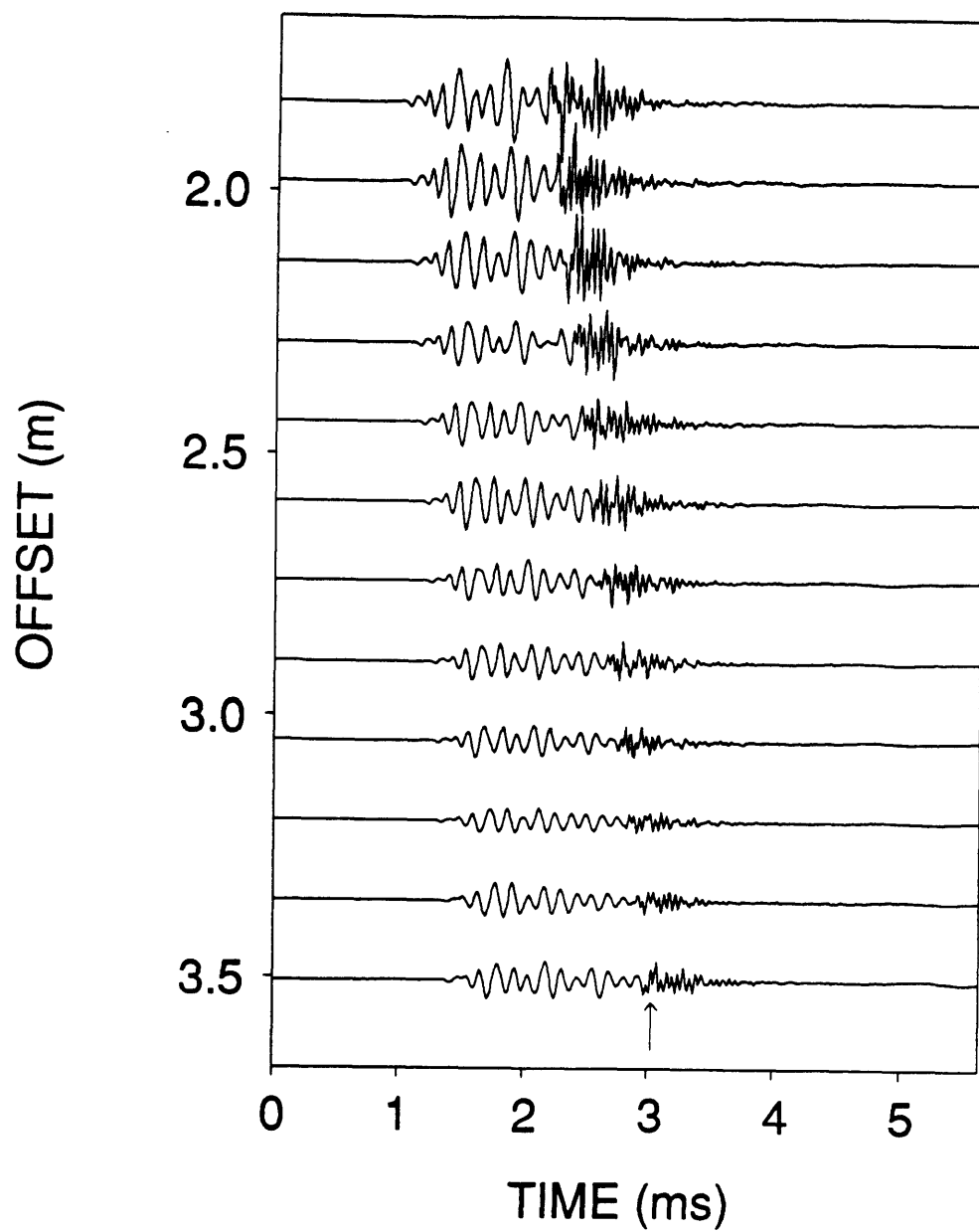


Figure 4-18: Seismograms used to estimate the acoustic velocity of the fluid using the leaky *P*-wave, which is indicated by the arrow.

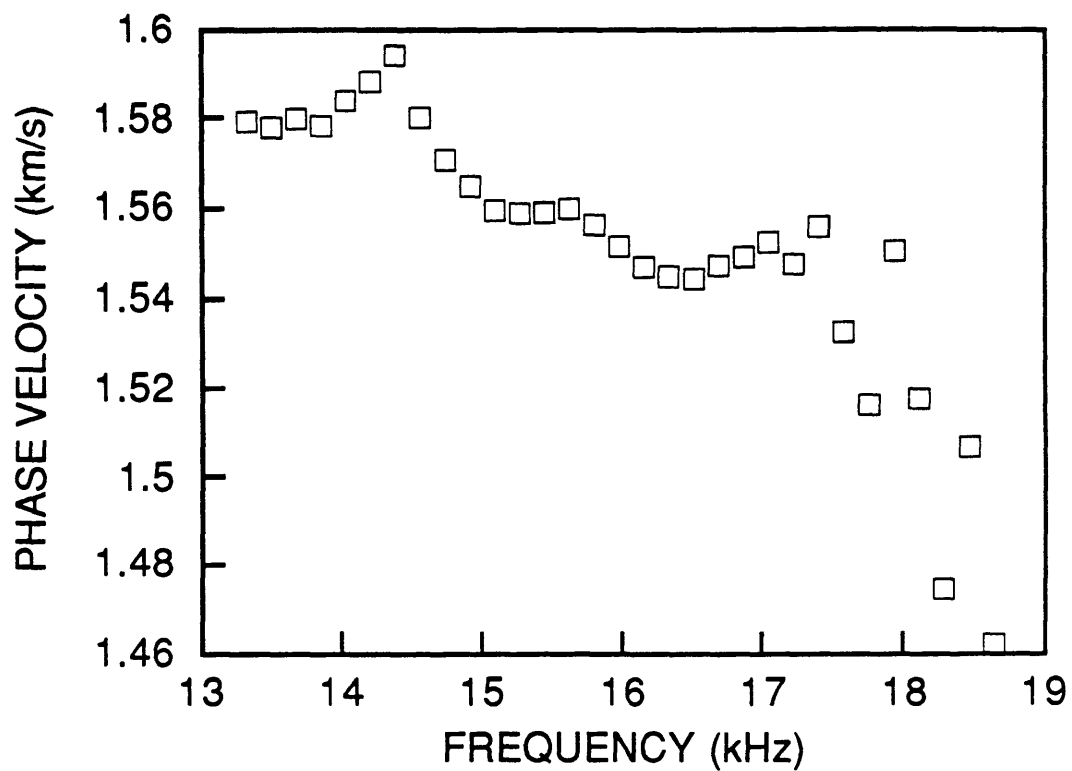


Figure 4-19: Phase velocity estimates for the high frequency portion of the leaky *P*-wave shown in Figure 4-18. These estimates are used to determine the acoustic velocity of the fluid.

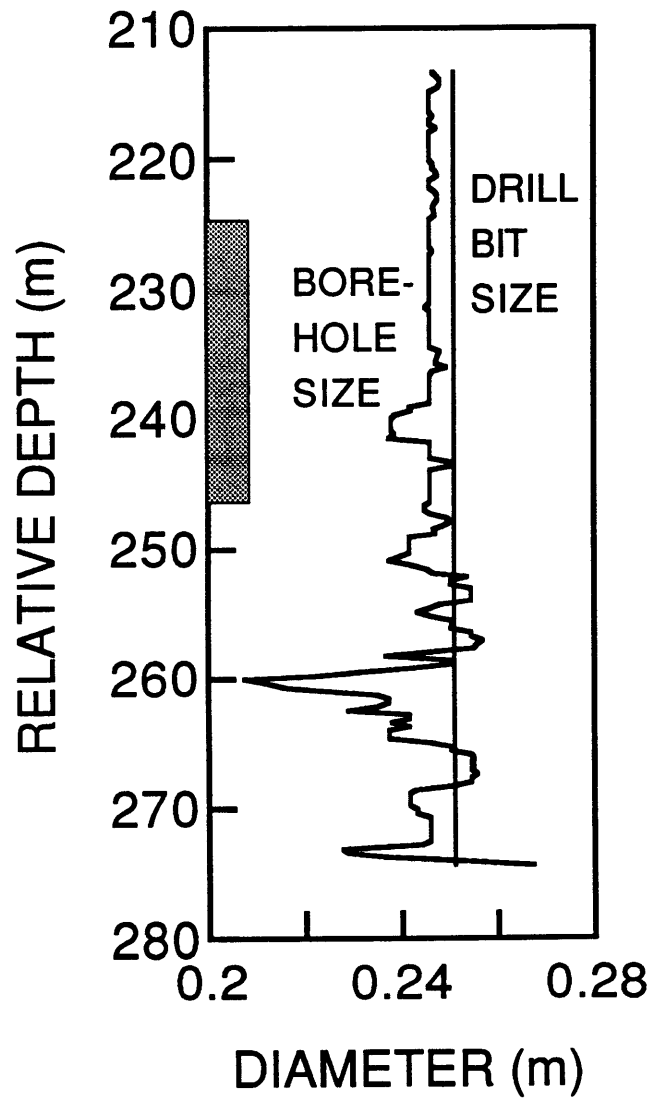


Figure 4-20: Caliper log. The shaded rectangle indicates the zone where c_{66} is estimated.

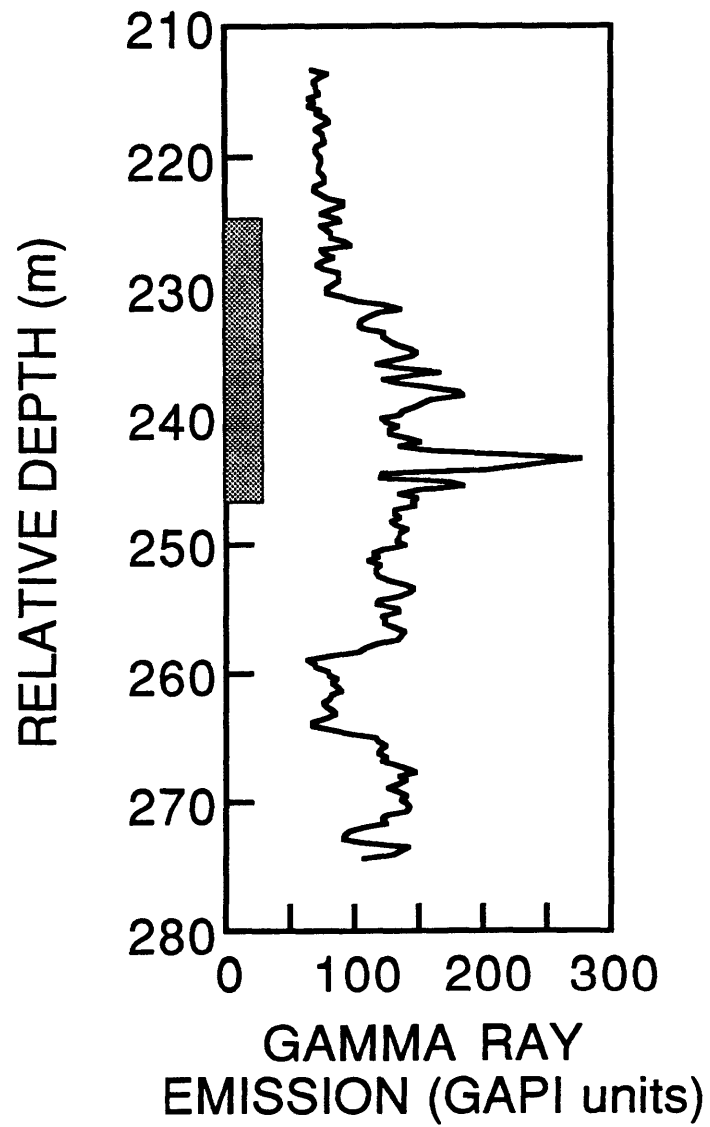


Figure 4-21: Conventional gamma ray log. The shaded rectangle indicates the zone where c_{66} is estimated.

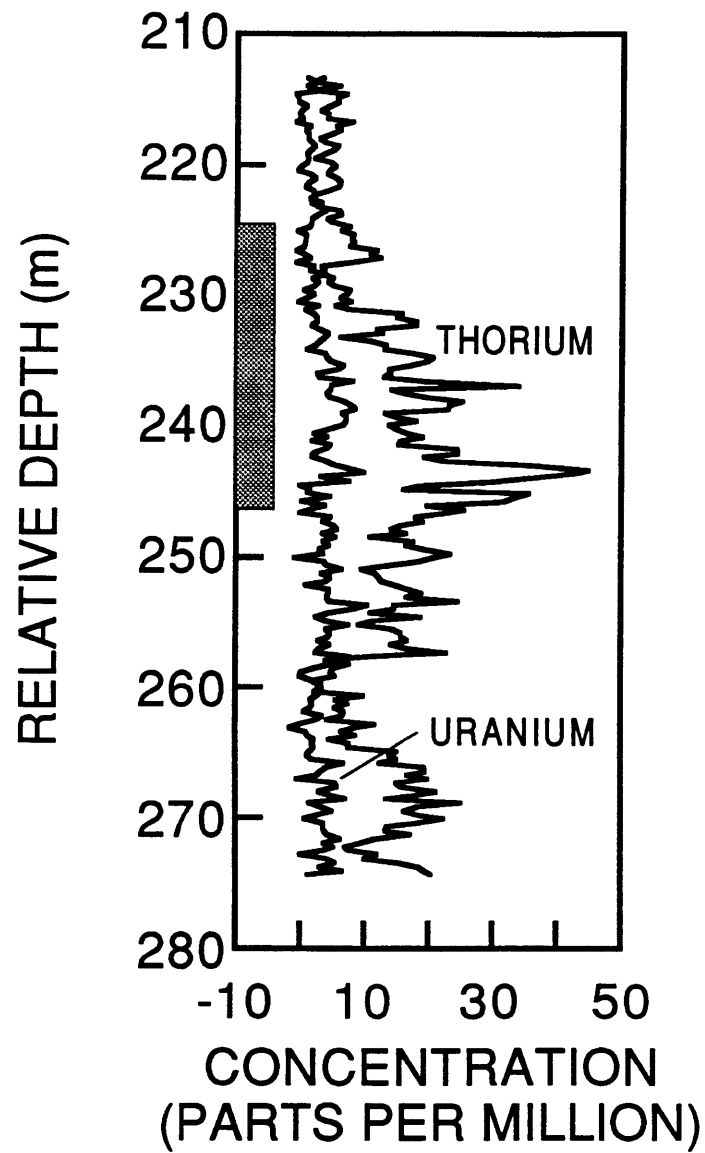


Figure 4-22: Spectral gamma ray log for thorium and uranium. The shaded rectangle indicates the zone where c_{66} is estimated.

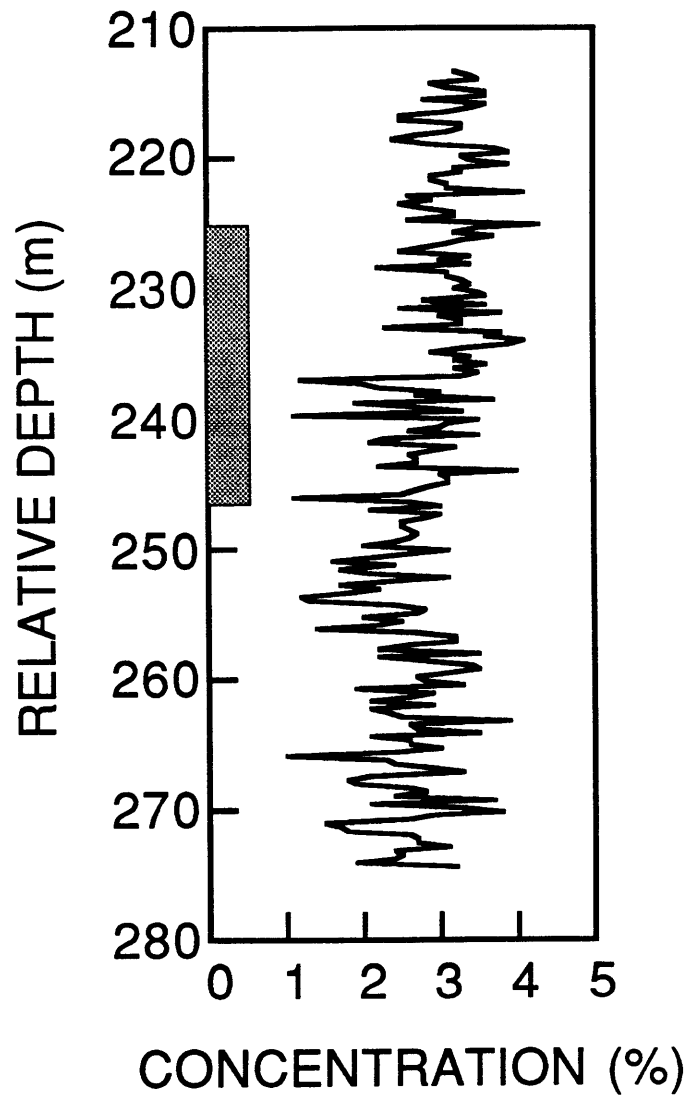


Figure 4-23: Spectral gamma ray log for potassium. The shaded rectangle indicates the zone where c_{66} is estimated.

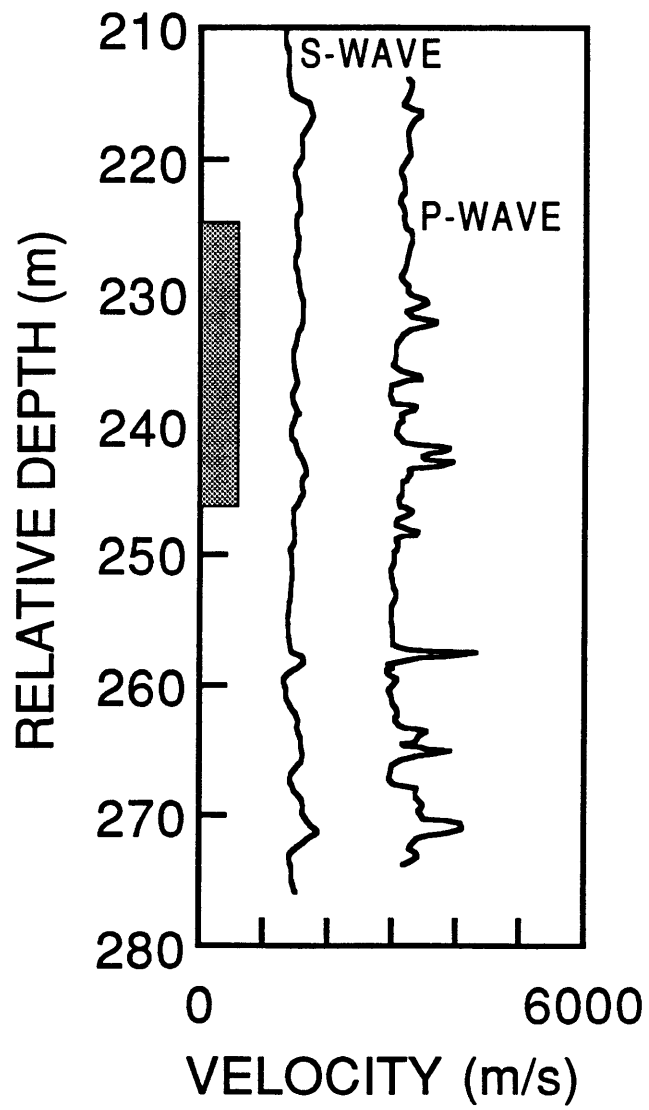


Figure 4-24: Velocity log calculated from the refracted *P*-wave and flexural wave. The shaded rectangle indicates the zone where c_{66} is estimated.

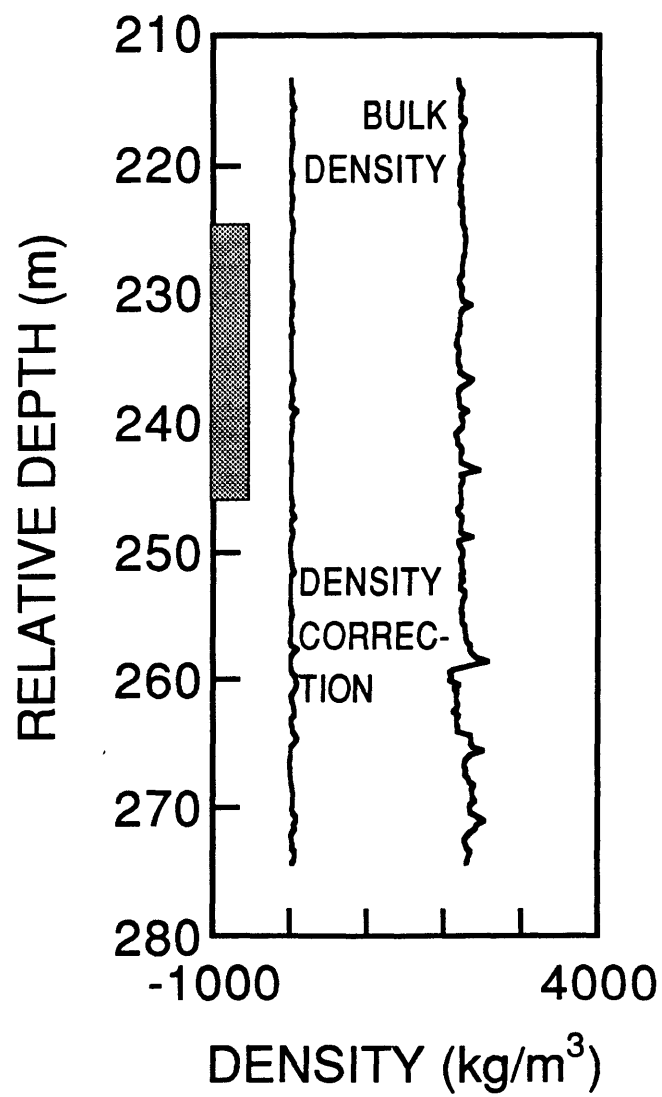


Figure 4-25: Density log. The shaded rectangle indicates the zone where c_{66} is estimated.

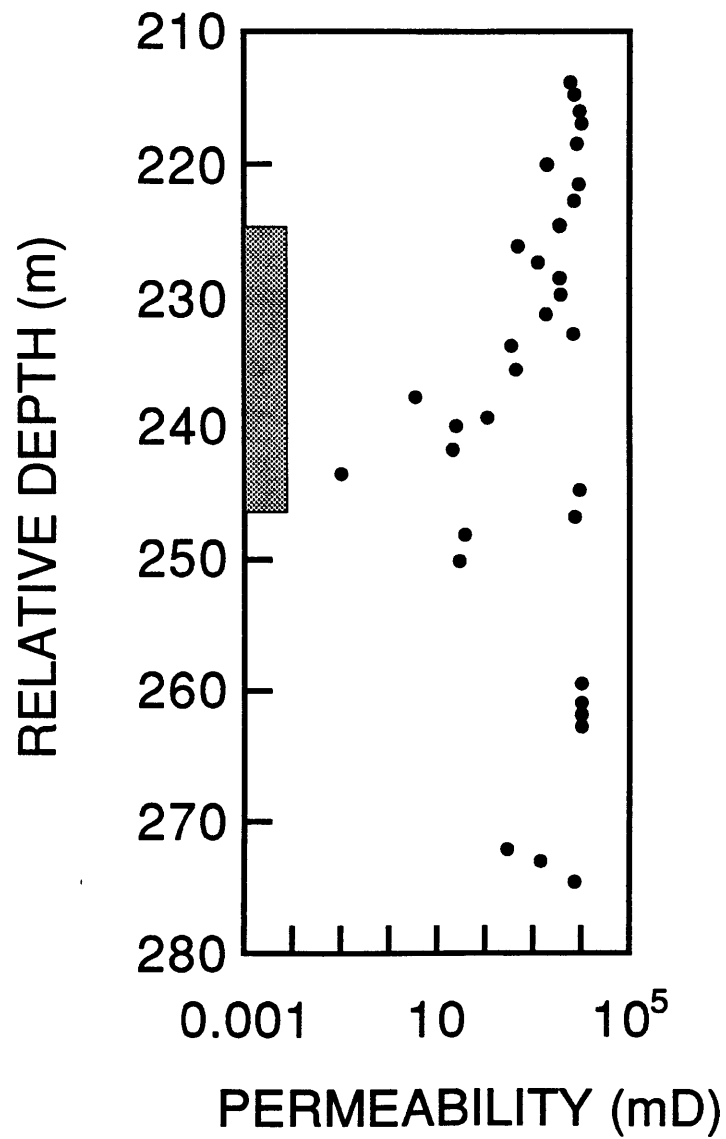


Figure 4-26: Permeability log. The shaded rectangle indicates the zone where c_{66} is estimated. When the permeability exceeds 10^4 mD, the value is plotted as being 10^4 mD because the laboratory that made the measurements reported the results in this manner.

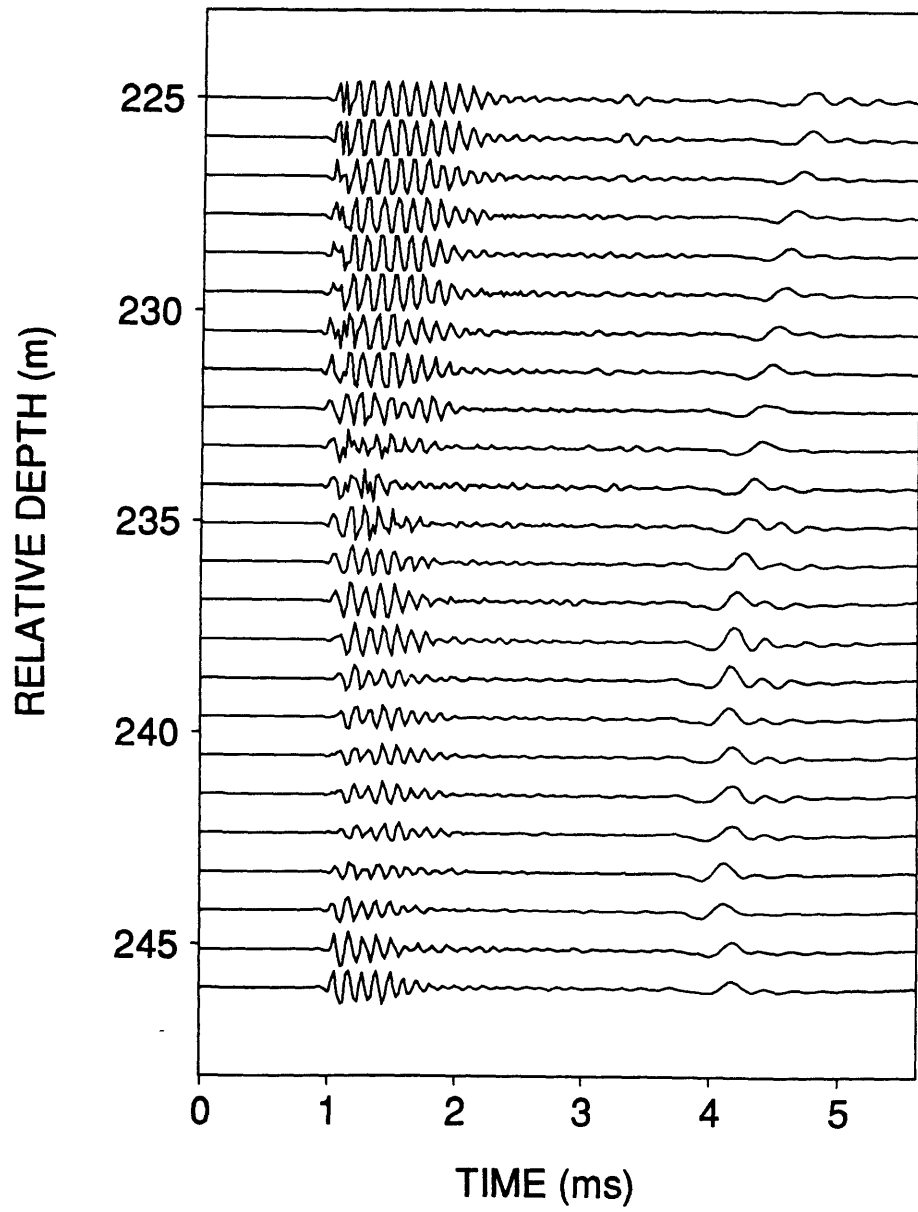


Figure 4-27: Seismograms recorded by the last receiver, from every sixth depth in the zone where c_{66} was estimated.

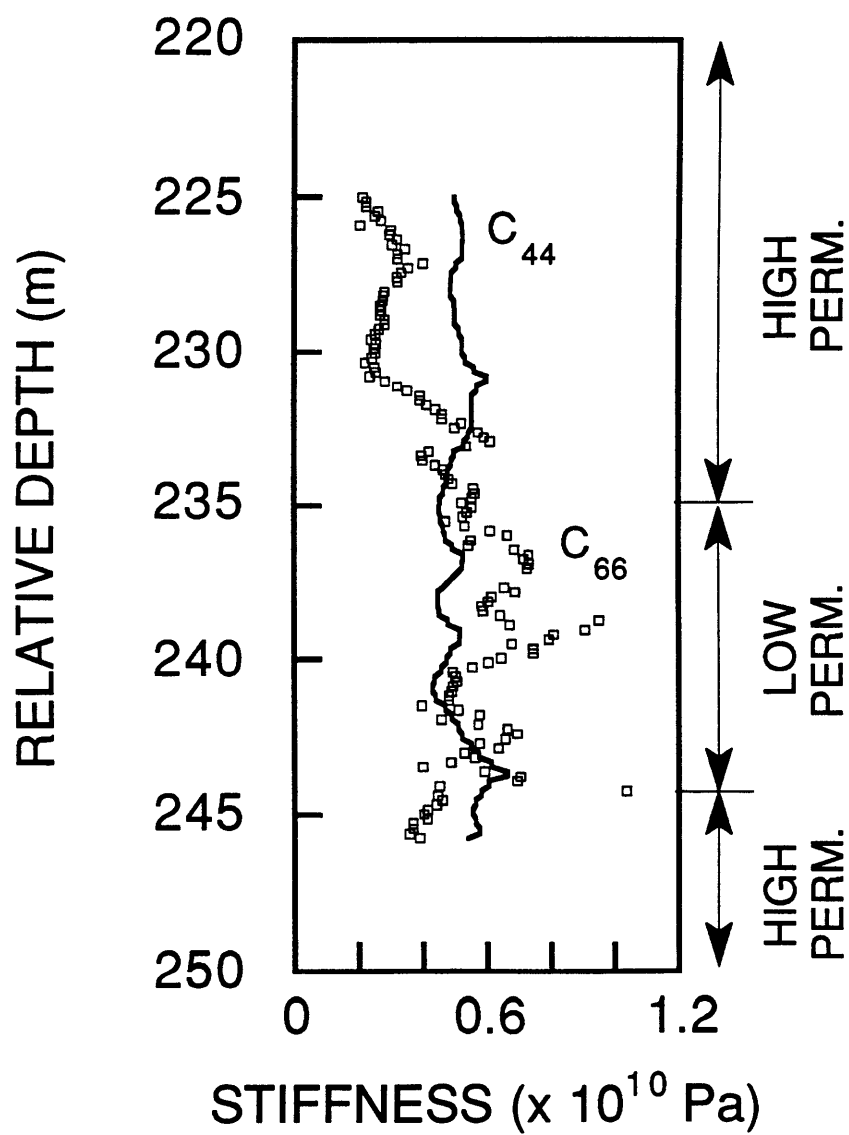


Figure 4-28: Estimates of c_{66} made from the tube wave, and the values for c_{44} calculated from the S -wave velocity (Figure 4-24).

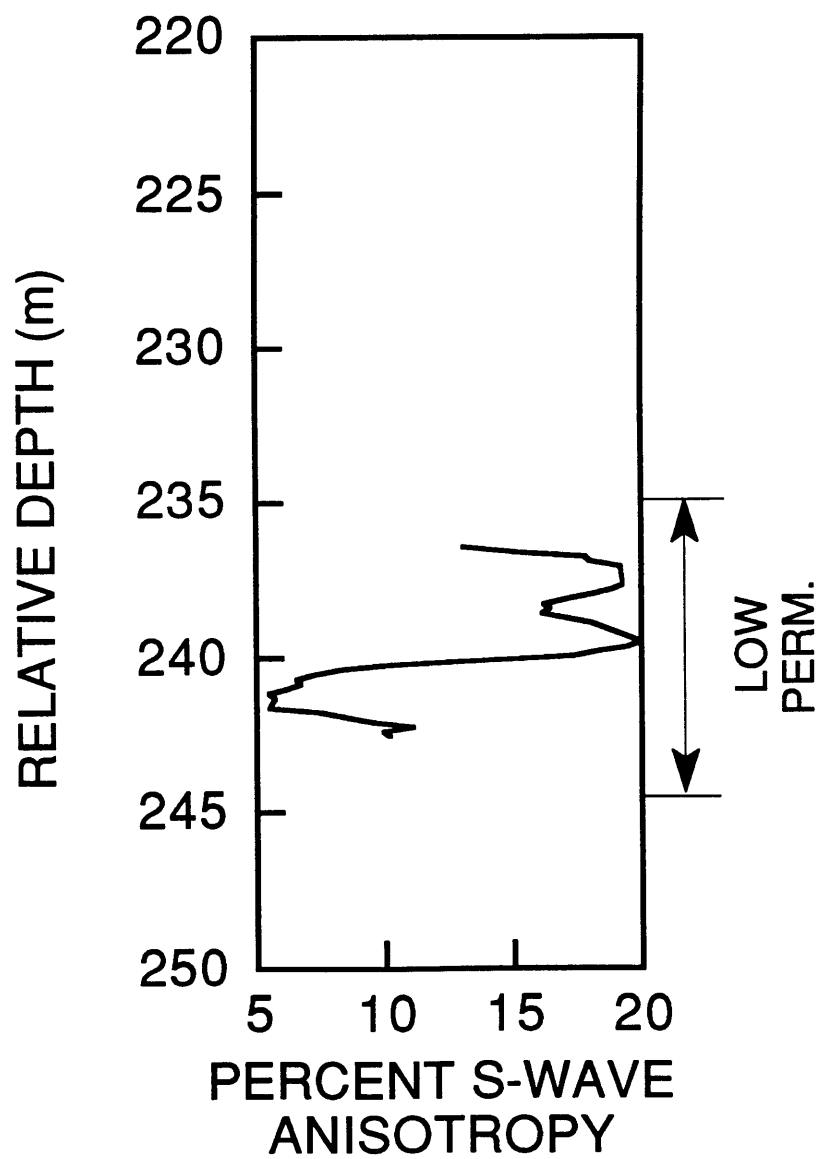


Figure 4-29: Percentage of *S*-wave anisotropy calculated with the estimates of c_{66} from the low permeability zone (Figure 4-28).

Chapter 5

Summary and Conclusions

The goal of this thesis was to determine how anisotropy can be detected with acoustic logging. To this end, the thesis addressed two issues: the effects of general anisotropy upon elastic wave propagation in a borehole and the estimation of a shear modulus of a transversely isotropic formation.

In Chapter 2, several applications of perturbation theory were developed. This theory is used to derive an equation which relates first order perturbations in frequency, wavenumber, elastic moduli, densities, and locations of interfaces. This perturbation equation, which is derived in the frequency-wavenumber domain, applies to a general model which can have many fluid or solid layers with any cross-sectional shape. To develop some useful formulas, the equation was applied to the two-layer model which is used throughout the thesis: the inner layer is a fluid, and the outer layer is a transversely isotropic solid with its symmetry axis parallel to the borehole. Because analytical expressions for the displacements exist for this particular model, the terms in the perturbation equation simplify greatly. Formulas were derived to calculate (1) phase velocities for a model with slight, general anisotropy, (2) partial derivatives of either the wavenumber or frequency with respect to either an elastic modulus or density, (3) group velocity, and (4) phase velocities for a model with a slightly irregular borehole. These formulas are also applicable to models with an

isotropic solid because it is a special case of a transversely isotropic solid. These applications were used in other parts of the thesis.

In Chapter 3, the effects of anisotropy upon elastic wave propagation were determined. The wave equation was solved in the frequency-wavenumber domain with a variational method, and the solution yielded the phase velocities, group velocities, pressures, and displacements for the normal modes. (The phase and group velocities obtained with this variational method equal those obtained with the perturbation method indicating that both are correctly formulated and implemented.) These properties were studied for two cases: a transversely isotropic model for which the borehole had several different orientations with respect to the symmetry axis and an orthorhombic model for which the borehole was parallel to the intersection of two symmetry planes. The normal modes for these two cases show several significant effects which do not exist when the solid is isotropic or transversely isotropic with its symmetry axis parallel to the borehole:

1. The phase velocities for the quasi-pseudo-Rayleigh, both quasi-flexural, and both quasi-screw waves do not exceed the phase velocity of the slowest qS -wave. (The phase velocities of the leaky modes, which were not investigated, will exceed this threshold.)
2. The two quasi-flexural waves have different phase and group velocities; the differences are greatest at low frequencies and diminish as the frequency increases. The two quasi-screw waves behave similarly.
3. The greater the difference between the the phase velocities of the qS -waves, the greater the difference between the phase velocities of the quasi-flexural waves at all frequencies. The two quasi-screw waves behave similarly.
4. Near the limiting qS -wave velocity, the difference between the phase velocities of the two quasi-flexural waves is greater than the difference between the phase velocities of the two quasi-screw waves.

5. For the slow quasi-flexural wave, the particle displacements in the plane perpendicular to the borehole, when viewed together, are aligned with the polarization of the slow qS -wave.
6. For the fast quasi-flexural wave, the particle displacements in the plane perpendicular to the borehole, when viewed together, are aligned with the polarization of the fast qS -wave.
7. For the slow quasi-screw wave, the particle displacements in the plane perpendicular to the borehole, when viewed together, are aligned along two mutually perpendicular directions which are rotated 45° with respect to the polarizations of both qS -waves.
8. For the fast quasi-screw wave, the particle displacements in the plane perpendicular to the borehole, when viewed together, are aligned along two mutually perpendicular directions which are parallel with the polarizations of both qS -waves.

(In this list, the qS -waves refer to those plane waves whose wavenumber vectors are parallel to the borehole.) Despite these significant effects, the general characteristics of the phase and group velocities, pressures, and displacements are similar (but not identical) to those that would exist if the solid were isotropic or transversely isotropic with its symmetry axis parallel to the borehole. This result is expected because the solid is only slightly anisotropic.

In Chapter 4, a method to estimate a shear modulus of a transversely isotropic formation (with its symmetry axis parallel to the borehole) was developed and tested. The estimation is performed in the frequency-wavenumber domain — the data are the wavenumbers at each frequency for the tube wave. To properly formulate the inversion, the sensitivity of the wavenumbers to the elastic moduli of the fluid and formation was determined. At low frequencies the wavenumbers for the tube wave in fast and slow formations are very sensitive to λ_1 and moderately sensitive to c_{66} .

Therefore, an accurate value for λ_1 must be obtained before a value for c_{66} is estimated. The wavenumbers are insensitive to c_{11} , c_{13} , c_{33} at all frequencies, and are only moderately sensitive to c_{44} near 5 kHz. Consequently, the inversion for c_{66} will not be adversely affected if slightly inaccurate values for these moduli are picked. In very slow formations, the wavenumbers for the tube wave are as sensitive to the unknown moduli, c_{11} and c_{13} as they are to c_{66} . Hence c_{66} cannot be estimated for this formation. A useful rule of thumb is that c_{66} should be estimated only when the vertical S -wave velocity is greater than or nearly equal to the acoustic velocity of the fluid.

The inversion for c_{66} is based upon a cost function which has three terms: a measure of the misfit between the observed and predicted wavenumbers, a measure of the misfit between the current estimate for c_{66} and the initial guess of its value, and penalty functions which constrain the estimate for c_{66} to physically acceptable values. The inversion was applied to synthetic data for fast and slightly slow formations, and the estimates for c_{66} were within 5% of their correct values and were moderately well resolved. The errors were probably due to the approximate values used for the elastic moduli of the formation. Then the inversion was applied to field data; the estimates for c_{66} were significantly higher than the values for c_{44} in a zone with low permeability and high clay content. The percentage of S -wave anisotropy ranged from 5 to 20%.

The results obtained in this thesis indicate that anisotropy can be detected with acoustic logging. The quasi-tube wave can be used to measure c_{66} in a transversely isotropic formations with its symmetry axis parallel to the borehole. The low frequency portions of the quasi-flexural waves should be able to detect the velocities and polarizations of the qS -waves propagating parallel to the borehole. The next research project should focus on the behavior of these modes when they are leaky.

Appendix A

Propagation along a Borehole in a Transversely Isotropic Medium

In this appendix, the wave equation will be solved in the circular cylindrical coordinate system for propagation in a fluid and a transversely isotropic solid (with the symmetry axis parallel to the z axis), and the solutions will be used to derive expressions for the particle displacements. Then a dispersion equation will be derived for wave propagation along a fluid-filled borehole in a transversely isotropic solid.

The mathematical model of the borehole environment consists of a fluid inside a cylindrical borehole through a transversely isotropic solid (Figure A-1). The fluid and solid extend to infinity along the axis of the borehole, and solid extends to infinity perpendicular to the borehole. The fluid is perfectly elastic; its incompressibility is λ_1 , and its density is ρ_1 . The solid is perfectly elastic and homogeneous. Because the symmetry axis for the anisotropy is parallel to the z axis, the properties of the solid are uniquely specified by only five moduli: c_{11} , c_{13} , c_{33} , c_{44} , and c_{66} . The density of the solid is ρ_2 .

A.1 Propagation in the Fluid

In this section, the wave equation for the fluid,

$$\nabla^2 \mathbf{u}_c = \frac{1}{\alpha_1^2} \ddot{\mathbf{u}}_c \quad (\text{A.1})$$

(where \mathbf{u}_c is the displacement, α_1 is the speed of a compressional wave in the fluid, and t is time) is solved. Using Lamé's theorem (Aki and Richards, 1980, p. 68-69), the wave equation is recast in terms of a displacement potential:

$$\nabla^2 \phi_1 = \frac{1}{\alpha_1^2} \ddot{\phi}_1 \quad , \quad (\text{A.2})$$

where

$$\nabla \phi_1 = \mathbf{u}_c \quad . \quad (\text{A.3})$$

The solution,

$$\phi_1(r, \theta, z, t) = \frac{1}{(2\pi)^2} \sum_{n=-\infty}^{\infty} e^{in\theta} \int_{-\infty}^{\infty} d\omega e^{i\omega t} \int_{-\infty}^{\infty} dk_z e^{ik_z z} A_1 I_n(m_1 r) \quad , \quad (\text{A.4})$$

is found using the separation of variables technique (Jacobi, 1949; Ben-Menahem and Singh, 1981, p. 49-50; Tongtaow, 1982; White, 1983, p. 181-182). n is the azimuthal order number, k_z the axial wavenumber, and ω the radian frequency. A_1 is a constant which depends upon n , k_z , and ω ; m_1 is a wavenumber and is computed with

$$m_1 = \sqrt{k_z^2 - \frac{\omega^2}{\alpha_1^2}} \quad . \quad (\text{A.5})$$

Since ϕ_1 applies to the region extending from $r = 0$ to $r = R$, it includes the modified Bessel function of the first kind, I_n , but not the modified Bessel function of the second kind, K_n , which is singular at $r = 0$. Using equation A.3, the displacements in the transform domain are calculated:

$$\begin{aligned} U_r(r, n, k_z, \omega) &= A_1 m_1 \left[\frac{n}{m_1 r} I_n(m_1 r) + I_{n+1}(m_1 r) \right] \\ U_\theta(r, n, k_z, \omega) &= -\frac{A_1 n}{r} I_n(m_1 r) \\ U_z(r, n, k_z, \omega) &= A_1 i k_z I_n(m_1 r) \quad . \end{aligned} \quad (\text{A.6})$$

The pressure in the fluid can be expressed in terms of the displacement potential. The pressure is defined as

$$p = -\lambda_1 \Theta \quad (\text{A.7})$$

where Θ is the dilatation (Bullen, 1963, p. 23). The dilatation is defined as

$$\Theta = \nabla \cdot \mathbf{u}_c \quad (\text{A.8})$$

(Bullen, 1963, p. 17). Substitute equation A.3 into the previous equation:

$$\Theta = \nabla^2 \phi_1 \quad . \quad (\text{A.9})$$

Now substitute equation A.2:

$$\Theta = \frac{\rho_1}{\lambda_1} \ddot{\phi}_1 \quad (\text{A.10})$$

where ρ_1/λ_1 equals $1/\alpha_1^2$. Finally, substitute this expression for the dilatation into equation A.7:

$$p = -\rho_1 \ddot{\phi}_1 \quad . \quad (\text{A.11})$$

A.2 Propagation in the Solid

The expressions for cylindrical wave propagation in a transversely isotropic solid with the symmetry axis parallel to the z axis have been derived by many researchers (Morse, 1954; Einspruch and Truell 1959; Mirsky, 1965; Eliot and Mott, 1967; Keck and Armenàkas, 1971; Tongtaow, 1980; White and Tongtaow, 1981; Tongtaow, 1982; Chan and Tsang, 1983), and the derivation presented here is based mostly on Tongtaow's work.

Using the Helmholtz's Theorem (Morse and Feshbach, 1953, p. 52-53), the displacements are expressed with three scalar, displacement potentials (ϕ_2 , γ_2 , and χ_2):

$$\mathbf{u}_c = \nabla \phi_2 + \nabla \times \nabla \times (0, 0, \gamma_2) + \nabla \times (0, 0, \chi_2) \quad . \quad (\text{A.12})$$

In an isotropic solid, the potentials that satisfy the wave equation are

$$\begin{aligned}
\phi_2(r, \theta, z, t) &= \frac{1}{(2\pi)^2} \sum_{n=-\infty}^{\infty} e^{in\theta} \int_{-\infty}^{\infty} d\omega e^{i\omega t} \int_{-\infty}^{\infty} dk_z e^{ik_z z} A_2 K_n(qr) \\
\chi_2(r, \theta, z, t) &= \frac{1}{(2\pi)^2} \sum_{n=-\infty}^{\infty} e^{in\theta} \int_{-\infty}^{\infty} d\omega e^{i\omega t} \int_{-\infty}^{\infty} dk_z e^{ik_z z} C_2 K_n(qr) \\
\gamma_2(r, \theta, z, t) &= \frac{1}{(2\pi)^2} \sum_{n=-\infty}^{\infty} e^{in\theta} \int_{-\infty}^{\infty} d\omega e^{i\omega t} \int_{-\infty}^{\infty} dk_z e^{ik_z z} B_2 K_n(qr) \quad .
\end{aligned} \tag{A.13}$$

A_2 , B_2 , and C_2 are constants which depend upon n , k_z , and ω ; q is a wavenumber. Since the potentials apply to the region extending from $r = R$ to $r = \infty$, they include K_n but not I_n which is singular at infinity. The potentials that are the solution to the wave equation in a transversely isotropic solid are assumed to have the same form.

To determine the wavenumber, the potentials are substituted into the equation of motion. To this end, the displacements are computed with equation A.12. Then the displacements are used to calculate the strain,

$$\mathbf{E}_c = \begin{pmatrix} \partial_r u_r \\ (\partial_\theta u_\theta + u_r) / 2 \\ \partial_z u_z \\ \partial_z u_\theta + \partial_\theta u_z / r \\ \partial_z u_r + \partial_r u_z \\ \partial_r u_\theta + (\partial_\theta u_r - u_\theta) / r \end{pmatrix} . \tag{A.14}$$

(The abbreviated subscript notation used in this section is described in Chapter 1.)

The strain is then used to calculate the stress,

$$\mathbf{T}_c = \mathbf{C}_c \mathbf{E}_c \tag{A.15}$$

where

$$\mathbf{T}_c = \begin{pmatrix} \tau_{rr} \\ \tau_{\theta\theta} \\ \tau_{zz} \\ \tau_{\theta z} \\ \tau_{rz} \\ \tau_{r\theta} \end{pmatrix}. \quad (\text{A.16})$$

The stiffness matrix is

$$\mathbf{C}_c = \begin{pmatrix} c_{11} & c_{12} & c_{13} & 0 & 0 & 0 \\ & c_{11} & c_{13} & 0 & 0 & 0 \\ & & c_{33} & 0 & 0 & 0 \\ & & & c_{44} & 0 & 0 \\ & & & & c_{44} & 0 \\ \text{symmetric} & & & & & c_{66} \end{pmatrix} \quad (\text{A.17})$$

with $c_{12} = c_{11} - 2c_{66}$. (The stiffness matrix in cylindrical coordinates is identical that in Cartesian coordinates, and this property can be proven using the transformation laws in Chapter 1.) Finally, the stress and displacements are substituted into the equation of motion:

$$\mathbf{D}_c \mathbf{T}_c = \rho \partial_{tt} \mathbf{u}_c \quad (\text{A.18})$$

where \mathbf{D}_c is a differential operator:

$$\mathbf{D}_c = \begin{pmatrix} \partial_r + 1/r & -1/r & 0 & 0 & \partial_z & \partial_\theta/r \\ 0 & \partial_\theta/r & 0 & \partial_z & 0 & \partial_r + 2/r \\ 0 & 0 & \partial_z & \partial_\theta/r & \partial_r + 1/r & 0 \end{pmatrix}. \quad (\text{A.19})$$

Performing this sequence of substitutions yields a system of three equations:

$$\begin{pmatrix} m_{11}(q) & m_{12}(q) & m_{13}(q) \\ m_{21}(q) & m_{22}(q) & m_{23}(q) \\ m_{31}(q) & m_{32}(q) & m_{33}(q) \end{pmatrix} \begin{pmatrix} A_2 \\ B_2 \\ C_2 \end{pmatrix} = \begin{pmatrix} 0 \\ 0 \\ 0 \end{pmatrix}. \quad (\text{A.20})$$

where

$$\begin{aligned}
m_{11}(q) &= [c_{11}q^2 - (c_{13} + 2c_{44})k_z^2 + \rho_2\omega^2] [K_{n-1}(qr) + K_{n+1}(qr)] \\
m_{12}(q) &= ik_z [(c_{11} - c_{13} - c_{44})q^2 - c_{44}k_z^2 + \rho_2\omega^2] [K_{n-1}(qr) + K_{n+1}(qr)] \\
m_{13}(q) &= i [c_{66}q^2 - c_{44}k_z^2 + \rho_2\omega^2] [K_{n-1}(qr) - K_{n+1}(qr)] \\
m_{21}(q) &= -i [c_{11}q^2 - (c_{13} + 2c_{44})k_z^2 + \rho_2\omega^2] [K_{n-1}(qr) - K_{n+1}(qr)] \\
m_{22}(q) &= k_z [(c_{11} - c_{13} - c_{44})q^2 - c_{44}k_z^2 + \rho_2\omega^2] [K_{n-1}(qr) - K_{n+1}(qr)] \quad (\text{A.21}) \\
m_{23}(q) &= [c_{66}q^2 - c_{44}k_z^2 + \rho_2\omega^2] [K_{n-1}(qr) + K_{n+1}(qr)] \\
m_{31}(q) &= ik_z [(c_{13} + 2c_{44})q^2 - c_{33}k_z^2 + \rho_2\omega^2] \\
m_{32}(q) &= -q^2 [c_{44}q^2 - (c_{33} - c_{13} - c_{44})k_z^2 + \rho_2\omega^2] \\
m_{33}(q) &= 0
\end{aligned}$$

A nontrivial solution to this system of equations exists only when the determinant of the matrix is zero. Therefore, the determinant is set to zero, and after much algebra the resulting equation is

$$(q^2 - k_z^2)(c_{66}q^2 - c_{44}k_z^2 + \rho_2\omega^2)(\mathcal{A}q^4 + \mathcal{B}\omega^2q^2 + \mathcal{C}\omega^4) = 0 \quad (\text{A.22})$$

where

$$\begin{aligned}
\mathcal{A} &= c_{11}c_{44} \\
\mathcal{B} &= \rho_2(c_{11} + c_{44}) - (c_{11}c_{33} - c_{13}^2 - 2c_{13}c_{44}) \left(\frac{k_z^2}{\omega^2} \right) \\
\mathcal{C} &= c_{33}c_{44} \left(\frac{\rho_2}{c_{44}} - \frac{k_z^2}{\omega^2} \right) \left(\frac{\rho_2}{c_{33}} - \frac{k_z^2}{\omega^2} \right) .
\end{aligned} \quad (\text{A.23})$$

Equation A.22 can be broken in three smaller equations. The first,

$$q^2 - k_z^2 = 0$$

is satisfied when $q \pm k_z$. Because this solution has no physical meaning, it will be ignored. The second equation

$$c_{66}q^2 - c_{44}k_z^2 + \rho_2\omega^2 = 0 \quad (\text{A.24})$$

is satisfied when

$$q = \bar{k}_2 = \sqrt{\frac{c_{44}k_z^2 - \rho_2\omega^2}{c_{66}}} . \quad (\text{A.25})$$

This solution applies only to potential χ_2 . (To prove this result, χ_2 is substituted into the equation of motion, and the other potentials are neglected. After taking the determinant, equation A.24 will be obtained.) Consequently χ_2 is not coupled to the other potentials.

Before continuing the derivation, the solution for χ_2 will be compared to a similar solution for plane wave propagation. The displacements associated with χ_2 , which are calculated with equation A.12, are

$$\mathbf{u}_c = \frac{1}{r} \frac{\partial \chi_2}{\partial \theta} \mathbf{r} + \frac{\partial \chi_2}{\partial r} \mathbf{\Theta} \quad (\text{A.26})$$

where \mathbf{r} and $\mathbf{\Theta}$ are the unit vectors in the r and θ directions. This equation shows that the motion associated with χ_2 does not occur in the z direction. Furthermore, because these displacements were calculated with the curl operator, their motion is transverse to the propagation direction. Therefore, the cylindrical wave derived from χ_2 is analogous to the planar S_2 -wave (see Chapter 1), which is also uncoupled from the other planar waves (see e.g., White, 1983, p. 38-45).

To understand why the square root is positive in equation A.25, consider the asymptotic expansion for K_n in equation A.13:

$$K_n(z) \sim \sqrt{\frac{\pi}{2z}} e^{-z}$$

which is valid for large $|z|$ and $|\arg z| < 3\pi/2$ (Abramowitz and Stegun, 1972, p. 377-378). If the argument of the square root function is positive and the positive root is taken, then $K_n(\bar{k}_2 r)$ will decay as r increases; this solution corresponds to a normal mode. However, if the argument of the square root function is positive and the negative root is taken, then $K_n(\bar{k}_2 r)$ will increase as r increases; and because this solution does not correspond to any mode, the negative root is ignored. A similar result applies when the argument of the square root function is negative.

The third equation, which can be obtained from equation A.22, is

$$\mathcal{A}q^4 + \mathcal{B}\omega^2 q^2 + \mathcal{C}\omega^4 = 0 \quad (\text{A.27})$$

and is satisfied when

$$q = m_2 = \omega \sqrt{\frac{-\mathcal{B} + \sqrt{\mathcal{B}^2 - 4\mathcal{A}\mathcal{C}}}{2\mathcal{A}}} \quad (\text{A.28})$$

or

$$q = k_2 = \omega \sqrt{\frac{-\mathcal{B} - \sqrt{\mathcal{B}^2 - 4\mathcal{A}\mathcal{C}}}{2\mathcal{A}}} . \quad (\text{A.29})$$

The positive square root was chosen for these wavenumbers for the same reason that it was chosen for \bar{k}_2 . These wavenumbers apply to potentials ϕ_2 and γ_2 , and the most general solution for these potentials in the transform domain is

$$\Phi_2(r, n, k_z, \omega) = A_2 K_n(m_2 r) + A'_2 K_n(k_2 r) \quad (\text{A.30})$$

$$\Gamma_2(r, n, k_z, \omega) = B'_2 K_n(m_2 r) + B_2 K_n(k_2 r) . \quad (\text{A.31})$$

These equations are not completely independent because they were derived from a more general equation than the equation of motion. That is, the equation of motion in terms of these potentials contains derivatives of third and fourth order whereas the equation of motion in terms of displacements only contains derivatives of second order.

To find how these coefficients are related, $\Phi_2(r, n, k_z, \omega)$ and $\Gamma_2(r, n, k_z, \omega)$ must be substituted into equation of motion. To avoid an enormous amount of algebra, a few changes in the equations can be made. Because the solutions for ϕ_2 and γ_2 are independent of that for χ_2 , the only part of equation A.20 that is needed is

$$\begin{pmatrix} m_{11}(q) & m_{12}(q) \\ m_{21}(q) & m_{22}(q) \\ m_{31}(q) & m_{32}(q) \end{pmatrix} \begin{pmatrix} A_2 \\ B_2 \end{pmatrix} = \begin{pmatrix} 0 \\ 0 \\ 0 \end{pmatrix} . \quad (\text{A.32})$$

The first two equations in this system are linearly dependent, and this redundancy is removed with some algebra. The new system of equations is

$$\begin{pmatrix} \hat{m}_{11}(q) & \hat{m}_{12}(q) \\ m_{31}(q) & m_{32}(q) \end{pmatrix} \begin{pmatrix} A_2 \\ B_2 \end{pmatrix} = \begin{pmatrix} 0 \\ 0 \end{pmatrix} \quad (\text{A.33})$$

where

$$\hat{m}_{11}(q) = c_{11}q^2 - (c_{13} + 2c_{44})k_z^2 + \rho_2\omega^2 \quad (\text{A.34})$$

$$\hat{m}_{12}(q) = \imath k_z(c_{11} - c_{13} - c_{44})q^2 - c_{44}k_z^2 + \rho_2\omega^2 \quad . \quad (\text{A.35})$$

(Because the determinant of this matrix is the left hand side of equation A.27, no fundamental changes have been made.) When $\Phi_2(r, n, k_z, \omega)$ and $\Gamma_2(r, n, k_z, \omega)$ are substituted into the equation of motion, the result is

$$\begin{pmatrix} \hat{m}_{11}(m_2) & \hat{m}_{11}(k_2) & \hat{m}_{12}(m_2) & \hat{m}_{12}(k_2) \\ m_{31}(m_2) & m_{31}(k_2) & m_{32}(m_2) & m_{32}(k_2) \end{pmatrix} \begin{pmatrix} A_2 \\ A'_2 \\ B'_2 \\ B_2 \end{pmatrix} = \begin{pmatrix} 0 \\ 0 \end{pmatrix} \quad . \quad (\text{A.36})$$

If

$$\begin{aligned} A'_2 &= -\frac{\hat{m}_{12}(k_2)}{\hat{m}_{11}(k_2)}B_2 \\ B'_2 &= -\frac{\hat{m}_{11}(m_2)}{\hat{m}_{12}(m_2)}A_2 \quad , \end{aligned} \quad (\text{A.37})$$

then the system of equations reduces to

$$\left(\hat{m}_{11}(m_2) - \hat{m}_{12}(m_2) \frac{\hat{m}_{11}(m_2)}{\hat{m}_{12}(m_2)} \right) A_2 + \left(\hat{m}_{11}(k_2) - \hat{m}_{12}(k_2) \frac{\hat{m}_{11}(k_2)}{\hat{m}_{12}(k_2)} \right) B_2 = 0 \quad (\text{A.38})$$

$$\left(\hat{m}_{31}(m_2) - \hat{m}_{32}(m_2) \frac{\hat{m}_{11}(m_2)}{\hat{m}_{12}(m_2)} \right) A_2 + \left(\hat{m}_{32}(k_2) - \hat{m}_{31}(m_2) \frac{\hat{m}_{12}(k_2)}{\hat{m}_{11}(k_2)} \right) B_2 = 0 \quad (\text{A.39})$$

The coefficients in the first equation equal zero. The coefficients in the second equation also equal zero because they can be derived from the determinant of the matrix in equation A.33. Therefore, A_2 and B_2 are arbitrary as they should be, and the relations in equations A.37 are correct. In summary, the potentials in the transform domain are

$$\Phi_2(r, n, k_z, \omega) = A_2 K_n(m_2 r) + b' B_2 K_n(k_2 r) \quad (\text{A.40})$$

$$\Gamma_2(r, n, k_z, \omega) = a' A_2 K_n(m_2 r) + B_2 K_n(k_2 r) \quad (\text{A.41})$$

where the coupling coefficients are

$$\begin{aligned} a' &= -\frac{1}{ik_z} \frac{(c_{13} + 2c_{44})k_z^2 - c_{11}m_2^2 - \rho_2\omega^2}{c_{44}k_z^2 - (c_{11} - c_{13} - c_{44})m_2^2 - \rho_2\omega^2} \\ b' &= -ik_z \frac{c_{44}k_z^2 - (c_{11} - c_{13} - c_{44})k_2^2 - \rho_2\omega^2}{(c_{13} + 2c_{44})k_z^2 - c_{11}k_2^2 - \rho_2\omega^2} . \end{aligned} \quad (\text{A.42})$$

(When the solid is isotropic, $a' = b' = 0$.)

These solutions for cylindrical waves can be compared to similar solutions for plane waves. In a transversely isotropic solid, the displacements computed from γ_2 have components which are parallel and perpendicular to the propagation direction. The magnitudes of these components depend upon the coupling coefficients, which in turn depend upon the amount of anisotropy. Similarly, a planar qS_1 wave has components which are parallel and perpendicular to the propagation direction, and the magnitudes of these components also depend upon the amount of anisotropy. The relationship between the displacement potential, ϕ_2 , and the planar qP -wave can be demonstrated with an analogous argument.

Using equation A.12 the displacements in the transform domain are calculated:

$$\begin{aligned} U_r(r, n, k_z, \omega) &= -A_2 m_2 (1 + ik_z a') \left[-\frac{n}{m_2 r} K_n(m_2 r) + K_{n+1}(m_2 r) \right] + \\ &\quad \frac{C_2 n}{r} K_n(\bar{k}_2 r) - B_2 k_2 (ik_z + b') \left[-\frac{n}{k_2 r} K_n(k_2 r) + K_{n+1}(k_2 r) \right] \\ U_\theta(r, n, k_z, \omega) &= -\frac{A_2 n}{r} (1 + ik_z a') K_n(m_2 r) + \\ &\quad C_2 \bar{k}_2 \left[-\frac{n}{k_2 r} K_n(\bar{k}_2 r) + K_{n+1}(\bar{k}_2 r) \right] - \frac{B_2 n}{r} (ik_z + b') K_n(k_2 r) \\ U_z(r, n, k_z, \omega) &= A_2 (ik_z - a' m_2^2) K_n(m_2 r) - B_2 (k_2^2 - ik_z b') K_n(k_2 r) . \end{aligned} \quad (\text{A.43})$$

A.3 Dispersion Equation

In this section the dispersion equation will be derived by satisfying the two boundary conditions at the fluid-solid interface. The first boundary condition is that the displacements, which are normal to the interface, are continuous:

$$u_r^{\text{fluid}} = u_r^{\text{solid}} . \quad (\text{A.44})$$

The second boundary condition is that the traction at the interface is normal to the interface and is continuous:

$$\begin{aligned} -p^{\text{fluid}} &= \tau_{rr}^{\text{solid}} \\ 0 &= \tau_{r\theta}^{\text{solid}} \\ 0 &= \tau_{rz}^{\text{solid}} \end{aligned} \quad (\text{A.45})$$

Equations A.6, A.11 and A.43 are substituted into these boundary conditions giving a system of four equations

$$\begin{pmatrix} n_{11} & n_{12} & n_{13} & n_{14} \\ n_{21} & n_{22} & n_{23} & n_{24} \\ n_{31} & n_{32} & n_{33} & n_{34} \\ n_{41} & n_{42} & n_{43} & n_{44} \end{pmatrix} \begin{pmatrix} A_1 \\ A_2 \\ C_2 \\ B_2 \end{pmatrix} = \begin{pmatrix} 0 \\ 0 \\ 0 \\ 0 \end{pmatrix} \quad (\text{A.46})$$

where

$$\begin{aligned} n_{11} &= m_1 W_1(m_1 R) \\ n_{12} &= (1 + \imath k_z a') m_2 Y_1(m_2 R) \\ n_{13} &= -\frac{n}{R} K_n(\bar{k}_2 R) \\ n_{14} &= (\imath k_z + b') k_2 Y_1(k_2 R) \\ n_{21} &= \lambda_1 (m_1^2 - k_z^2) I_n(m_1 R) \\ n_{22} &= -\left[c_{11} m_2^2 - c_{13} k_z^2 + (c_{11} - c_{13}) \imath k_z a' m_2^2 \right] K_n(m_2 R) - \\ &\quad \frac{2c_{66} m_2}{R} (1 + \imath k_z a') Y_2(m_2 R) \\ n_{23} &= 2c_{66} n \bar{k}_2^2 Y_3(\bar{k}_2 R) \\ n_{24} &= -\left[(c_{11} k_2^2 - c_{13} k_z^2) b' + (c_{11} - c_{13}) \imath k_z k_2^2 \right] K_n(k_2 R) - \\ &\quad \frac{2c_{66} k_2}{R} (\imath k_z + b') Y_2(k_2 R) \\ n_{31} &= 0 \\ n_{32} &= \frac{2c_{66} n m_2}{R} (1 + \imath k_z a') Y_4(m_2 R) \\ n_{33} &= -c_{66} \bar{k}_2^2 Y_5(\bar{k}_2 R) \end{aligned} \quad (\text{A.47})$$

$$\begin{aligned}
n_{34} &= \frac{2c_{66}nk_2}{R}(\imath k_z + b')Y_4(k_2R) \\
n_{41} &= 0 \\
n_{42} &= -c_{44}m_2 \left[2\imath k_z - a'(k_z^2 + m_2^2) \right] Y_1(m_2R) \\
n_{43} &= \frac{\imath k_z n c_{44}}{R} K_n(\bar{k}_2R) \\
n_{44} &= c_{44}k_2 \left[(k_z^2 + k_2^2) - 2\imath k_z b' \right] Y_1(k_2R)
\end{aligned}$$

and where

$$\begin{aligned}
W_1(x) &= \frac{n}{x}I_n(x) + I_{n+1}(x) \\
Y_1(x) &= -\frac{n}{x}K_n(x) + K_{n+1}(x) \\
Y_2(x) &= \frac{n(n-1)}{x}K_n(x) + K_{n+1}(x) \\
Y_3(x) &= \frac{-n+1}{x^2}K_n(x) + \frac{1}{x}K_{n+1}(x) \\
Y_4(x) &= \frac{-n+1}{x}K_n(x) + K_{n+1}(x) \\
Y_5(x) &= \left[1 + \frac{2n(n-1)}{x^2} \right] K_n(x) + \frac{2}{x}K_{n+1}(x) \quad .
\end{aligned} \tag{A.48}$$

A nontrivial solution to this system of equations exists when the determinant of the matrix is zero. Therefore, the determinant is set to zero, and the resulting equation is called the dispersion equation. The wavenumbers, k_z , satisfying the dispersion equation are found numerically.

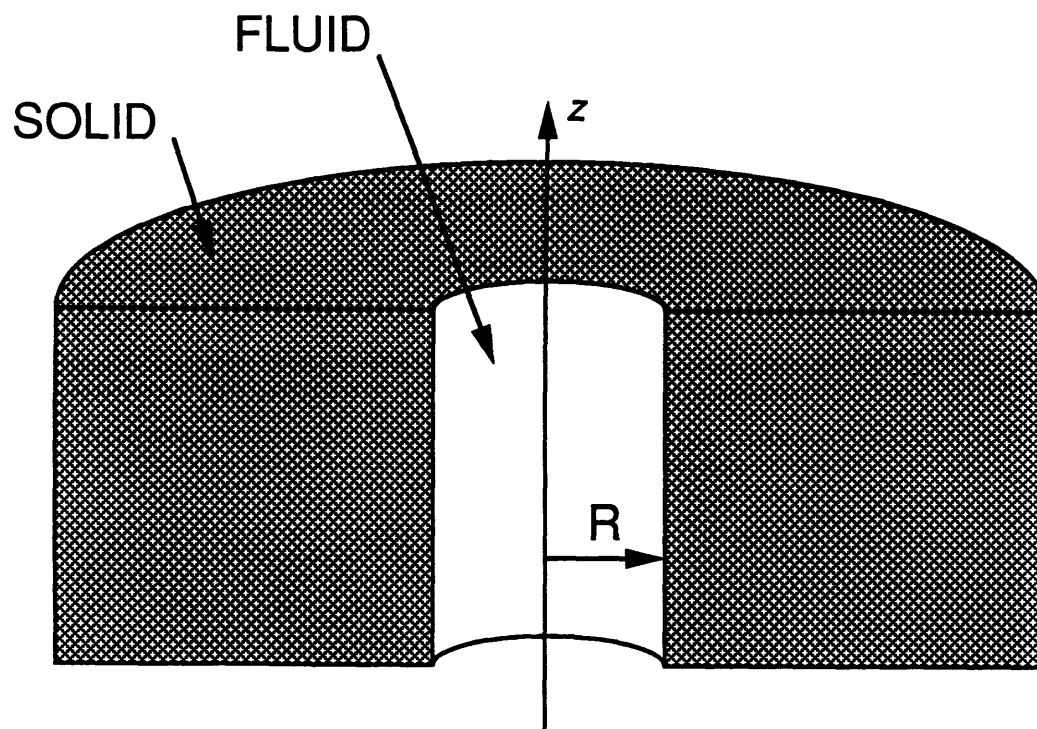


Figure A-1: Borehole model showing the orientation of the z axis of the circular cylindrical coordinate system. The radius of the borehole is R .

Appendix B

Evaluation of an Integrand in the Perturbation Equation

In this appendix, the integrand, $[n_j \tau_{ji} \delta u_i]_-^+$, which appears in equation 2.10, will be manipulated to remove the unknown, δu_i . Woodhouse and Dahlen (1978) presented the solution without any derivation; here the derivation will be given in detail.

The boundary conditions on the perturbed interfaces will be expressed in terms of the boundary conditions on the unperturbed interfaces. These equations were published by Smith (1974) and Dahlen (1976). On a perturbed, welded interface (i.e., a solid-solid interface) the displacements are continuous:

$$[u_i + \delta u_i + h n_k u_{i,k}]_-^+ = 0 \quad . \quad (\text{B.1})$$

The second term is the perturbation in the displacement due to the perturbed interface, and the third term is a linear extrapolation of the original displacement from the original to the perturbed interface. Because $[u_i]_-^+ = 0$,

$$[\delta u_i]_-^+ = [-h n_k u_{i,k}]_-^+ \quad . \quad (\text{B.2})$$

On a perturbed, frictionless interface (i.e., a fluid-solid interface) the normal component of displacement is continuous:

$$[(n_i - h_{,i})(u_i + \delta u_i + h n_k u_{i,k})]_-^+ = 0 \quad . \quad (\text{B.3})$$

The term, $-h_{,i}$, is the change in the normal between the perturbed and unperturbed interfaces, and $h_{,i} = h_{,i} - n_i(n_j h_{,j})$. To first order, this equation is

$$[n_i \delta u_i]_-^+ = [-h n_i n_k u_{i,k} + h_{,i} u_i]_-^+ \quad (\text{B.4})$$

because $[n_i u_i]_-^+ = 0$. On all perturbed interfaces the traction is continuous:

$$[(n_i - h_{,i})(\tau_{ij} + \delta \tau_{ij} + h n_k \tau_{ij,k})]_-^+ = 0 \quad (\text{B.5})$$

The second term in the expression for the stress, $\delta \tau_{ij}$, is the perturbation in the stress due to the perturbed interface, and the third term is a linear extrapolation of the original stress from the original to the perturbed interface. To first order, this equation is

$$[n_i \delta \tau_{ij}]_-^+ = [-h n_i n_k \tau_{ij,k} + h_{,i} \tau_{ij}]_-^+ \quad (\text{B.6})$$

because $[n_i \tau_{ij}]_-^+ = 0$.

These boundary conditions will now be used to derive an expression for $[n_j \tau_{ji} \delta u_i]_-^+$. On a welded interface, equation B.2 may be directly substituted into $[n_j \tau_{ji} \delta u_i]_-^+$:

$$[n_j \tau_{ji} \delta u_i]_-^+ = [-h n_j \tau_{ji} n_k u_{i,k}]_-^+ \quad (\text{B.7})$$

The traction, T_i , will be used to simplify the derivation for a frictionless interface. Because the traction is normal to the interface,

$$[T_i \delta u_i]_-^+ = [n_j T_j n_i \delta u_i]_-^+ \quad (\text{B.8})$$

Equation B.4 is substituted into the previous equation:

$$[T_i \delta u_i]_-^+ = [-h T_i n_k u_{i,k} + h_{,i} u_i n_j T_j]_-^+ \quad (\text{B.9})$$

and the traction is replaced by the normal component of the stress:

$$[n_j \tau_{ji} \delta u_i]_-^+ = [-h n_j \tau_{ji} n_k u_{i,k} + h_{,i} u_i n_j n_k \tau_{kj}]_-^+ \quad (\text{B.10})$$

On a welded interface, this equation would reduce to equation B.7 because the last term would be zero. Therefore, equation B.10 holds for all interfaces.

Appendix C

Evaluation of the Integrals in the Perturbation Equation

The integrals in the perturbation equation (2.11) will be evaluated in this appendix for the two-layer model of the borehole environment (Figure 2-1).

The real displacements have this general form:

$$\begin{aligned} u_r(r, \theta, z, t) &= \frac{1}{2} \left[U_r(r, n, k_z, \omega) e^{ik_z z} + U_r^*(r, n, k_z, \omega) e^{-ik_z z} \right] \cos(n\theta) \cos(\omega t) \\ u_\theta(r, \theta, z, t) &= \frac{1}{2} \left[U_\theta(r, n, k_z, \omega) e^{ik_z z} + U_\theta^*(r, n, k_z, \omega) e^{-ik_z z} \right] \sin(n\theta) \cos(\omega t) \quad (\text{C.1}) \\ u_z(r, \theta, z, t) &= \frac{1}{2} \left[U_z(r, n, k_z, \omega) e^{ik_z z} + U_z^*(r, n, k_z, \omega) e^{-ik_z z} \right] \cos(n\theta) \cos(\omega t) \quad . \end{aligned}$$

To simplify the notation, the Fourier transforms of the displacements will be designated simply U_r , U_θ , and U_z and are given in equations A.6 and A.43. The strains are found by differentiating the displacements, and their transforms will be designated E_{rr} , $E_{\theta\theta}$, E_{zz} , $E_{z\theta}$, E_{rz} , and $E_{r\theta}$. The displacements and strains are substituted into equation 2.11, and almost all of the integrals are computed analytically. In the final expressions for the integrals, ζ is 2 when $n = 0$; otherwise ζ is 1. When $n = 0$, all displacements and strains containing $\sin(n\theta)$ cancel. Because the transforms of these particular displacements and strains are also zero when $n = 0$, they may be included in the integrals eliminating the need to write the equations twice.

The integral associated with a perturbation in wavenumber is

$$\int_t^{t+T} dt \int_V dV \delta_{k_z} e_{ji} c_{ijkl} e_{lk} = \delta_{k_z} \frac{\zeta \pi \Lambda T}{4} I^{k_z} \quad (\text{C.2})$$

where

$$\begin{aligned} I^{k_z} = & \int_0^R dr r \lambda_1 \left[|E_{rr}| |iU_z| \cos(\arg E_{rr} - \arg(iU_z)) + \right. \\ & |E_{\theta\theta}| |iU_z| \cos(\arg E_{\theta\theta} - \arg(iU_z)) + \\ & \left. |E_{zz}| |iU_z| \cos(\arg E_{zz} - \arg(iU_z)) \right] + \\ & \int_R^\infty dr r \left\{ c_{13} \left[|E_{rr}| |iU_z| \cos(\arg E_{rr} - \arg(iU_z)) + \right. \right. \\ & |E_{\theta\theta}| |iU_z| \cos(\arg E_{\theta\theta} - \arg(iU_z)) \left. \right] + \\ & c_{33} \left[|E_{zz}| |iU_z| \cos(\arg E_{zz} - \arg(iU_z)) \right] + \\ & c_{44} \left[2 |E_{z\theta}| |iU_\theta| \cos(\arg E_{z\theta} - \arg(\frac{iU_\theta}{2})) + \right. \\ & \left. \left. 2 |E_{rz}| |iU_r| \cos(\arg E_{rz} - \arg(\frac{iU_r}{2})) \right] \right\} . \end{aligned}$$

The integral associated with a perturbation in frequency is

$$\int_t^{t+T} dt \int_V dV \rho u_i u_i = \frac{\zeta \pi \Lambda T}{4} I^\omega \quad (\text{C.3})$$

where

$$I^\omega = \int_0^\infty dr r \rho (|U_r|^2 + |U_\theta|^2 + |U_z|^2) . \quad (\text{C.4})$$

Two integrals are associated with perturbations in the boundary locations. To write these two integrals, this notation will be helpful:

$$I_{cc} = \int_0^{2\pi} d\theta \cos^2(n\theta) h \quad (\text{C.5})$$

$$I_{ss} = \int_0^{2\pi} d\theta \sin^2(n\theta) h \quad (\text{C.6})$$

$$I_{cs} = \int_0^{2\pi} d\theta \cos(n\theta) \sin(n\theta) \frac{dh}{d\theta} , \quad (\text{C.7})$$

in which h is only a function of azimuth. The first integral is

$$\int_t^{t+T} dt \int_{\Sigma^i} dS h \left[\mathcal{L} + n_i \tau_{ij} n_k u_{j,k} \right]_-^+ = \frac{\Lambda T}{4} I^{\Sigma^i, 1} \quad (\text{C.8})$$

where

$$\begin{aligned}
I^{\Sigma^*,1} = & \frac{R}{2} \left[\rho \omega^2 \left[I_{cc} |U_r|^2 + I_{ss} |U_\theta|^2 + I_{cc} |U_z|^2 \right] - \right. \\
& c_{11} I_{cc} \left[-|E_{rr}|^2 + |E_{\theta\theta}|^2 \right] - \\
& c_{13} I_{cc} \left[2|E_{\theta\theta}| |E_{zz}| \cos(E_{\theta\theta} - \arg E_{zz}) \right] - \\
& c_{33} I_{cc} \left[|E_{zz}|^2 \right] - \\
& c_{44} \left[4I_{ss} |E_{z\theta}|^2 + 4I_{cc} |E_{rz}|^2 \right] - \\
& \left. c_{66} I_{ss} \left[4|E_{r\theta}|^2 \right] \right]_{-}^{+}.
\end{aligned}$$

The second integral is

$$\int_t^{t+T} dt \int_{\Sigma^*} dS h_{;i} \left[u_i n_j n_k \tau_{kj} \right]_{-}^{+} = \frac{\Lambda T}{4} I^{\Sigma^*,2} \quad (C.9)$$

where

$$\begin{aligned}
I^{\Sigma^*,2} = & I_{cs} \left[c_{11} \left[|E_{rr}| |U_\theta| \cos(\arg E_{rr} - \arg U_\theta) + \right. \right. \\
& \left. |E_{\theta\theta}| |U_\theta| \cos(\arg E_{\theta\theta} - \arg U_\theta) \right] + \\
& c_{13} \left[|E_{zz}| |U_\theta| \cos(\arg E_{zz} - \arg U_\theta) \right] + \\
& \left. c_{66} \left[-2|E_{\theta\theta}| |U_\theta| \cos(\arg E_{\theta\theta} - \arg U_\theta) \right] \right]_{-}^{+}.
\end{aligned}$$

The integral associated with a perturbation in density is

$$\int_t^{t+T} dt \int_V dV \delta \rho u_i u_i = \frac{\zeta \pi \Lambda T}{4} (\delta \rho_1 I^{\rho_1} + \delta \rho_2 I^{\rho_2}) \quad (C.10)$$

where

$$\begin{aligned}
I^{\rho_1} &= \int_0^R dr r \left(|U_r|^2 + |U_\theta|^2 + |U_z|^2 \right) \\
I^{\rho_2} &= \int_R^\infty dr r \left(|U_r|^2 + |U_\theta|^2 + |U_z|^2 \right).
\end{aligned}$$

The integral, in which the incompressibility of the fluid and the five elastic moduli of the transversely isotropic solid are perturbed, is

$$\int_t^{t+T} dt \int_V dV e_{ij} \delta c_{ijkl}^{TI} e_{kl} = \quad (C.11)$$

$$\frac{\zeta \pi \Lambda \mathcal{T}}{4} \left(\delta \lambda_1 I^{\lambda_1} + \delta c_{11}^{TI} I^{c_{11}^{TI}} + \delta c_{33}^{TI} I^{c_{33}^{TI}} + \delta c_{13}^{TI} I^{c_{13}^{TI}} + \delta c_{44}^{TI} I^{c_{44}^{TI}} + \delta c_{66}^{TI} I^{c_{66}^{TI}} \right)$$

where

$$\begin{aligned} I^{\lambda_1} &= \int_0^R dr r \left[|E_{rr}|^2 + |E_{\theta\theta}|^2 + |E_{zz}|^2 + \right. \\ &\quad 2|E_{rr}||E_{\theta\theta}| \cos(\arg E_{rr} - \arg E_{\theta\theta}) + \\ &\quad 2|E_{rr}||E_{zz}| \cos(\arg E_{rr} - \arg E_{zz}) + \\ &\quad \left. 2|E_{\theta\theta}||E_{zz}| \cos(\arg E_{\theta\theta} - \arg E_{zz}) \right] \\ I^{c_{11}^{TI}} &= \int_R^\infty dr r \left[|E_{rr}|^2 + |E_{\theta\theta}|^2 + 2|E_{rr}||E_{\theta\theta}| \cos(\arg E_{rr} - \arg E_{\theta\theta}) \right] \\ I^{c_{33}^{TI}} &= \int_R^\infty dr r \left[|E_{zz}|^2 \right] \\ I^{c_{13}^{TI}} &= \int_R^\infty dr r \left[2|E_{rr}||E_{zz}| \cos(\arg E_{rr} - \arg E_{zz}) + \right. \\ &\quad \left. 2|E_{\theta\theta}||E_{zz}| \cos(\arg E_{\theta\theta} - \arg E_{zz}) \right] \\ I^{c_{44}^{TI}} &= \int_R^\infty dr r \left[4|E_{z\theta}|^2 + 4|E_{rz}|^2 \right] \\ I^{c_{66}^{TI}} &= \int_R^\infty dr r \left[4|E_{r\theta}|^2 - 4|E_{rr}||E_{\theta\theta}| \cos(\arg E_{rr} - \arg E_{\theta\theta}) \right] \quad . \end{aligned}$$

The integral, in which the elastic moduli are perturbed to make the solid have general anisotropy, is

$$\int_t^{t+T} dt \int_V dV e_{ji} \delta c_{ijkl} e_{lk} = \frac{\zeta \pi \Lambda \mathcal{T}}{4} I^{c_{IJ}} \quad (C.12)$$

where

$$\begin{aligned} I^{c_{IJ}} &= \int_R^\infty dr r \left\{ d_{11} |E_{rr}|^2 + \right. \\ &\quad d_{12} 2|E_{rr}||E_{\theta\theta}| \cos(\arg E_{rr} - \arg E_{\theta\theta}) + \\ &\quad d_{13} 2|E_{rr}||E_{zz}| \cos(\arg E_{rr} - \arg E_{zz}) + \\ &\quad \left. d_{16} 4|E_{rr}||E_{r\theta}| \cos(\arg E_{rr} - \arg E_{r\theta}) + \right. \end{aligned}$$

$$\begin{aligned}
& d_{22}|E_{\theta\theta}|^2 + \\
& d_{23}2|E_{\theta\theta}||E_{zz}|\cos(\arg E_{\theta\theta} - \arg E_{zz}) + \\
& d_{26}4|E_{\theta\theta}||E_{r\theta}|\cos(\arg E_{\theta\theta} - \arg E_{r\theta}) + \\
& d_{33}|E_{zz}|^2 + \\
& d_{36}4|E_{zz}||E_{r\theta}|\cos(\arg E_{zz} - \arg E_{r\theta}) + \\
& d_{44}4|E_{z\theta}|^2 + \\
& d_{45}8|E_{z\theta}||E_{rz}|\cos(\arg E_{z\theta} - \arg E_{rz}) + \\
& d_{55}4|E_{rz}|^2 + \\
& d_{66}4|E_{r\theta}|^2 \} .
\end{aligned}$$

When $n = 0$,

$$\begin{aligned}
d_{11} &= \frac{1}{2}\delta c_{66} + \frac{3}{8}\delta c_{22} + \frac{1}{4}\delta c_{12} + \frac{3}{8}\delta c_{11} \\
d_{12} &= -\frac{1}{2}\delta c_{66} + \frac{1}{8}\delta c_{22} + \frac{3}{4}\delta c_{12} + \frac{1}{8}\delta c_{11} \\
d_{13} &= \frac{1}{2}\delta c_{23} + \frac{1}{2}\delta c_{13} \\
d_{16} &= 0 \\
d_{22} &= \frac{1}{2}\delta c_{66} + \frac{3}{8}\delta c_{22} + \frac{1}{4}\delta c_{12} + \frac{3}{8}\delta c_{11} \\
d_{23} &= \frac{1}{2}\delta c_{23} + \frac{1}{2}\delta c_{13} \\
d_{26} &= 0 \\
d_{33} &= \delta c_{33} \\
d_{36} &= 0 \\
d_{44} &= 0 \\
d_{45} &= 0 \\
d_{55} &= \frac{1}{2}\delta c_{55} + \frac{1}{2}\delta c_{44} \\
d_{66} &= 0 ,
\end{aligned} \tag{C.13}$$

and when $n = 1$,

$$\begin{aligned}
d_{11} &= \frac{1}{2}\delta c_{66} + \frac{1}{8}\delta c_{22} + \frac{1}{4}\delta c_{12} + \frac{5}{8}\delta c_{11} \\
d_{12} &= -\frac{1}{2}\delta c_{66} + \frac{1}{8}\delta c_{22} + \frac{3}{4}\delta c_{12} + \frac{1}{8}\delta c_{11} \\
d_{13} &= \frac{1}{4}\delta c_{23} + \frac{3}{4}\delta c_{13} \\
d_{16} &= \frac{1}{8}\delta c_{22} - \frac{1}{8}\delta c_{11} \\
d_{22} &= \frac{1}{2}\delta c_{66} + \frac{5}{8}\delta c_{22} + \frac{1}{4}\delta c_{12} + \frac{1}{8}\delta c_{11} \\
d_{23} &= \frac{3}{4}\delta c_{23} + \frac{1}{4}\delta c_{13} \\
d_{26} &= \frac{1}{8}\delta c_{22} - \frac{1}{8}\delta c_{11} \\
d_{33} &= \delta c_{33} \\
d_{36} &= \frac{1}{4}\delta c_{23} - \frac{1}{4}\delta c_{13} \\
d_{44} &= \frac{3}{4}\delta c_{55} + \frac{1}{4}\delta c_{44} \\
d_{45} &= \frac{1}{4}\delta c_{44} - \frac{1}{4}\delta c_{55} \\
d_{55} &= \frac{3}{4}\delta c_{55} + \frac{1}{4}\delta c_{44} \\
d_{66} &= \frac{1}{2}\delta c_{66} + \frac{1}{8}\delta c_{22} - \frac{1}{4}\delta c_{12} + \frac{1}{8}\delta c_{11} \quad ,
\end{aligned} \tag{C.14}$$

and when $n = 2$,

$$\begin{aligned}
d_{11} &= \frac{1}{4}\delta c_{66} + \frac{7}{16}\delta c_{22} + \frac{1}{8}\delta c_{12} + \frac{7}{16}\delta c_{11} \\
d_{12} &= -\frac{1}{4}\delta c_{66} + \frac{1}{16}\delta c_{22} + \frac{7}{8}\delta c_{12} + \frac{1}{16}\delta c_{11} \\
d_{13} &= \frac{1}{2}\delta c_{23} + \frac{1}{2}\delta c_{13} \\
d_{16} &= \frac{1}{4}\delta c_{66} - \frac{1}{16}\delta c_{22} + \frac{1}{8}\delta c_{12} - \frac{1}{16}\delta c_{11} \\
d_{22} &= \frac{1}{4}\delta c_{66} + \frac{7}{16}\delta c_{22} + \frac{1}{8}\delta c_{12} + \frac{7}{16}\delta c_{11} \\
d_{23} &= \frac{1}{2}\delta c_{23} + \frac{1}{2}\delta c_{13} \\
d_{26} &= -\frac{1}{4}\delta c_{66} + \frac{1}{16}\delta c_{22} - \frac{1}{8}\delta c_{12} + \frac{1}{16}\delta c_{11}
\end{aligned} \tag{C.15}$$

$$d_{33} = \delta c_{33}$$

$$d_{36} = 0$$

$$d_{44} = \frac{1}{2}\delta c_{55} + \frac{1}{2}\delta c_{44}$$

$$d_{45} = 0$$

$$d_{55} = \frac{1}{2}\delta c_{55} + \frac{1}{2}\delta c_{44}$$

$$d_{66} = \frac{1}{4}\delta c_{66} + \frac{3}{16}\delta c_{22} - \frac{3}{8}\delta c_{12} + \frac{3}{16}\delta c_{11} \quad .$$

Appendix D

Separability of the Wave Equation

In this appendix the separability of the the wave equation in cylindrical coordinates will be studied when the waves are propagating in a solid whose anisotropy is defined in Cartesian coordinates.

Using the separation of variables technique (see e.g., Mathews and Walker, 1970, p. 226-239; Ben-menahem and Singh, 1981, p. 47-62), the displacements will be assumed to be separable in z and t :

$$u_r(r, \theta, z, t) = \frac{1}{(2\pi)^2} \int_{-\infty}^{\infty} d\omega \int_{-\infty}^{\infty} dk_z U_r(r, \theta, k_z, \omega) e^{i(k_z z - \omega t)} \quad (\text{D.1})$$

$$u_\theta(r, \theta, z, t) = \frac{1}{(2\pi)^2} \int_{-\infty}^{\infty} d\omega \int_{-\infty}^{\infty} dk_z U_\theta(r, \theta, k_z, \omega) e^{i(k_z z - \omega t)} \quad (\text{D.2})$$

$$u_z(r, \theta, z, t) = \frac{1}{(2\pi)^2} \int_{-\infty}^{\infty} d\omega \int_{-\infty}^{\infty} dk_z U_z(r, \theta, k_z, \omega) e^{i(k_z z - \omega t)} . \quad (\text{D.3})$$

To verify this assumption, the displacements will be substituted into the wave equation. To this end, the displacements will be used to calculate the strain which will be used to calculate the stress and the divergence of the stress. The tensors will be expressed in abbreviated subscript notation, which is described in Chapter 1.

Using the expressions for the displacements, the strain vector is

$$\mathbf{E}_c(r, \theta, z, t) = \frac{1}{(2\pi)^2} \int_{-\infty}^{\infty} d\omega \int_{-\infty}^{\infty} dk_z [\mathbf{E}_{c1}(r, \theta, k_z, \omega) + ik_z \mathbf{E}_{2c}(r, \theta, k_z, \omega)] e^{i(k_z z - \omega t)} \quad (\text{D.4})$$

where

$$\mathbf{E}_{c1}(r, \theta, k_z, \omega) = \begin{pmatrix} \partial_r U_r \\ (\partial_\theta U_\theta + U_r)/2 \\ 0 \\ \partial_\theta U_z / r \\ \partial_r U_z \\ \partial_r U_\theta + (\partial_\theta U_r - U_\theta)/r \end{pmatrix} \quad (\text{D.5})$$

$$\mathbf{E}_{c2}(r, \theta, k_z, \omega) = \begin{pmatrix} 0 \\ 0 \\ U_z \\ U_\theta \\ U_r \\ 0 \end{pmatrix} \quad (\text{D.6})$$

(see equation 1.12).

The stiffness matrix in cylindrical coordinates, $\mathbf{C}_c(\theta)$, is computed from the stiffness matrix in Cartesian coordinates, \mathbf{C} using this property: at a point in space, the components of a tensor in cylindrical coordinates equal the components of the equivalent tensor in Cartesian coordinates when the axes of the Cartesian and cylindrical coordinate systems are aligned (Malvern, 1969, p. 531). This alignment is performed with equation 1.28:

$$\mathbf{C}_c(\theta) = \mathbf{M}(\theta) \mathbf{C} \mathbf{M}^T(\theta) \quad (\text{D.7})$$

where $\mathbf{M}(\theta)$ is given in equation 1.29 .

The stress is calculated with Hooke's Law (equation 1.17):

$$\mathbf{T}_c(r, \theta, z, t) = \frac{1}{(2\pi)^2} \int_{-\infty}^{\infty} d\omega \int_{-\infty}^{\infty} dk_z \mathbf{C}_c(\theta) [\mathbf{E}_{c1}(r, \theta, k_z, \omega) + ik_z \mathbf{E}_{c2}(r, \theta, k_z, \omega)] e^{i(k_z z - \omega t)} \quad (\text{D.8})$$

The operator which is used to calculate the divergence of the stress (equation 1.15)

is split into two parts:

$$\mathbf{D}_c = \mathbf{D}_{r\theta} + \mathbf{D}_z \quad (\text{D.9})$$

where

$$\mathbf{D}_{r\theta} = \begin{pmatrix} \partial_r + 1/r & -1/r & 0 & 0 & 0 & \partial_\theta/r \\ 0 & \partial_\theta/r & 0 & 0 & 0 & \partial_r + 2/r \\ 0 & 0 & 0 & \partial_\theta/r & \partial_r + 1/r & 0 \end{pmatrix} \quad (\text{D.10})$$

$$\mathbf{D}_z = \begin{pmatrix} 0 & 0 & 0 & 0 & \partial_z & 0 \\ 0 & 0 & 0 & \partial_z & 0 & 0 \\ 0 & 0 & \partial_z & 0 & 0 & 0 \end{pmatrix}. \quad (\text{D.11})$$

Equations D.8 and D.9 are substituted in the the wave equation (1.16):

$$\begin{aligned} & [\mathbf{D}_{r\theta} + \mathbf{D}_z] \frac{1}{(2\pi)^2} \int_{-\infty}^{\infty} d\omega \int_{-\infty}^{\infty} dk_z \\ & \times \mathbf{C}_c(\theta) [\mathbf{E}_{c1}(r, \theta, k_z, \omega) + ik_z \mathbf{E}_{2c}(r, \theta, k_z, \omega)] e^{i(k_z z - \omega t)} \\ & = -\frac{\rho}{(2\pi)^2} \int_{-\infty}^{\infty} d\omega \int_{-\infty}^{\infty} dk_z \omega^2 \mathbf{U}_c(r, \theta, k_z, \omega) e^{i(k_z z - \omega t)} \end{aligned} \quad (\text{D.12})$$

where

$$\mathbf{U}_c(r, \theta, k_z, \omega) = \begin{pmatrix} U_r(r, \theta, k_z, \omega) \\ U_\theta(r, \theta, k_z, \omega) \\ U_z(r, \theta, k_z, \omega) \end{pmatrix}. \quad (\text{D.13})$$

Because \mathbf{D}_z only operates on the exponential, the wave equation in the frequency-wavenumber domain is

$$[\mathbf{D}_{r\theta} + ik_z \mathbf{F}] \mathbf{C}_c(\theta) [\mathbf{E}_{c1}(r, \theta, k_z, \omega) + ik_z \mathbf{E}_{c2}(r, \theta, k_z, \omega)] = -\rho \omega^2 \mathbf{U}_c(r, \theta, k_z, \omega) \quad (\text{D.14})$$

where

$$\mathbf{F} = \begin{pmatrix} 0 & 0 & 0 & 0 & 1 & 0 \\ 0 & 0 & 0 & 1 & 0 & 0 \\ 0 & 0 & 1 & 0 & 0 & 0 \end{pmatrix}. \quad (\text{D.15})$$

Since equation D.14 contains neither z nor t , the wave equation is separable in these variables. The equation is not separable in r and θ because the stiffness matrix

is a function of θ . Note that this result applies to a medium having general anisotropy defined in Cartesian coordinates. Two exceptions to this rule exist when the medium is isotropic or transversely isotropic with the symmetry axis parallel to the z axis. For these two cases, the stiffness matrix does not depend upon θ , and the wave equation is separable in r and θ . (In Chapter 1 are many references to researchers who have performed this separation).

Appendix E

Sensitivities of the Wavenumbers for the Normal Modes

In this appendix, the sensitivities of the wavenumbers for the normal modes in three different formations will be presented and analyzed. This sensitivity is defined as the normalized partial derivative of the wavenumber with respect to an elastic modulus. This quantity indicates how the wavenumber of a normal mode is affected by a change in an elastic modulus — such information is needed to formulate properly an inversion for the moduli of the formation.

The sensitivities are calculated for a two-layer model of the borehole environment (Figure E-1). The fluid is perfectly elastic, its incompressibility is λ_1 , and its density is ρ_1 . The borehole wall is perfectly round, and its radius is R . The formation is perfectly elastic and homogeneous. Because the formation is transversely isotropic with its symmetry axis parallel to the borehole, its elastic properties are specified by only five moduli: c_{11} , c_{13} , c_{33} , c_{44} , and c_{66} which are written in abbreviated subscript notation (see Chapter 1). The density of the formation is ρ_2 .

The sensitivity associated with an elastic modulus of the transversely isotropic

formation, c_{IJ}^{TI} , is defined formally as

$$\frac{c_{IJ}^{TI}}{k_z} \frac{\partial k_z}{\partial c_{IJ}^{TI}}$$

where k_z is the wavenumber. Similarly, the sensitivity associated with the incompressibility of the fluid is

$$\frac{\lambda_1}{k_z} \frac{\partial k_z}{\partial \lambda_1}.$$

The partial derivatives were calculated using the perturbation method described in Chapter 2.

The phase velocities of the normal modes in fast, slow, and very slow formations (Tables E.1, E.2, and E.3, respectively) were computed with equation A.46 and are shown in Figures E-2, E-11, and E-18. The sensitivities for the normal modes in the fast formation are shown in Figures E-3, E-4, E-5, E-6, E-7, E-8, E-9, and E-10; the sensitivities for the modes in the slow formation in Figures E-12, E-13, E-14, E-15, E-16, and E-17; and the sensitivities for the modes in the very slow formation in Figures E-19, E-20, E-21, E-22, E-23, and E-24.

The general characteristics of the sensitivities for the three different formations are summarized conveniently in Tables E.4, E.5, and E.6. From these tables several generalizations, which are true for most (but not all) situations, can be made:

1. The wavenumbers for all modes are sensitive to λ_1 .
2. The wavenumbers of the pseudo-Rayleigh, flexural, and screw waves are very sensitive to the c_{44} , a modulus which is related to S -wave propagation.
3. The wavenumbers for all modes are insensitive to c_{11} , c_{13} , and c_{33} , moduli which are related to P -wave propagation.
4. At low frequencies, the wavenumbers for the tube wave are moderately sensitive to c_{66} and insensitive to c_{44} . At high frequencies, the wavenumbers are moderately sensitive to c_{44} and insensitive to c_{66} .

The exceptions to these generalizations are usually for the very slow formation.

When trying to estimate an elastic modulus, its sensitivity must be greater than the sensitivities associated with the other elastic moduli. The unknown moduli, for which an inversion might be performed, are c_{11} , c_{13} , and c_{66} because c_{33} , c_{44} , and λ_1 can be determined with other methods. The sensitivities indicate that c_{11} and c_{13} cannot be estimated from the normal modes. c_{66} can be estimated only with the low frequency portion of the tube wave in fast and slow formations.

Quantity	Value
c_{11}	3.126×10^{10} Pa
c_{13}	0.345×10^{10} Pa
c_{33}	2.249×10^{10} Pa
c_{44}	0.649×10^{10} Pa
c_{66}	0.882×10^{10} Pa
ρ_2	2075. kg/m ³
λ_1	0.225×10^{10} Pa
ρ_1	1000. kg/m ³
R	0.1016 m

Table E.1: Model with a fast formation which represents the Green River shale (Thomsen, 1986).

Quantity	Value
c_{11}	3.395×10^{10} Pa
c_{13}	1.058×10^{10} Pa
c_{33}	2.248×10^{10} Pa
c_{44}	0.537×10^{10} Pa
c_{66}	1.053×10^{10} Pa
ρ_2	2420. kg/m ³
λ_1	0.225×10^{10} Pa
ρ_1	1000. kg/m ³
R	0.1016 m

Table E.2: Model with a slow formation which represents shale (5000) (Thomsen, 1986).

Quantity	Value
c_{11}	1.387×10^{10} Pa
c_{13}	0.803×10^{10} Pa
c_{33}	0.998×10^{10} Pa
c_{44}	0.177×10^{10} Pa
c_{66}	0.283×10^{10} Pa
ρ_2	2250. kg/m ³
λ_1	0.225×10^{10} Pa
ρ_1	1000. kg/m ³
R	0.1016 m

Table E.3: Model with a very slow formation which represents the Pierre shale (Thomson, 1986).

Quantity	Relative Sensitivities for Pseudo-Rayleigh Wave	
	near cutoff frequency	at high frequencies
λ_1	low	moderate
c_{44}	high	moderate
c_{66}	low	low
c_{11}, c_{13}, c_{33}	low	low

Table E.4: Relative sensitivities for the pseudo-Rayleigh wave in the model with the fast formation (Table E.1).

Quantity	Relative Sensitivities for the Flexural and Screw Waves			
	Fast and Slow Formations		Very Slow Formation	
	near cutoff frequency	at high frequencies	near cutoff frequency	at high frequencies
λ_1	low	moderate	low	low
c_{44}	high	moderate	high	high
c_{66}	low	low	low	low
c_{11}, c_{13}, c_{33}	low	low	low	moderate

Table E.5: Relative sensitivities for the flexural and screw waves in the models with the fast, slow, and very slow formations (Tables E.1, E.2, and E.3, respectively).

Quantity	Relative Sensitivities for the Tube Wave		
	Fast and Slow Formations		Very Slow Formation
	at low frequencies (< 5 kHz)	at high frequencies	at nearly all frequencies
λ_1	high	moderate to high	low
c_{44}	low	moderate	high
c_{66}	moderate	low	low to moderate
c_{11}, c_{13}, c_{33}	low	low	moderate

Table E.6: Relative sensitivities for the tube waves in the models with the fast, slow, and very slow formations (Tables E.1, E.2, and E.3, respectively).

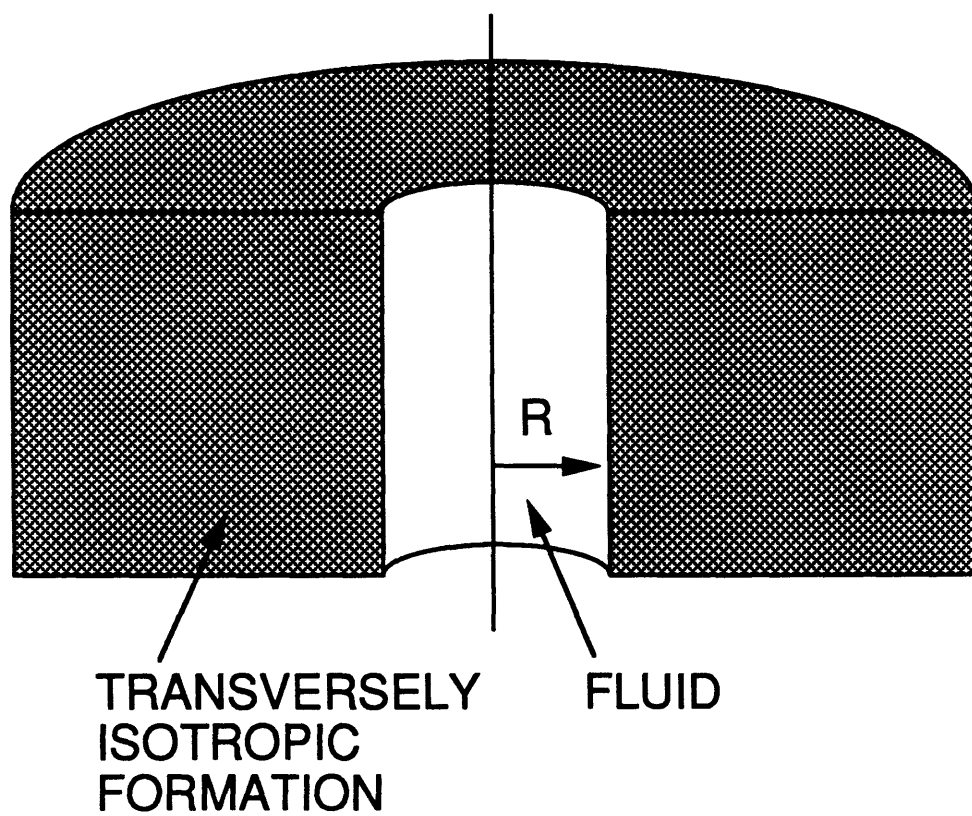


Figure E-1: Mathematical model used to calculate the sensitivities.

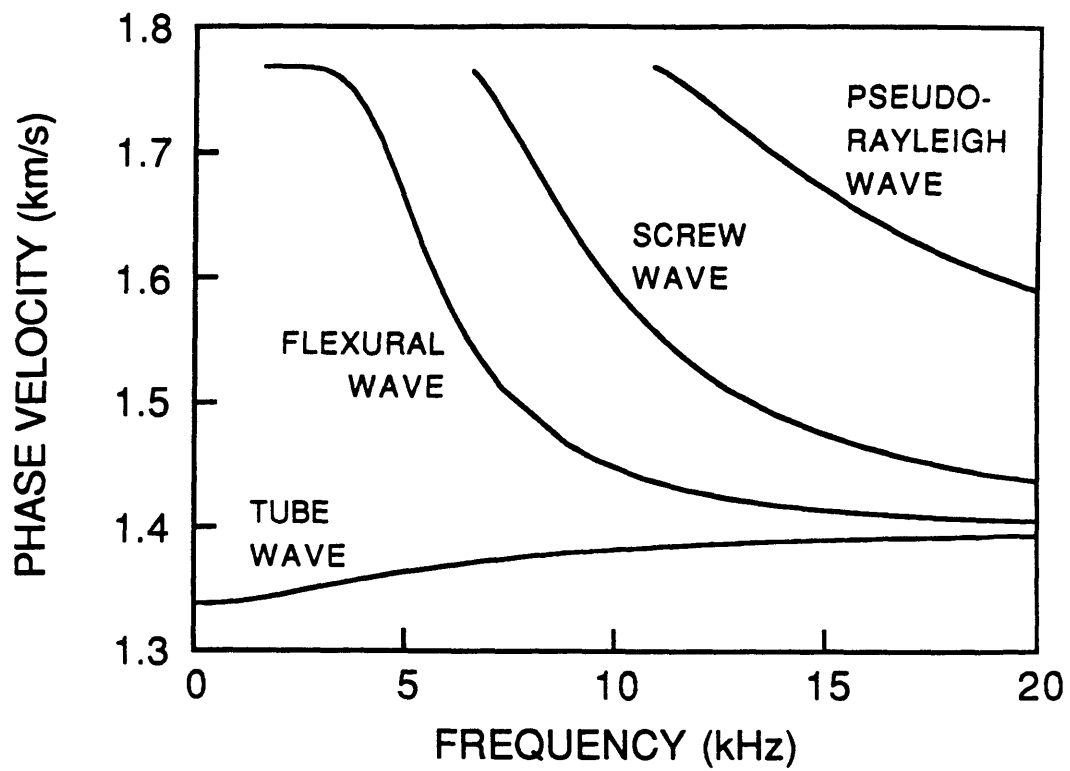


Figure E-2: Phase velocities of the normal modes in the model with the fast formation (Table E.1).

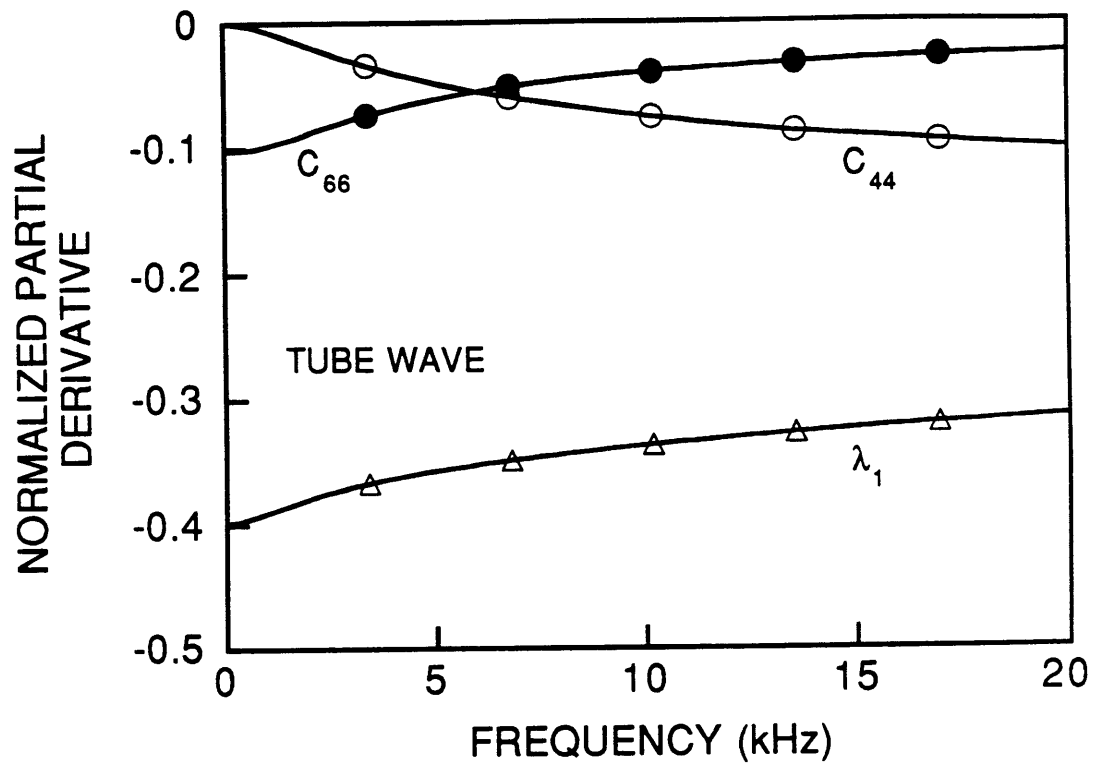


Figure E-3: Sensitivities for the tube wave in the model with the fast formation (Table E.1). See also Figure E-4.

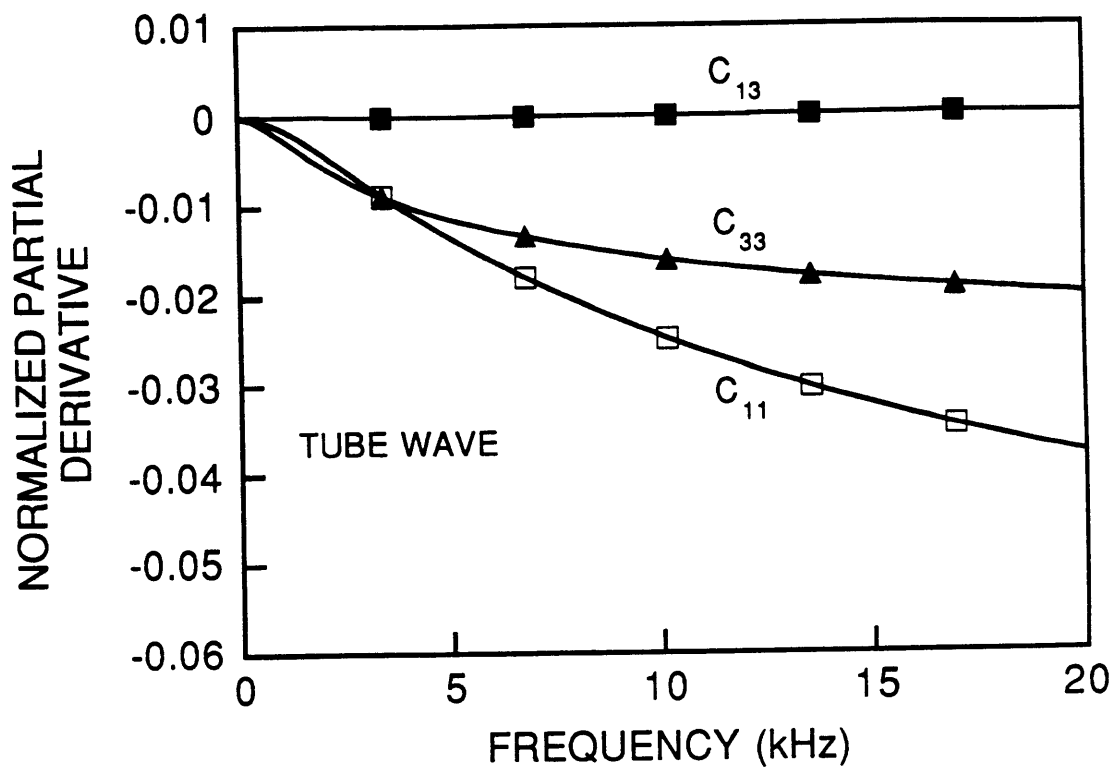


Figure E-4: Sensitivities for the tube wave in the model with the fast formation (Table E.1). See also Figure E-3.

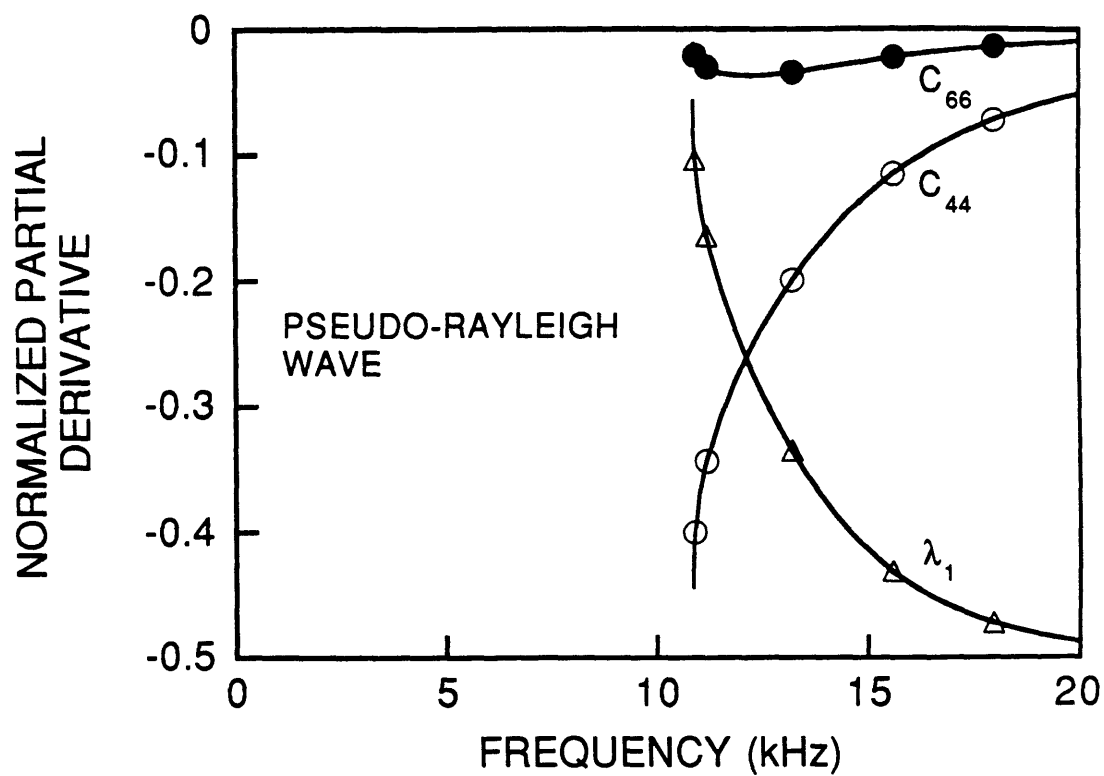


Figure E-5: Sensitivities for the pseudo-Rayleigh wave in the model with the fast formation (Table E.1). See also Figure E-6.

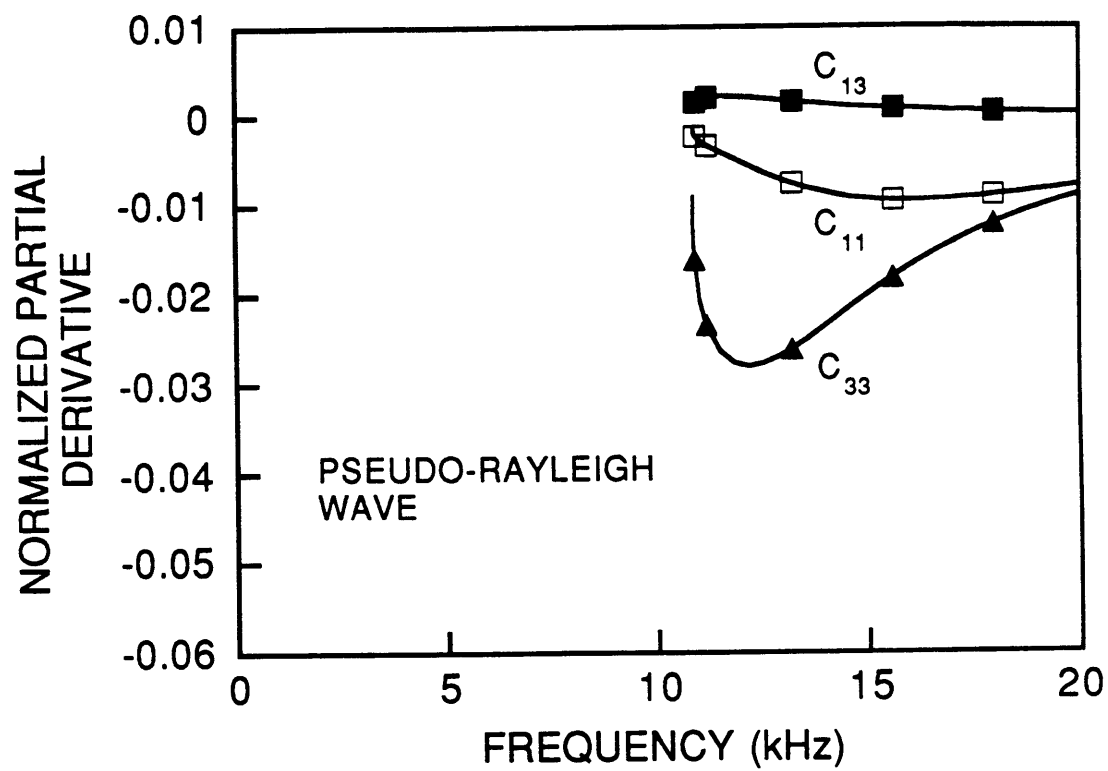


Figure E-6: Sensitivities for the pseudo-Rayleigh wave in the model with the fast formation (Table E.1). See also Figure E-5.

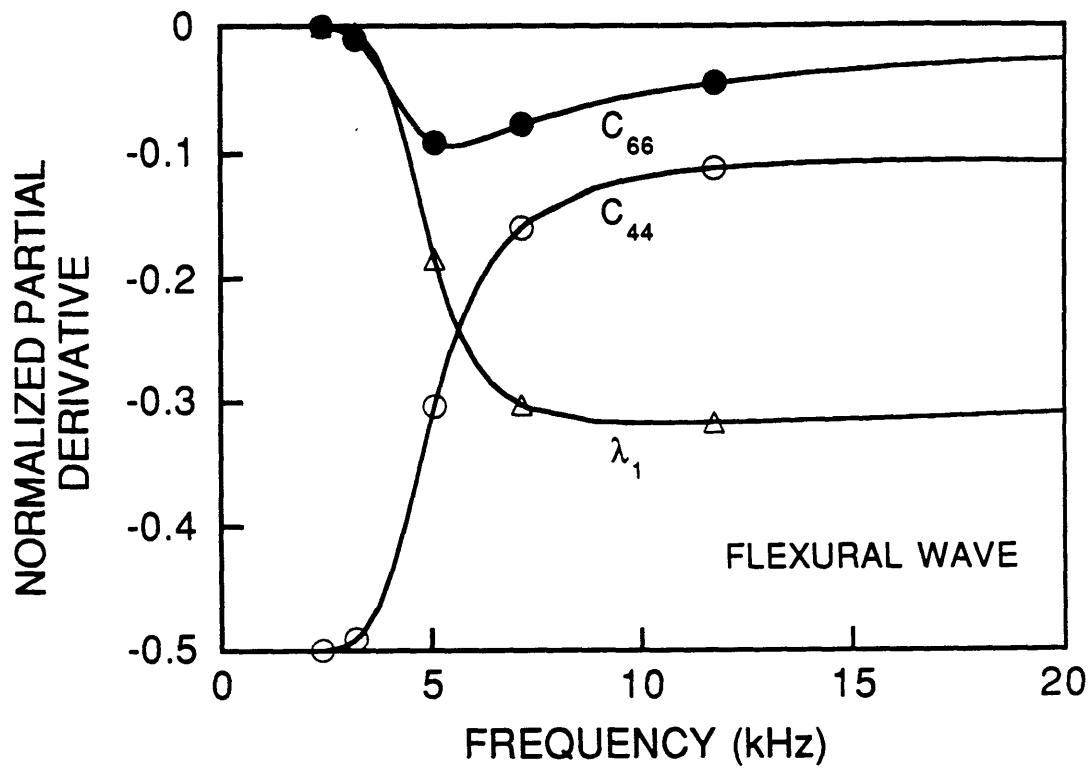


Figure E-7: Sensitivities for the flexural wave in the model with the fast formation (Table E.1). See also Figure E-8.

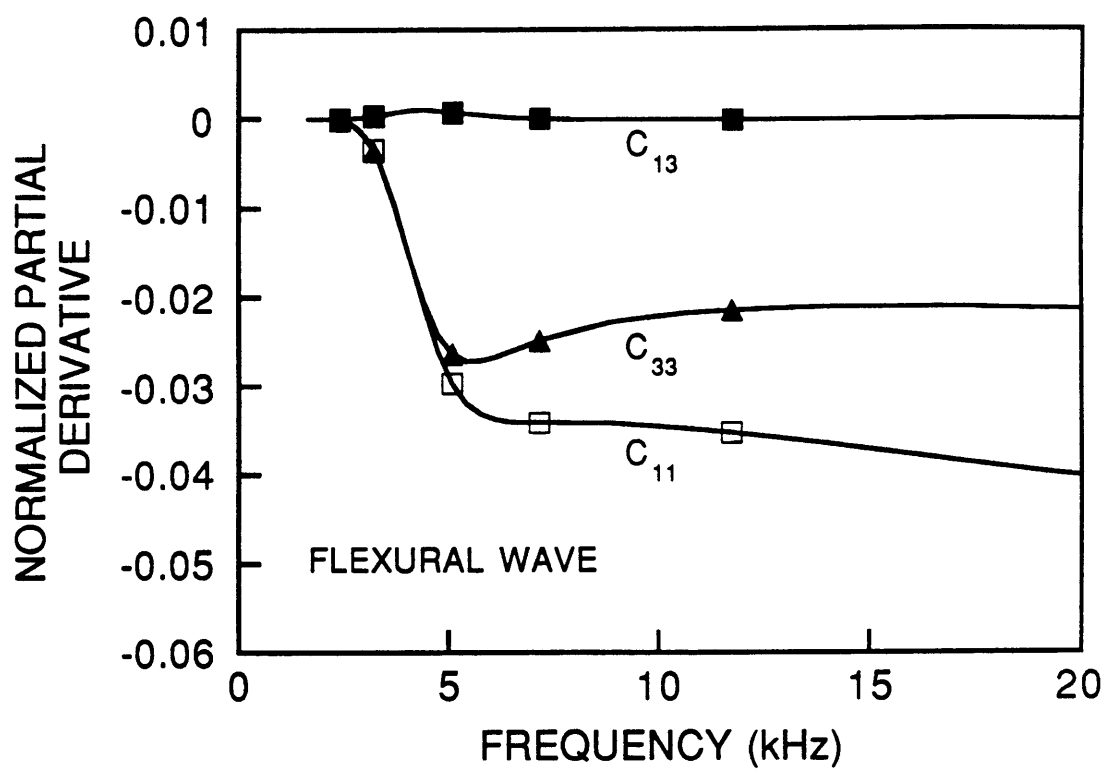


Figure E-8: Sensitivities for the flexural wave in the model with the fast formation (Table E.1). See also Figure E-7.

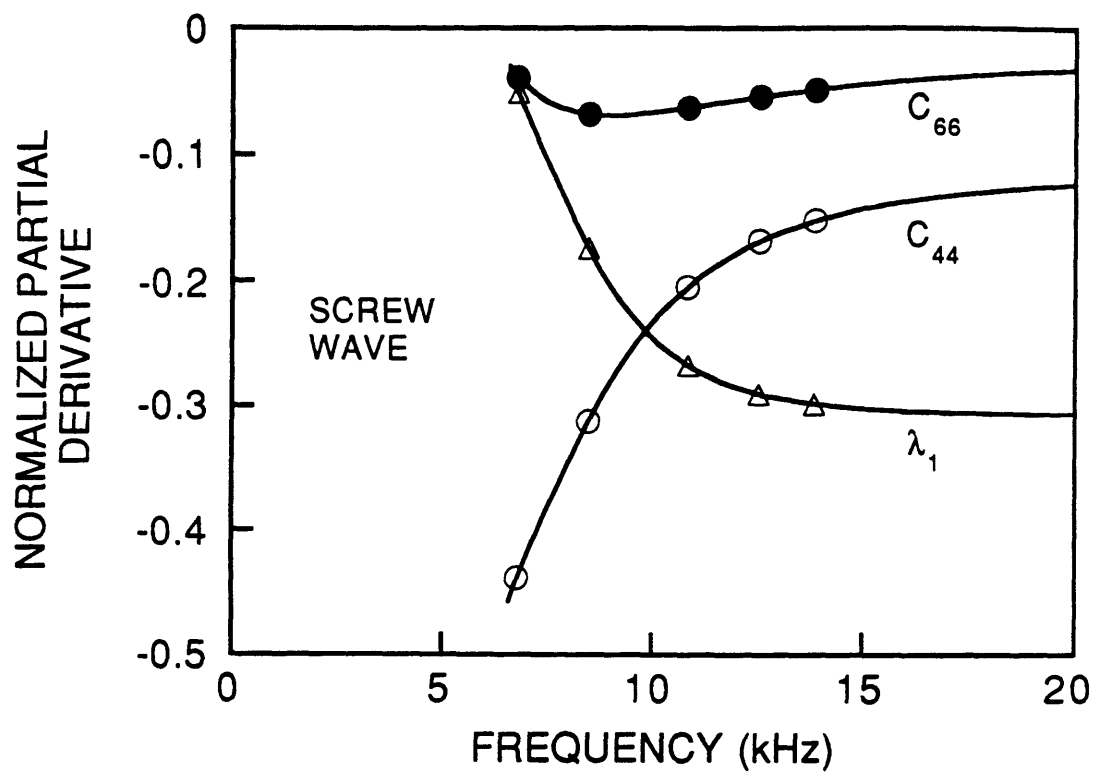


Figure E-9: Sensitivities for the screw wave in the model with the fast formation (Table E.1). See also Figure E-10.

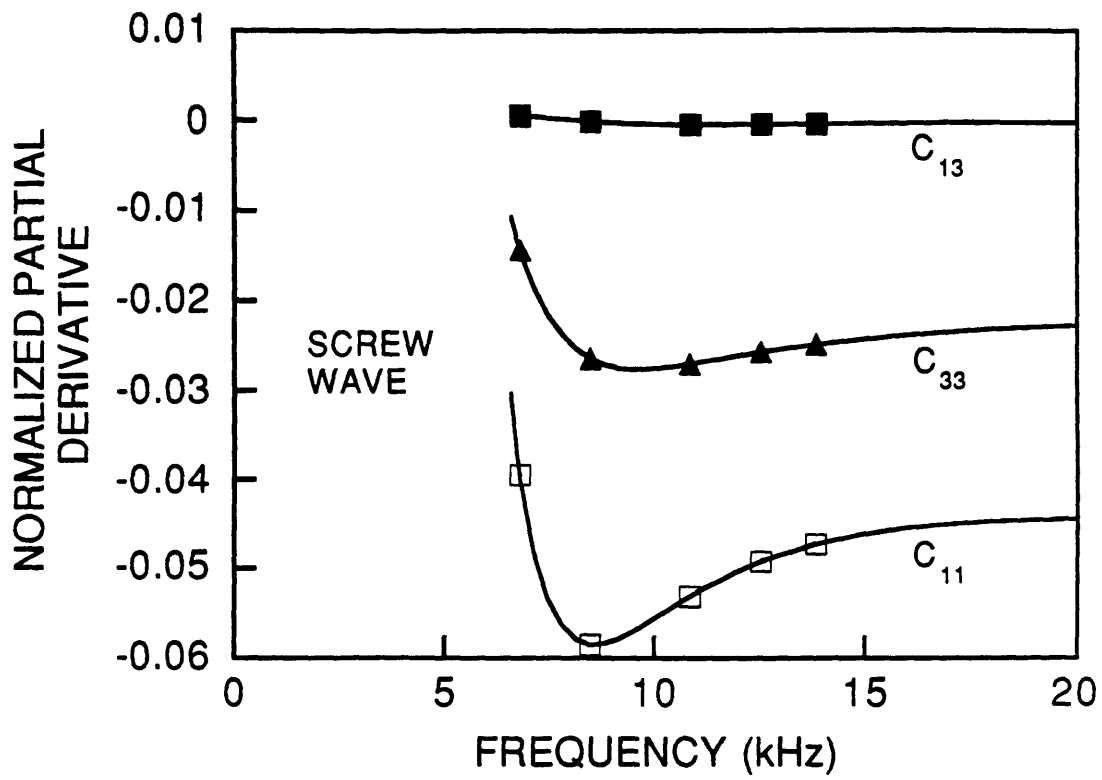


Figure E-10: Sensitivities for the screw wave in the model with the fast formation (Table E.1). See also Figure E-9.

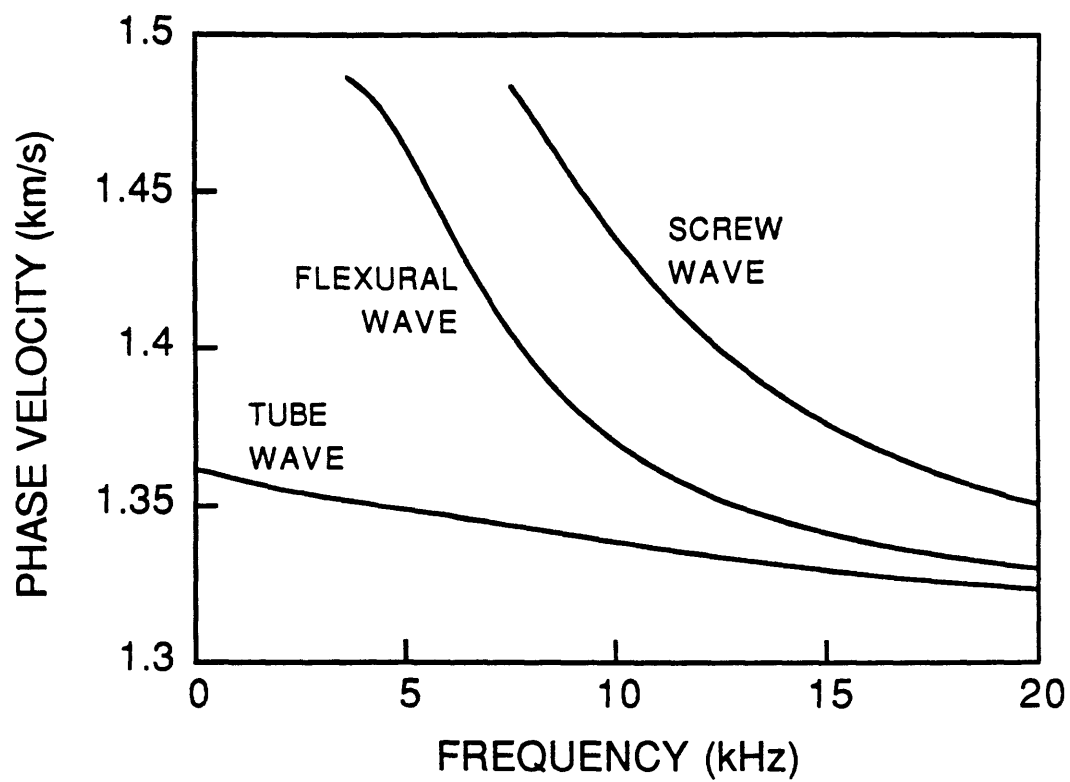


Figure E-11: Phase velocities of the normal modes in the model with the slow formation (Table E.2).

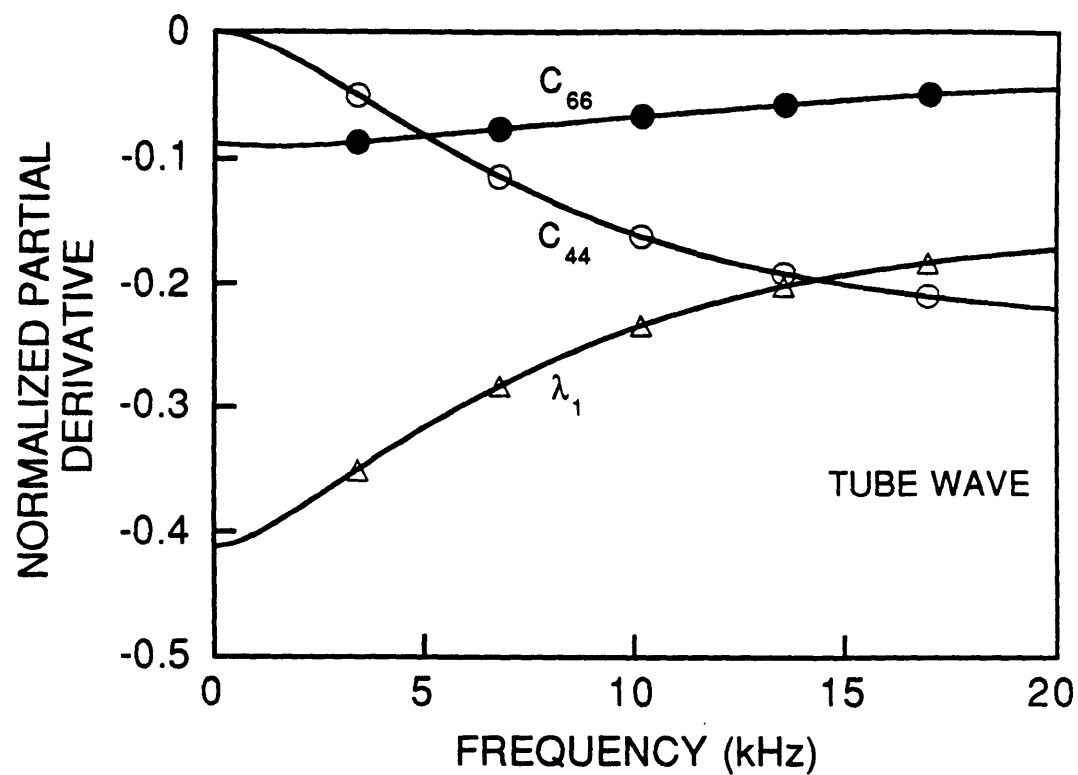


Figure E-12: Sensitivities for the tube wave in the model with the slow formation (Table E.2). See also Figure E-13.

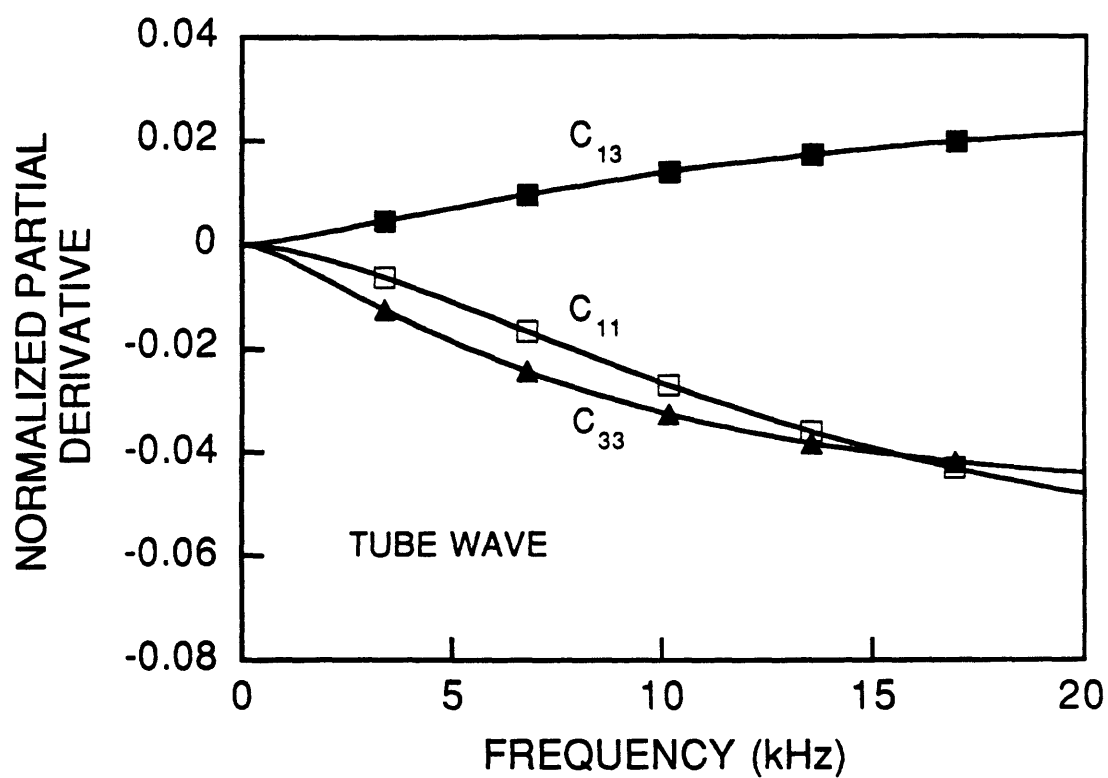


Figure E-13: Sensitivities for the tube wave in the model with the slow formation (Table E.2). See also Figure E-12.

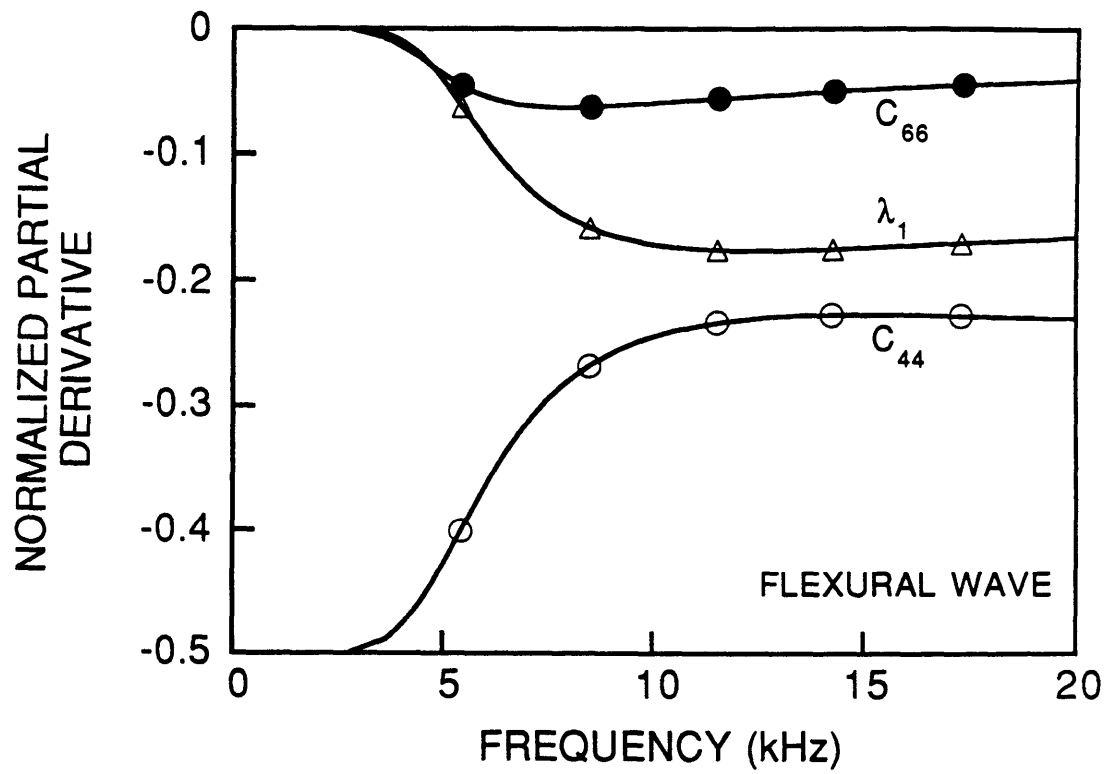


Figure E-14: Sensitivities for the flexural wave in the model with the slow formation (Table E.2). See also Figure E-15.

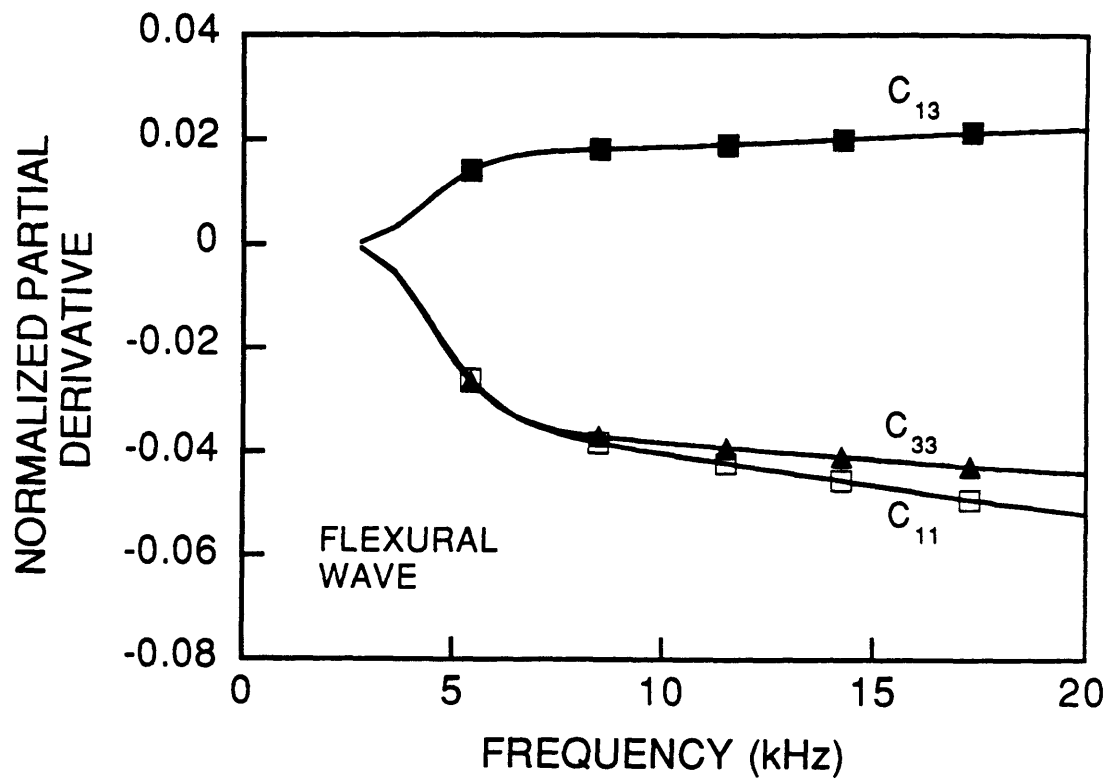


Figure E-15: Sensitivities for the flexural wave in the model with the slow formation (Table E.2). See also Figure E-14.

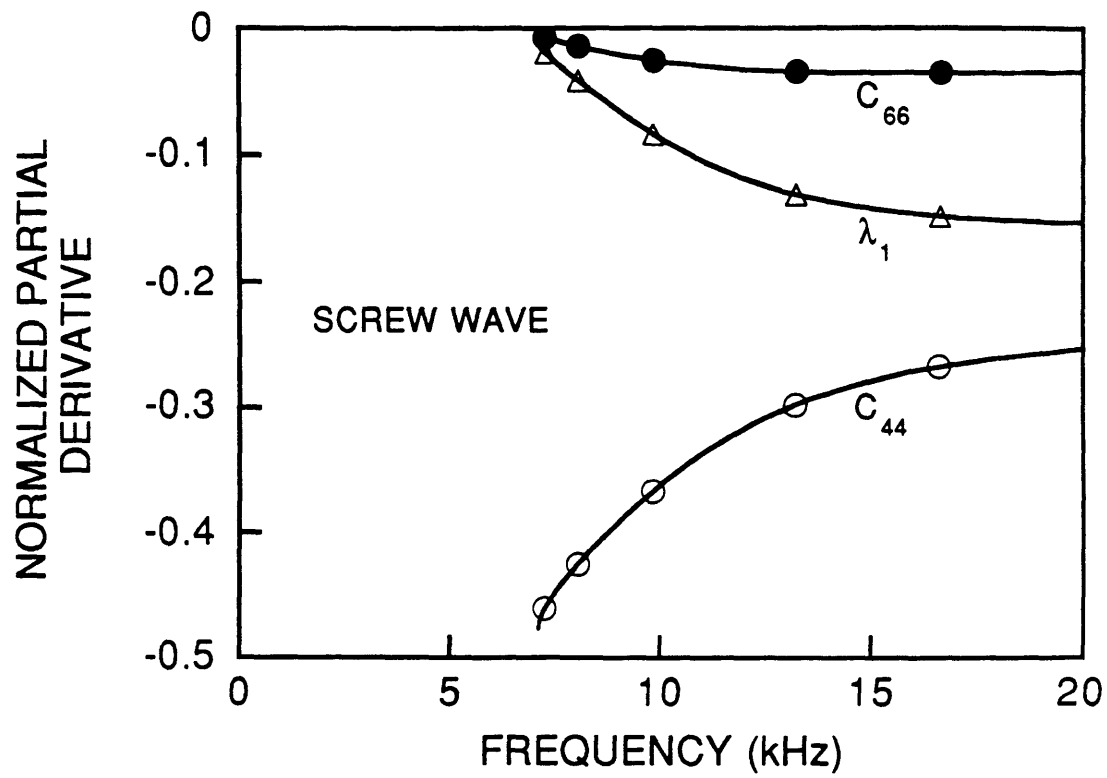


Figure E-16: Sensitivities for the screw wave in the model with the slow formation (Table E.2). See also Figure E-17.

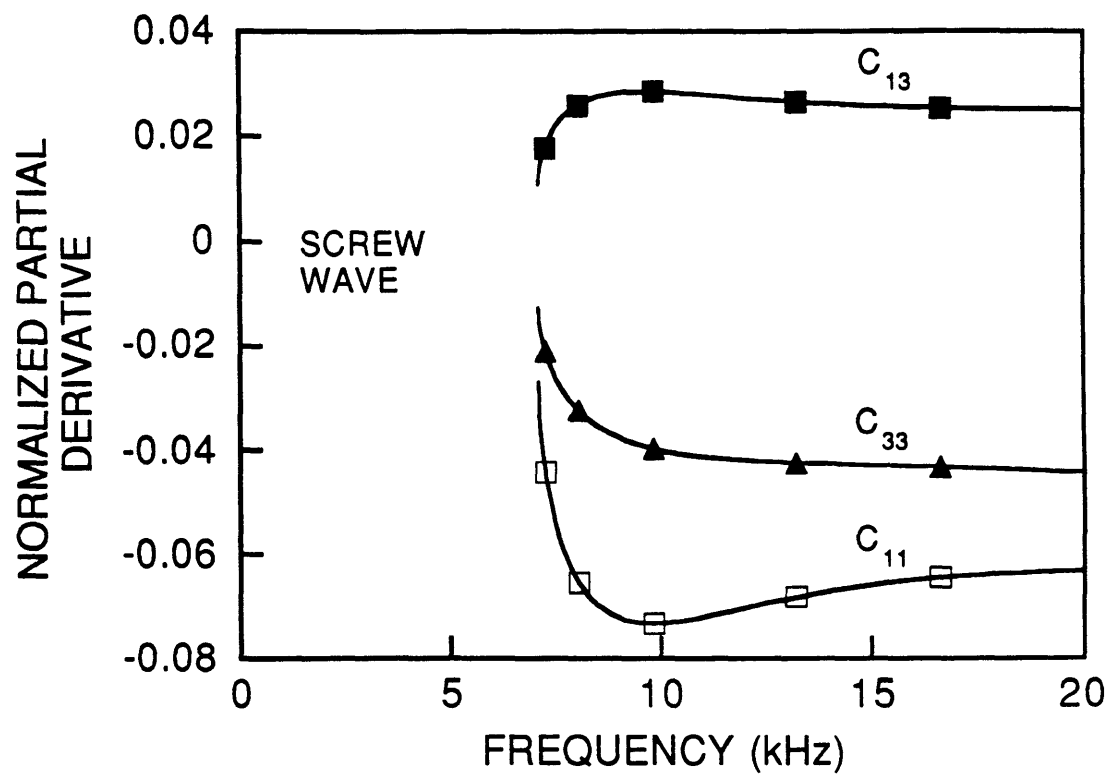


Figure E-17: Sensitivities for the screw wave in the model with the slow formation (Table E.2). See also Figure E-16.

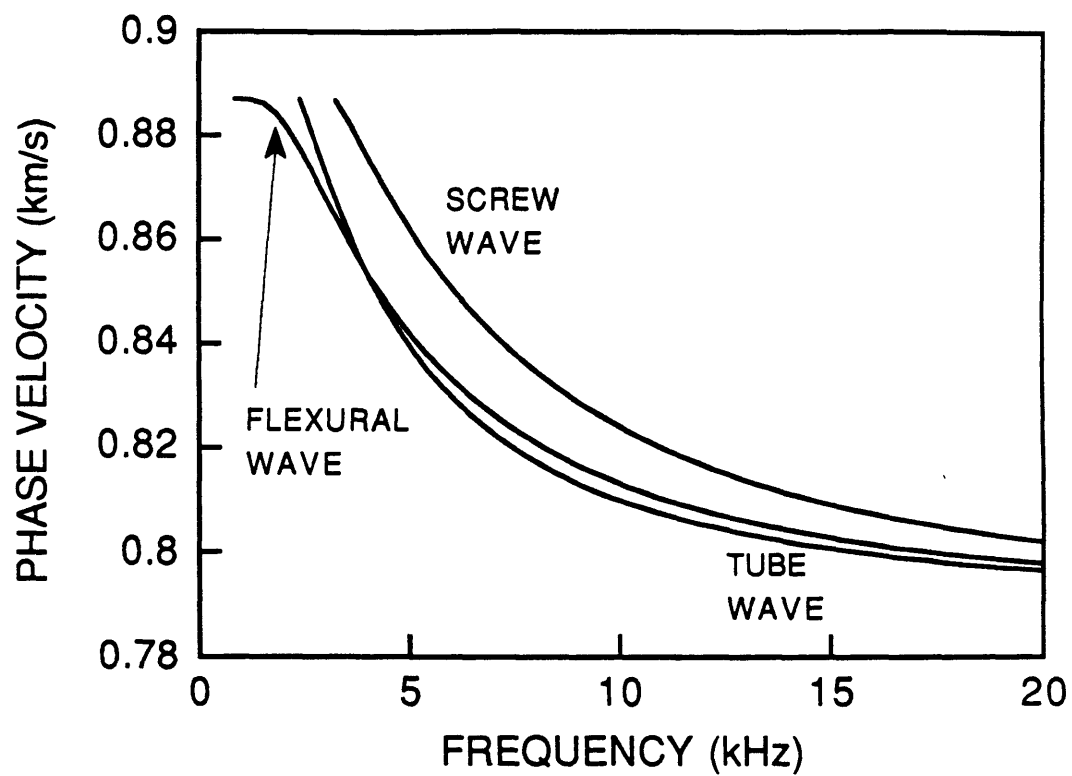


Figure E-18: Phase velocities of the normal modes in the model with the very slow formation (Table E.3).

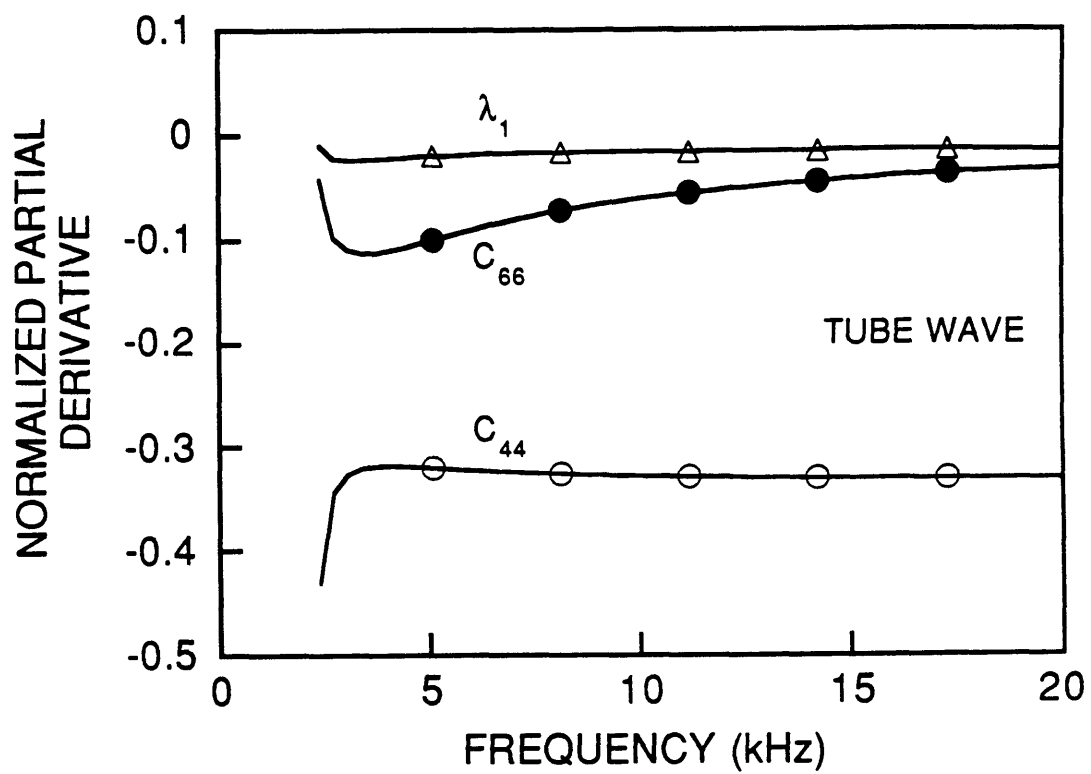


Figure E-19: Sensitivities for the tube wave in the model with the very slow formation (Table E.3). See also Figure E-20.

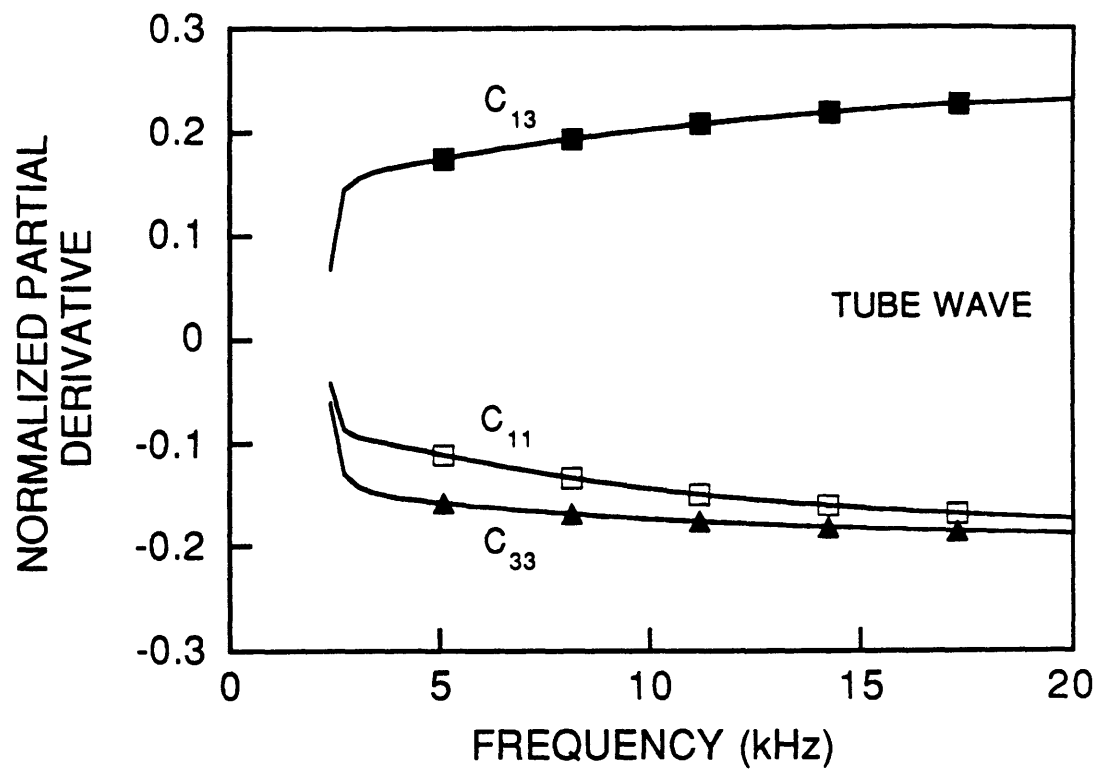


Figure E-20: Sensitivities for the tube wave in the model with the very slow formation (Table E.3). See also Figure E-19.

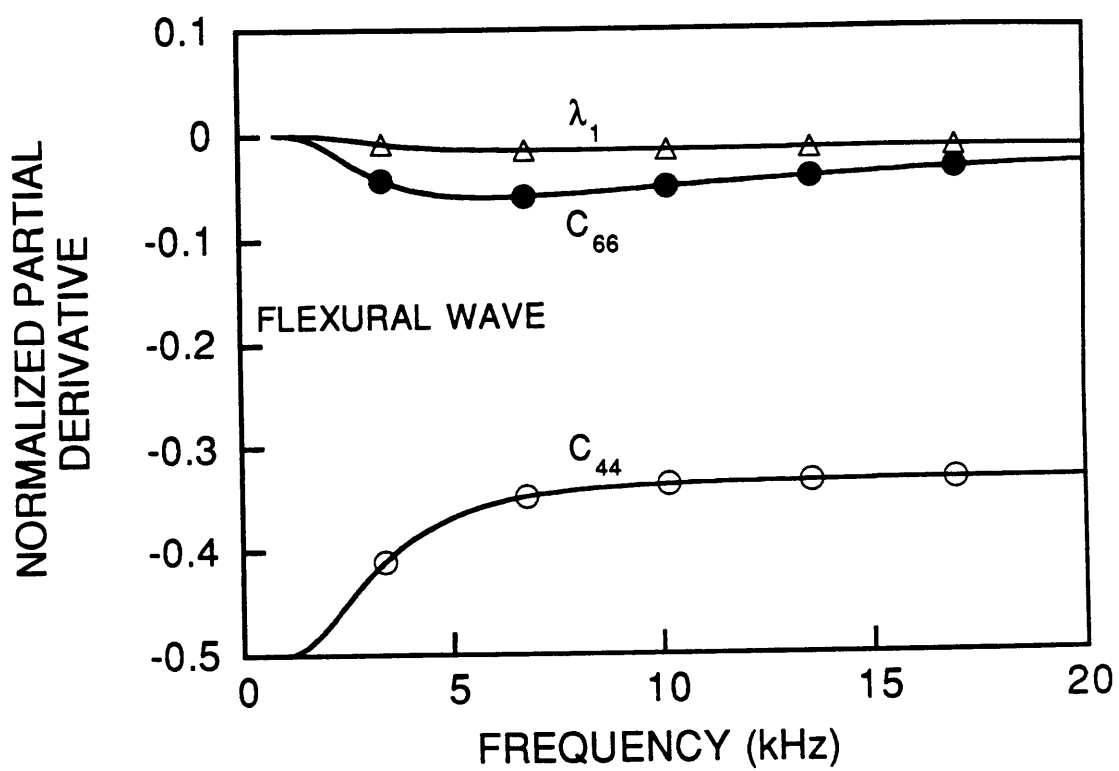


Figure E-21: Sensitivities for the flexural wave in the model with the very slow formation (Table E.3). See also Figure E-22.

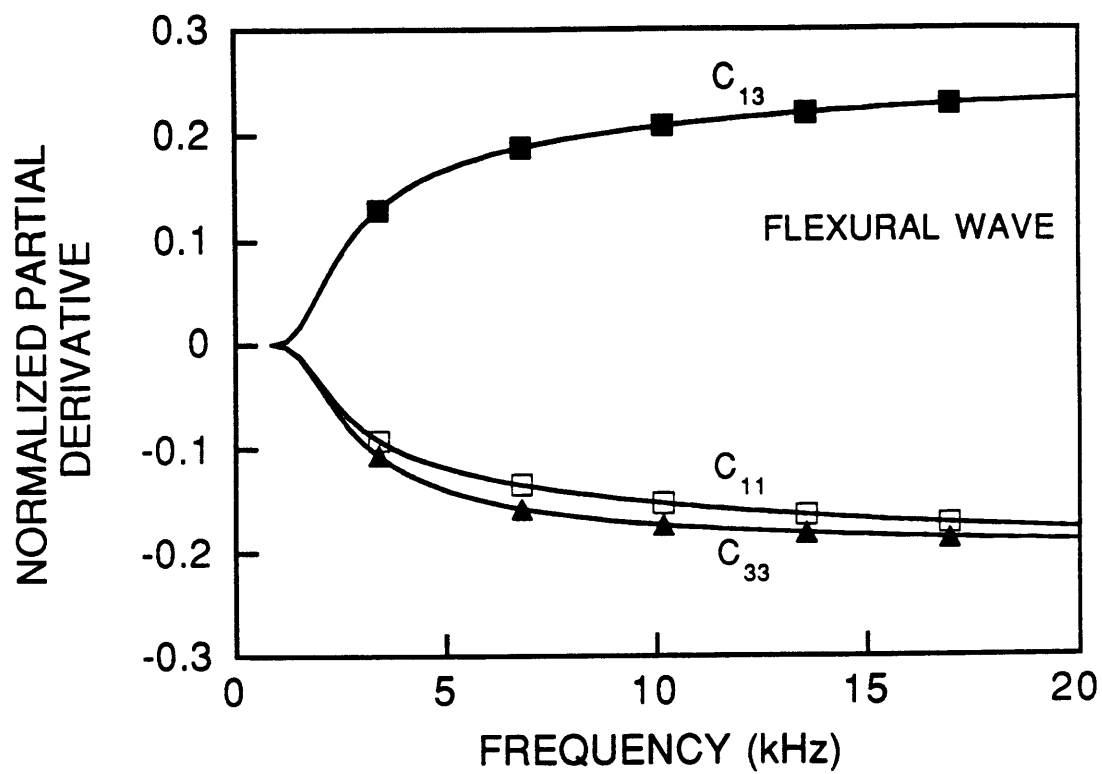


Figure E-22: Sensitivities for the flexural wave in the model with the very slow formation (Table E.3). See also Figure E-21.

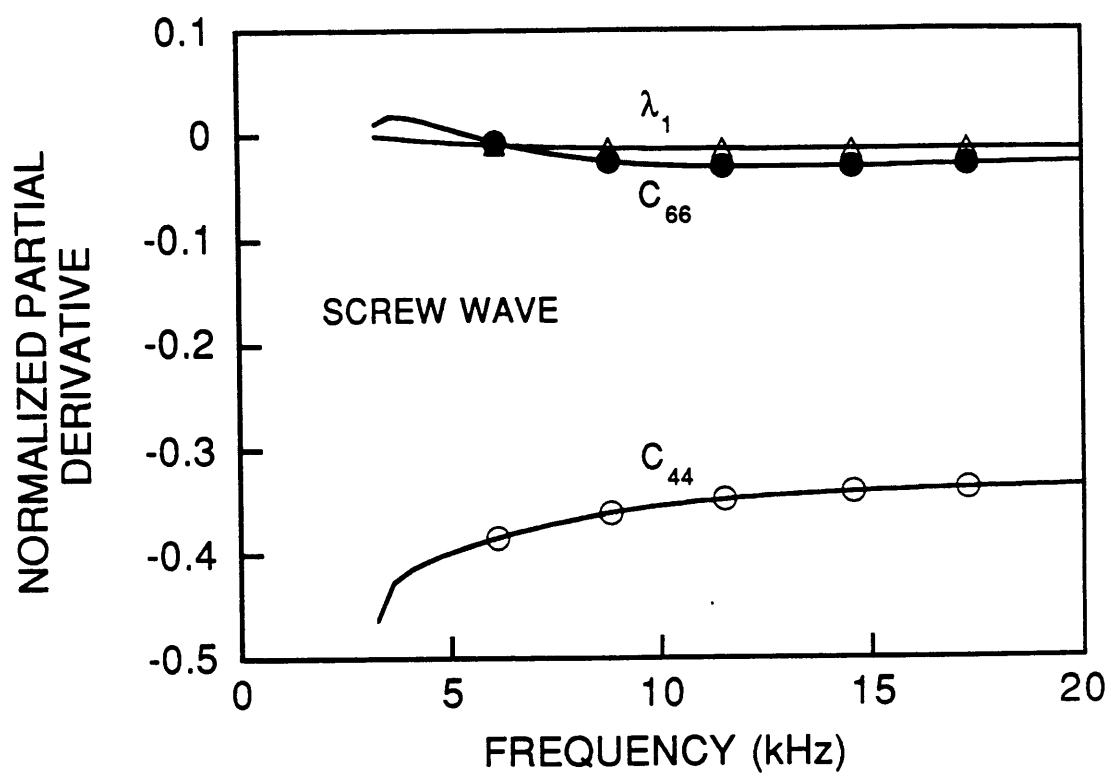


Figure E-23: Sensitivities for the screw wave in the model with the very slow formation (Table E.3). See also Figure E-24.

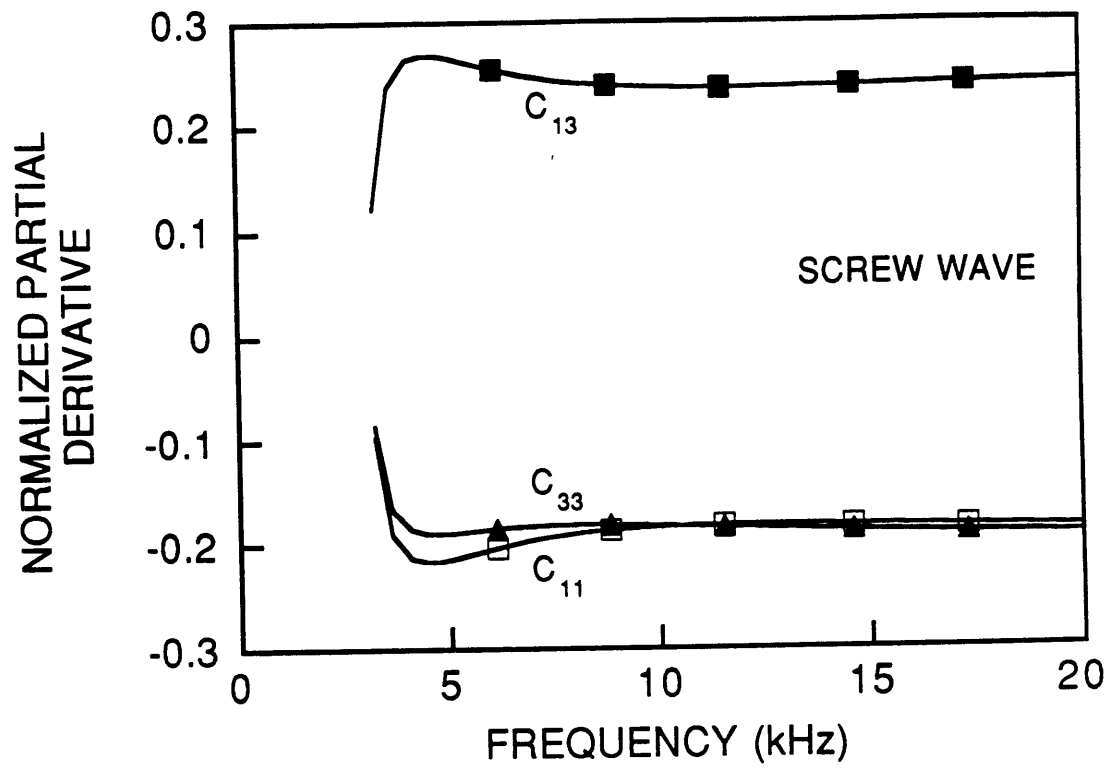


Figure E-24: Sensitivities for the screw wave in the model with the very slow formation (Table E.3). See also Figure E-23.

References

- Abramowitz, M. and I. A. Stegun, *Handbook of Mathematical Functions*, Dover Publ. Inc., 1972.
- Aki, K. and P. G. Richards, *Quantitative Seismology*, W. H. Freeman & Co., 1980.
- Armenàkas, A. E. and E. S. Reitz, Propagation of harmonic waves in orthotropic circular cylindrical shells, *J. Appl. Mech.*, 40, 168–174, 1973.
- Armenàkas, A. E., D. C. Gazis, and G. Herrman, *Free Vibrations of Circular Cylindrical Shells*, Pergamon Press Ltd., 1969.
- Auld, B. A., *Acoustic Fields and Waves in Solids*, vol. 1, John Wiley & Sons, Inc., 1973.
- Backus, G. E., Long-wave anisotropy produced by horizontal layering, *J. of Geophys. Res.*, 67, 4427–4400, 1962.
- Bard, Y., *Nonlinear Parameter Estimation*, Academic Press Inc., 1974.
- Bathe, K., *Finite Element Procedures in Engineering Analysis*, Prentice-Hall, Inc., 1982.
- Ben-Menahem, A. and S. J. Singh, *Seismic Waves and Sources*, Springer-Verlag, 1981.
- Bettess, P., Infinite elements, *Int. J. Numer. Meth. Engng.*, 11, 53–64, 1977.
- Bhagavantam, S., *Crystal Symmetry and Physical Properties*, Academic Press Inc., 1966.
- Bhasavanija, K., *A Finite Difference Model of an Acoustic Logging Tool: The Borehole in a Horizontally Layered Geologic Medium*, PhD thesis, Colorado School of Mines, 1983.
- Biot, M. A., Propagation of elastic waves in cylindrical bore containing a fluid, *J. Appl. Phys.*, 23, 997–1005, 1952.

- Bond, W., The mathematics of the physical properties of crystals, *Bell System Tech. Jour.*, 22, 1–72, 1943.
- Bouchon, M. and D. P. Schmitt, Full-wave acoustic logging in an irregular borehole, *Geophysics*, 54, 758–765, 1989.
- Buerger, M. J., *Introduction to Crystal Geometry*, McGraw-Hill Book Co., 1971.
- Buland, R. and F. Gilbert, Computation of the free oscillations of the earth, *J. Comp. Phys.*, 54, 95–114, 1984.
- Bullen, K. E., *An Introduction to the Theory of Seismology*, Cambridge University Press, 1963.
- Burns, D. R., *Formation Property Estimation from Guided Waves in a Borehole*, PhD thesis, Massachusetts Institute of Technology, 1986.
- Burns, D. R., Viscous fluid effects on guided wave propagation in a borehole, *J. Acoust. Soc. Am.*, 83, 463–469, 1988.
- Burns, D. R. and C. H. Cheng, Inversion of borehole guided wave amplitudes for formation shear wave attenuation values, *J. of Geophys. Res.*, 92, 12713–12725, 1987.
- Carrier, G. F. and C. E. Pearson, *Partial Differential Equations*, Academic Press Inc., 1976.
- Chan, A. K. and L. Tsang, Propagation of acoustic waves in a fluid-filled borehole surrounded by a concentrically layered transversely isotropic formation, *J. Acoust. Soc. Am.*, 74, 1605–1616, 1983.
- Chen, H. C. and R. L. Taylor, Solution of eigenproblems for damped structural systems by the Lanczos algorithm, *Comput. Struct.*, 30, 151–161, 1988.
- Cheng, C. H. and M. N. Toksöz, Elastic wave propagation in a fluid-filled borehole and synthetic acoustic logs, *Geophysics*, 46, 1042–1053, 1981.

- Cheng, C. H. and M. N. Toksöz, Determination of shear wave velocities in slow formations, in *Trans., Soc. Prof. Well Log Analysts, 24th Ann. Log. Symp.*, 1983, paper V.
- Cheng, C. H., M. N. Toksöz, and M. E. Willis, Determination of *in situ* attenuation from full waveform acoustic logs, *J. of Geophys. Res.*, *87*, 5477–5484, 1982.
- Cheng, C. H., J. Zhang, and D. R. Burns, Effects of in-situ permeability on the propagation of Stoneley (tube) waves in a borehole, *Geophysics*, *52*, 1279–1289, 1987.
- Chou, F. H. and J. D. Achenbach, Three-dimensional vibrations of orthotropic cylinders, *J. of Engineering Mechanics Division, Proc. ASCE*, *98*, 813–822, 1972.
- Chree, C., Longitudinal vibrations of a circular bar, *Quarterly Journal of Pure and Applied Mathematics*, *21*, 287–298, 1886.
- Chree, C., The equations of an isotropic elastic solid in polar and cylindrical coordinates, their solutions and applications, *Trans. Cambridge Philosophical Society*, *14*, 250–369, 1889.
- Chree, C., On the longitudinal vibrations of aeolotropic bars with one axis of symmetry, *Quarterly Journal of Pure and Applied Mathematics*, *24*, 340–358, 1890.
- Christoffel, E. B., *Ann. di Mat. (Ser. 2)*, *t. 8*, 1877.
- Crampin, S., Effective elastic constants for wave propagation through cracked solids, *Geophys. J. Roy. Astron. Soc.*, *76*, 135–145, 1984.
- Dahlen, F. A., Reply, *J. of Geophys. Res.*, *81*, 4951–4956, 1976.
- Einspruch, N. G. and R. Truell, Propagation of traveling waves in a circular cylinder having hexagonal elastic symmetry, *J. Acoust. Soc. Am.*, *31*, 691–693, 1959.
- Eliot, F. C. and G. Mott, Elastic waves propagation in circular cylinders having hexagonal crystal symmetry, *J. Acoust. Soc. Am.*, *44*, 423–430, 1967.

- Ellefsen, K. J., C. H. Cheng, and K. M. Tubman, Estimating phase velocity and attenuation of guided waves in acoustic logging data, *Geophysics*, *54*, 1054–1059, 1989.
- Everstine, G. C., A symmetric potential formulation for fluid-structure interaction, *J. Sound Vib.*, *79*, 157–160, 1981.
- Farnell, G. W., Properties of elastic surface waves, in *Physical Acoustics, Principles and Methods*, edited by W. P. Mason and R. N. Thurston, pp. 109–166, Academic Press Inc., 1970.
- Fedorov, F. I., *Theory of Elastic Waves in Crystals*, Plenum Press, 1968.
- Goldstein, H., *Classical Mechanics*, Addison-Wesley Publishing Co., 1980.
- Hamdi, M. A. and Y. Ousset, A displacement method for the analysis of vibrations of coupled fluid-structure systems, *Int. J. Numer. Meth. Engng.*, *13*, 139–150, 1978.
- Hearmon, R. F. S., *An Introduction to Applied Anisotropic Elasticity*, Oxford University Press, 1961.
- Helbig, K. and M. Schoenberg, Anomalous polarizations of elastic waves in transversely isotropic media, *J. Acoust. Soc. Am.*, *81*, 1235–1245, 1987.
- Hornby, B. E., Imaging of near-borehole structure using full-waveform sonic data, *Geophysics*, *54*, 747–757, 1989.
- Hornby, B. E., D. L. Johnson, K. W. Winkler, and R. A. Plumb, Fracture evaluation using reflected Stoneley-wave arrivals, *Geophysics*, *54*, 1274–1288, 1989.
- Huang, K. H. and S. B. Dong, Propagating waves and edge vibrations in anisotropic composite cylinders, *J. Sound Vib.*, *96*, 363–379, 1984.
- Jacobi, W. J., Propagation of sound waves along liquid cylinders, *J. Acoust. Soc. Am.*, *21*, 120–127, 1949.
- Jeffreys, H., *Cartesian Tensors*, Cambridge University Press, 1931.

- Kausel, E., Wave propagation in anisotropic layered media, *Int. J. Numer. Meth. Engng.*, *23*, 1567–1578, 1986.
- Kausel, E. and J. M. Roësset, Stiffness matrices for layered soils, *Bull. Seis. Soc. Am.*, *71*, 1743–1761, 1981.
- Keck, H. E. and A. E. Armenàkas, Wave propagation in transversely isotropic, layered cylinders, *J. of Engineering Mechanics Division, Proc. ASCE*, *97*, 541–558, 1971.
- Kelvin, W. T., *Baltimore Lectures on Molecular Dynamics and the Wave Theory of Light*, C. J. Clay and Sons, 1904.
- Kennett, B. L. N., *Seismic Wave Propagation in Stratified Media*, Cambridge University Press, 1983.
- Kurkjian, A. L., Numerical computation of individual far-field arrivals excited by an acoustic source in a borehole, *Geophysics*, *50*, 852–856, 1985.
- Kurkjian, A. L. and S. K. Chang, Acoustic multipole sources in fluid-filled boreholes, *Geophysics*, *51*, 148–163, 1986.
- Kynch, G. J., Longitudinal and screw vibrations of beams, *Nature*, *175*, 559, 1955.
- Lamb, H., *Hydrodynamics*, Cambridge University Press, 1879.
- Lanczos, C., *The Variational Principles of Mechanics*, University of Toronto Press, 1970.
- Landau, L. D. and E. M. Lifshitz, *Theory of Elasticity*, Pergamon Press Ltd., 1970.
- Lathi, B. P., *Signals, Systems and Communication*, John Wiley & Sons, Inc., 1965.
- Leveille, J. P. and A. J. Seriff, Borehole wave particle motion in anisotropic formations, *J. of Geophys. Res.*, *94*, 7183–7188, 1989.
- Love, A. E. H., *A Treatise on the Mathematical Theory of Elasticity*, Cambridge University Press, 1892.
- Lysmer, J., Lumped mass method for Rayleigh waves, *Bull. Seis. Soc. Am.*, *60*, 89–104, 1970.

- Lysmer, J. and L. A. Drake, A finite element method for seismology, in *Methods in Computational Physics; Seismology: Surface Waves and Earth Oscillations*, edited by B. A. Bolt, pp. 181–216, Academic Press Inc., 1982.
- Malvern, L. E., *Introduction to the Mechanics of a Continuous Medium*, Prentice-Hall, Inc., 1969.
- Mason, W. P., *Physical Acoustics and the Properties of Solids*, D. Van Nostrand Co., Inc., 1958.
- Mathews, J. and R. L. Walker, *Mathematical Methods of Physics*, Benjamin-Cummings Publishing Co., 1970.
- Mathieu, F., *Application of Full Waveform Acoustic Logging Data to the Estimation of Reservoir Permeability*, Master's thesis, Massachusetts Institute of Technology, 1984.
- McClellan, J. H., Two-dimensional spectrum analysis in sonic logging, *Acoustics, Speech, Signal Processing Magazine*, 3, 12–18, 1986.
- Miklowitz, J., *The Theory of Elastic Waves and Waveguides*, North-Holland Publishing Co., 1978.
- Mirsky, I., Axisymmetric vibrations of orthotropic cylinders, *J. Acoust. Soc. Am.*, 36, 2106–2112, 1964.
- Mirsky, I., Wave propagation in transversely isotropic circular cylinders, Part I: Theory, *J. Acoust. Soc. Am.*, 37, 1016–1021, 1965.
- More, J. J., The Levenberg-Marquardt algorithm: Implementation and theory, in *Lecture Notes in Mathematics*, no. 630, edited by G. A. Watson, pp. 105–116, Springer-Verlag, 1978.
- More, J. J., B. S. Garbow, and K. E. Hillstrom, *Users Guide for Minpack-1*, Argonne National Laboratory, 1982.

- Morse, R. W., Compressional waves along an anisotropic circular cylinder having hexagonal symmetry, *J. Acoust. Soc. Am.*, *26*, 1018–1021, 1954.
- Morse, P. M. and H. Feshbach, *Methods of Theoretical Physics*, McGraw-Hill Book Co., 1953.
- Musgrave, M. J. P., *Crystal Acoustics*, Holden-Day, Inc., 1970.
- Nelson, R. B., Natural vibrations of laminated orthotropic spheres, *Int. J. Solids Structures*, *9*, 305–311, 1973.
- Nelson, R. B., S. B. Dong, and R. D. Kalra, Vibrations and waves in laminated orthotropic circular cylinders, *J. Sound Vib.*, *18*, 429–444, 1971.
- Nicoletis, L. M. A., A. Bamberger, J. A. Quiblier, P. Joly, and M. Kern, Hole geometry and anisotropic effects on tube-wave propagation: A quasi-static study, *Geophysics*, *55*, 167–175, 1990.
- Norris, A. N., Stoneley-wave attenuation and dispersion in permeable formations, *Geophysics*, *54*, 330–341, 1989.
- Nowinski, J. L., Propagation of longitudinal waves in circular cylindrical orthotropic bars, *J. of Engineering for Industry, Trans. ASME*, *89*, 408–412, 1967, Series B.
- Nur, A. and G. Simmons, Stress-induced velocity anisotropy in rock: An experimental study, *J. of Geophys. Res.*, *74*, 6667–6674, 1969.
- Nye, N. F., *Physical Properties of Crystals*, Oxford University Press, 1957.
- Olsen, L. G. and K. Bathe, Analysis of fluid-structure interactions. a direct symmetric coupled formulation based on the fluid velocity potential, *Comput. Struct.*, *21*, 21–32, 1985.
- Parks, T. W., J. H. McClellan, and C. F. Morris, Algorithms for full-waveform sonic logging, in *Proceedings of the Second Acoustics, Speech, and Signal Processing Workshop on Spectral Estimation*, pp. 186–191, Tampa, Florida, 1983.

- Paternoster, B. J., *Effects of Layer Boundaries on Full Waveform Acoustic Logs*, Master's thesis, Massachusetts Institute of Technology, 1985.
- Peterson, E. W., Acoustic wave propagation along a fluid-filled cylinder, *J. Appl. Phys.*, *45*, 3340–3350, 1974.
- Phillips, F. C., *An Introduction to Crystallography*, Longmans, Green and Co., Ltd., 1963.
- Pochhammer, L., Über die Fortpflanzungsgeschwindigkeiten kleiner Schwingungen in einem unbegrenzten isotropen Kreiszylinder, *Journal für reine und angewandte Mathematik*, *81*, 324–336, 1876.
- Rayleigh, J. W. S., *The Theory of Sound*, vol. 1, The MacMillan Co., 1878.
- Redwood, M., *Mechanical Waveguides*, Pergamon Press Ltd., 1960.
- Roever, W. L., J. H. Rosenbaum, and T. F. Vining, Acoustic waves from an impulsive source in a fluid-filled borehole, *J. Acoust. Soc. Am.*, *55*, 1144–1157, 1974.
- Rosenbaum, J. H., Synthetic microseismograms: Logging in porous formations, *Geophysics*, *39*, 14–32, 1974.
- Schmitt, D. P., Effects of radial layering when logging in saturated porous formations, *J. Acoust. Soc. Am.*, *84*, 2200–2214, 1988a.
- Schmitt, D. P., Shear wave logging in elastic formations, *J. Acoust. Soc. Am.*, *84*, 2215–2229, 1988b.
- Schmitt, D. P., Acoustic multipole logging in transversely isotropic poroelastic formations, *J. Acoust. Soc. Am.*, *86*, 2397–2421, 1989.
- Schmitt, D. P., Y. Zhu, and C. H. Cheng, Shear wave logging in semi-infinite saturated porous formations, *J. Acoust. Soc. Am.*, *84*, 2230–2244, 1988.
- Schoenberg, M. and J. Douma, Elastic wave propagation in media with parallel fractures and aligned cracks, *Geophys. Prosp.*, *36*, 571–590, 1988.

- Simmons, G. and H. Wang, *Single Crystal Elastic Constants and Calculated Aggregate Properties: A Handbook*, Massachusetts Institute of Technology Press, 1971.
- Smith, M. L., The scalar equations of infinitesimal elastic-gravitational motion for a rotating, slightly elliptical Earth, *Geophys. J. Roy. Astron. Soc.*, *37*, 491–526, 1973.
- Smith, M. L. and F. A. Dahlen, The azimuthal dependence of Love and Rayleigh wave propagation in a slightly anisotropic medium, *J. of Geophys. Res.*, *78*, 3321–3333, 1973.
- Stephen, R. A., F. Cardo-Casas, and C. H. Cheng, Finite-difference synthetic acoustic logs, *Geophysics*, *50*, 1588–1609, 1985.
- Stevens, J. L. and S. M. Day, Shear velocity logging in slow formations using the Stoneley wave, *Geophysics*, *51*, 137–147, 1986.
- Strang, G., *Linear Algebra and Its Applications*, Academic Press Inc., 1980.
- Tarantola, A., *Inverse Problem Theory*, Elsevier Science Publ. Co., Inc., 1987.
- Thill, R. E., T. R. Bur, and R. C. Steckley, Velocity anisotropy in dry and saturated rock spheres and its relation to rock fabric, *Int. J. Rock Mech. Min. Sci. and Geomech.*, *10*, 535–557, 1973.
- Thomsen, L., Weak elastic anisotropy, *Geophysics*, *51*, 1954–1966, 1986.
- Thurston, R. N., Elastic waves in rods and clad rods, *J. Acoust. Soc. Am.*, *64*, 1–37, 1978.
- Toksöz, M. N., C. H. Cheng, and M. E. Willis, Seismic waves in a borehole — A review, in *Vertical Seismic Profiling, Part B: Advanced Concepts*, edited by M. N. Toksöz and R. R. Stewart, pp. 256–275, Geophysical Press, 1984.
- Tongtaow, C., *Transient response of an acoustic logging tool in transversely isotropic media*, Master's thesis, Colorado School of Mines, 1980.

- Tongtaow, C., *Wave propagation along a cylindrical borehole in a transversely isotropic formation*, PhD thesis, Colorado School of Mines, 1982.
- Tsang, L. and J. A. Kong, Asymptotic method for the first compressional head wave arrival in a fluid-filled borehole, *J. Acoust. Soc. Am.*, *65*, 647–654, 1979.
- Tsang, L. and D. Rader, Numerical evaluation of the transient acoustic waveform due to a point source in a fluid-filled borehole, *Geophysics*, *44*, 1706–1720, 1979.
- Tubman, K. M., C. H. Cheng, and M. N. Toksöz, Synthetic full waveform acoustic logs in cased boreholes, *Geophysics*, *49*, 1051–1059, 1984.
- Tubman, K. M., C. H. Cheng, S. P. Cole, and M. N. Toksöz, Synthetic full-waveform acoustic logs in cased boreholes, II – Poorly bonded casing, *Geophysics*, *51*, 902–913, 1986.
- White, J. E., *Underground Sound*, Elsevier Science Publ. Co., Inc., 1983.
- White, J. E. and F. A. Angona, Elastic wave velocities in laminated media, *J. Acoust. Soc. Am.*, *27*, 310–317, 1955.
- White, J. E. and C. Tongtaow, Cylindrical waves in transversely isotropic media, *J. Acoust. Soc. Am.*, *70*, 1147–1155, 1981.
- White, J. E. and R. E. Zechman, Computed response of an acoustic logging tool, *Geophysics*, *33*, 302–310, 1968.
- White, J. E., L. Martineau-Nicholetis, and C. Monash, Measured anisotropy in Pierre shale, *Geophys. Prosp.*, *31*, 709–729, 1983.
- Wiggins, R. A., A fast, new computational algorithm for free oscillations and surface waves, *Geophys. J. Roy. Astron. Soc.*, *47*, 135–150, 1976.
- Willen, D. E., A perturbative approach to sonic logging in a borehole, in *53th Ann. Internat. Mtg., Soc. Expl. Geophys., Expanded Abstracts*, pp. 1–2, Las Vegas, Nevada, 1983.

Winterstein, D. F., Anisotropy effects in *P*-wave and *SH*-wave stacking velocities contain information on lithology, *Geophysics*, *51*, 661–672, 1986.

Woodhouse, J. H. and F. A. Dahlen, The effect of a general aspherical perturbation on the free oscillations of the Earth, *Geophys. J. Roy. Astron. Soc.*, *53*, 335–354, 1978.

Zoback, M. D., D. Moos, and L. Mastin, Well bore breakouts and in situ stress, *J. of Geophys. Res.*, *90*, 5523–5530, 1985.